Micro-Hall Devices Based on High-Electron-Velocity Semiconductors

DISSERTATION
zur Erlangung des akademischen Grades
doctor rerum naturalium
(Dr. rer. nat.)
im Fach Physik

eingereicht an der
Mathematisch-Naturwissenschaftlichen Fakultät I
der Humboldt-Universität zu Berlin

von
Diplom-Physiker Vasyl Kunets
geboren am 20.02.1975 in Kiev, Ukraine

Präsident der Humboldt-Universität zu Berlin
Prof. Dr. Jürgen Mlynek

Dekan der Mathematisch-Naturwissenschaftlichen Fakultät I
Prof. Dr. Michael Linscheid

Gutachter:

1. Prof. Dr. W. T. Masselink
2. Prof. Dr. K. H. Ploog
3. Prof. Dr. K. R. Hofmann

eingereicht am:	13. Januar 2004
Tag der mündlichen Prüfung:	1. November 2004

Zusammenfassung

AlGaAs/GaAs- und AlGaAs/GaAs/InGaAs-Quantengraben-Strukturen mit dotiertem Kanal sowie modulationsdotierte AlGaAs/InGaAs/GaAs-Heterostrukturen auf Halbleitermaterialien mit hoher Elektronendriftgeschwindigkeit werden erfolgreich zur Herstellung von Mikro-Hall-Bauelementen eingesetzt. Mit Blick auf ihre Eignung als Magnetfeldsensoren werden die Signal-Linearität, die Sensitivität und das Rauschen bei schwachen und starken elektrischen Feldern untersucht.

Auch bei höheren elektrischen Feldern von mehr als 1.8 $\mathrm{kV \cdot cm^{-1}}$ zeigen die Bauelemente mit dotiertem Kanal eine ausgezeichnete Linearität des Signals. Magnetische Empfindlichkeiten von bis zu 600 $\mathrm{V \cdot A^{-1} \cdot T^{-1}}$ werden im Konstantstrombetrieb gemessen. Unter Verwendung eines Si-δ-dotierten pseudomorphen InGaAs-Quantengrabens wird sowohl eine bessere Sensitivität als auch ein besseres Rausch-verhalten erzielt als bei homogen dotiertem GaAs-Kanal. Als beste Signal-Rausch-Empfindlichkeit wird ein Wert von 138 $\mathrm{dB \cdot T^{-1}}$ erreicht für ein Bauelement von $10 \cdot 10$ μm Fläche (bei 300 K, 100 kHz Messfrequenz und 1 Hz Bandbreite). Da das elektrische Verhalten dieser Strukturen besonders durch die hohen Elektronendriftgeschwindigkeiten bestimmt wird, tritt auch bei hohen elektrischen Feldern bis zu 2.4 $\mathrm{kV \cdot cm^{-1}}$ keine Degradation des Bauelementes auf. Als niedrigste Nachweisgrenze für Magnetfelder wird ein Wert von 127 $\mathrm{nT \cdot Hz^{-1/2}}$ bestimmt.

Verglichen damit, zeigen die modulationsdotierten Bauelemente von $20 \cdot 20$ μm Größe zwar eine höhere Signal-Rausch-Empfindlichkeit von 141 $\mathrm{dB \cdot T^{-1}}$ bei geringen elektrischen Feldern, die sich aber bei höheren Feldstärken stark verschlechtert.

Daher haben die Bauelemente mit dotiertem Kanal und pseudomorph verspanntem InGaAs-Quantengraben unter Ausnutzung hoher Elektronendriftgeschwindigkeit bei hohen elektrischen Feldern einige Vorteile gegenüber den modulationsdotierten Strukturen mit hoher Elektronenbeweglichkeit.

Untersuchungen der thermischen Stabilität von Bauelementen mit modulationsdotiertem Quantengraben zeigen, dass eine dicke InGaAs-Schicht (innerhalb fixierter Gesamtdicke des GaAs/InGaAs-Kanals) erforderlich ist, um die parasitäre Parallel-Leitfähigkeit des GaAs-Kanals zu vermeiden. Unter Berücksichtigung dieser Erkenntnis und bei Verwendung eines hohen Dotierungsgrades werden ausgezeichnete Temperaturstabilitäten von 90 $\mathrm{ppm \cdot K^{-1}}$ im Konstantstrombetrieb und 192 $\mathrm{ppm \cdot K^{-1}}$ im Konstantspannungsbetrieb erzielt.

Unabhängig davon zeigen optische Untersuchungen mit Photolumineszenz-Spektroskopie und Raman-Streuung einen hohen Fehlordnungsgrad in dünnen InGaAs-Quantengräben, der dagegen für dicke pseudomorphe InGaAs-Schichten vernachlässigbar ist. Daher resultiert eine dickere InGaAs-Schicht nicht nur in einer höheren absoluten magnetischen Sensitivität und besseren thermischen Sta-

bilität, sondern auch in geringerem $1/f$-Rauschen als Ergebnis von Leitfähigkeitsfluktuationen.

Besondere Anstrengungen werden unternommen zum Einsatz der Rauschspektroskopie tiefer Zentren zur Untersuchung der Qualität von Halbleitervolumina bzw. -schichten. In Kombination mit den Untersuchungen der betriebsstromabhängigen Sensitivität erweist sich diese Methode als am Besten geeignet für die Optimierung von Mikro-Hall-Bauelementen.

Der Einfluss der Skalierung des Bauelementes auf seine Charakteristika wie Rauschen und magnetische Empfindlichkeit wird untersucht. Sowohl die Signal-Rausch-Empfindlichkeit als auch die Grenzempfindlichkeit sind größenabhängig. Der Einfluss der Geometrie auf die Verteilung des elektrischen Feldes wird für die Form eines Griechischen Kreuzes durch numerische Rechnungen simuliert und diskutiert. Abgerundete Ecken erweisen sich als am Besten geeignet für die Herstellung hochsensitiver und rauscharmer Mikro-Hall-Bauelemente.

Abstract

Doped-channel quantum well (QW) AlGaAs/GaAs and AlGaAs/GaAs/InGaAs as well as modulation-doped AlGaAs/InGaAs/GaAs heterostructures based on high electron drift velocity semiconductors are successfully applied to the fabrication of micro-Hall devices. Considering these devices as magnetic sensors, their properties were characterized in terms of signal linearity, sensitivity and noise at low and high electric fields.

Even at electric fields higher than 1.8 $\mathrm{kV \cdot cm^{-1}}$, the doped-channel devices exhibit an excellent signal linearity. Magnetic sensitivities up to 600 $\mathrm{V \cdot A^{-1} \cdot T^{-1}}$ in current drive mode are measured. The usage of a Si-δ-doped pseudomorphic InGaAs QW results in better sensitivity and noise performance than does uniformly doped GaAs. A maximal signal-to-noise sensitivity (SNS) of 138 $\mathrm{dB \cdot T^{-1}}$ is achieved in a 10 μm square size device at 300 K, 100 kHz frequency and 1 Hz bandwidth. Because the performance in these structures is driven in part by the high electron drift velocity, it does not degrade even at high electric fields up to 2.4 $\mathrm{kV \cdot cm^{-1}}$ and corresponds to a lowest detection limit of 127 $\mathrm{nT \cdot Hz^{-1/2}}$. Comparatively, the modulation-doped devices of 20 μm square size exhibit a higher SNS of 141 $\mathrm{dB \cdot T^{-1}}$ at low electric fields, but degrade at higher fields. Thus, the doped-channel pseudomorphically strained InGaAs QW high-velocity devices have several advantages over modulation-doped high-mobility structures at high electric fields.

Thermal stability studies of doped-channel QW devices reveal a thick InGaAs layer (within a fixed total thickness of the GaAs/InGaAs channel) necessary to avoid the parasitic parallel conductivity in GaAs channel. Using this result and a high doping level, superior temperature stabilities of 90 $\mathrm{ppm \cdot K^{-1}}$ in the current drive mode and 192 $\mathrm{ppm \cdot K^{-1}}$ in the voltage drive mode are attained.

Independently, optical studies like photoluminescence and Raman scattering reveal a high degree of disorder in thin InGaAs QWs, being negligible for thick pseudomorphic InGaAs layers. Hence, a thick InGaAs layer causes not only a higher absolute magnetic sensitivity and a better thermal stability, but also lower $1/f$ noise being a result of conductivity fluctuations.

Special effort is devoted to the application of deep level noise spectroscopy as a very sensitive probe for semiconductor bulk and layer quality. Combined with supply-current-related sensitivity studies, this method is most suitable for micro-Hall device optimization.

The effect of device scaling on device characteristics like noise and absolute magnetic sensitivity is studied. Both the SNS and detection limit are shown as size-dependent. Additionally, geometry effects on the electric field distribution for Greek cross shapes are simulated by numerical calculations and discussed. Rounded corners appear as most appropriate for the fabrication of highly sensitive low-noise micro-Hall devices.

Contents

List of Publications

Parts of this work have already been published or accepted for publication:

Vas.P. Kunets, H. Kissel, U. Müller, C. Walther, W.T. Masselink, Yu.I. Mazur, G.G. Tarasov, Z.Ya. Zhuchenko, S.R. Lavoric, M.Ya. Valakh, *Thickness dependence of disorder in pseudomorphic modulation-doped* $Al_xGa_{1-x}As/In_yGa_{1-y}As/GaAs$ *heterostructures*, Semicond. Sci. Technol. **15** (11), 1035-1038 (2000).

Vas.P. Kunets, W. Hoerstel, H. Kostial, H. Kissel, U. Müller, G.G. Tarasov, Yu.I. Mazur, Z.Ya. Zhuchenko, W.T. Masselink, *High electric field performance of* $Al_{0.3}Ga_{0.7}As/GaAs$ *and* $Al_{0.3}Ga_{0.7}As/GaAs/In_{0.3}Ga_{0.7}As$ *quantum well micro-Hall devices*, Sens. Actuators A **101** (1-2), 62-68 (2002).

H. Kissel, U. Zeimer, A. Maaßdorf, M. Weyers, R. Heitz, D. Bimberg, Yu.I. Mazur, G.G. Tarasov, Vas.P. Kunets, U. Müller, Z.Ya. Zhuchenko, W.T. Masselink, *Behavior of the Fermi-edge singularity in the photoluminescence spectra of a high-density two-dimensional electron gas*, Phys. Rev. B **65** (23), 235320, 6 p., (2002).

Yu.I. Mazur, G.G. Tarasov, Z.Ya. Zhuchenko, H. Kissel, U. Müller, Vas.P. Kunets, W.T. Masselink, *Interaction between the Fermi-edge singularity and optical phonons in* $Al_xGa_{1-x}As/In_yGa_{1-y}As/GaAs$ *heterostructures*, Phys. Rev. B **66** (3), 035308, 7 p., (2002).

Vas.P. Kunets, Z.Ya. Zhuchenko, H. Kissel, U. Müller, G.G. Tarasov, W.T. Masselink, *Many-body effects as probe of defects presence in heavily doped AlGaAs/InGaAs/GaAs heterostructures*, 29th Int. Symposium on Compound Semiconductors, Lausanne/Switzerland, 7.-10. October 2002, in: Inst. Phys. Conf. Ser. No.174: Section 2, 81-83 (2003).

Vas.P. Kunets, J. Dobbert, W. Hoerstel, H. Kostial, H. Kissel, U. Müller, G.G. Tarasov, Yu.I. Mazur, W.T. Masselink, *Sensitivity and noise in doped-channel* $Al_{0.3}Ga_{0.7}As/In_yGa_{1-y}As$ *quantum well micro-Hall devices operated at high electric fields*, DPG-Frühjahrstagung, Dresden/Germany, 24.-28. March 2003, in: Verhandlungen der Deutschen Physikalischen Gesellschaft, Reihe VI, Band 38, 238 (2003).

Vas.P Kunets, U. Müller, J. Dobbert, R. Pomraenke, G.G. Tarasov, W.T. Masselink, H. Kostial, H. Kissel, Yu.I. Mazur, *Generation-recombination noise in doped-channel* $Al_{0.3}Ga_{0.7}As/GaAs/In_{0.2}Ga_{0.8}As$ *quantum well micro-Hall devices*, J. Appl. Phys. **94** (12), 7590-7593 (2003).

Vas.P. Kunets, R. Pomraenke, J. Dobbert, H. Kissel, U. Müller, H. Kostial, E. Wiebicke, G.G. Tarasov, Yu.I. Mazur, W.T. Masselink, *Generation-recombination noise in pseudomorphic modulation-doped $Al_{0.2}Ga_{0.8}As/In_{0.1}Ga_{0.9}As/GaAs$ micro-Hall devices*, IEEE Sensors Journal (2004) (accepted).

Vas.P. Kunets, J. Dobbert, W. Hoerstel, U. Müller, G.G. Tarasov, W.T. Masselink, H. Kostial, E. Wiebicke, H. Kissel, Yu.I. Mazur, *Low thermal drift in highly sensitive doped-channel $Al_{0.3}Ga_{0.7}As/GaAs/In_{0.2}Ga_{0.8}As$ micro-Hall element*, (2004) (to be published).

Chapter 1

Introduction

One of the unique and fundamental features studied in solid state physics is the movement of charge carriers (electrons or holes) in bulk semiconductors. The investigation of this phenomenon over the past decades initiated the ongoing development of solid state electronics as a branch of solid state physics and its practical application to electronic devices.

Two carrier movement types are distinguished: coherent and random. The first one relies on the effect of internal or external electromagnetic forces on charged particles. For the first time observed in 1879 by the American physicist E.H. Hall [1], just the Hall effect is one of the striking examples demonstrating the carrier behavior in an external electromagnetic field. The two main quantities characterizing the coherent movement are the drift velocity and the mobility of the carriers, respectively. Both are essential for electronic device applications since devices rely on the carrier movement. Indeed, they determine both the operational speed and the threshold sensitivity of an electronic solid state device. On the other hand, the random carrier movement and its local fluctuations define the device noise and the carrier scattering processes on their part having impact on electron drift velocity and electron mobility.

The recent progress in modern semiconductor technology allows to restrict the carrier movement in one, two or even all three spatial dimensions. This reduced dimensionality of the electron gas offers the purposive application of the quantum phenomena, targeting to new and superior electron devices.

For example, extremely high electron mobilities were gained in two-dimensional (2D) systems based on III-V materials, using an undoped spacer layer to separate the 2D electron gas and the ionized impurities spatially [2, 3, 4]. Furthermore, the electron devices based on these modulation-doped systems exhibit a very low noise level due to the high electron mobility and the nanoscale conductive channel thickness. Thus, high performance low-noise high electron mobility transistors (HEMTs) were fabricated [5].

Beside these specific electron devices, magnetic field sensors are of particular interest for application purposes. Hall effect devices are the most commonly used magnetic field sensors. For the detection of very small magnetic fields, only a very high drift velocity electron provides an adequate deflection. Therefore, materials with a high electron drift velocity are most appropriate.

Compared to Hall devices on bulk semiconductor materials, a significant improvement of the basic device characteristics was attained by the usage of high electron drift velocity materials and selective doping with different profiles and corresponding doping levels in two-dimensional systems [6, 7]. Relying on these advanced Hall sensors with micron-range lateral sizes and an absolute magnetic detectivity in the nT-range, improved scanning techniques for magnetic field imaging like the scanning Hall probe microscopy (SHPM) [8, 9] and the magnetic force microscopy (MFM) [10] were introduced. Furthermore, these micro-Hall devices were applied to studies of highly inhomogeneous magnetic fields produced by ferromagnetic nanoparticles [11, 12, 13] and vortices in superconductors [14, 15, 16]. Recently, a new method for the detection of nuclear magnetic resonance (NMR) and electron spin resonance (ESR) was proposed [17], using advanced micro-Hall devices successfully.

Beside their application in physical and material sciences, techniques using micro-Hall devices are of particular interest in other fields. Recently, natural magnetic nanoparticles in living organisms like magnetotactic bacteria [18, 19] were investigated. Using micro-Hall devices as scanning tips in the noncontact magnetic force microsopy, the magnetic moment of an individual bacterial cell was measured, being about 10^{-13} emu [20]. However, so far these experiments revealed a poor spatial resolution and a difficulty in quantifying the results. Obviously, the spatial resolution could be significantly improved by down-scaled device active sizes in the sub-micron range. Unfortunately, any device size reduction results in a decreased absolute magnetic sensitivity which scales with the device width.

Furthermore, the strength of the electric field in the device active area rises considerably. On their part, the high electric fields result in an increased noise level and decreased mobility, restricting both the signal-to-noise sensitivity and the detection limit. These drawbacks are most critical for micro-Hall sensors based on modulation-doped heterostructures. Additionally, a thick doped barrier serving as an electron supply layer within a selectively-doped system can be an additional source of generation-recombination noise and constitute an undesirable parallel conductive channel, thus degrading the device thermal stability.

Alternatively, the application of doped-channel quantum well heterostructures allows partially to defuse these drawbacks of modulation-doped micro-Hall devices. Although their low-field mobility is much lower compared to modulation-doped heterostructures due to prevailing scattering on ionized impurities [21], their basic characteristics are expected to be comparable to that of the competing modulation-doped devices. This anticipation relies on the high electron drift velocity, much more dramatically defining the device performance than the low-field mobility [22].

Since the scattering on ionized impurities has a considerable impact on carrier transport in these heterosystems, one has to account for a completely different behavior of the electron mobility at high electric fields [23], compared to modulation-doped systems. Out of it, one can expect a positive effect on both signal-to-noise sensitivity and detection limit of the micro-Hall device. Because scattering on ionized impurities does not contribute significantly to 1/f (flicker) noise [24], the noise level should be very low. Using a proper heterostructure design, doped-channel micro-Hall devices can exhibit a superior device temperature stability due to the almost temperature independent behavior of both low-field electron mobility and electron concentration.

This thesis targets to doped-channel micro-Hall devices with low noise, high sensitivity and high temperature stability - operating also at high electric fields - using III-V semiconductors with high electron drift velocities. In-depth studies of the structural, transport and noise properties are applied for a comparison of doped-channel $\mathrm{Al}_x\mathrm{Ga}_{1-x}\mathrm{As}/\mathrm{GaAs}$ and $\mathrm{Al}_x\mathrm{Ga}_{1-x}\mathrm{As}/\mathrm{GaAs}/\mathrm{In}_y\mathrm{Ga}_{1-y}\mathrm{As}$ to modulation-doped $\mathrm{Al}_x\mathrm{Ga}_{1-x}\mathrm{As}/\mathrm{In}_y\mathrm{Ga}_{1-y}\mathrm{As}/\mathrm{GaAs}$ heterostructures.

Using a gas source molecular beam epitaxy system Riber 32-P, various doped-channel and modulation-doped heterostructures were grown. Different experimental techniques like photoluminescence and Raman spectroscopy, electrical measurements (Hall effect and noise spectroscopy) and x-ray diffraction were applied. Based on these results, the growth of the lattice matched and the pseudomorphically strained heterostructures was optimized. Micro-Hall sensors of different geometries and sizes were fabricated by standard optical photolithography, followed by contact metallization and formation. Using geometrical magnetoresistance and different modified Hall measurements, the main device characteristics were studied. Being a quite powerful and informative experimental technique for the investigation of planar devices, the deep level noise spectroscopy (DLNS) proved itself to prominently contribute to both improved understanding and subsequent optimization of micro-Hall devices.

The thesis is organized as follows: Chapter 2 reviews the main experimental and theoretical fundamentals serving as the necessary prerequisites for an optimized micro-Hall device design. The device fabrication, the x-ray studies and the optimization of the contact resistance are described in Chapter 3. In Chapter 4, the photoluminescence and the Raman studies of modulation-doped heterostructures are described. Being very sensitive to the layer and interface quality, these methods were successfully applied for the layer quality evaluation and for the growth optimization of the strained AlGaAs/InGaAs/GaAs heterostructures. Deep levels acting as an additional sources of generation-recombination noise negatively contributing to the micro-Hall device noise performance were investigated by DLNS. These studies together with that of crystal quality are subject of Chapter 5. Studies of the main device characteristics like linearity, sensitivity, signal-to-noise sensitivity and detection limit are discussed in detail in Chapter 6. Some effort was devoted to the optimization of thermal drift performance and geometry of the studied micro-Hall devices also in Chapter 6.

Chapter 2

Physics of quantum well Hall effect devices

2.1 Electronic properties

Using modern semiconductor technology such as molecular-beam epitaxy (MBE) [25, 26], metal-organic chemical vapor deposition (MOCVD) [27, 28], hot-wall epitaxy (HWE) [29] or liquid-phase epitaxy (LPE) [30], the epitaxial growth of low-dimensional systems can be realized. The low-dimensional systems are classified corresponding to the confinement of charge carriers in one, two or all three dimensions as quantum wells (2D), quantum wires (1D), and quantum dots (0D), respectively. The confinement of the carriers leads to the so-called quantum size effects when the de Broglie wavelength of carriers $\lambda = h/\sqrt{2m\bar{\varepsilon}}$ is comparable to the characteristic specimen size d. Here h is Planck's constant, m the mass of charge carriers, and $\bar{\varepsilon}$ the characteristic conduction electron energy. As a result of carrier confinement, the optical and electrical properties of low-dimensional systems are modified with respect to bulk semiconductor materials due to a quantization of the eigenenergies in the direction of restriction and a parabolic dispersion due to free motion in all remaining directions. To find energy spectra and wave functions for electrons and holes, one has to solve the quantization problem for both cases.

2.1.1 Energy spectrum of electrons and holes

The electronic states in a two-dimensional system can be described within the effective mass approximation (EMA). The criterion for the validity of this approach in a two-dimensional system has been discussed in detail [31]. We consider the simplest quantum problem when the low band gap GaAs layer (quantum well or material A) is embedded between two thick AlGaAs layers with larger band gap (quantum barriers or material B). The heterostructure is schematically shown in Fig. 2.1. In this system, the band gap difference is distributed between valence

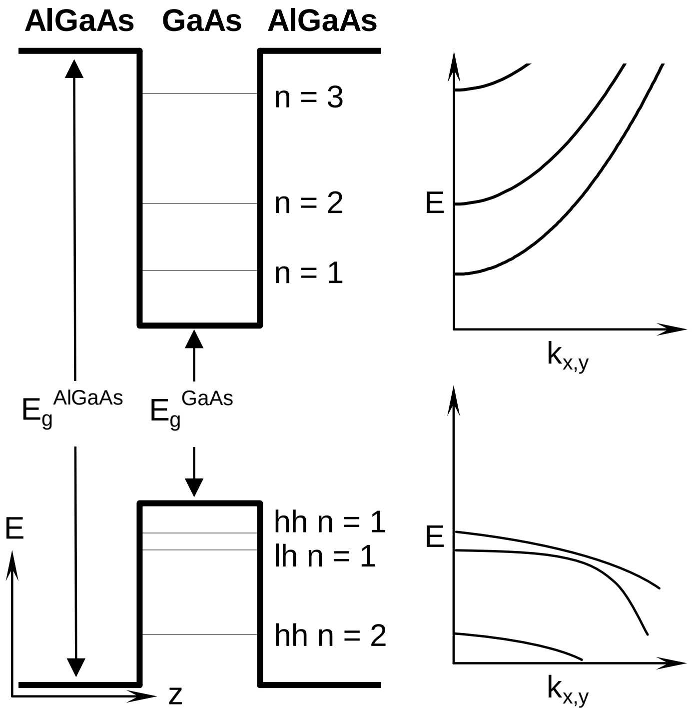

Figure 2.1: Schematic representation of the GaAs quantum well embedded between AlGaAs barriers in real and k spaces.

and conduction bands in a such way that both electrons and holes are confined to the smaller band gap GaAs layer. Such a heterojunction type is called a type I system. In the present work, we will consider only this type of heterosystem. The thickness of the AlGaAs layers is much greater than the penetration length of the confined electron wave function. The wave function in each material takes the form [32]

$$\Psi = \sum_{A,B} u_{c\mathbf{k}}^{A,B}(\mathbf{r}) e^{i\mathbf{k}_\perp \cdot \mathbf{r}} \chi_n(z), \tag{2.1}$$

where z is the direction of growth, $\mathbf{k}_\perp$ the transverse electron wave vector, $u_{c,\mathbf{k}}(\mathbf{r})$ the Bloch wave function, $\chi_n(z)$ the envelope wave function, and n labels the eigenstates.

In order to find the wave functions and energy spectrum of electrons in a quantum well of thickness t, one has to solve the Schrödinger-like equation

$$\left(\frac{\hbar^2}{2} \frac{\partial}{\partial z} \frac{1}{m^*(z)} \frac{\partial}{\partial z} + V_{eff}(z) \right) \chi_n(z) = E_n \chi_n(z), \tag{2.2}$$

where $m^*(z)$ is the electron effective mass, and $V_{eff}(z)$ the effective potential energy

$$V_{eff}(z) = E_c(z) + V_D(z) + V_{ee}(z), \tag{2.3}$$

where $E_c(z)$ is the heterojunction conduction band discontinuity, $V_D(z)$ the electrostatic potential due to ionized donors and acceptors, and V_{ee} the self-consistent Hartree and exchange potentials due to free carriers.

Assuming parabolic bands for simplicity, the total energy relative to the band minima (maxima) can be found as

$$E_{n,k} = \frac{\hbar^2 k^2}{2m^*_{\|}} + E_n, \tag{2.4}$$

where $m^*_{\|}$ is the electron effective mass parallel to the interface.

At the interfaces, continuity of both the envelope wave function χ_n and $[1/m^*]\,[\partial\chi_n(z)/\partial z]$ has to be postulated.

Assuming a low free carrier density ($< 10^{10}$ cm^{-2}), the terms $V_D(z)$ and $V_{ee}(z)$ are small and can be neglected. Assuming potential barriers being large compared to the bound state energies E_n (infinitely deep well approximation) and vanishing envelope functions at the points $z = 0,\, t$ (the left interface is taken as the origin), the solutions are

$$\chi_n(z) = \sqrt{\frac{2}{t}} \sin\left(\frac{n\pi z}{t}\right), \quad n = 1,\, 2, ... \tag{2.5}$$

The corresponding eigen-energies are given by

$$E_n = \frac{n^2\hbar^2\pi^2}{2m^*_z t^2}. \tag{2.6}$$

The solution of the quantization problem for hole states in the quantum well is much more complicated. For the case of a finite quantum well, only numerical results could be obtained [33].

In bulk material, hole bands can be described by the Kane model, using a basis function with angular momentum $J = 3/2$ symmetry. Then the 4 - fold degeneracy at $k = 0$ is implied and the spin-orbit split-off valence band is neglected. The dispersion near $k = 0$ is given by the Luttinger Hamiltonian [34]:

$$\begin{array}{l} H = \frac{\hbar^2}{2m_0}[\left(\gamma_1 + \frac{5}{2}\gamma_2\right) k^2 - 2\gamma_2 \left(k_x^2 J_x^2 + k_y^2 J_y^2 + k_z^2 J_z^2\right) \\ -4\gamma_3 \left(\{k_x \cdot k_y\} \{J_x \cdot J_y + \cdots\}\right)] \end{array}, \tag{2.7}$$

where γ_1, γ_2, γ_3 are the Luttinger parameters of the valence band and the symbol $\{\cdot\}$ reperesents the anticommutation, i.e.

$$\{k_x \cdot k_y\} = k_x k_y + k_y k_x. \tag{2.8}$$

Taking as the quantization axes, z and k_z in a [100] direction, the kinetic energy of the heavy holes ($J_z = \pm 3/2$) and light holes ($J_z = \pm 1/2$) can be expressed as

$$\begin{array}{l} E = \frac{\hbar^2 k_z^2}{2m_0}\left(\gamma_1 - 2\gamma_2\right), \quad J_z = \pm\frac{3}{2} \\ E = \frac{\hbar^2 k_z^2}{2m_0}(\gamma_1 + 2\gamma_2), \quad J_z = \pm\frac{1}{2} \end{array}, \tag{2.9}$$

where the heavy hole and light hole masses in the [100] direction are $m_0/(\gamma_1 - 2\gamma_2)$ and $m_0/(\gamma_1 + 2\gamma_2)$, respectively.

In the infinitely deep quantum well in the spherical approximation, i.e. $\gamma_2 = \gamma_3 = \overline{\gamma}$, the hole levels at $k = 0$ are given by

$$E_{(1,h)z} = n^2 \frac{\pi^2 \hbar^2}{2m_0 t^2}(\gamma_1 \pm 2\overline{\gamma}) \tag{2.10}$$

and the hole effective mass can be derived as

$$\frac{1}{m_{(1,h)z}} = 2\left(\frac{\partial^2 E_{(1,h)z}}{\partial k_\perp^2}\right)_{k_\perp = 0}. \tag{2.11}$$

2.1.2 Density of states of 2D electron gas

The density of states of the two-dimensional electron gas (2DEG) is a necessary prerequisite for the calculation of the two-dimensional (2D) electron concentration n_{2D} in the quantum well. The density of states can be calculated as

$$D(E) = \sum_{\alpha_s, \eta_v, n, \mathbf{k}} \delta\left(E - E_{n,k}\right), \tag{2.12}$$

where α_s, η_v are the spin and valley degeneracy in the case of multi-valley minima. Assuming parabolic conduction band minima and using Eq. (2.4) in this approximation, the two-dimensional density of states can be rewritten as

$$\begin{array}{l} D(E) = 2\eta_v \sum\limits_n \frac{1}{2\pi} \int\limits_0^\infty dkk\delta\left(E - E_n - \frac{\hbar^2 k^2}{2m_\parallel}\right) dk \\ = \sum\limits_n \frac{\eta_v m_\parallel}{\pi\hbar^2}\theta\left(E - E_n\right) = \sum\limits_n D_0 \theta\left(E - E_n\right) \end{array}, \tag{2.13}$$

where a two-fold spin degeneracy per state is considered and θ is the unit step function. This result will now be compared to the three-dimensional density of states of a 3D system (bulk material). The density of states for the 3D system is given by

$$D_{3D} = \frac{\sqrt{2} m_\parallel^{3/2} E^{1/2}}{\pi^2 \hbar^3}. \tag{2.14}$$

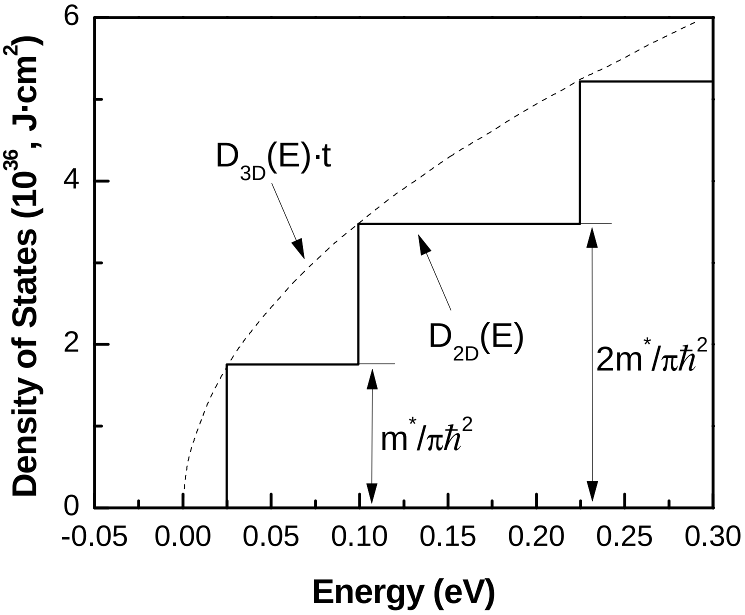

Figure 2.2: 2D density of states in comparison with 3D density of states as function of energy for 15 nm $Al_{0.3}Ga_{0.7}As$/GaAs quantum well (after Ferry [35]).

In the infinitely deep quantum well approximation, the relation $D_{3D} \cdot t = D_{2D}$ holds true. Figure 2.2 represents the 2D compared to the 3D density of states for a 15-nm GaAs infinite quantum well [35].

Thus, the two-dimensional electron concentration in the quantum well of thickness t can be calculated, using

$$n_{2D} = \int_0^\infty D(E) f_0(E) dE = k_B T D_0 \sum_n \ln\left(1 + e^{(E_F - E_n)/k_B T}\right), \tag{2.15}$$

where f_0 is the Fermi function for electrons, k_B the Boltzmann constant, E_F the Fermi energy and T the temperature of the electron gas.

2.2 Electrical properties

The successful design of any semiconductor device is based on the proper knowledge of semiconductor material properties and the operational physical phenomena in device structures. The electron scattering has to be considered as such a main physical phenomenon. Actually, just electron scattering determines the upper limits of both the electron mobility and the drift velocity, thus defining the speed of semiconductor device operation. Furthermore, scattering as a random process establishes the lower limit on electron noise and thus defines the threshold sensitivity of semiconductor devices. One has to distinguish between devices based on parallel and perpendicular transport phenomena.

The first device type relies on electron motion along the layers, i.e. parallel to the interfaces [high electron mobility transistor (HEMT), modulation doped field effect transistor (MODFET), Hall effect devices, etc.]. The second one uses electron transfer in the direction perpendicular to the layers and interfaces, respectively [heterojunction bipolar transistor (HBT), hot electron transistor (HET), tunneling hot electron transistor amplifier (THETA), quantum cascade lasers (QCL), etc.].

Here we will only briefly describe parallel transport phenomena at low and high electric fields, being the basic operational processes of quantum well Hall effect devices. The influence of different scattering mechanisms on basic device characteristics such as sensitivity, thermal stability and noise will be discussed.

2.2.1 Electron scattering: low-field mobility

The scattering mechanisms in bulk materials are well studied. An overview of various scattering mechanisms in bulk GaAs was given by Nag [36] and is presented in Fig. 2.3.

The influence of various scattering mechanisms on the mobility of bulk GaAs is presented in Fig. 2.4, including experimental data for high-purity VPE GaAs [37].

Obviously, the electron mobility of bulk GaAs is mainly determined by scattering on polar optical phonons at high temperatures and on ionized impurities

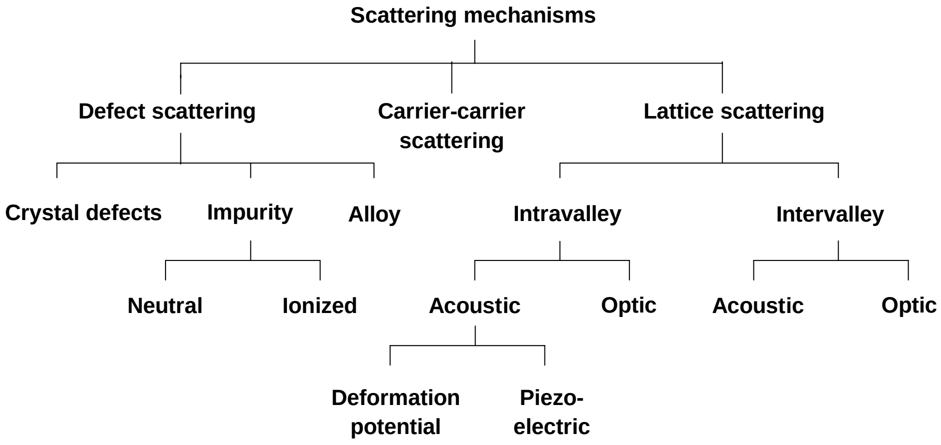

Figure 2.3: The outline of different scattering mechanisms in bulk GaAs (after Nag [36]).

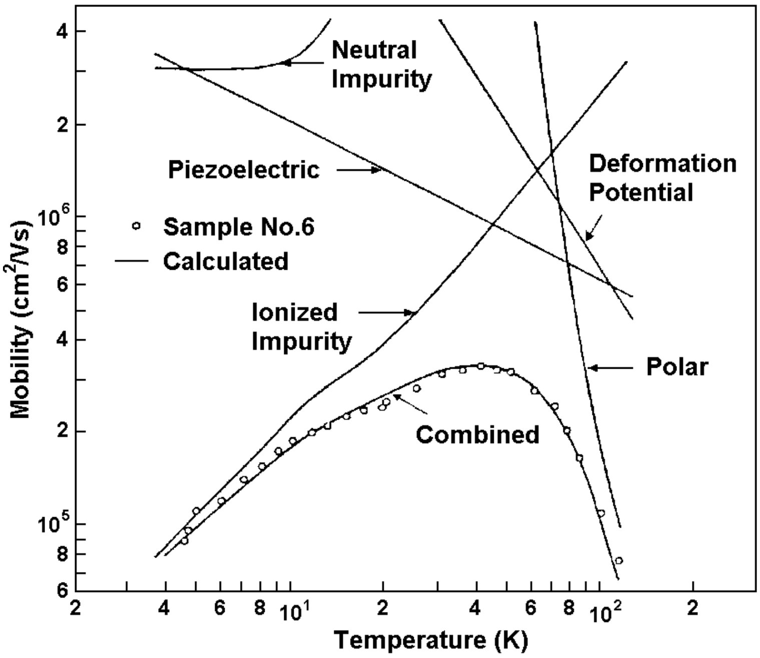

Figure 2.4: Experimental temperature variation of the mobility of the high purity GaAs VPE sample and calculated mobility curves for each scattering process acting separately and for all scaterring process combined (after Stilman et al. [37]).

at low temperatures. The scattering due to electron-electron interaction for electron concentrations less than 10^{18} cm^{-3} has negligible influence and will not be considered.

For heterostructures, some additional scattering mechanisms have to be accounted for: (1) interface roughness scattering; (2) intersubband scattering between the quantized levels of the quantum well; (3) remote impurity scattering in the barrier material; (4) scattering on the barrier phonons (observed in AlGaAs/GaAs heterostructures); (5) scattering by alloy disorder when compound semiconductor materials are used as barrier or channel. Subsequently, some of these scattering mechanisms being most important for Hall effect device application will be reviewed.

Scattering by remote ionized impurities is an essential scattering process within modulation-doped heterostructures. It was well demonstrated for GaAs/AlGaAs modulation-doped heterostructures, which have been studied extensively [38].

Doping the barrier AlGaAs material apart from the interface, the free carriers in the channel are spatially separated from ionized donors located in the barrier. Thus, the influence of ionized-impurity scattering on the 2DEG can be nearly suppressed. Results of self-consistent calculations for a GaAs/AlGaAs heterojunction are presented in Fig. 2.5 (after Ando [39]). Referring to this work, the relaxation time for scattering electrons in the lowest (first) subband is given by

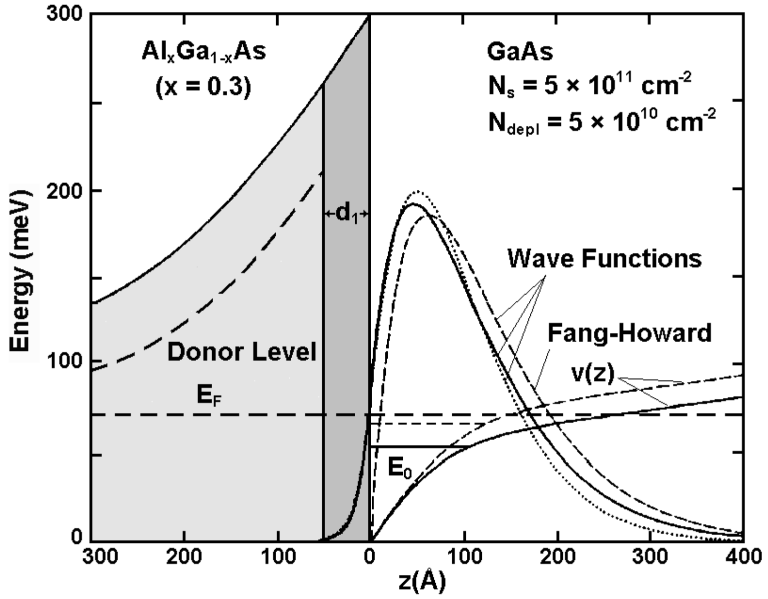

Figure 2.5: Calculations of the lowest subband of an GaAs/Al$_{0.3}$Ga$_{0.7}$As heterojunction, the electron wave function and the self-consistent potential by using variational wave functions. The dotted line represents the wave function calculated numerically in comparison with Fang-Howard results [40]. The spacer thickness d_1 is 50 Å and the binding energy E_B of donor levels in Al$_x$Ga$_{1-x}$As is about 50 meV (after [39]).

$$\frac{\hbar}{\tau_c(k)} = 2\pi \int dz N(z) \sum_q \left[\frac{2\pi e^2}{q\varepsilon(q)}\right] |F(q,z)|^2 (1-\cos\theta)\delta(E_{\mathbf{k}} - E_{\mathbf{k-q}}) \ , \tag{2.16}$$

where $N(z)$ is the doping profile, $q = 2k\sin(\theta/2)$, and $E_k = \hbar^2k^2/2m^*$, where $\mathbf{k}$ is the wave vector and θ the scattering angle. The static dielectric function is given by

$$q\varepsilon(q) = q + (2\pi e^2/\xi)(2m^*/2\pi\hbar^2)F(q), \tag{2.17}$$

where ξ is the dielectric constant and m^* the electron effective mass.

The doping profile for a modulation-doped heterostructure, $N(z)$, is assumed to be

$$N(z) = \begin{cases} 0 & (-d_1 < z), \\ N_D + N_A & (-d_1 - d_2 < z < -d_1), \\ 2N_A & (z < -d_1 - d_2), \end{cases} \tag{2.18}$$

where N_A and N_D are donor and acceptor concentrations respectively, and d_2 the thickness of AlGaAs barrier.

The form factor F is defined as

$$F(q,z) = \int dz' \left|\chi\left(z'\right)\right|^2 \exp\left(-q\left|z - z'\right|\right), \tag{2.19}$$

$$F(q) = \int dz \int dz' \left|\chi\left(z\right)\right|^2 \left|\chi\left(z'\right)\right|^2 \exp\left(-q\left|z - z'\right|\right), \tag{2.20}$$

where $\chi(z)$ is a wave function given by

$$\chi(z) = \begin{cases} Bb^{1/2}(bz + \beta)\exp(-bz/2) & (z > 0), \\ B'b'^{1/2}\exp(b'z/2) & (z < 0), \end{cases} \tag{2.21}$$

where b, b', β, B, B' are variational parameters. The parameters β, B, B' can be expressed in terms of b and b' through the boundary conditions at $z = 0$ and the normalization.

The sum over q in Eq. (2.16) may be replaced by an integral over θ, so that Eq. (2.16) is written as [21]

$$\frac{\hbar}{\tau_c(k)} = \frac{4\pi m^* e^4}{\hbar^2} \int_0^\pi d\theta (1 - \cos\theta) \frac{1}{[q\varepsilon(q)]^2} \int dz \, |F(q,z)|^2 \, N(z). \tag{2.22}$$

Finally, the mobility is given by

$$\mu(T) = e\,\langle \tau_c \rangle / m^*. \tag{2.23}$$

Thus, the temperature dependence of $\mu(T)$ is determined by the k-averaged relaxation time τ_c.

Numerical simulations of this mechanism revealed the following results for larger spacer thicknesses [39]: suppressed scattering by remote ionized impurities and increased electron mobility. Some results are shown in Fig. 2.6 for a GaAs/AlGaAs heterojunction.

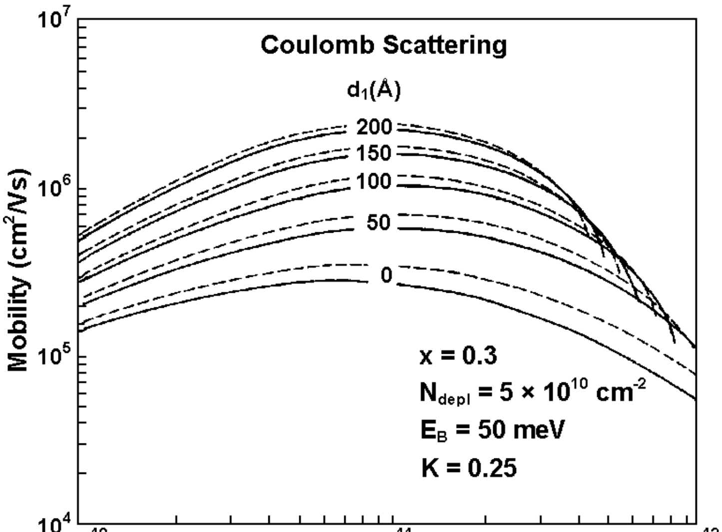

Figure 2.6: An example of calculated mobility limited by charged centers in the Al$_x$Ga$_{1-x}$As layer. At each electron concentration N_s, the effective doping $N_D - N_A$ is determined by the charge neutrality condition and the equulibrium condition between the electron system and donors levels in the Al$_x$Ga$_{1-x}$As layer. The total concentration of charges, $N_D + N_A$, is determined by assuming $N_A/N_D = 0.25$. (after [39]).

Ionized-impurity scattering of two-dimensional quantum-confined carriers in a quantum well has to be considered as the second important mechanism here. If the quantum well region is intentionally doped, this type of scattering dominates at low temperatures.

All the above considered equations also hold true as in case of scattering by remote ionized impurities. However, the doping profile, $N(z)$ differs significantly: According to Masselink [21], the doping profile $N(z)$ for symmetrically doped samples is expressed as

$$N(z) = \begin{cases} (1/ut)\, n_{2D}, & |z| < ut/2, \\ 0, & |z| > ut/2, \end{cases} \tag{2.24}$$

where t is the quantum well width and u the doped well fraction. In case of δ-doping, the doping profile is written as

$$N(z) = n_{2D}\delta\left(z - z_\delta\right), \tag{2.25}$$

where z_δ is the position of the δ-doping spike.

For an electron confinement in two dimensions as here, one has to consider (i) the screening effects of the two dimensional electron gas being quite different from 3D case [41] and (ii) the overlap of the electron wave function with ionized impurities. The overlap with impurities is described by

$$N_{eff}(q) = \frac{1}{t}\int \left|F(q,z)\right|^2 N(z)dz. \tag{2.26}$$

Experimental data on electron mobility vs. temperature dependence for a 100 Å-wide Si-doped GaAs quantum well are presented in Fig. 2.7 after [21] and compared to bulk GaAs material with the same electron concentration. The doping profile comprises 84 % of the well width, in order to prevent a DX-center formation near the interfaces. Obviously, the 2DEG electron mobility of the 100 Å-wide GaAs well is significantly lower than the bulk GaAs value at the same doping level. The dashed line shows the mobility (corrected measurement data) of a GaAs quantum well, assuming the same doping concentration but with doping profile spread over the whole thickness of the quantum well. Moreover, progressively wider wells lead to progressively higher mobilities, apparently asymptotically approaching the bulk GaAs value [21].

These results indicate ionized impurity scattering being more effective over a broad temperature range for electron gas in quantum well compared to bulk material. Accordingly, just a quantum well δ-doping profile is of particular interest. Experimental results on mobility vs. temperature dependence for different doped GaAs quantum well fractions are shown in Fig. 2.8. The data include the case of a center-δ-doped quantum well. Obviously, the lowest mobility is observed for the δ-doped quantum well. An increased thickness of the doped GaAs layer enhances the mobility as well as displaces the δ-doping spike sidewards.

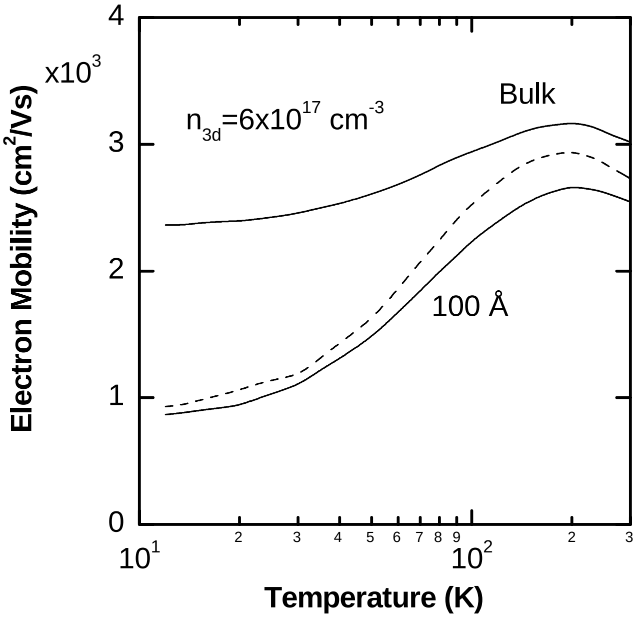

Figure 2.7: Temperature dependence of Hall mobility for bulk GaAs and 100 Å-wide Si-doped GaAs quantum wells (average doping concentration of 6×10^{17} cm^{-3}). Measured data are represented by solid lines. The dashed curve depicts experimental data for a GaAs quantum well, corrected due to doping profile (after Masselink [21]).

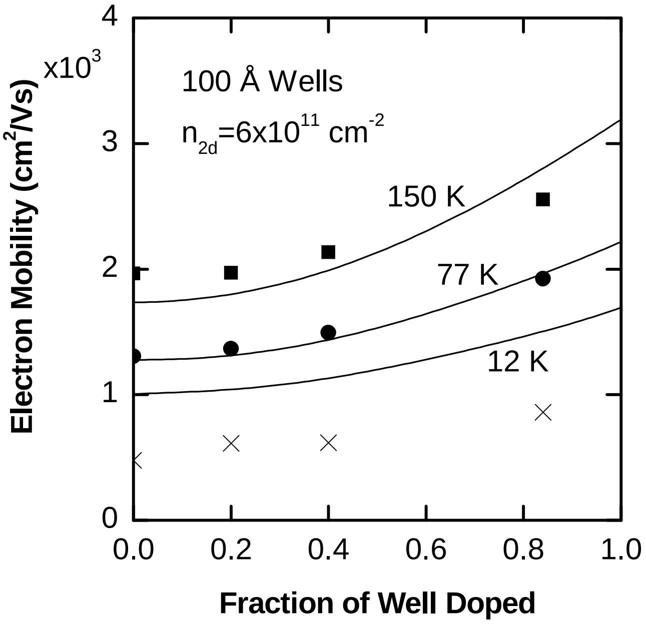

Figure 2.8: Electron mobility for 100 Å GaAs quantum wells as a function of temperature and doped well fraction. The solid curves represent calculated mobilities determined by scattering on ionized impurities. The scattering on interface roughness and on phonons is not included in the calculations (after Masselink [21]).

Scattering of electrons by optical phonons is significant in all bulk polar semiconductors and in systems of any dimensionality. Using appropriate heterostructure design and growth conditions, the influence of the most scattering mechanisms on device performance can be minimized. However, electron-phonon scattering is an inherent feature of any material due to lattice atom vibrations, being more effective at higher temperatures. Interaction of electrons with polar optical phonons provides the dominant contribution to the scattering in III-V materials. Scattering by optical phonons has been discussed by various authors like Ferry [42], Hess [43], Basu et al. [44] and Price [45].

For heterostructures, three different types of optical phonons have to be considered: (i) confined optical phonons within a quantum well, (ii) interfacial and (iii) bulk-like optical phonons (in the materials enclosing the quantum well). A strong electron confinement leads to negligible electron wave penetration into the barrier region. Provided that this approximation of infinitely high barriers is valid, the interaction of electrons with bulk-like optical phonons can be omitted.

The interaction of an electron with longitudinal confined phonons in a quantum well is described by the scattering rate [46]

$$\begin{gathered}\frac{1}{\tau(k_0,n_0)}=\frac{2e^2\omega_{LO}}{t}\left(\frac{1}{\varepsilon_\infty}-\frac{1}{\varepsilon_0}\right)\left(N_{LO}+\frac{1}{2}\pm\frac{1}{2}\right)\\ \times\sum_{n,m}G_{n_0,n,m}\int d^2q\frac{\delta\left[E_n\left(\overrightarrow{k_0}+\overrightarrow{q}\right)-E_{n_0}\left(\overrightarrow{k_0}\right)\mp\hbar\omega_{LO}\right]}{q^2+\left(\frac{\pi m}{t}\right)^2}\end{gathered}, \tag{2.27}$$

where $\overrightarrow{q}$ and m are the in-plane wave vector and the discrete (transverse) number being characteristics of the confined optical modes. ω_{LO} is the frequency of the confined phonons, ε_∞ and ε_0 are the low- and high-frequency permittivities of the material. N_{LO} is the number of longitudinal optical phonons, $\overrightarrow{k_0}$, n_0 and n are the electron wave vector near the energy minimum ($\overrightarrow{k} = \overrightarrow{k_0}$) and discrete numbers characterizing different electron states, respectively. Here, $G_{n_0,n,m}$ as the square of the overlap integral is given by

$$G_{n_0,n,m}=\left[\frac{2}{t}\int\limits_{-t/2}^{t/2}dz\cos\frac{\pi n_0 z}{t}\cos\frac{\pi n}{t}H_m(z)\right]^2, \tag{2.28}$$

where $H_m(z)$ describes longitudinal vibrations by

$$H_m(z)=\left\{\begin{array}{ll}\cos(\pi mz/t), & odd\ m\\ \sin(\pi mz/t), & even\ m\end{array}\right. . \tag{2.29}$$

An analysis of the overlap integral form provides two selection rules:

1) Intraband transitions ($n_0 = n$) occur if one of the symmetric modes (i.e. $H_m = cos(\pi mz/t)$ for odd m) is involved.

2) Scattering between the electron states with the same symmetry is possible with a phonon mode of the same symmetry.

Simulations reveal decreasing electron scattering by confined optical phonons with diminishing well width. Figure 2.9 illustrates the total scattering rate due to interaction of electrons with polar optical phonons in the first subband. Monte Carlo simulations were performed for a finite 150 Å GaAs quantum well between $Al_{0.23}Ga_{0.77}As$ barriers [47]. Compared to the 3D scattering rate, the 2D rate exhibits a much steeper emission threshold and sharp discontinuities corresponding to the onset of emission and absorption for higher subbands. The edge steepness is related to the discontinuous density of states of a two-dimensional system.

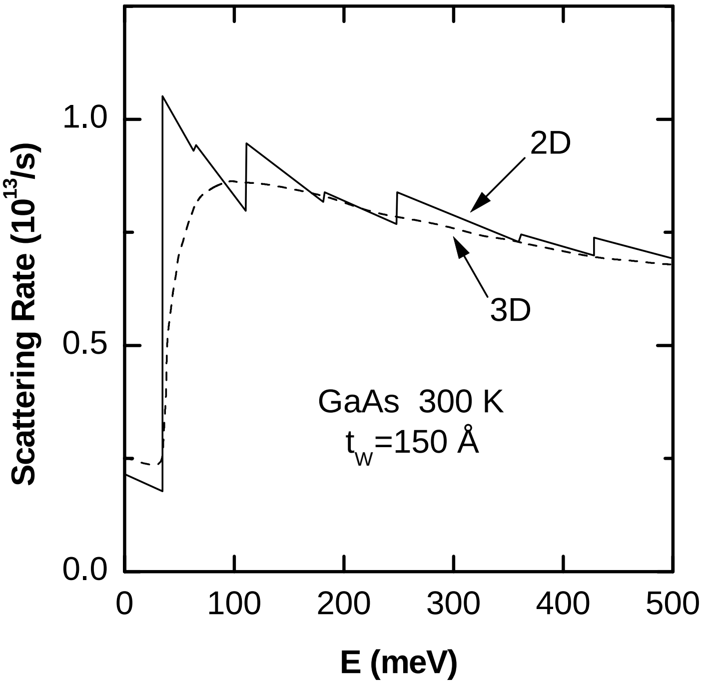

Figure 2.9: Total scattering rate due to interaction of electrons with polar optical phonons for a 150 Å GaAs quantum well (first subband considered only). Calculation results are shown for both the 2D system and bulk GaAs material for comparison (after Goodnick [47]).

2.2.2 High-field electron transport

Parallel transport phenomena have to be considered in their dependency on the electric field. Accordingly, one distinguishes between low-field transport and hot-electron transport, i.e. transport at high electric fields. Here, the electron effective temperature T_e serves as a criterion. The electron effective temperature and the mean electron energy E_e in thermal equilibrium are related by

$$E_e = \frac{1}{2} q k_B T_e, \tag{2.30}$$

where q is the structure dimensionality. Depending on the experimental conditions, three situations can be met: (i) the thermal equilibrium, i.e. the electron temperature is comparable to the lattice temperature (low-field regime), (ii) the electron temperature only slightly exceeds the lattice temperature, but transport still obeys Ohm's law (warm electrons at moderate electric fields) and (iii) the hot-electron regime with $T_e \gg T_{lattice}$. In this section we will focus on recent studies of electron mobility and drift velocity in 2D and 3D systems at high electric fields.

High-field transport in modulation-doped heterostructures was studied by various authors like M. B. Das et al. [22], M. Ionue et al. [48], W.T. Masselink et al. [49, 50], and W.T. Masselink [51, 52].

The low-field mobility of the two-dimensional electron gas is quite high in modulation-doped heterostructures, compared to bulk materials or doped-channel heterostructures. For example, mobilities of about 5×10^6 cm^2/Vs were found in the modulation-doped AlGaAs/GaAs heterosystem at temperatures near absolute zero [53]. However, experimental observations proved a significant decrease of electron mobilities with increasing electric fields. Typical electron mobility vs. field dependencies were found as $\mu \sim E^{-0.8}$ at medium (roughly 0.2-2 kV/cm) and as $\mu \sim E^{-1}$ at high electric fields [48, 49]. The observed dependencies are typical for modulation-doped heterojunctions with prevailing scattering on polar optical phonons.

As reported earlier [22], just the saturation of the electron drift velocity much more than the low-field mobility affects the device performance. The electron drift velocity vs. electric field dependency in AlGaAs/GaAs heterostructures is shown in Fig. 2.10, compared to bulk GaAs.

Obviously, the electron drift velocity peaks at a higher value for slightly doped bulk material than for the 2DEG in the modulation-doped system. However, the peak drift velocity occurs at much lower electric fields for the 2DEG. Furthermore, the peak electron velocity increases with lowering temperature for all systems considered herein. The same behavior was found in InGaAs/InAlAs heterostructures studied in comparison with slightly doped bulk In$_{0.53}$Ga$_{0.47}$As material [52].

The peak velocity decrease observed for modulation-doped heterostructures can be explained by of two different causes [50]:

(i) Due to spatial confinement of electrons in a two-dimensional system [54], the energy of the electrons in the first subband of the Γ valley is about 40 meV higher with respect to the conduction band edge of bulk GaAs. This is not applicable to the L valley of electrons, because of their larger effective mass and the much smaller L valley conduction-band discontinuity between AlGaAs and GaAs. Hence, the Γ-L separation for the heterostructure is about 40 meV smaller

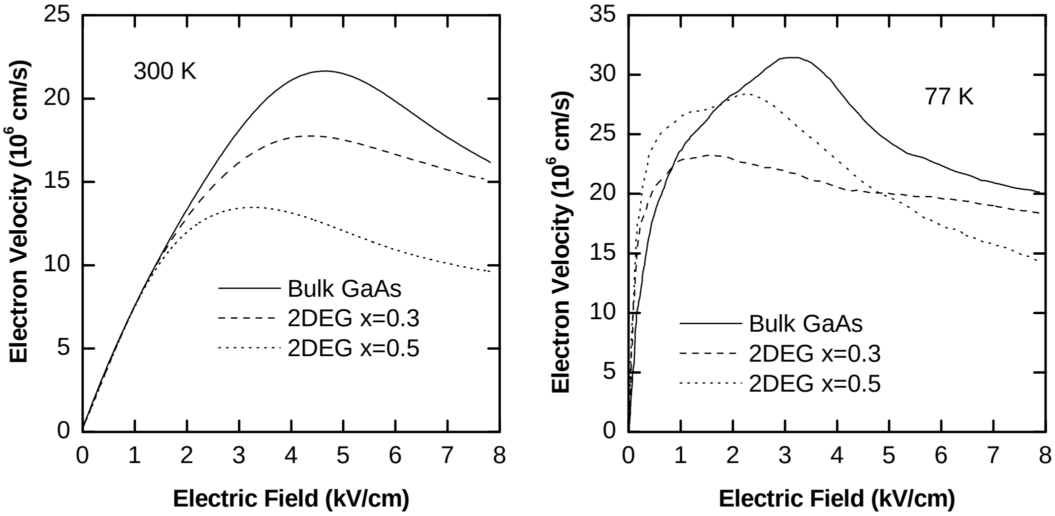

Figure 2.10: Electron drift velocity vs. electric field at 300 K and 77 K. The results represent $Al_xGa_{1-x}As$ heterostructures with $x = 0.3$ and $x = 0.5$ (after Masselink [50]), compared to bulk GaAs with an electron concentration of about $n = 10^{15}$ cm^{-3}.

than in GaAs bulk material. This difference results in a about 10 % lower value of the peak drift velocity.

(ii) The real space transfer of electrons from the GaAs quantum well to the AlGaAs barrier has to be accounted for, too. Usually, it is considered as a transfer of electrons from the first to a higher electron subband in the Γ valley, neglecting the other possible real space transfer mechanisms as from the Γ into the Ł valley in GaAs. For higher Al mole fractions in AlGaAs, a real space transfer occurs from the Γ valley in GaAs into the X valley of AlGaAs. Furthermore, an increase of the Al mole fraction between 0 and 0.5 causes a decrease of the peak velocity due to the transfer into the X valleys.

In modern electronic devices like the modulation-doped field effect transistor (MODFET), high doping levels and accordingly high electron concentrations are usually applied. Compared to bulk material at the same high doping level, the peak drift velocity of a heterostructure is greater [51]. Therefore, the drift transport performance of devices based on modulation-doped heterostructures is superior to bulk material devices.

High-field transport in doped bulk materials and doped-channel quantum wells is of great interest for device applications. Compared to slightly doped bulk materials or modulation-doped heterostructures, the low-field mobilities in heavily doped bulk materials and doped-channel heterostructures are much lower due to scattering on ionized impurities. Nevertheless, devices based on these systems exhibit some advantages. Usually, the temperature dependence of the main device parameters is negligible weak. Consequently, these devices do not need an additional recalibration. Moreover, regardless of low mobilities, the high peak electron drift velocity results in both high device speed and sensitivity.

Transport studies of doped bulk materials and doped-channel heterostructures at high fields were done by different authors [23, 51, 55, 56, 57, 58].

Typical velocity vs. field characteristics for doped bulk GaAs materials at 300 K are shown in Fig. 2.11, with the electron concentration as a paramater (after Masselink [58]). Initially, the drift velocity rises linearly with increasing field, being characteristic for the low-field mobility region. At higher electric fields, the velocity peaks and saturates. The observed saturation is due to electron acceleration by the electric field, causing electron energies high enough to transfer them from Γ valley into L valley of GaAs.

The electron energy in a uniform electric field is described by

$$\varepsilon = e\mu(E)E^2\tau_\varepsilon, \tag{2.31}$$

where e is the electronic charge, μ the electron mobility, E the applied electric field and τ_ε the energy relaxation time [58].

Obviously, a higher doping level in bulk materials causes a lower peak velocity. Furthermore, the peak shifts to higher electric fields and broadens. At lower

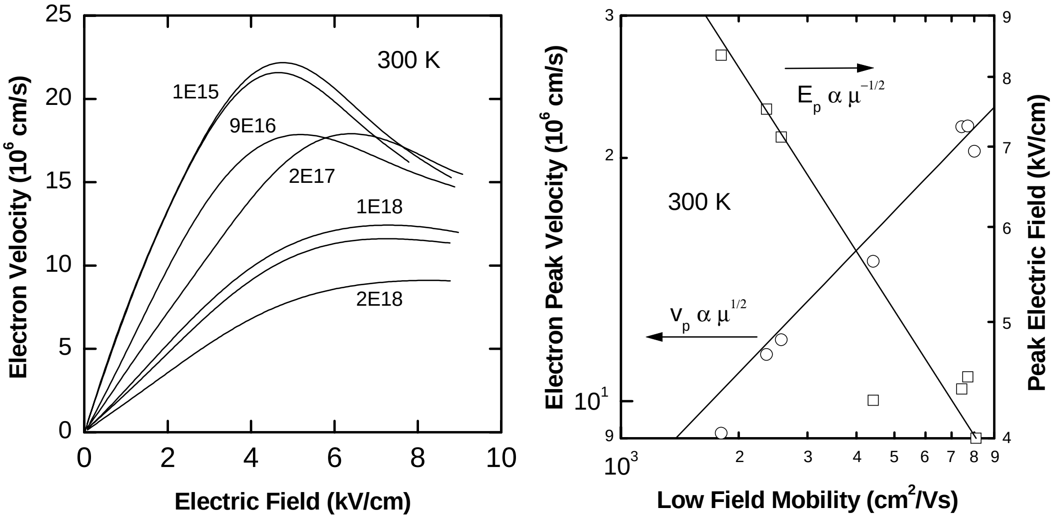

Figure 2.11: The velocity-field characteristics of bulk GaAs for different electron concentrations at 300 K. The electron concentrations were measured by the van der Pauw Hall technique. Electron peak velocities and threshold electric fields, i.e. fields for saturating electron peak velocity, are shown vs. low-field mobility at room temperature. The straight lines represent simple approximations for both peak velocities and threshold electric fields vs. low-field mobility dependencies as $v_p \propto \mu^{1/2}$ and $E_{th} \propto \mu^{-1/2}$, respectively. The approximations are based on the following assumptions: (i) the Γ-L energy is a constant, (ii) the mobility $\mu(E)$ is nearly constant until the velocity is near the peak velocity and (iii) the energy relaxation time τ_ε is constant (after Masselink [58]).

temperatures, in particular at 77 K, the electron velocities exhibit a behavior similar to increasing doping concentration [58]. However, the peak velocities are higher than at room temperature.

A presentation of the peak electron velocity and peak electric field vs. low field mobility dependencies based on experimental data for bulk GaAs is given in Fig. 2.11, too.

Velocity-field characteristics of doped-channel heterostructures are presented after Masselink [23] in Fig. 2.12. The data were obtained for different doping profiles within a 100 Å GaAs quantum well embedded between $Al_{0.4}Ga_{0.6}As$ barriers: (i) a uniformly doped quantum well (doping profile comprising about 84 % of the total well thickness in order to avoid DX center formation near the AlGaAs/GaAs interfaces); (ii) a δ-doping centered in the quantum well and (iii) a δ-doped quantum well with the doping spike 25 Å apart from the bottom interface.

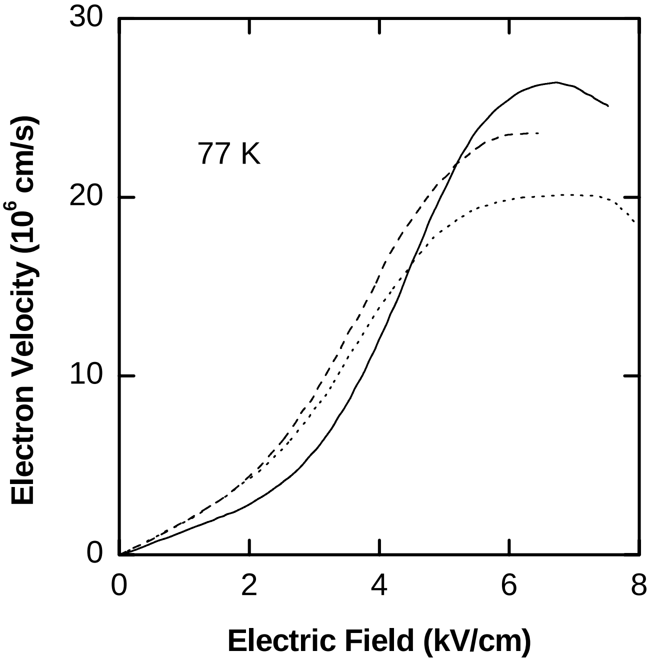

Figure 2.12: Measured velocities versus electric field for 100-Å-wide GaAs quantum wells uniformly doped (dashed curve), δ-doped in the center (solid curve), and δ -doped midway between the center and an edge (dotted curve). The sheet density in each well is 6×10^{11} cm^{-2} (after Masselink [23]).

Regardless of the smaller low-field mobility compared to the other studied structures, the highest electron peak drift velocity is found for the quantum well with δ-doping at the center. The lowest peak velocity was determined for the heterostructures with the δ-doping spike between the quantum well center and an interface. These experimental data strongly support the following conclusion: With respect to device performance, the velocity saturation is much more crucial than the low-field mobility.

In order to understand the observed effects, the author of [23] proposed to consider the behavior of differential electron mobilities measured on the same samples. The differential mobility vs. electric field dependencies are shown in Fig. 2.13. All three samples exhibit an initial increase of the differential mobility with electric field. Some increase has to be expected due to the following consideration: Scattering on ionized impurities is the dominant mechanism at low lattice temperatures, but less effective at higher electron temperatures. But an increased electric field just leads to a heating of the electron gas. At still higher electric fields, the mobility diminishes due to increasing phonon scattering. Eventually, intervalley scattering prevails, leading to a negative differential mobility. The same behavior of differential electron mobility was observed for bulk GaAs layers at low temperatures [58].

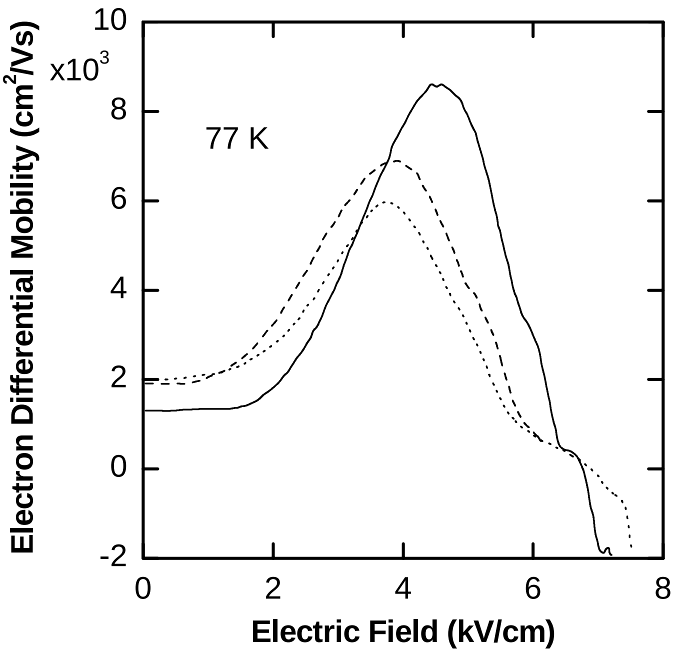

Figure 2.13: Measured differential mobilities versus electric field for 100-Å-wide GaAs quantum wells uniformly doped (dashed curve), δ - doped in the center of quantum well (solid curve), and δ - doped midway between the center and an edge (dotted curve). The measured sheet electron density in each well is 6×10^{11} cm^{-2} (after Masselink [23]).

Obviously, the highest increase in the electron gas differential mobility is found for the center δ-doped quantum well. This behavior was explained by a heating of the electrons from the ground-state (even parity) quantum well subband into the first excited (odd parity) subband [23]. The odd-parity state has a node at the center of the quantum well, exactly at the ionized impurity location. Hence, the electrons heated by the electric field start to occupy the first excited subband. Within this subband, the electrons suffer much less from ionized impurity scattering. Consequently, both the differential mobility and the electron velocity of an on-center δ-doped quantum well are much higher.

2.2.3 Noise in semiconductors

The noise of semiconductor materials can be reviewed from completely different points of view. At a first glance, noise is an undesirable signal and has to be reduced in order to improve the operational characteristics of an electronic device. But with respect to device diagnostics, noise measurement and analysis is a very powerful tool for reliability and quality studies of semiconductor devices [59, 60, 61, 62, 63, 64, 65]. Noise measurement techniques are well suited for studies of semiconductor energy structures [66, 67, 68, 69, 70, 71, 72]. In the following, we will review the most relevant noise types: thermal noise, $1/f$ noise and generation-recombination noise.

Thermal noise due to random carrier motion is always present in semiconductors. The spontaneous fluctuations in the voltage across a resistor due to the Brownian carrier motion are described by a white (random) noise spectrum [24]

$$S_{V,noise} = 4k_B T R, \tag{2.32}$$

where k_B, T, R are Boltzmann's constant, the absolute temperature and the resistance of the ohmic sample, respectively. Usually, thermal noise is observed at high frequencies in terms of a frequency independent plateau. It can be used for the estimation of: (i) lattice or electron temperature [73]; (ii) the quality of the heat contact between a film resistance and its substrate [59]. Just thermal noise of a known resistor is often used for the calibration of a noise measurement setup.

1/f or flicker noise caused by conductance fluctuations is observed in a variety of semiconductor materials. The noise is inversely proportional to the frequency for a very wide frequency range. These fluctuations can originate from: 1) fluctuations in the number of free charge carriers or 2) fluctuations in the mobility. For the present, there is no definite decision on the appropriate cause for the $1/f$ noise. Apparently, both origins of $1/f$ noise exist [24, 74].

An empirical relation for the characterization of $1/f$ noise was proposed by Hooge [75]

$$\frac{S_{R,noise}}{R^2} = \frac{S_{V,noise}}{V^2} = \frac{S_{I,noise}}{I^2} = \frac{\alpha}{fN} \tag{2.33}$$

where S is the noise spectral density, R, V, I are the sample resistance, applied voltage and bias current, respectively. f is the frequency, N is the number of carriers and α is the so-called Hooge parameter. Initially, the Hooge parameter α was assumed as a constant of about $\alpha = 2 \times 10^{-3}$ [76]. However, further experimental studies revealed α being not constant, depending on the quality of the crystal and the scattering mechanisms determining the mobility [24, 77, 78, 79, 80, 81].

In order to prove $1/f$ noise being caused by mobility fluctuations, it is reasonable to consider a semiconductor sample with two scattering mechanisms determining the mobility: lattice scattering and impurity scattering. Accordingly, the (measured) mobility is given by Matthiessen's rule

$$\frac{1}{\mu_{meas}} = \frac{1}{\mu_{latt}} + \frac{1}{\mu_{imp}}. \tag{2.34}$$

Mobility fluctuations are expressed via

$$\Delta\left(\frac{1}{\mu_{meas}}\right) = \Delta\left(\frac{1}{\mu_{latt}}\right) + \Delta\left(\frac{1}{\mu_{imp}}\right). \tag{2.35}$$

Let us suppose the scattering on ionized impurities having no noteworthy contribution to the noise, i.e. $\Delta\mu_{imp} = 0$. From Eqs. (2.35) and (2.33) one concludes

$$\alpha_{meas} = \left(\frac{\mu_{meas}}{\mu_{latt}}\right)^2 \alpha_{latt}. \tag{2.36}$$

From noise measurements of various samples with different doping (thus different contribution of μ_{imp}), a straight line can be drawn in a $log(\alpha_{mess})$ versus $log(\mu_{mess})$ plot. The estimated slope of about 2 in [24] coincides well with Eq. (2.36).

For intentionally doped quantum wells or doped bulk materials, ionized impurity scattering dominates. Accordingly, Eq. (2.36) has to be rewritten as

$$\alpha_{meas} = \left(\frac{\mu_{meas}}{\mu_{latt}}\right)^2 \alpha_{latt} + \left(\frac{\mu_{meas}}{\mu_{imp}}\right)^2 \alpha_{imp}, \tag{2.37}$$

assuming $\langle\Delta\mu_{latt} \cdot \Delta\mu_{imp}\rangle = 0$. For ionized impurity scattering prevailing over lattice scattering, the second term of Eq. (2.37) dominates. Then $\mu_{mess} \cong \mu_{imp}$ and the relation $\alpha_{mess} \cong \alpha_{imp}$ holds true. The noise characterized by α_{imp} is proportional to the number of impurity centers, being inversely proportional to $\mu_{mess} \cong \mu_{imp}$, i.e.

$$\alpha_{mess} \cong \alpha_{imp} \propto \mu_{imp}^{-1} \cong \mu_{meas}^{-1}. \tag{2.38}$$

Accordingly, one can expect a slope of -1 in the $log(\alpha_{mess})$ vs. $log(\mu_{mess})$ plot.

Supposing conductivity fluctuations due to fluctuations in the number of carriers, the following situations can be met [24]:

(a) α is proportional to the number of generation-recombination centers creating the $1/f$ spectrum and not scattering electrons: $\alpha_{mess} \cong \mu_{meas}^0$.

(b) α is proportional to the number of centers scattering electrons: $\alpha_{meas} \propto \mu_{imp}^{-1}$. For $\mu_{meas} \cong \mu_{imp}$ follows $\alpha_{meas} \propto \mu_{meas}^{-1}$.

(c) α is proportional to the number of centers scattering electrons, but $\mu_{meas} \cong \mu_{latt}$: $\alpha_{meas} \propto \mu_{meas}^{-k}$, where $k \gg 1$.

All these fluctuations will result in negative slopes in $log(\alpha)$ vs. $log(\mu)$ plots.

Generation-recombination noise is caused by conductivity fluctuations due to random variations in the number of carriers. The number of free carriers may fluctuate due to generation and recombination processes between the bands and centers located in the bandgap. For compound semiconductors and heterostructures with lattice defects being often a problem, this type of noise usually appears as one or two Lorentzians superimposed on $1/f$ noise. The noise spectral density of generation-recombination noise is given by [59]

$$S_{g-r} = \sum_i \frac{B_i}{1 + (2\pi f \tau_i)^2}, \tag{2.39}$$

where B_i is the amplitude and f is the frequency. The characteristic time constant τ_i can be expressed in terms of the capture τ_c and emission τ_e time constants via

$$\frac{1}{\tau} = \frac{1}{\tau_e} + \frac{1}{\tau_c}. \tag{2.40}$$

The study of generation-recombination noise depending on temperature proves to be one of the most powerful experimental methods for the investigation of local levels acting as generation and recombination centers. This method is known as deep level noise spectroscopy (DLNS). The results obtained with this technique correlate very well with the findings of the classical deep level transient spectroscopy (DLTS).

However, the DLNS has some advantages over DLTS: It is well known, that DLTS fails in case of the Fermi level E_F located below the level under investigation over the entire range of temperatures. Additionally, DLTS detects local levels with very small cross section ($\sigma < 10^{-20}$ cm^2) only with difficulties. Furthermore, the trap parameter estimation can not be done correctly for cross sections depending exponentially on temperature (e.g. multiphonon capture [82]). On the other hand, the DLNS proves to be a quite effective tool for all the situations pointed out above.

Usually, the noise data are presented in two different forms (see Fig. 2.14):

(1) The voltage $S_{V,noise}$ or current $S_{I,noise}$ noise spectral density is presented as a function of the frequency f in a wide temperature range [67, 69, 70, 80, 83, 84, 85, 86, 87, 88]. Then the activation energy can be estimated from the temperature dependence of the characteristic time constant τ, using the $\ln(\tau)$ vs. $1/T$ plot [or $\ln(T^2\tau)$ vs. 1/T]. This procedure is advantageous in case of more than one Lorentzian observed in noise spectra. It allows an adequate interpretation of each of them.

(2) Fixing the measurement at different (characteristic) frequencies, the voltage $S_{V,noise}$ or current $S_{I,noise}$ noise spectral density vs. temperature can be

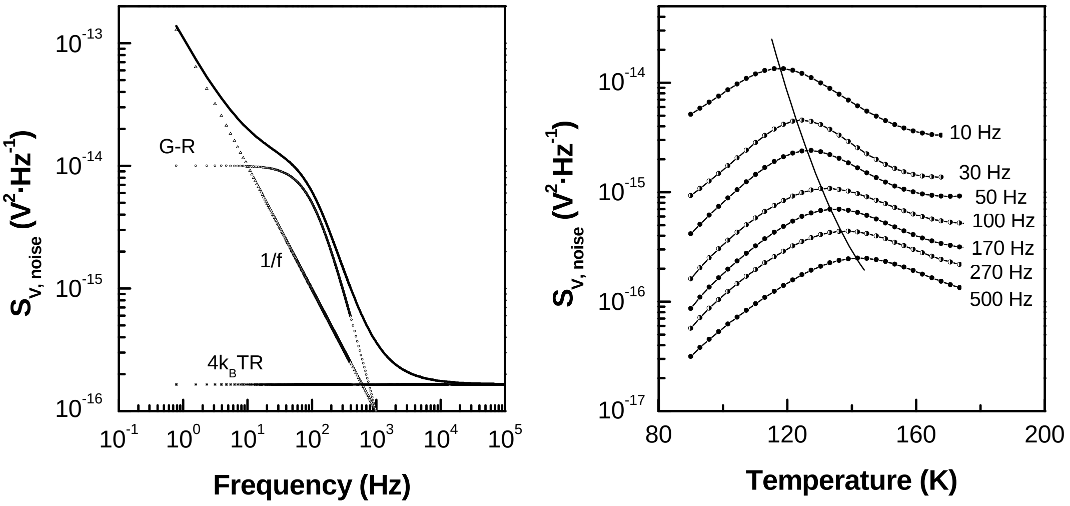

Figure 2.14: Two different representations of the noise data.

presented [68, 89, 90]. At some temperature, a peak occurs in the noise density, shifting to higher temperatures for increasing measurement frequency. The time constant τ is equal to $1/(2\pi f)$. The $\ln(\tau)$ vs. $1/T$ [or $\ln(T^2\tau)$ vs. $1/T$] plot allows an estimation of the activation energy. According to Carey et al. [90], there is no general way determining the capture and emission activation energies. Thus, additional approaches are needed. However, in Ref. [68] the local level parameters were estimated correctly in case of electron capture cross section σ_n depending exponentially on temperature. The developed procedure is applicable when the Fermi level E_F is located significantly below or above the local level E_0. This theory will be used in our studies and is outlined in Appendix A.

2.3 Basic characteristics of Hall devices

Different types of magnetic sensors such as Hall effect devices, magnetodiodes, magnetotransistors, MAGFETs (magnetic-sensitive field-effect transistors), and carrier-domain magnetometers [91] have found wide application in research and industry. These devices are often used for the characterization of semiconductor [92, 93], ferromagnetic [94] and superconductive materials [14, 95, 96, 97].

In the present work, Hall effect devices of micron-range lateral sizes will be considered. We define the most important device parameters as the Hall absolute sensitivity, the Hall supply-current-related sensitivity or magnetic sensitivity, the Hall supply-voltage-related sensitivity, signal-to-noise sensitivity, cross-sensitivity and linearity.

A Hall device is an electronic device based on the homonymous effect. Any electrically conductive plate of length L and width W with four Ohmic contacts

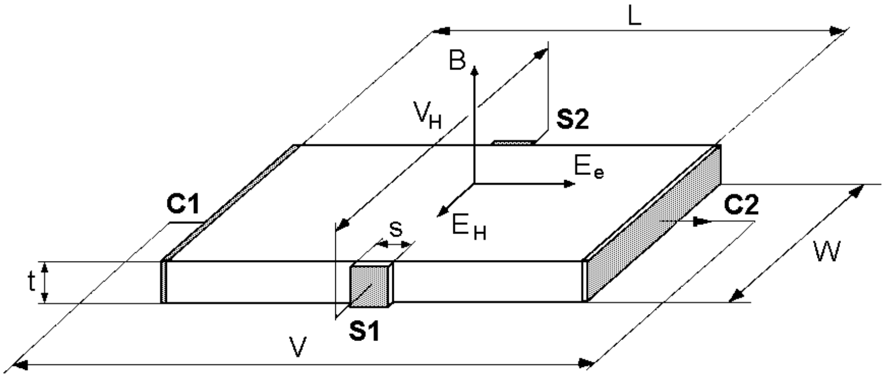

Figure 2.15: Hall device in the form of a rectangular plate with length L and width W. $C1$ and $C2$ are bias contacts and $S1$ and $S2$ are sense contacts. The Hall voltage is measured between the sense contacts at a magnetic field applied perpendicular to the Hall plate.

positioned at the boundary of the plate and far away from each other can be considered as a Hall effect device (see Fig. 2.15). This device is usually biased via two non-neighboring contacts $C1$ and $C2$ and the other two contacts $S1$ and $S2$ are used as sensing contacts. Depending on the biasing condition between contacts $C1$ and $C2$, two device operation modes are defined: device is driven by a constant voltage or by a constant current.

2.3.1 The Hall effect

When a constant voltage is applied between the contacts $C1$ and $C2$, the electric field $\mathbf{E}$ rises along the device length L. As a result, the electric force $\mathbf{F}$ collinear to the electric field $\mathbf{E}$ appears. This force causes drift of charge carriers and is given by

$$\mathbf{F}_e = q\mathbf{E}, \tag{2.41}$$

where q is the charge of carriers. From now on, we restrict our consideration to n - type conductivity ($q = -e$, where e is the electron charge). The coordinate system is chosen according to Fig. 2.16. The electron drift velocity υ_d is given by

$$\upsilon_d = \mu\mathbf{E}, \tag{2.42}$$

where μ is the electron mobility. The current density $\mathbf{j}$ can be defined as

$$\mathbf{j} = q\mu n\mathbf{E}. \tag{2.43}$$

Let us suppose that electrons move only due to an external electric field and the velocities of all electrons are the same and equal to the drift velocity given by Eq. (2.42). The thermal motion of carriers will not be considered.

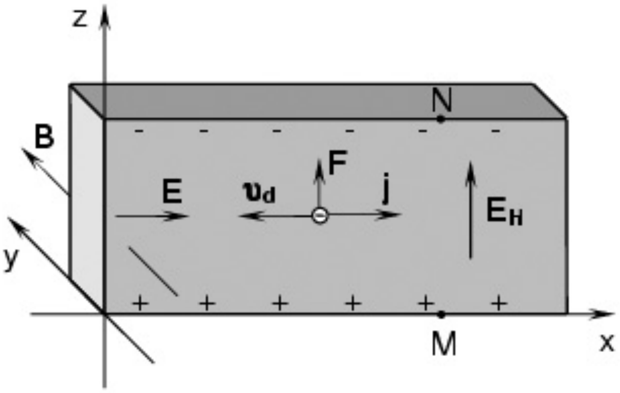

Figure 2.16: Schematic representation of the Hall effect. Only n-type conductivity is considered. E and E_H are the external electric field and Hall electric field, respectively. j is the density of current, F the Lorentz force appearing for a magnetic field B applied perpendicular to the surface of the conductive plate. υ_d is the drift velocity of the electrons.

If we apply a magnetic field perpendicular to device length L and device width W, i.e. in our notation along axis y, then the total force acting on charged carriers is given by

$$\mathbf{F} = q\mathbf{E} + q\left[\upsilon_d \times \mathbf{B}\right] = q\mathbf{E} + q\mu\left[\mathbf{E} \times \mathbf{B}\right]. \tag{2.44}$$

The second term describes the magnetic force deflecting the charge carriers to the upper edge of the strip. As a result, the charge carriers (electrons here) are collected near the upper edge of the conductive strip. Consequently, the electron concentration at the lower edge will be negligible small. Due to the violation of the charge neutrality condition, a compensating electric field $\mathbf{E}_H$ appears. It is directed upwards between the lower and the upper edges of the conductive strip. This field is called the Hall field. Due to this field, the excess charge carrier concentration decreases at the edge of the strip. Finally, the transversal electrical force compensates the magnetic force and equation

$$q\left[\upsilon_d \times \mathbf{B}\right] + q\mathbf{E}_H = 0 \tag{2.45}$$

holds true. Accordingly, the charge carriers move parallel to the x axis. The Hall electric field can be easily found from the balance equation

$$\mathbf{E}_H = -\left[\upsilon_d \times \mathbf{B}\right]. \tag{2.46}$$

Using (2.43), (2.46) and (2.42), the Hall electric field can be expressed as

$$\mathbf{E}_H = \frac{1}{en}\left[\mathbf{J} \times \mathbf{B}\right] = -R_H\left[\mathbf{J} \times \mathbf{B}\right], \tag{2.47}$$

where R_H is the so-called Hall coefficient. The sign of the Hall coefficient coincides with the charge sign of the majority carriers. For electron conduction, R_H is negative:

$$R_H = -\frac{1}{en}. \tag{2.48}$$

To be more accurate, the value R_H should be rewritten as

$$R_H = -\frac{r_H}{en}, \tag{2.49}$$

where r_H is the Hall scattering factor depending on the scattering mechanism. For III-V 2D systems, the Hall scattering factor r_H is equal to unity, because the 2DEG is degenerate due to the low 2D density of states in a quantum well.

The Hall electric field results from the transversal Hall voltage between the edges of the strip

$$V_H = \int_M^N \mathbf{E}_H dz. \tag{2.50}$$

The current flowing across the device of thickness t is given by $I = jWt$ and the Hall voltage can be expressed via (2.48) and (2.50) as

$$V_H = \frac{R_H}{t} I B_y. \tag{2.51}$$

In the presence of a magnetic field perpendicular to both width and length of the device, the total electric field in the sample is $\mathbf{E}_{total} = \mathbf{E} + \mathbf{E}_H$. This total electric field is not collinear to the external electric field $\mathbf{E}$ forming some angle θ_H with it. This inclination angle of the total electric field with respect to the external electric field is called the Hall angle and given by

$$\tan(\theta_H) = |\mathbf{E}_H|/|\mathbf{E}|. \tag{2.52}$$

Then $\tan(\theta_H)$ can be written as

$$\tan(\theta_H) = -\mu B_y, \tag{2.53}$$

where the negative sign of the Hall angle coincides with the sign of the carrier charge.

2.3.2 The geometrical correction factor

The Hall voltage given by Eq. (2.51) holds true for an infinitely long or point-contacted device. For finite Hall effect devices being not point-contacted, the influence of the geometry should be considered by using a geometrical correction factor G. This correction factor describes the Hall voltage decrease due to a non-perfect current confinement and can be defined as

$$G = V_H / V_\infty, \tag{2.54}$$

where V_H is the Hall voltage of the finite Hall effect device and V_∞ the Hall voltage of the infinitely long or point-contacted device.

Thus, the Hall voltage of a finite Hall effect device is given by

$$V_H = G \frac{R_H}{t} I B_y. \tag{2.55}$$

We will review here the results of the geometrical correction factor available in the literature for two geometries: a rectangular Hall bar device and a Greek cross device with contacts of nonzero length. Both shapes are shown in Fig. 2.17.

The geometrical correction factor for a rectangular Hall bar geometry was calculated by different authors Lippmann and Kuhrt [98], Versnel [99], Haeusler [100]. Calculations results for a rectangular Hall plate with point sense contacts ($s \rightarrow 0$) positioned at mid-length of the Hall strip are shown as a function of the length-to-width ratio (L/W) for different Hall angles in Fig. 2.18. The geometrical correction factor for a rectangular Hall plate with point sense contacts at $0.85 < L/W < \infty$ and $0 \leq \theta_H \leq 0.45$ can be approximated as [98]

$$G \cong 1 - \frac{16}{\pi^2} \exp\left(-\frac{\pi L}{2W}\right) \left[1 - \frac{8}{9} \exp\left(-\frac{\pi L}{W}\right)\right] \left(1 - \frac{\theta_H^2}{3}\right). \tag{2.56}$$

The factor for a short rectangular Hall device with point sense contacts is approximated by [98]

$$G \cong 0.742 \frac{L}{W} \left[1 + \frac{\theta_H^2}{6} \left(3.625 - 3.257 \frac{L}{W}\right)\right]. \tag{2.57}$$

This equation is most accurate for $L/W < 0.35$ and $\theta_H < 0.45$.

The Hall effect device with the Greek cross shape was examined by Versnel [101]. Using the Schwarz-Cristoffel transformation, the according geometrical

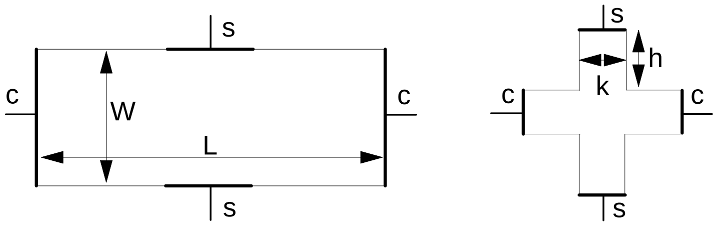

Figure 2.17: Two different shapes of Hall effect devices: rectangular Hall bar geometry and Greek cross geometry. Current contacts are denoted as c, sense contacts as s.

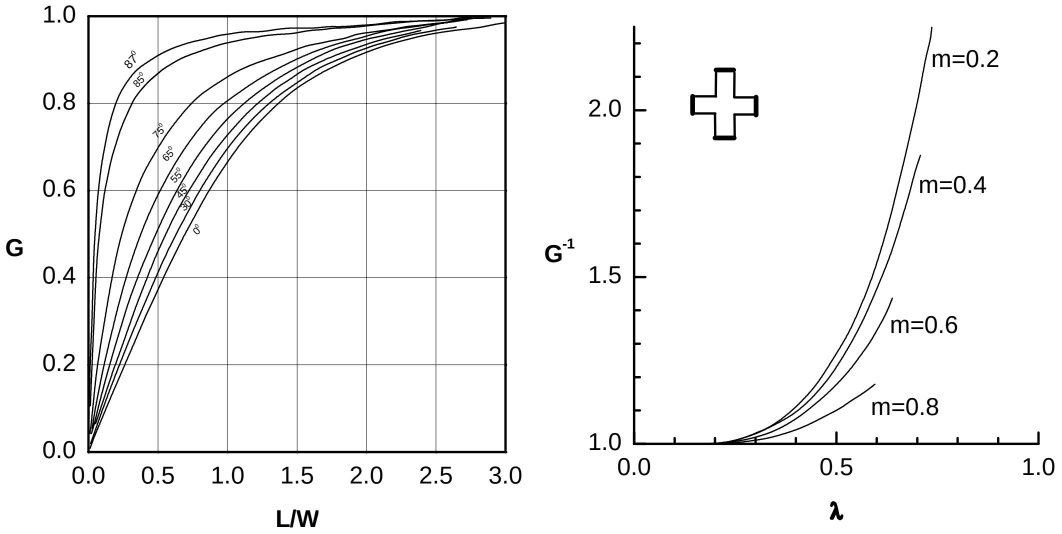

Figure 2.18: The geometrical correction factor of a rectangular Hall effect device with point sense contacts ($s \to 0$) as a function of length-to-width ratio (L/W) for different Hall angles (after Lippmann et al. [98]). The reciprocal value of the geometrical correction factor for the Greek cross Hall device as a function of $\lambda = h/k$ [91].

correction factor was calculated. The results are shown in Fig. 2.18. For small Hall angles θ_H and $k/2h \leq 0.38$, the geometrical correction factor for the Greek cross shape can be approximated via

$$G\left(\frac{h}{k}, \theta_H\right) \cong 1 - 1.045 \exp\left(-\pi\frac{h}{k}\right)\frac{\theta_H}{\tan\left(\theta_H\right)}, \tag{2.58}$$

where h and k are the length of the boundary of the plate and the length of the contact, respectively (see Fig. 2.17).

2.3.3 Sensitivity

The sensitivity of the Hall effect device is the most crucial figure of merit of the sensor. Usually, three types of sensitivities are considered: the absolute sensitivity S_A, the supply-current-related sensitivity or magnetic sensitivity S_I (both names are adequate) and supply-voltage-related sensitivity S_V.

The absolute sensitivity of the Hall effect device is defined as

$$S_A = \left|\frac{V_H}{B}\right|, \tag{2.59}$$

where V_H is the Hall voltage and B is the magnetic field applied perpendicular to both width W and length L directions.

The ratio of the absolute sensitivity to the varied quantity (either voltage or current) is a relative sensitivity. Thus, the supply-current-related sensitivity is defined as

$$S_I = \frac{S_A}{I} = \left|\frac{V_H}{BI}\right|. \tag{2.60}$$

Using (2.48) and (2.55), the Eq. (2.60) can be rewritten as

$$S_I = \frac{G}{qn_{2D}}, \tag{2.61}$$

where n_{2D} is the two-dimensional electron concentration. The two-dimensional electron concentration n_{2D} is given by $n_{2D} = n_{3D}t$, where n_{3D} is the three-dimensional electron concentration and t the thickness of the doped material.

At a given bias current, the sensitivity can be increased by scaling the L/W ratio up, so that $G \approx 1$. Using this criterion, the highest sensitivity is achieved for as small as possible n_{2D}. However, lightly-doped material is often characterized by high temperature and light sensitivities, high thermal drift and poor contacts, leading to additional noise. Typical values of the supply-current-related sensitivity for Hall devices based on a III-V material systems are in the 80 $\mathrm{V \cdot A^{-1} \cdot T^{-1}}$ up to 1200 $\mathrm{V \cdot A^{-1} \cdot T^{-1}}$ range. The largest magnetic sensitivity of about 3100 $\mathrm{V \cdot A^{-1} \cdot T^{-1}}$ is measured for n-type Si Hall effect devices with $n_{2D} = 2 \times 10^{11}$ $\mathrm{cm^{-2}}$ [102].

For a given supply voltage V, the supply-voltage-related sensitivity S_V is defined as

$$S_V = \frac{S_A}{V} = \left|\frac{V_H}{BV}\right|. \tag{2.62}$$

Accordingly, the current density across the device is

$$j = qn_{3D}\mu E, \tag{2.63}$$

where the electric field is given by $E = V_x/L$. Furthermore,

$$S_V = \mu G \frac{W}{L}. \tag{2.64}$$

If the electric field is small enough, so that the mobility is approximately constant, structures with a small L/W ratio are favored, so long as G does not become too small. For $W \approx L$, the correction factor is approximately $G \approx 0.74L/W$, so that S_V reaches a value of 0.7μ. At room temperature, values of around 1 $\mathrm{T^{-1}}$ are reachable.

2.3.4 Signal-to-noise sensitivity

For the application of Hall devices, a parameter being crucial is the signal-to-noise sensitivity (SNS). We define it as

$$SNS \equiv \frac{S_A}{\overline{V}_{noise}}, \tag{2.65}$$

where S_A is the absolute sensitivity of Hall effect device and $\overline{V}_{noise}$ is the noise voltage in a band of frequencies Δf, given by

$$\overline{V}_{noise} = \sqrt{S_{V,noise}(f)\Delta f}. \tag{2.66}$$

On the other hand, the signal-to-noise sensitivity of a Hall effect device defines the minimum detectable magnetic field. Thus, the other major figure of merit of a Hall device is its detection limit. The detection limit of the Hall sensor is defined as

$$B_{DL} = \left[\frac{S_{V,noise}(f)\Delta f}{S_A^2}\right]^{1/2} = \frac{1}{SNS}. \tag{2.67}$$

Obviously, the highest possible signal-to-noise sensitivity and the lowest possible detectable magnetic field, respectively, are determined by the maximum of the absolute sensitivity and the minimum value of the noise.

Thus, it is necessary to give an affirmative answer to the following question: How can the absolute sensitivity S_A of a Hall device be maximized or which fundamental physical quantity limits the absolute sensitivity? Thus, we have to rewrite Eq. (2.59) in terms of other physical quantities. If the current flowing across the Hall device is

$$I = jWt = n_{3D}q\mu EWt, \tag{2.68}$$

then Eq. (2.55) can be rewritten as

$$\begin{aligned} V_H &= G\tfrac{1}{qn_{3D}t}jWtB \\ &= G\tfrac{jWB}{qn_{3D}}. \end{aligned} \tag{2.69}$$

Using Eq. (2.63) and defining the carrier velocity v as $v = \mu E$, the absolute sensitivity of the Hall device is

$$S_A = GvW, \tag{2.70}$$

where v in case of a large electric field is denoted as its saturated value v_{max}.

Hence, the maximum absolute sensitivity of a Hall device will be obtained on semiconductor materials with high peak drift velocity.

On the other hand, both the bulk device noise and contact noise will limit the signal-to-noise sensitivity and detection limit of the Hall sensor. For $1/f$ noise, the voltage noise spectral density for a rectangular Hall device across the contacts measuring the Hall voltage is given by [103]

$$S_{V,1/f} = \alpha E^2(2\pi n_{2D}f)^{-1}\ln(W/s), \tag{2.71}$$

where α is the Hooge parameter depending on material quality and electron scattering mechanisms in the bulk of the device. For a rectangular Hall device with $W \approx L$, the Hall voltage is $V_H \approx 0.7vBW$ [98]. Then the signal-to-noise sensitivity in the low frequency range with prevailing $1/f$ noise is given by

$$\begin{aligned} SNS &= \frac{0.7vW}{E(\alpha \ln(W/s))^{1/2}(2\pi n_{2D} f/\Delta f)^{-1/2}} \\ &= \frac{0.7vW}{E} \frac{\sqrt{2\pi n_{2D} f/\Delta f}}{\sqrt{\alpha \ln(W/s)}} \qquad , \\ &= 0.7\mu W \sqrt{\frac{2\pi}{\alpha \ln(W/s)}} \sqrt{n_{2D}} \sqrt{\frac{f}{\Delta f}} \end{aligned} \tag{2.72}$$

where μ is the chordal mobility (ratio of v to E). Thus, within the frequency range with prevailing $1/f$ noise, the SNS increases with higher mobility, larger device active size ($W \approx L$), better material quality resulting in smaller α, and higher concentration n_{2D}.

At higher frequencies, with prevailing white noise, the signal-to-noise sensitivity for a short rectangular Hall effect device is given by

$$\begin{aligned} SNS &= \frac{0.7vW}{(4k_B T \Delta f)^{1/2}(n_{2D} q \mu)^{-1/2}} \\ &= \frac{0.7vW}{\sqrt{4\frac{k_B T}{q}\Delta f}} \sqrt{n_{2D}\mu} \end{aligned} \quad . \tag{2.73}$$

Here, the SNS is proportional to both carrier velocity and device size. Both higher two-dimensional carrier concentration and mobility also enhance the device performance.

2.3.5 Cross-sensitivity and non-Linearity

In addition to the above discussed, one also has to consider any undesirable sensitivity of the Hall effect devices to other environmental parameters like temperature T and pressure P. This is called the cross-sensitivity [91].

For example, Hall devices based on modulation-doped systems or lightly doped bulk materials exhibit an extremely large absolute Hall sensitivity. On the other hand, these devices suffer by a high temperature sensitivity, because of both electron mobility and electron concentration being strongly temperature dependent. Thus, a device re-calibration is permanently required.

The cross-sensitivity $K_{cs,j}$ of the Hall device is defined as

$$K_{cs,j} = \frac{1}{S}\frac{\partial S}{\partial P}, \tag{2.74}$$

where S is the sensitivity of the Hall device (S_A, S_I or S_V), P the environmental parameter: temperature T or pressure P, and j denotes the biasing mode: $j = I$ for constant current and $j = V$ for constant voltage.

Let us consider the cross-sensitivity of the Hall device to temperature, i.e. its thermal drift.

Here we suppose that the device is biased by a constant current. Then the thermal drift of the Hall device is defined by the temperature dependence of the supply-current-related sensitivity

$$K_{cs,I} = \frac{1}{S_I}\frac{\partial S_I}{\partial T}. \tag{2.75}$$

Using Eq. (2.61) and considering a degenerate electron gas with Hall scattering factor $r_H = 1$, the Hall device thermal drift is defined by the temperature dependence of the two-dimensional electron concentration n_{2D} via

$$K_{cs,I} = \frac{1}{n_{2D}}\frac{\partial n_{2D}}{\partial T}. \tag{2.76}$$

On the other hand, the supply-voltage-related sensitivity defines the thermal drift of a Hall device driven by constant voltage

$$K_{cs,V} = \frac{1}{S_V}\frac{\partial S_V}{\partial T}. \tag{2.77}$$

Using Eq. (2.64), the thermal drift of Hall device in this mode is defined by the temperature dependence of the mobility μ as

$$K_{cs,V} = \frac{1}{\mu}\frac{\partial \mu}{\partial T}. \tag{2.78}$$

For magnetic sensor application of Hall devices, the proportionality relation $V_H \sim IB_\perp$ or $V_H \sim VB_\perp$ must hold true to a high degree of accuracy. Accordingly, the non-linearity is an important figure of merit here. It can be defined as [91]

$$P_{non-linearity} = \frac{V_H(I,B) - V_{H0}}{V_{H0}} = \frac{\Delta V_H}{V_{H0}}, \tag{2.79}$$

where V_H denotes the measured Hall voltage at bias current I and magnetic induction B, and V_{H0} is the best linear fit to the measured values.

If the Hall voltage is given by $V_H = S_I IB$, Eq. (2.79) can be written in terms of the supply-current-related sensitivity S_I as

$$P_{non-linearity} = \frac{S_I(I,B) - S_{I0}}{S_{I0}} = \frac{\Delta S_I}{S_{I0}}, \tag{2.80}$$

where S_{I0} is the magnetic current-related sensitivity at $I \simeq 0$ and $B \simeq 0$

$$S_{I0} = \left.\frac{\partial^2 V_H}{\partial B \partial I}\right|_{I=0,\, B=0}. \tag{2.81}$$

Chapter 3

Micro-Hall device fabrication

3.1 Materials, structures and epitaxial growth

The fabrication of high performance micro-Hall devices relies on the following prerequisites: availability of advanced semiconductor technology, appropriate semiconductor material systems as well as optimized structure and device design.

Subsequently, we will concentrate on the micro-Hall device design assessment, relying on the most essential III-V material characteristics reviewed in Chapter 2. Accordingly, the emphasis is set on high sensitivity and low noise, respectively. Molecular-beam epitaxy proves to be the most appropriate growth technique for the required semiconductor structures. Within device fabrication, the specific contact resistivity of the metal-semiconductor barrier turns out as a crucial device parameter and has to be optimized therefore.

3.1.1 Choice of material and structure design

The choice of an appropriate semiconductor material is the first and most essential step in device design. The usage of micro-Hall device as efficient magnetic sensors for isothermal applications requires high sensitivity, low noise and high signal linearity. Furthermore, measurements at non-constant temperatures demand a high thermal stability.

The absolute sensitivity of a Hall sensor scales with the electron drift velocity [see Eq. (2.70)]. Hence, high electron drift velocity materials are most appropriate. InAs, InGaAs, InP and GaAs are verified by simulation [104] as semiconductors with very high saturation drift velocities.

Due to its impact on electron drift velocity, the doping level affects the device performance, too. The highest drift velocities are observed for slightly doped materials [51, 57, 105, 106, 107]. An increased doping level of bulk materials causes lower electron drift velocity [51] and, accordingly, electron mobility [108]. From a detailed analysis of the magnetic sensor signal-to-noise sensitivity, a material possessing a high low-field mobility as well as a huge high-field drift velocity proves to be the best choice. On the other hand, due to decreasing $1/f$ and thermal noise (see Eqs. (2.72) and (2.73)), a higher doping level contributes positively to the signal-to-noise sensitivity and results in an excellent thermal stability of Hall devices in a wide temperature range [109, 110]. Additionally, high quality low-noise ohmic contacts can be more easily fabricated on highly doped materials [111].

According to the above consideration, a trade-off decision has to be made between the doping level, the low-field mobility and the high-field electron drift velocity.

The precise choice of an appropriate semiconductor heterostructure is the most essential decision within the micro-Hall device design assessment. The most contemporary micro-Hall elements are based on III-V semiconductor modulation-doped heterostructures. In such strucures, both a high absolute sensitivity and a low noise level can be achieved due to the huge low-field mobility at high barrier doping levels.

Despite to their advantages, modulation-doped heterostructures exhibit some deficiencies.

The electric field within the Hall devices, being small enough to probe the magnetic material microstructure, will normally be quite large. This causes a decrease in mobility and in supply-voltage-related sensitivity as well as signal-to-noise sensitivity, accordingly. Additionally, the sheet carrier concentration in modulation-doped heterostructures often increases with rising electric field. As a result, the supply-current-related sensitivity diminishes.

At high electric fields, electrons can also be trapped on deep centers located in the doped barrier region [112]. The associated generation and recombination processes contribute to the device noise. Furthermore, the trapping/detrapping effects will change the electron concentration and cause the Hall device instability. Besides, the thermal activation/deactivation of carriers from/on deep levels located in the barrier region results in a thermal instability.

Biasing a micro-Hall device with constant voltage, the voltage-related sensitivity scales with mobility. Thus, the thermal drift is defined by the strong temperature dependence of the mobility and will be significant.

Due to the high doping level in the thick barriers of modulation-doped heterostructures, a strong band bending appears, resulting in an unattended conductive channel within the barrier. Thus, a parasitic parallel conductivity negatively contributes to the thermal device stability.

Alternatively, a micro-Hall devices based on the doped-channel heterostructures are proposed here. These devices exhibit lower mobilities and maximum electron drift velocities. Consequently, compared to micro-Hall elements on modulation-doped heterostructures, lower absolute Hall sensitivities are obtained. This is caused by the strong effect of electron scattering on ionized impurities at low temperatures and, to lesser degree, at high temperatures. Nevertheless, these devices are preferred to the above mentioned modulation-doped micro-Hall elements because of their excellent thermal stability, low noise level and high signal linearity.

In this work, the AlGaAs/GaAs doped-channel heterostructure is considered as a reference or model structure for the further improvement of the absolute Hall sensitivity and the noise performance, respectively. An increased doped GaAs quantum well thickness was shown to enhance the low-field mobility approaching the bulk value for the same doping level [21]. Based on these results, a GaAs quantum well thickness of 350 Å is used here.

The absolute Hall sensitivity can be improved by an InGaAs layer inserted into the doped GaAs quantum well due to the following effects: (i) both the lower effective mass in conduction band and larger intervalley separation between Γ and L valleys in the InGaAs result in a higher peak drift velocity; (ii) growing InGaAs on GaAs (with a thickness well below the critical one) introduces additional lattice strain due to the different lattice constants. This compressive strain enhances both the low-field mobility and the peak electron drift velocity due to increased intervalley separation $\Delta E_{\Gamma L}$ in InGaAs.

The absolute sensitivity of a micro-Hall device is mainly determined by the maximum electron drift velocity, only to a smaller degree by the carrier mobility. Hence, a critical consideration of both doping level and profile in the quantum well is justified.

A decreased doping level would result in higher mobility and higher peak electron drift velocity. Two doping profiles can be realized during epitaxial growth: uniform and/or δ-doping. According to [21], δ-doping results in lower mobilities than uniform doping. Furthermore, the electron mobility depends strongly on the δ-spike position within the quantum well. Centering the δ-spike results in the smallest low-field mobility but highest maximum electron drift velocity compared to other delta or uniform doping profiles [23].

Additionally, the noise level will be lower due to negligible influence of ionized impurity scattering and lattice scattering dominating in the $1/f$ noise [77]. The lowest mid-frequency noise was estimated for center-δ-doped InGaAs quantum wells [113]. Due to the spacial separation between the δ-spike and the AlGaAs layer (using a GaAs subwell), the creation of DX centers at both AlGaAs/GaAs interfaces is less likely during the epitaxial growth.

Apparently, InAs and InGaAs are the most appropriate candidates for highly sensitive and low-noise micro-Hall sensors. However, both materials show drawbacks, too. The deficiencies of InAs are the following: (1) the narrow band gap limiting high-temperature applications like in internal combustion engine environments and (2) impact ionization already under moderate electric fields, leading to catastrophic breakdown. InGaAs has similar drawbacks, although not such extreme ones.

Most of these ideas were realized by molecular beam epitaxial growth of AlGaAs/GaAs/InGaAs heterostructures.

3.1.2 Gas-source molecular-beam epitaxy

Vacuum requirements for MBE

The epitaxial growth of thin films requires a high enough vacuum in the UHV (ultra-high vacuum) range within the growth chamber. This requirement is associated with the main feature of all MBE techniques, being the beam nature of the mass flow towards the substrate. For pressures being not sufficiently low, a degradation of the beam nature may occur due to scattering between the beam molecules and residual gas molecules. As a result, a high quality epitaxial growth is impossible.

To estimate the admissible pressure of residual gases in the chamber, two characteristics of the molecular beam have to be considered: (i) the mean free path of the gas molecules penetrating the vacuum L_b; and (ii) the concentration of the gas molecules n_b [114]. The highest admissible residual gas pressure in the chamber can be estimated from the following condition: The mean free path of the molecules in the reactant beam penetrating the environment of the residual gases has to be larger than the distance l between an effusion cell and the substrate crystal surface. In modern UHV chambers, l is about 200 mm, i.e. $L_b > 200$ mm. Calculations based on the kinetic theory of an ideal gas [115] reveal the maximum admissible pressure of the residual gases being about $p = 7.7 \times 10^{-4}$ mbar for

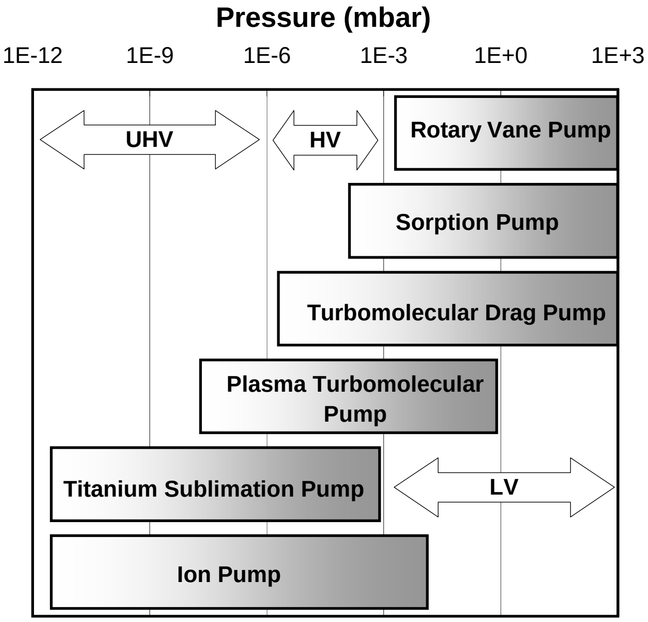

Figure 3.1: Schematic representation of the different pressure and vacuum ranges: low vacuum, high vacuum and ultra-high vacuum. The pumps available in our MBE system and their covered pressure ranges are indicated as horizontal bars.

the growth of GaAs at a temperature of 1250 K for the Ga effusion cell and a temperature of 300 K in the UHV chamber [114].

According to Fig. 3.1, this evaluated pressure is within the high vacuum (HV) range and would preserve the beam nature of the mass transport. However, this value is by far not good enough for the growth of sufficiently pure epitaxial layers: At the low growth rates used in MBE techniques (usually in the order of 1 μm/h or 1 monolayer/s), an unintentional impurity incorporation into a growing film would be inevitable. Correspondingly, a more accurate numerical calculation indicates that the MBE growth of very high purity epitaxial layers at low growth rates should be carried out in an UHV environment at a residual gas pressure of less than 1.7×10^{-11} mbar in the vacuum reactor [114, 116]. Practically, a residual gas pressure of 1×10^{-11} mbar can be achieved in a conventional MBE system [117].

Riber 32-P gas-source molecular-beam epitaxy system

We used an ISA-RIBER 32-P gas-source molecular-beam epitaxy (GSMBE) system for the growth of 2D heterostructures. Figure 3.2 schematically represents the main parts of this system: (1) two UHV chambers [the growth chamber (GC) and an intro chamber (IC)]; (2) the gas line (GL); (3) the pumping systems; (4) the power supplies and the additional electronic components for precise temperature and pressure controls; (5) the cooling system for the growth chamber; and (6) a specially designed filtering system.

The effusion cells are arranged on the rear panel of the growth chamber. For the growth of III-V compounds we used Ga, In and Al solid sources for the group III elements. The group V elements As and P were obtained from AsH_3 and PH_3 hydride gas sources, with the gases cracked at temperatures of $830 - 850$ °C. An additional As cracker cell producing As_4 tetramers is fitted on the rear panel. This type of a low temperature cracker cell is commonly used in solid source MBE (SSMBE). For n and p-type doping, Si and Be solid sources were used.

The temperatures of the effusion cells are measured by thermocouple sets and controlled by high-precision PID controllers. The substrate temperature is measured by a thermocouple and a calibrated infrared optical pyrometer. The epitaxial growth was performed at substrate rotation being necessary for the homogeneous growth of thin films without thickness gradients.

For the studies of the growth dynamics on the crystal surface, we used the reflection high energy electron diffraction (RHEED) technique. A well focused electron beam generated by an e^- gun penetrates into the substrate surface at low angles (grazing incidence geometry) [119] and is diffracted. The according RHEED pattern is imaged on a fluorescent screen.

Additionally, the MBE chamber is equipped with a mass spectrum analyzer (MSA). Using the MSA, the residual gases in the UHV environment can be identified and their concentrations can be measured.

On the one hand, the intro chamber serves as a lock necessary for substrate loading without breaking UHV in the growth chamber. On the other hand, it is

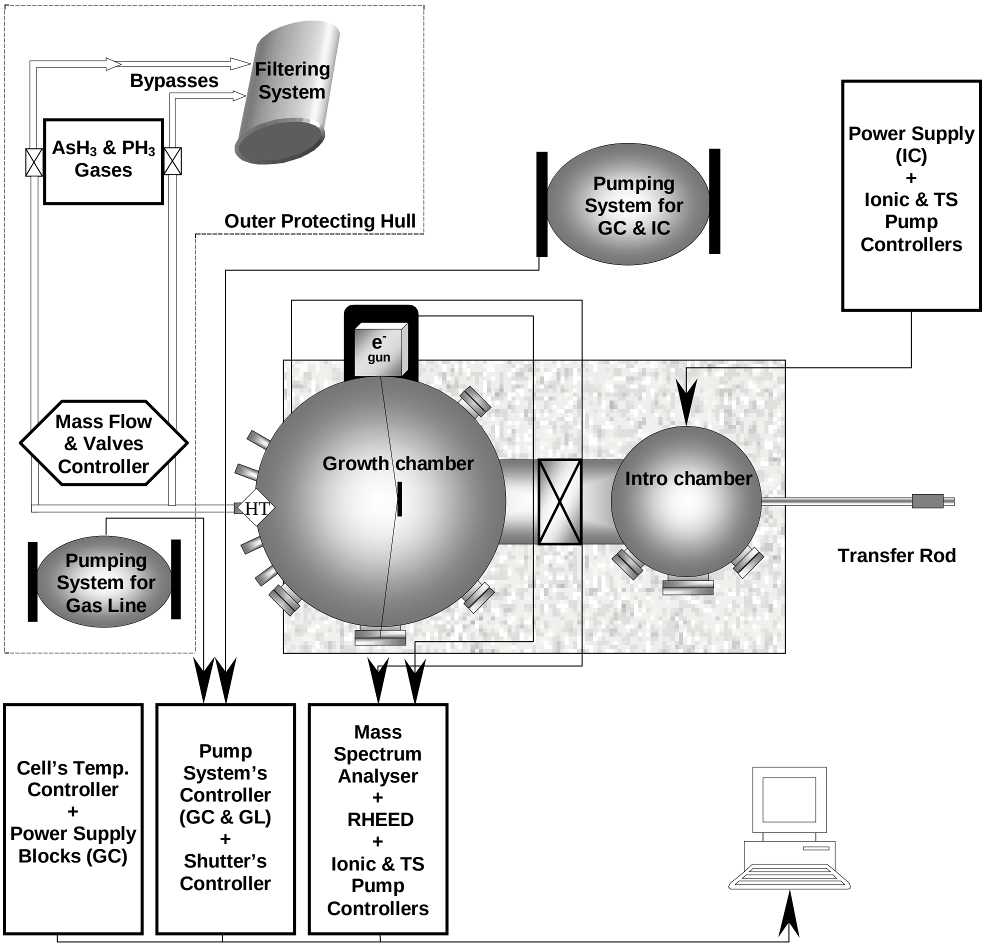

Figure 3.2: The schematic illustration of the ISA-RIBER 32-P gas-source molecular-beam epitaxy (GSMBE) system (adapted after [118]).

used for a further thermal cleaning of the substrate crystal surface. Therefore, a heater and an additional sample holder are installed inside the intro chamber. The heater temperature is controlled by a PID controller.

To provide an UHV inside both chambers, different types of pumps are used: sorption pump, turbomolecular drag pump, plasma turbomolecular pump, ionic pumps and titanium sublimation pumps. Figure 3.1 depicts the pressure ranges covered by these different pumps.

The feed of the AsH_3 and PH_3 gases to the low pressure cracking cells is provided by a gas line. The pressure inside the gas line is always kept in the UHV region.

The MBE growth procedure is completely software-controlled by a computer program developed in our group [120].

Epitaxial growth and related processes on the crystal surface

The MBE technique of thin semiconductor layer growth consists of two basic procedures: the pre-growth preparations and the epitaxial growth. The first includes the chemical cleaning of the substrate surface, substrate loading into the intro chamber (IC) with subsequent heating to temperatures in the 200 − 250 °C range (depending on substrate type) and further substrate transfer into the growth chamber (GC).

Now we consider the basic physical phenomena occuring in the GC during thin film epitaxial growth. The area within the GC can be divided into three main zones [114]: the generation zone of the molecular beams, vapor elements mixing zone and the substrate crystallization zone. A schematic illustration is shown in Fig. 3.3.

Detailed studies of the first zone were conducted in [114]. Comparatively, the second zone with intersecting molecular beams is studied only sparsely at present. The third zone is the most prominent for the epitaxial growth. Altogether, five physical processes have to be considered within this zone [114, 121]:

(1) thermal desorption of the oxide layer at continuous flux flow of group V elements;

(2) adsorption of atoms or molecules incoming from effusion cells onto the substrate surface;

(3) migration and dissociation of adsorbed molecules on the substrate surface;

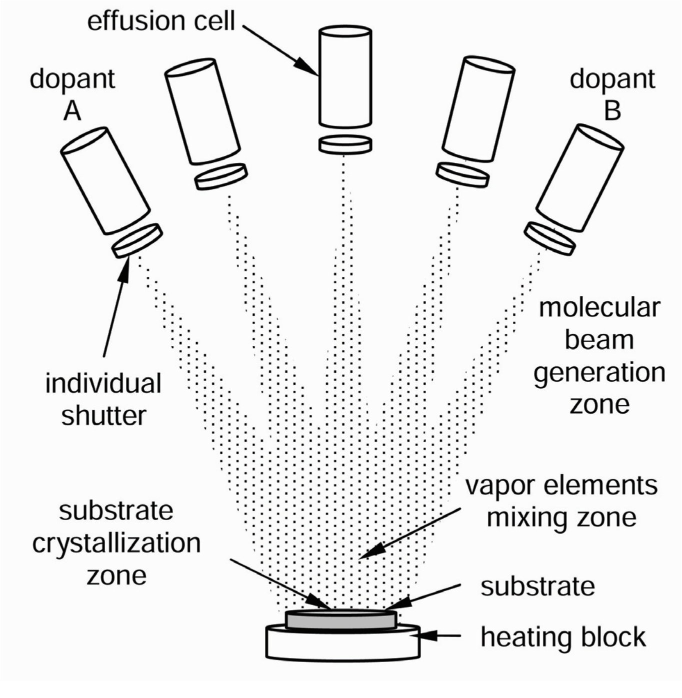

Figure 3.3: Schematic illustration of the growth chamber of a conventional MBE system (adapted after [114]).

(4) incorporation of constituent atoms into the crystal lattice of the substrate (growth of the first monolayer) or into already grown epilayer;

(5) thermal desorption of atoms being not incorporated into the crystal lattice.

A schematic representation of these processes is given in Fig. 3.4.

The desorption of the oxidized surface at continuous flux flow of group V elements is a necessary prerequisite for the subsequent high quality epitaxial growth. This process is usually monitored by RHEED technique. While the substrate surface is gradually cleaned with increasing substrate temperature, the corresponding RHEED pattern exhibits streaks with increasing intensity and decreasing background scattering. For GaAs crystals, a desorption process is usually observed at temperatures higher than 580 °C. The temperature of desorption was shown to correlate with the photoluminescence intensity of the grown structure.

In general, two types of adsorption are distinguished: the physical adsorption (physisorption) and the chemical adsorption (chemisorption) [114]. Physisorption is due to attractive van der Waals forces. No electron transfer occurs between the adsorbate and adsorbent. In contrast to physisorption, chemisorption is due to electron transfer, i.e. a chemical reaction takes place between the adsorbate and the adsorbent. Experimentally, the crystal growth in MBE was shown to

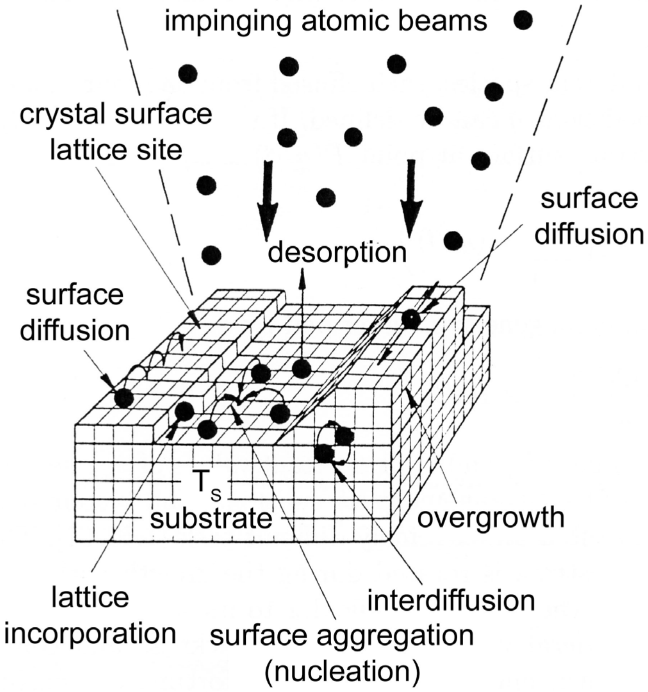

Figure 3.4: Schematic representation of basic physical processes occurring in the substrate crystallization zone (adapted after [114]).

proceed through a two-phase condensation process [122]:

$$A_{gas} \rightleftarrows A_{physisorption} \rightarrow A_{chemisorption}, \tag{3.1}$$

where A_{gas}, $A_{physisorption}$, $A_{chemisorption}$ are gas, physisorption and chemisorption states, respectively. The physisorption state is less stable than the chemisorption state [123]. Hence, the physisorbed state may disappear and the atom returns back to gas state due to desorption process.

The appropriate quantity characterizing the number of oncoming atoms aggregated into the crystal lattice is the sticking coefficient. With the total concentration N_{tot} of impinging atoms and the concentration N_{adh} of atoms adhering to the substrate surface, the sticking coefficient may be defined as

$$s \equiv \frac{N_{adh}}{N_{tot}}. \tag{3.2}$$

For all impinging atoms adhering to the substrate surface, the sticking coefficient is equal to unity. In practice, the sticking coefficient is less than unity and depends on the growth conditions [124, 125, 126].

Detailed studies of the migration processes at the crystal surface were a necessary precondition for the high quality epitaxial growth of compositional lattice matched and pseudomorphically strained semiconductor layers. Based on the obtained results, a modified MBE technology was developed, called migration enhanced epitaxy (MEE) [127, 128]. Using MEE, high quality low temperature GaAs epilayers and GaAs/AlAs quantum well structures were successfully grown [129].

3.1.3 Growth of lattice matched and strained heterostructures

In practice, three possible crystal growth modes can be realized: (1) islands or Volmer-Weber growth [131]; (2) layer plus islands or Stranski-Krastanov growth [132]; and (3) layer-by-layer or Frank - van der Merwe growth [133]. Figure 3.5 schematically depicts the differences between them.

Volmer-Weber growth is usually observed for growing metals on insulators. This mode is possible for atoms or molecules of the deposited material being more strongly bound to each other than to the substrate.

Using *Stranski-Krastanov* growth mode, a growth of self-organized low dimensional systems can be realized. After forming one (or a few) monolayer, the subsequent layer growth is unfavorable and islands are formed on top of this intermediate layer.

Here, we will focus on the third type of growth, i.e. *Frank-van der Merwe* growth, successfully used in our applications.

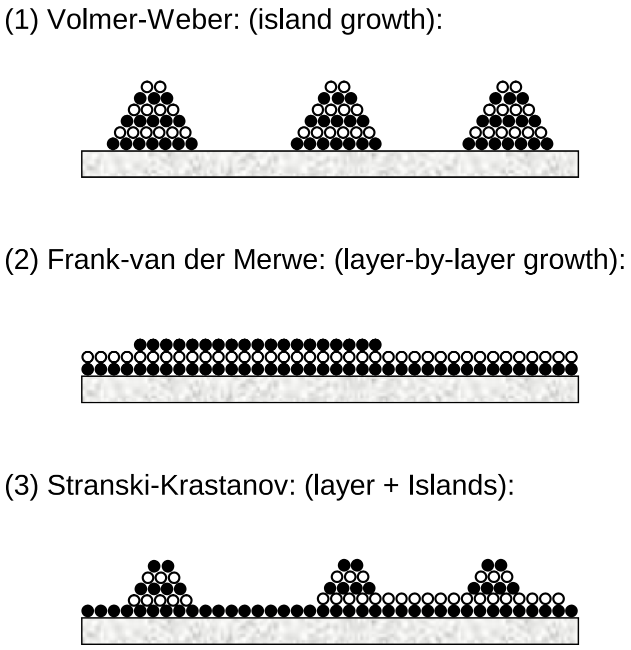

Figure 3.5: The three possible epitaxial growth modes: 1) Volmer-Weber or island growth, 2) Frank-van der Merwe or ideal layer-by-layer growth and 3) Stranski-Krastanov growth or layer + islands growth.

The main feature of the Frank - van der Merwe growth relies on the stronger binding of the atoms to the substrate. The first atoms oncoming from the effusion cells, form a complete monolayer on the crystal surface becoming covered with a somewhat less tightly bound second layer. The next (third) layer covers the second layer, providing a monotonous decrease in the binding energy and so on. Under these conditions, a layer-by-layer or two dimensional growth can be realized.

Depending on the deposited material lattice constant, generally two systems created by coherent layer-by-layer epitaxial growth can be distinguished: (i) lattice matched and (ii) pseudomorphically strained systems. A high quality growth of lattice-matched heterosystems does not face one with difficulties. However, a high-quality two-dimensional growth of materials with different lattice constants is quite troublesome.

Let us consider a two-layer system: a strained InGaAs epilayer grown on a GaAs substrate. Since the lattice constant of the InGaAs is bigger than that of the GaAs substrate, the InGaAs epilayer will be strained in order to match the substrate lattice constant. The misfit between layer and substrate results in a tetragonal compression of the InGaAs layer, i.e. the epilayer lattice is compressively strained in-plane (see Fig. 3.6). This strain is homogeneous and known as misfit strain [130]. The epitaxial growth at such condition is pseudomorphic.

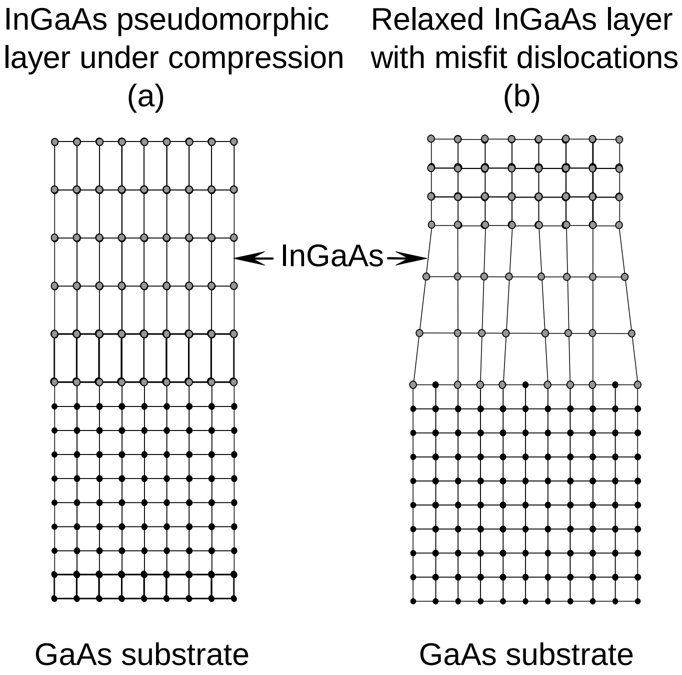

Figure 3.6: Schematic representation of InGaAs epilayer under biaxial compression: (a) pseudomorphic and (b) relaxed with misfit dislocations (adapted after [130]).

However, an increase of the epilayer thickness results in an increase of its homogeneous strain energy. At some certain thickness, the homogeneous strain energy is so large that misfit dislocation nucleation becomes energetically favorable. The corresponding thickness is known as critical thickness [114]. A relaxed InGaAs epilayer with misfit dislocation is schematically shown in Fig. 3.6.

The tetragonal compression of the InGaAs lattice leads to corresponding strains in-plane [(x, y) plane] as well as in the perpendicular direction to the (x, y) plane, i.e. in the z direction. These two strains are different. The strain in the (x, y) plane can be characterized by diagonal components ϵ_{xx} and ϵ_{yy} of the strain tensor [130]

$$\epsilon_{xx} = \epsilon_{yy} = -f_m(X), \tag{3.3}$$

where $f_m(X)$ is the misfit parameter due to lattice mismatch between substrate and epilayer, given by

$$f_m\left(X\right) = \frac{a_{layer}\left(X\right) - a_{sub}}{a_{sub}}. \tag{3.4}$$

The values of the strain in-plane ϵ_{xx} and ϵ_{yy} are negative for epitaxial layer under compressive and positive under tensile strain [130], respectively.

The strain in the direction perpendicular to the (x, y) plane, i.e. in the growth direction, is defined via

$$\epsilon_{zz} = \frac{2C_{12}}{C_{11}} f_m\left(X\right), \tag{3.5}$$

where C_{12} and C_{11} are the elastic constants for III-V materials according to [134].

As outlined in Section 3.1.1, the strain positively contributes to both the electron drift velocity and the low-field mobility and, consequently, to the micro-Hall device performance. However, strained InGaAs layers can not be grown infinitely thick due to the critical layer thickness for a given composition.

Different experimental techniques were used for detailed studies of the InGaAs critical layer thickness: photoluminescence spectroscopy [136, 138, 139, 140, 142, 143], RHEED [141], Raman spectroscopy [144, 145, 146], transport measurements [142], x-ray diffraction methods [147], transmission electron microscopy [138, 148, 149], etc.

The InGaAs critical thickness was shown to depend on the growth temperature [140]. Thicker InGaAs layers without misfit dislocations can be grown at low temperatures. Increased growth temperatures cause a lower critical thickness [140]. A summary plot of the InGaAs critical thickness vs. In composition is presented in Fig. 3.7. Obviously, the critical thickness is low for an increased In composition and vice versa. Theoretical studies of the critical thickness were done by Frank and van der Merwe [133] and by Matthews and Blakeslee [135]. The theory of Frank and van der Merwe is based on the principle of energy minimization. The theory of Matthews and Blakeslee is known as the force balance theory. Both theories arrive at the same numerical results for calculated critical

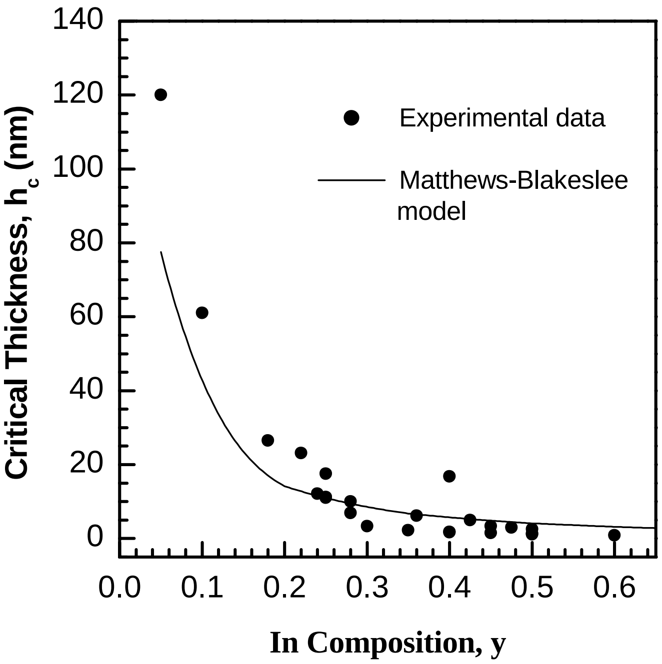

Figure 3.7: Calculated critical layer thickness of $In_yGa_{1-y}As$ (solid curve), using the heterogeneous force equilibrium model of Matthews and Blakeslee [135], compared to experimental data [136, 137, 138, 139, 140, 141].

thickness, supposing the same values of the dislocation energy [150, 151].

Within the frame of the force balance theory, the critical layer thickness h_c is given by [130]:

$$h_c = \frac{b^2 \left(1 - \nu \cos^2(\beta)\right)}{8\pi f_m (1+\nu)\, b \cos(\beta)} \ln \frac{\rho_c h_c}{q}, \tag{3.6}$$

where b is the Burgers vector and ν the Poisson's ratio. β is the angle between the dislocation line and its Burgers vector ($\beta = 60^0$ for the 60^0 dislocations and $\beta = 90^0$ for the 90^0 dislocations), ρ_c the core energy parameter, q the core cut-off parameter assumed to be equal to Burgers vector b. Corresponding results of numerical calculations based on the Matthews and Blakeslee theory are presented in Fig. 3.7, too.

3.1.4 Details on heterostructures

Using monitoring by the RHEED technique, we optimized the growth of lattice matched and pseudomorphically strained heterostructures. As an example, we consider here the optimized growth of a pseudomorphically strained AlGaAs/InGaAs/GaAs modulation-doped heterostructure. Other structures were grown at the same conditions. Figure 3.8 represents the structure used for growth optimization using the RHEED technique.

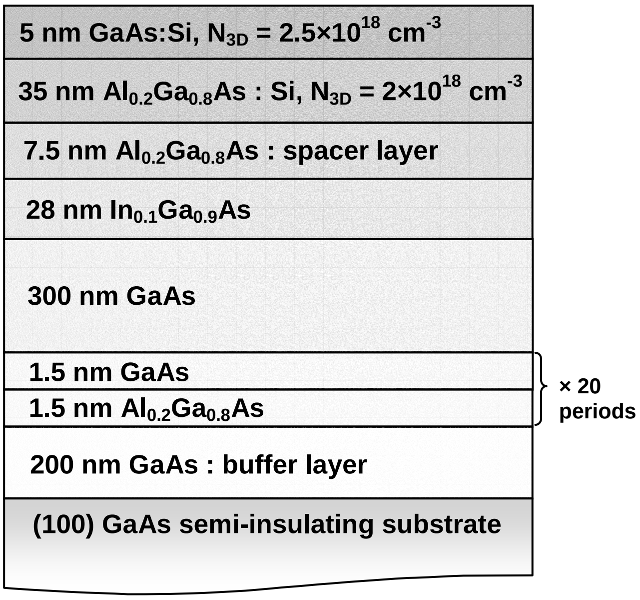

Figure 3.8: Details on AlGaAs/InGaAs/GaAs modulation-doped heterostructure used as reference structure for growth optimization (sample MD22).

Before growth, the GaAs (001) substrate was thermally cleaned at continuous As beam flux arising from AsH_3 hydride gas source at a fixed temperature of

830°C. During the thermal cleaning process, the substrate surface was monitored by RHEED observation. While the substrate surface was gradually cleaned with increasing substrate temperature, the corresponding RHEED pattern exhibited streaks with increasing intensity and decreasing background scattering. Controlling the substrate temperature by a thermocouple and an infrared pyrometer, the desorption of the native oxide layer of most GaAs (001) substrates was observed in the $580°\mathrm{C} - 610°\mathrm{C}$ temperature range, being in agreement with data reported in [152, 153]. Usually, the desorption of the oxide layer was monitored in the [110] azimuth. As an example, Fig. 3.9 presents the observed reconstruction of the (001) GaAs surface in the [110] azimuth. The RHEED pattern observed in the $[\bar{1}10]$ azimuth after desorption usually exhibits spots indicating surface imperfection due to roughness [154].

In order to grow a high quality two-dimensional GaAs, we applied a growth technique successfully used in layer epitaxy. Depositing only a few monolayers in the beginning, the substrate roughness can be smoothed [154]. At the epitaxial growth start, we always deposited 5 ML of GaAs with subsequent growth interruption for a 60 s time interval after each deposition. This procedure was repeated about 20 times and resulted in a smoothed growth front. The surface quality improvement was always monitored by RHEED in both [110] and $[\bar{1}10]$ azimuths. A clear evidence was given by the following findings: In the [110] azimuth, an elongation and sharpening of the diffraction streaks was observed. In the $[\bar{1}10]$ azimuth, sharp streaks instead of spots were monitored. Depending on growth conditions, additional streaks in the $[\bar{1}10]$ azimuth were revealed as a result of different atom's arrangement on the surface.

The further optimization procedure was dedicated to the trade-off decision between growth temperature and III/V flux ratio. The surface reconstruction of

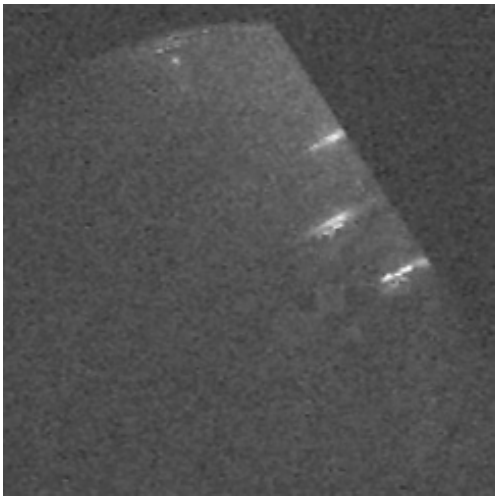

Figure 3.9: RHEED pattern observed in the [110] azimuth for (001) GaAs surface after desorption.

MBE grown layers correlates with the growth temperatures and the flux ratio of III/V elements, respectively. Observing the RHEED intensity oscillation for the specular beam in the [110] azimuth, the optimal surface reconstruction can be found. Detailed studies of both GaAs (001) and $Al_xGa_{1-x}As$ (001) surfaces were done by different groups [154, 155, 156]. Accordingly, the phase diagram of the GaAs (001) surface can be divided into five principal regions [155]:

(1) As-rich surfaces with a (2×4) or (2×1) structure;

(2) a transition range with a (3×1) or apparent (1×1) structure;

(3) Ga-rich surfaces with a (4×1), (4×2), (4×6) or (3×6) structure;

(4) adsorption structures of the type $c(4 \times 4)$, (2×3) and (1×3);

(5) a region with occurring degradation of the surface by Ga droplet formation and roughening or facetting.

Figure 3.10 depicts the surface phase diagram of GaAs(001) (after Däweritz and Hey [155]). All transitions between different reconstructions are reversible, except the one for Ga-rich (4×2) reconstruction [154]. Obviously, the most stable reconstruction in wide temperature and flux ratio ranges is (2×4). Accordingly to Farrell et al. [157] and Däweritz et al. [154], the (2×4) reconstruction can be principally divided into three experimentally observable sub-reconstructions of the GaAs surface: $(2 \times 4) - \alpha$, $(2 \times 4) - \beta$ and $(2 \times 4) - \gamma$. The difference between these types of (2×4) surface reconstructions is observed as a change

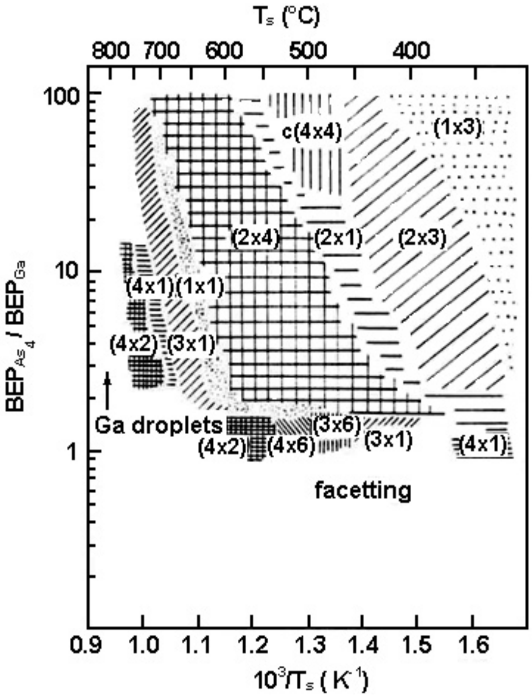

Figure 3.10: Possible surface reconstructions of GaAs, experimentally observed in wide substrate temperature range and at different V/III flux ratios after Däweritz and Hey [155].

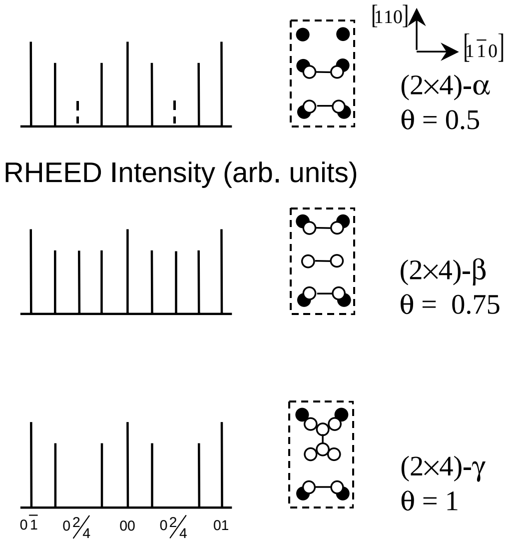

Figure 3.11: Schematic overview of RHEED patterns observed in the [$\bar{1}$10] azimuth (after [154]). Different types of (2 × 4) reconstruction can be distinguished due to changes of the relative intensity. As and Ga atoms are shown as open and full circles.

in the relative intensities of fractional diffraction features within the RHEED pattern recorded in the [$\bar{1}$10] azimuth [154, 157]. This is supposed to be due to different numbers of dimers per unit mesh: The $(2 \times 4) - \alpha$ reconstruction has two dimers per unit mesh corresponding to an As coverage of 0.50 ML and $(2 \times 4) - \beta$ has three dimers per unit mesh corresponding to an As coverage of 0.75 ML. The $(2 \times 4) - \gamma$ corresponds to an As coverage of 1 ML. The intensity distribution of the RHEED pattern and a schematic representation of the unit meshes for the three possible types of the (2 × 4) reconstruction are shown in Fig. 3.11. Experiments based on RHEED intensity oscillation studies reveal the $(2 \times 4) - \beta$ phase corresponding to the smoothest and the best ordered surface structure [154].

Using a growth temperature of $T_s = 580°\mathrm{C}$ and a $\mathrm{AsH_3}$ flux of 1.65 sccm, cracked at 830°C, we grew the GaAs layers, monitoring the best ordered GaAs(001) $(2 \times 4) - \beta$ surface. During the epitaxial growth of the GaAs(001) surface, RHEED patterns were recorded during substrate rotation by a camcorder. The shutter of the Ga effusion cell was kept open during the record. Corresponding still-images in the [110] [image (a)] and [$\bar{1}$10] [image (b)] azimuths were extracted from the video stream. They are shown in Fig 3.12. Obviously, the observed surface reconstruction is $(2 \times 4) - \beta$.

After the growth of a 2000 Å GaAs buffer layer, a short period 15 Å $\mathrm{Al_{0.2}Ga_{0.8}As}$/15 Å GaAs superlattice was grown at the same substrate temperature. Due to the short period superlattice, dislocations proceeding from the GaAs substrate can be suppressed. Subsequently, 3000 Å of GaAs were grown,

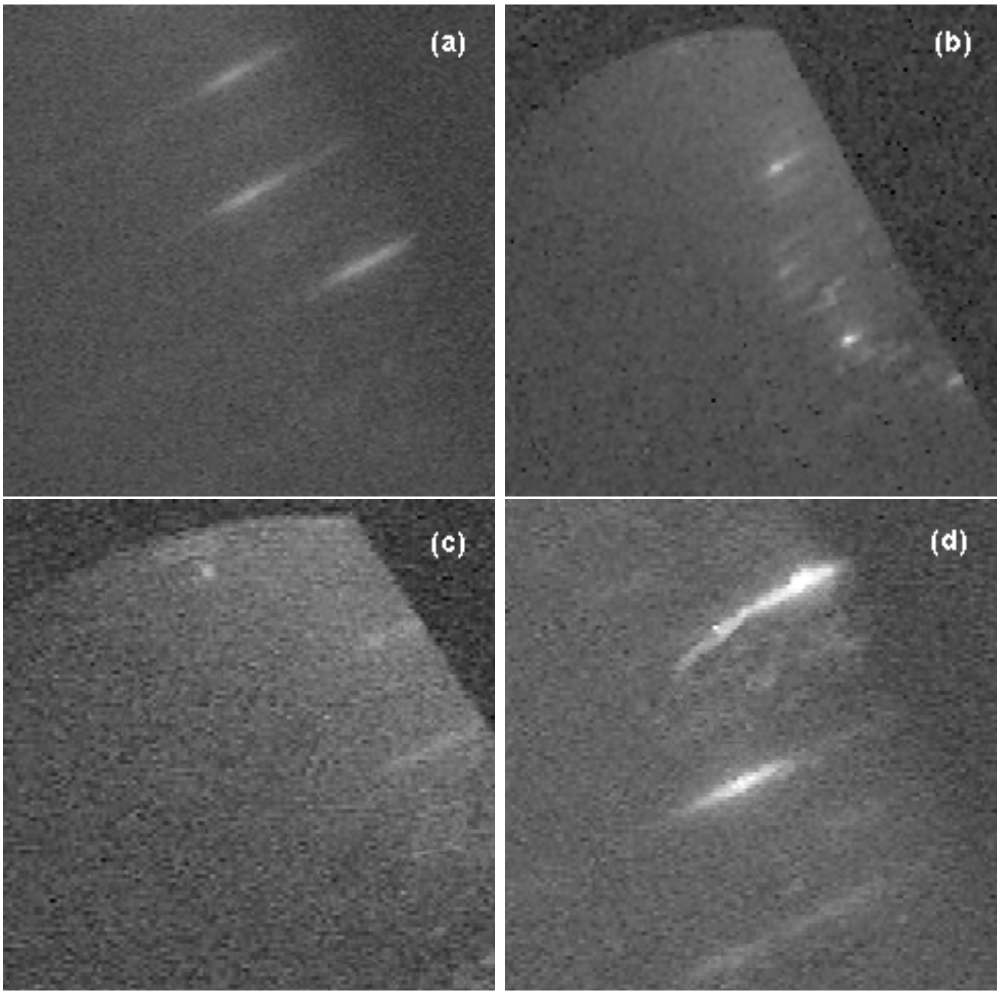

Figure 3.12: RHEED patterns of the GaAs(001) surface for [110] [image (a)] and [$\bar{1}$10] [image (b)] azimuths, revealing the $(2 \times 4) - \beta$ reconstruction. The shutters of both the Ga cell and the hydride gas source were opened. Image (c) corresponds to the end of 280 Å of $In_{0.1}Ga_{0.9}As$ layer growth. The observed reconstruction was (1×1) with a growth temperature of $T_s = 565°C$. Image (d) exhibits the RHEED pattern of the AlGaAs:Si layer, recorded in the [110] azimuth and grown after the AlGaAs spacer layer. The substrate temperature during the AlGaAs growth was $T_s = 610°C$.

using a substrate temperature ramping down to $T_s = 565°C$ during the growth of the last 425 Å of GaAs. This temperature ramp is necessary for high quality growth of pseudomorphically strained InGaAs quantum wells. The InGaAs layer growth was always monitored by RHEED observation. As an example, we present in Fig. 3.12 [image (c)] the RHEED pattern at the end of the growth of a 280 Å of $In_{0.1}Ga_{0.9}As$ layer. It reveals fully two-dimensional growth even for such a thick InGaAs layer. The observed surface reconstruction of the InGaAs layer was (1×1).

After a growth interruption of 30 s at a continued AsH_3 gas flux of 1.85 sccm, the InGaAs layer was capped by a 75 Å AlGaAs spacer layer. On top of this, a 350 Å AlGaAs:Si barrier layer was grown at a temperature of 610°C. We found the doping efficiency of AlGaAs layers grown at higher substrate temperatures being considerably higher than at temperatures less than 600°C. The corresponding RHEED pattern recorded during AlGaAs:Si growth in the [110] azimuth is shown in Fig. 3.12, image (d). Obviously, this diffraction pattern is more diffuse compared to the ones taken during GaAs layer growth. It indicates a higher disorder degree and roughness for the epitaxial growth of AlGaAs compared to GaAs.

The structural and electronic parameters of AlGaAs/GaAs/InGaAs doped-channel heterostructures that were grown using same recipes are represented by Table 3.1. Details on the other AlGaAs/InGaAs/GaAs modulation-doped heterostructures studied in this work can be found in Table 3.2.

		DC8	DC9	DC13
GaAs	d (nm)	7.5	7.5	7.5
(cap layer)	N_D (10^{18} cm^{-3})	2.0	2.0	2.0
$Al_xGa_{1-x}As$	d (nm)	35	35	35
(undoped barrier)	x	0.30	0.30	0.30
GaAs	d (nm)	17.5	10.3	16
(quantum well)	N_D (10^{18} cm^{-3})	2.0	2.0	2.0
Si-δ-doped $In_yGa_{1-y}As$:Si	d (nm)		144	30
(quantum well)	y		0.20	0.30
	n_{2D} (10^{12} cm^{-2})		0.58	0.21
GaAs	d (nm)	17.5	10.3	16
(quantum well)	N_D (10^{18} cm^{-3})	2.0	2.0	2.0
$Al_xGa_{1-x}As$	d (nm)	35	35	35
(undoped barrier)	x	0.30	0.30	0.30
GaAs	d (nm)	10	10	10
	N_A (10^{18} cm^{-3})	1.5	1.5	1.5
GaAs	d (nm)	200	200	200
(buffer layer)				
Hall				
measurements	n_s (10^{12} cm^{-2})	1.3	1.3	1.5
at $T = 300$ K	μ_e (cm^2/(Vs))	1651	2193	2046

Table 3.1: Structural and electronic parameters of pseudomorphically strained AlGaAs/GaAs/InGaAs doped-channel heterostructures studied in this work.

		MD1	MD2	MD3	MD4	MD5	MD6	MD28	MD11	MD22	MD98
GaAs	d (nm)	5	5	5	5	5	5	5	5	5	5
(cap layer)	N_D (10^{18} cm^{-3})	2.5	2.5	2.5	2.5	2.5	2.5	2.5	2.5	2.5	2.5
$Al_xGa_{1-x}As$	d (nm)	35	35	35	35	35	35	35	35	35	35
(supply layer)	x	0.20	0.20	0.20	0.15	0.15	0.15	0.20	0.20	0.20	0.20
	N_D (10^{18} cm^{-3})	2.0	2.0	2.0	2.0	2.0	2.0	2.0	2.0	2.0	2.0
$Al_xGa_{1-x}As$	d (nm)	7.5	7.5	7.5	7.5	7.5	7.5	7.5	7.5	7.5	7.5
(spacer layer)	x	0.20	0.20	0.20	0.15	0.15	0.15	0.20	0.20	0.20	0.20
$In_yGa_{1-y}As$	d (nm)	20	15	10	20	13	10	15	25	28	80
(quantum well)	y	0.09	0.10	0.10	0.15	0.15	0.15	0.10	0.09	0.10	0.08
GaAs	d (nm)	300	300	300	300	300	300	300	300	300	300
GaAs/AlGaAs	d_{GaAs} (nm)	1.5	1.5	1.5	1.5	1.5	1.5	1.5	1.5	1.5	1.5
(10 periods	d_{AlGaAs} (nm)	1.5	1.5	1.5	1.5	1.5	1.5	1.5	1.5	1.5	1.5
superlattice)	x	0.20	0.20	0.20	0.15	0.15	0.15	0.20	0.20	0.20	0.20
GaAs	d (nm)	200	200	200	200	200	200	200	200	200	200
GaAs substrate	d (μm)	500	500	500	500	500	500	500	500	500	500
Hall measurements	n_s (10^{12} cm^{-2})	0.99	1.03	1.28	0.93	0.93	0.89	0.96	2.71	2.46	2.81
at $T = 300$ K	μ_e (cm^2/(Vs))	6900	6600	6100	5300	6900	6700	6800	4410	4110	3580

Table 3.2: Structural and electronic parameters of pseudomorphically strained AlGaAs/InGaAs/GaAs modulation-doped heterostructures studied in this work.

3.2 X-ray characterization of thin heterostructures

Commonly, the structural parameters of grown epilayers like thickness and composition are controllable to a high degree of accuracy in MBE technique. However, additional structural studies by high resolution x-ray diffractometry (HRXRD) are often necessary. Since the HRXRD method is nondestructive and exhibits a high strain sensitivity of about 10^{-7}, it can be successfully used not only for an accurate estimation of both the layer thicknesses and the ternary compound compositions, but also for a precise determination of the other essential characteristics of the crystal lattice like misfit strain, lattice relaxation, dislocation content, etc. As discussed in Section 3.1.1, the tetragonal strain positively contributes to the micro-Hall sensor performance and the presence of any lattice defect will result in sensor parameter degradation. Therefore, we have applied the HRXRD technique as an appropriate post-growth characterization method for our structures.

3.2.1 Double crystal x-ray diffractometer

The measurements of x-ray rocking curves for the symmetrical (004) reflection were performed on a commercial double crystal Bede QC1a diffractometer. A schematic illustration of a standard high resolution double crystal x-ray diffractometer is presented in Fig. 3.13. The measurement configuration consists of the following main parts: the x-ray source with a copper target, the collimator, a reference crystal (we used a GaAs (001) oriented crystal), the sample under investigation and the detector.

For a given x-ray wavelength λ being comparable to the interatomic distances in the crystal (we are using $\mathrm{Cu-K}\alpha_1$ radiation with $\lambda = 1.5406$ Å), a constructive interference of x-ray scattered rays from atomic planes appears for the Bragg condition satisfied

$$n\lambda = 2d\sin\left(\theta_B\right), \tag{3.7}$$

where d is the spacing between neighboring atomic planes, θ_B the Bragg angle for diffraction and n an integer referring to the number of the diffraction order (Fig. 3.13). The Bragg angle θ_B depends on the experiment geometry. For example, for a symmetric geometry, i.e. for (004) reflection, $\theta_B = 33.024^0$ holds true. $\theta_B = 41.873^0$ results for the asymmetric geometry in (224) reflection.

The double crystal x-ray diffractometer working principle relies on the comparison of the lattice constants between the epilayer and the reference crystal. For the (004) symmetric reflection, the maximum intensity of the diffracted x-ray beams will be observed when the lattice hkl planes of the reference crystal are parallel to the $\overline{\mathrm{h}}\overline{\mathrm{k}}\overline{\mathrm{l}}$ planes of studied sample. Within this geometry, measurements of both the lattice constant and the real strain in growth direction z can

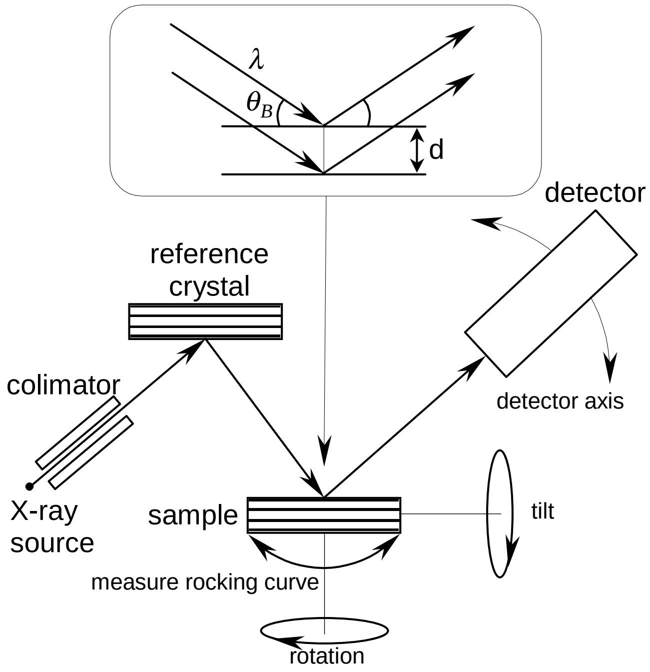

Figure 3.13: Schematic representation of a high resolution double crystal x-ray diffractometer. The Bragg condition necessary for the observation of the maximum of diffracted intensity is illustrated in the insert (see Eq. 3.7).

be performed. Usually, measurements in symmetric (004) reflection are effectual in order to characterize a lattice matched system. However, additional asymmetric measurements are necessary for the characterization of epitaxial systems consisting of layers with different lattice constants. Using the asymmetric geometry for (224) or (113) reflections, one can measure the strain in the (x, y) plane. Furthermore, the layer state can also be examined: one can estimate if the layer is pseudomorphically strained, partially relaxed or fully relaxed.

3.2.2 X-ray rocking curves: (004) reflection

To characterize the grown heterostructures, we measured x-ray rocking curves in symmetric (004) reflection. A typical result is shown in Fig. 3.14 for sample MD11.

Two main peaks are well resolved. The intense and narrow peak located at 0 arcsec corresponds to the GaAs substrate. The other peak on the left side of the GaAs substrate peak at -1420 arcsec is caused by diffraction of the x-ray beam on the InGaAs layer. Since the InGaAs lattice constant is larger than that of GaAs, the InGaAs peak will be always observed at smaller Bragg angles than for GaAs. A rough estimate of the In content of the $\mathrm{In}_y\mathrm{Ga}_{1-y}\mathrm{As}$ layer can be made by measuring the peak separation $\Delta\theta$. The experimental x-ray mismatch

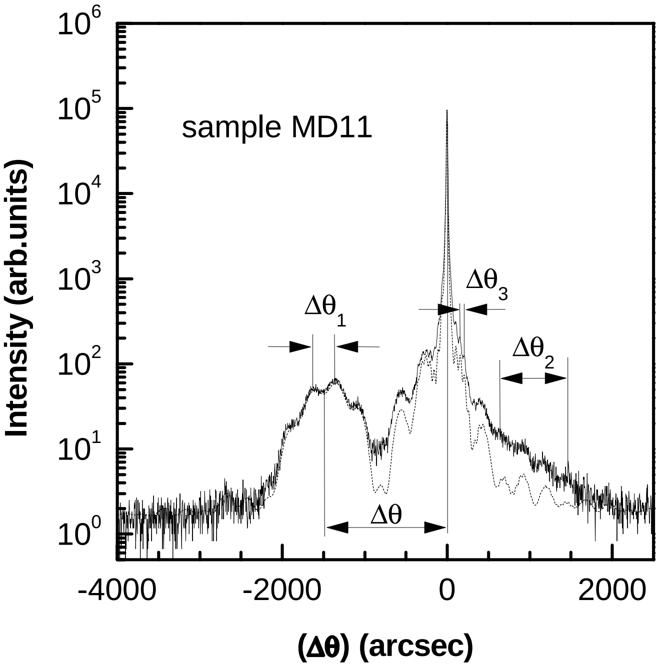

Figure 3.14: X-ray measured (solid line) and best-fit simulated (dotted line) rocking curve. The layer sequence and thicknesses are the same as for the heterostructure shown in Fig. 3.8, except for InGaAs layer thickness. The best fit corresponds to an $\mathrm{In}_y\mathrm{Ga}_{1-x}\mathrm{As}$ layer thickness of 253 Å ± 5 Å and a composition of y = 0.09 ± 0.005.

is given by

$$f_m^* = \frac{\Delta d}{d} = -\frac{\Delta\theta}{\tan(\theta)} = f_m\left(\frac{1+\nu}{1-\nu}\right), \tag{3.8}$$

where f_m is the true mismatch due to lattice constants difference given by Eq. (3.4), ν the Poisson ratio and d the interplanar spacing normal to the substrate. Assuming $\nu \sim 1/3$ as for III-V materials, the real mismatch can be estimated as $f_m = f_m^*/2$. For a peak separation of about 1458 arcsec, a Bragg angle of $\theta_B = 33.024^0$ and x-ray CuKα_1 radiation, the real mismatch f_m is about 5440 ppm. Assuming the lattice constant of InGaAs ternary compound complying to Vegard's law [158], In composition can be easily evaluated. We estimate In composition of about 8.5 %.

The intensity distribution between different peaks in the rocking curve depends on the layer thicknesses [158]. The peak intensity increases with corresponding larger layer thickness. On the other hand, the peak intensity also depends on the layer quality. Thereby, an epilayer with dislocations exhibits a broadened peak of lowered intensity. For an epitaxial layer thickness evaluation, one has to measure the integral peak intensity, i.e. the area under the peak.

Measuring the angular distance within the periodic oscillation vicinal to the layer peak, the epilayer thickness can be estimated. Supposing $\Delta\theta_j$ as the angular distance between these oscillations and using simple relations between the incident x-ray beam wavelength λ, $\Delta\theta_j$ and the Bragg angle θ_B, the layer thickness is given by

$$t = \frac{\lambda}{2\Delta\theta_j \cos(\theta_B)}. \tag{3.9}$$

The oscillation period $\Delta\theta_1 = 266$ arcsec as measured from the rocking curve (see notation in Fig. 3.14) reveals a thickness of about 713 Å for the whole layer package, beginning from the highly strained InGaAs layer [159].

The oscillations with the smallest period $\Delta\theta_3$ are resolved due to the buffer GaAs layer grown on the AlGaAs/GaAs superlattice. The oscillation period $\Delta\theta_2$ amounts about 762 arcsec and corresponds to the finite InGaAs layer thickness of about 248 Å.

Using numerical calculations based on dynamical diffraction theory, precise estimates of both layer thicknesses and compositions for ternary compounds can be performed. Solving the Takagi-Taupin second-order nonlinear differential equations [160, 161] by numerical means like the Runge-Kutta method [162] or the recurrence formalism [163], an accurate fit to the measured rocking curve can be done. We used the commercial software package RADS/MERCURY from Bede Scientific Instruments Ltd. for simulation purposes. Results are shown in Fig. 3.14 for σ-polarization according to the experimental conditions. Obviously,

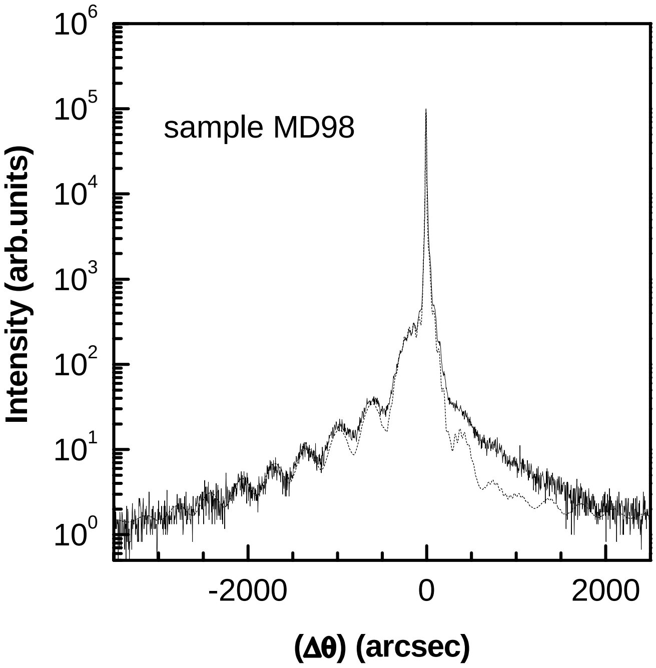

Figure 3.15: Measured (solid line) and simulated (dotted line) x-ray rocking curves for a strained AlGaAs/InGaAs/GaAs heterostructure. A thickness of 80 ± 5 Å is estimated for the $In_{0.08}Ga_{0.92}As$ strained layer.

the simulated rocking curve is well fitted to the experimental data. The data set contained an In composition of y = 0.09 ± 0.005 and 253 Å ± 5 Å thickness.

Figure 3.15 exhibits a x-ray rocking curve measured on a similar heterostructure, but containing a much thinner strained InGaAs layer. Left from GaAs substrate peak, no pronounced peak is observed. Instead, we see periodical oscillations with a period of about 367 arcsec. Accordingly, a total thickness of about 515 Å can be estimated. These oscillations are due to interference effects of the whole layer package, beginning from InGaAs. Using the numerical simulations, a In composition of $y = 0.08$ and a layer thickness of $d = 80$ Å were estimated.

3.3 From heterostructures to devices

The micro-Hall device fabrication of different sizes and geometries (see Fig. 3.16) with high symmetry on MBE-grown heterostructures requires further device technology treatment: (i) lateral structuring by optical or electron beam lithography and (ii) metallization and contacting.

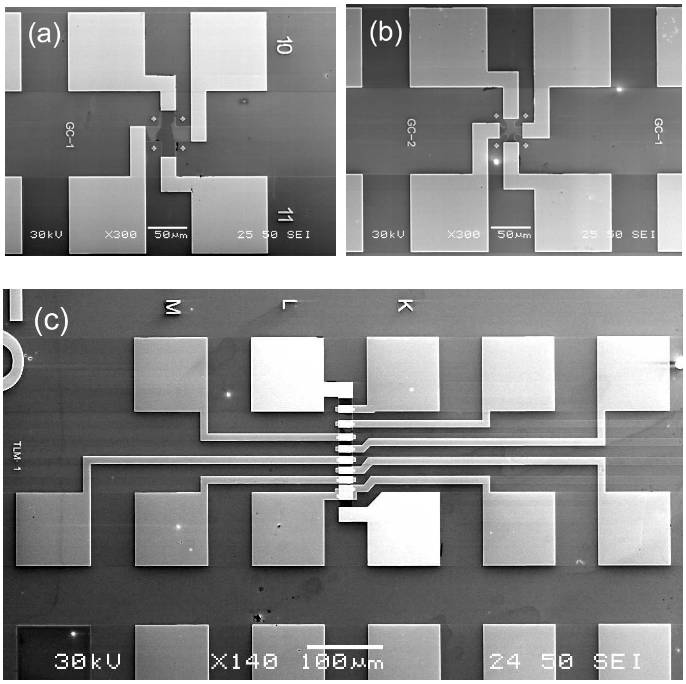

Figure 3.16: Secondary electron images (SEI) of micro-Hall devices with different sizes [164]: 20 μm [image (a)] and 10 μm [image (b)] square size, fabricated by standard optical lithography. Measurements of the contact resistance were performed on the patterned structure [image (c)] using transmission-line model.

The aim of the metallization step is creation of the low noise Ohmic contacts. As a matter of fact, just the contact preparation appears as a crucial technology step. A poor contact performance significantly degrades the micro-Hall device noise properties and, respectively, signal-to-noise sensitivity and detection limit.

Here we concentrate on optimization of the contact resistance. Thus, the low-noise Ohmic contacts can be realized. Those contacts do not affect the I-V characteristics of the material under test or, in other words, the voltage drop across the contacts is negligible small compared to the voltage drop across the active device area [165].

3.3.1 Metal-semiconductor system

A wide variety of the different metal-semiconductor systems was reported in the literature [166, 167, 168, 169, 170, 171]. In our studies, we restrict our consideration to Au/Ge/Ni metal films in contact with n-type GaAs/AlGaAs/GaAs/InGaAs and GaAs/AlGaAs/InGaAs/GaAs heterostructures.

Standard optical photolithography was used for the lateral structuring of Greek cross micro-Hall sensors with different sizes [172]. Depositing Au/Ge/Ni metal films on the semiconductor surface, the contacts were defined. Figure 3.16 demonstrates two different sizes of Greek cross micro-Hall devices. Additionally, it shows the transmission-line model (TLM) structure successfully used for contact resistance measurements.

For a metal in contact with a n-type semiconductor, the energy diagram at applied voltage V is shown in Fig. 3.17. Electron transport across the metal-semiconductor interface is affordable by two processes: (i) thermionic emission (TE) of electrons over the barrier and (ii) tunnel effects of electrons through the barrier [173]. On their part, the tunnel effects can be subdivided into field

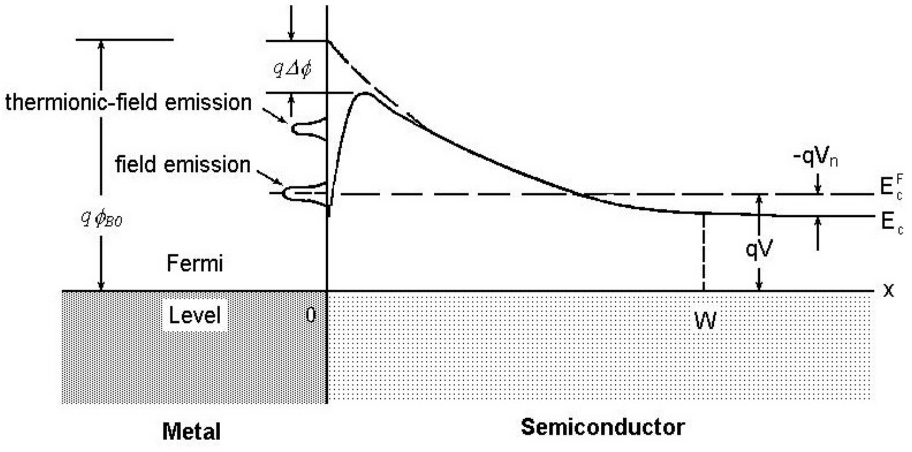

Figure 3.17: Schematic presentation of the energy band diagram of a metal-semiconductor interface at forward bias. E_c^F is the Fermi level of the semiconductor shifted with respect to the metal Fermi level by the applied voltage V (after [173]).

emission (FE) and thermionic field emission (TFE), respectively. The field emission (FE) takes place at an energy near the Fermi level, whereas thermionic field emission (TFE) appears as a thermally assisted tunnel process above the Fermi level.

The key parameter of the Ohmic contact is the specific contact resistance ρ_c, also known as the specific contact resistivity or contact resistivity. This value characterizes the transport properties across the metal-semiconductor barrier. Obviously, the specific contact resistivity has to be minimized for high quality Ohmic contacts. The specific contact resistivity defined in [173] is

$$\rho_c = \left[\frac{\partial j}{\partial V}\right]^{-1}_{V=0}. \tag{3.10}$$

The current density for a thermionic emission (TE) process is given via [174]

$$j_{TE} = AT^2 \exp\left[\frac{-q\left(\phi_{B0} - \Delta\phi\right)}{k_B T}\right]\left[\exp\left(\frac{qV}{k_B T}\right) - 1\right], \tag{3.11}$$

where T is the absolute temperature, q the electrical charge, k_B the Boltzman's constant and V the bias voltage. $\phi_B = \phi_{B0} - \Delta\phi$ denotes the effective potential barrier height for a thermally excited electron flux (see Fig. 3.17). A is the so-called Richardson constant

$$A = \frac{4\pi q k_B^2 m^*}{h^3}, \tag{3.12}$$

where h is the Planck's constant and m^* the effective mass of charge carriers.

The current density for field emission (FE) and thermionic field emission (TFE) is

$$j_{FE,\,TFE} = \int\limits_0^{\phi_{B0}-\Delta\phi} P\left(E\right) N\left(E\right) dE, \tag{3.13}$$

where $P(E)$ is the transmission probability. For a uniformly doped semiconductor with the simple parabolic band-bending, an analytical solution for the transmission probability is given by

$$P\left(E\right) = \exp\left[\frac{-E_b y\left(\alpha\right)}{E_{00}}\right], \tag{3.14}$$

where

$$E_b = q\left(\phi_B - V - V_n\right) \tag{3.15}$$

and

$$y\left(\alpha\right) = y\left(\frac{E}{E_b}\right) = \sqrt{1 - \frac{E}{E_b}} - Ln\left(\frac{1 + \sqrt{1 - \frac{E}{E_b}}}{\sqrt{\frac{E}{E_b}}}\right). \tag{3.16}$$

The parameter E_{00} is mainly determined by the band-bending at the metal-semiconductor interface according to

$$E_{00} = \frac{qh}{4\pi}\sqrt{\frac{N_D}{m_r \varepsilon}}, \tag{3.17}$$

where m_r is the tunneling effective mass, N_D the impurity concentration and ε the static dielectric constant.

If $k_BT \sim E_{00}$, then the thermionic field emission (TFE) dominates [173]. Then the specific contact resistivity at conditions fixed by Padovani [175] can be expressed as

$$\begin{aligned} \rho_{c,\,TFE} = & \left[\frac{k_BT}{qAT^2}\right]\left[k_BT\cosh\left(\frac{E_{00}}{k_BT}\right)\right] \\ & \times\sqrt{\frac{\coth\left(\frac{E_{00}}{k_BT}\right)}{\pi(\phi_B-V_n)E_{00}}}\exp\left[\frac{\phi_B-V_n}{E_{00}\coth\left(\frac{E_{00}}{k_BT}\right)}+\frac{V_n}{k_BT}\right] \end{aligned} . \tag{3.18}$$

On the other hand, for $k_BT \ll E_{00}$ and therefore dominating field emission (FE), the specific contact resistivity is given by

$$\rho_c = \left[\frac{AT^2\pi q\exp\left(-{}^{\phi_B}\!/\!{}_{E_{00}}\right)}{k_BT\sin\left(\pi c_1 k_BT\right)} - \frac{AT^2 c_1 q\exp\left(-{}^{\phi_B}\!/\!{}_{E_{00}}+c_1V_n\right)}{\left(c_1k_BT\right)^2}\right]^{-1}, \tag{3.19}$$

where c_1 is mainly a function of E_{00}, ϕ_B and V_n [173].

For $k_BT \gg E_{00}$, thermionic emission (TE) dominates. Accordingly, the specific contact resistivity is defined by

$$\rho_c = \frac{k_BT}{qAT^2}\exp\left(\frac{\phi_B}{k_BT}\right). \tag{3.20}$$

3.3.2 Optimization of contact resistance

We have optimized the contact resistance by thermal annealing, probing the 320°C to 450°C temperature range. The alloying temperature was controlled by a thermocouple set. The oven was calibrated prior to annealing, using the melting points of different materials like In, Sn, Zn and Au:Ge(12 %).

Transport-relevant parameters of the whole metal-semiconductor system like contact resistance R_c, specific contact resistivity ρ_c, sheet resistance R_s of the semiconductor material below the contact and sheet resistance r_s of the bulk material between the contacts can be extracted from the application of the transmission line model (TLM) to electrical measurements.

The TLM pattern consists of a planar contact sequence of the length L and the width W, separated by sequentially spacing l_i of 2, 3, 4, 5, 6, 8 and 10 μm width. An according structure is shown in Fig. 3.16, image (c).

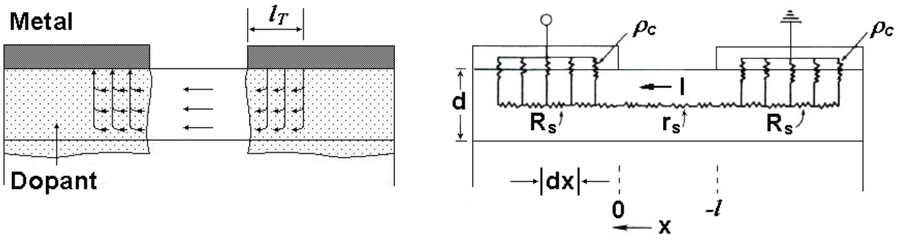

Figure 3.18: A transmission line model: possible scenarios of diffusion of metal into semiconductor epilayer; equivalent circuit of transmission-line model used for calculations of contact resistance R_c, specific contact resistance ρ_c, and sheet resistance of semiconductor material between contacts r_s and below the planar contact R_s (after [176]).

At constant supply current I, the voltage drop V between neighboring contacts, separated by spacing l_i, can be measured. Then the total resistance $R = V/I$ contains two terms:

$$R = 2R_c + r_s \frac{l_i}{W}. \tag{3.21}$$

Knowing the geometrical sizes of the planar metal contacts, both the contact resistance R_c and the bulk sheet resistance r_s can be directly extracted from a plot of total resistance R vs. spacing l_i. However, the contact resistance alone does not give complete information about the metal-semiconductor barrier properties. Additional necessary information is provided by measurements of the specific contact resistivity ρ_c being possible also in the frame of transmission line model. Therefore, a short review of the main TLM aspects is necessary.

Since any metal does not completely, but only partially, diffuse into a semiconductor material during thermal annealing (see Fig. 3.18), the current is assumed to flow vertically from the metal to the semiconductor and then bend over to a nearly horizontal direction, before entering the bulk region [176]. The characteristic distance for the vertical flow along the metal is called transfer length l_T (see designation in Fig. 3.18).

In order to calculate the specific contact resistivity ρ_c, the metal-semiconductor system can be considered as a distributed resistance circuit [176] (see Fig. 3.18), with a current I flowing from the right to the left side. Assuming a small enough layer thickness d, the current density varies not significantly over the cross section Wd. Thus, in the region $0 \leq x \leq L$, the circuit can be described by the following differential equations [176]:

$$dV(x) = -\frac{R_s}{W} I(x) dx \tag{3.22}$$

and

$$dI(x) = \frac{W}{\rho_c} \left[V_c - V(x)\right] dx, \tag{3.23}$$

where V_c is negative for a given current flow.

Assuming no current flowing at the end of the contacts (i.e. $I(l_c) = 0$) and solving both coupled equations (3.22) and (3.23), the contact resistance R_c is expressed via

$$R_c = \frac{\sqrt{R_s \rho_c}}{W} \coth(kL), \tag{3.24}$$

where k is denoted as $k \equiv \sqrt{\frac{R_s}{\rho_c}}$. Assuming the semiconductor material resistance under the contact being approximately the same as the sheet resistance between the contacts ($R_s \approx r_s$) and setting the condition $kL \geq 2$ of electrically long contacts, Eq. (3.24) can be approximated by

$$\rho_c \approx \frac{W^2 R_c^2}{R_s}. \tag{3.25}$$

This approximation is widely used in practice. Actually, the assumption $R_s \approx r_s$ is not really valid. In order to overcome this obstacle, Reeves and Harrison [177] proposed the additional measurement of the so-called end resistance. This proposal was improved later [178, 179, 180, 181]. For electrically long contacts and $R_s \approx r_s$, the transfer length is given by

$$l_T = \frac{W R_c}{R_s} = \sqrt{\frac{\rho_c}{R_s}}. \tag{3.26}$$

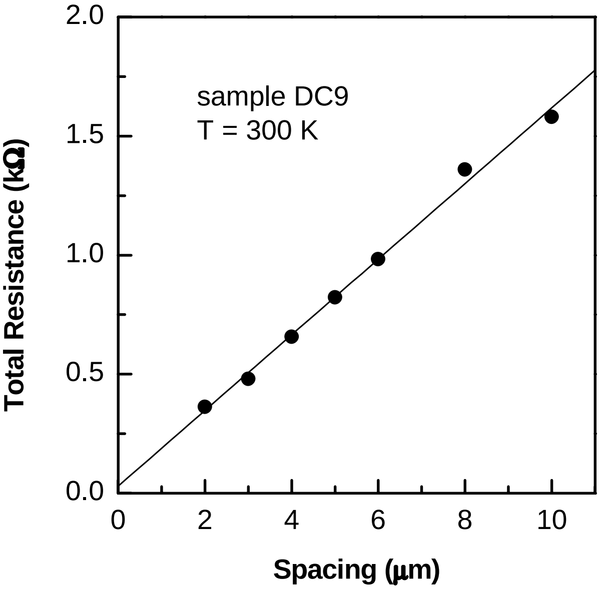

Figure 3.19: Measured total resistance R given by Eq. (3.21) vs. spacing l_i between planar contacts of length L and width W. The intersection of a linear fit with resistance axis reveals twice the value of contact resistance, i.e. $2R_c$. The slope is determined by the ratio of the sheet resistance of semiconductor material between contacts to the contact width (r_s/W).

Measurement results of the total resistance R vs. spacing l_i dependency are shown in Fig. 3.19 for sample DC9 based on a $Al_{0.3}Ga_{0.7}As/GaAs/In_{0.2}Ga_{0.8}As$ heterostructure. The sample was biased with a constant current of 10 μA. Corresponding to Eq. (3.21), the total resistance depends linearly on the spacing between the planar contacts. Using a linear fit, the contact resistance was estimated as 14.9 Ω. The normalized contact resistance for the planar contact of 20 μm width amounted about 0.3 $\Omega \times$ mm. Other parameters estimated by the TLM method are shown in Table 3.3.

In order to minimize the specific contact resistivity, we carried out additional studies of the annealing procedure, varying both the annealing temperature and time. Using the TLM model, the measurements of the specific contact resistivity were performed after each annealing procedure. Figure 3.20 shows appropriate results on sample DC9, being representative for all investigated structures. Apparently, the specific contact resistivity exhibits no changes within the 350°C to 410°C temperature range, regardless of varied annealing temperature and time. However, an appreciable decrease was found for increasing temperature within the 410°C to 450°C range. Similar dependencies of the specific contact resistivity vs. annealing temperatures were also observed for Au/Ge/Ni metal films in contact to n-type bulk GaAs [182, 183, 184, 185, 186], exhibiting a U-shape.

In order to explain the observed specific contact resistivity vs. annealing

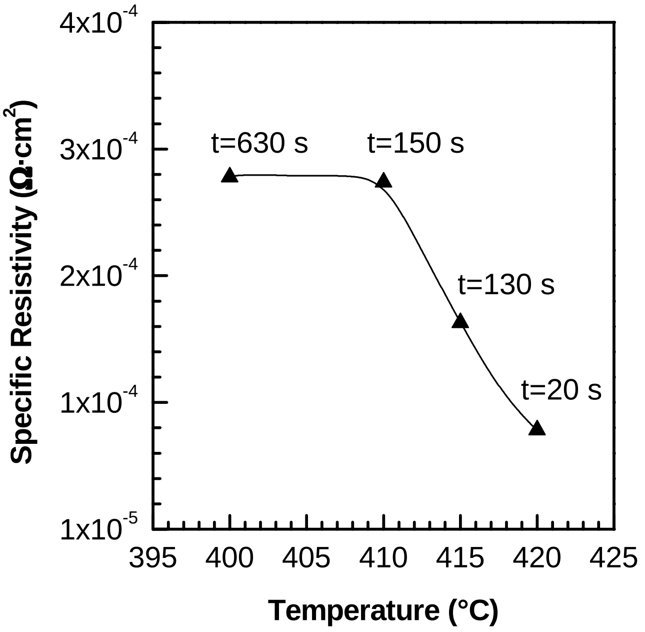

Figure 3.20: Specific contact resistivity ρ_c vs. annealing temperature and time for Au/Ge/Ni metals in contact with a n-doped GaAs cap layer on top of a $Al_{0.3}Ga_{0.7}As/GaAs/In_{0.2}Ga_{0.8}As$ heterostructure. The indicated line serves as a guide to the eye only.

Sample	Parameter	Symbol	Value
DC8	contact resistance	R_c	7.13 Ω
	normalized contact resistance	r_c	0.14 $\Omega \times$ mm
	bulk material sheet resistance	r_s	5.5×10^3 Ω
	specific contact resistivity	ρ_c	2.9×10^{-6} $\Omega \times \mathrm{cm}^2$
DC9	contact resistance	R_c	14.9 Ω
	normalized contact resistance	r_c	0.3 $\Omega \times$ mm
	bulk material sheet resistance	r_s	3.18×10^3 Ω
	specific contact resistivity	ρ_c	8.8×10^{-5} $\Omega \times \mathrm{cm}^2$
DC13	contact resistance	R_c	13.6 Ω
	normalized contact resistance	r_c	0.27 $\Omega \times$ mm
	bulk material sheet resistance	r_s	3.66×10^3 Ω
	specific contact resistivity	ρ_c	5.9×10^{-6} $\Omega \times \mathrm{cm}^2$

Table 3.3: Measured parameters of a metal-semiconductor system using the transmission line model (TLM). Measurements were performed at 300 K and a bias current of 10 μA.

temperature behavior, detailed studies by x-ray diffraction, Auger electron spectroscopy (AES) and x-ray photoelectron spectroscopy (XPS) were performed: Starting the annealing process, Ni and Ge layers interdiffuse and form Ni_3Ge compounds. Then the Ga and As atoms diffuse out of the GaAs cap layer and form compounds with Au, Ni and Ge atoms [183]. As a result of the interdiffusion processes at the metal-semiconductor interface, β-AuGa and NiAs(Ge) phases are formed. Past to the formation of NiAs(Ge) phases, Ge atoms diffuse into the GaAs cap layer and occupy free Ga vacancies. Just the formation of β-AuGa and NiAs(Ge) phases with further diffusion of the Ge atoms into the semiconductor has drastic influence on the specific resistivity decrease [187]. As a result, the depletion region at the metal-semiconductor interface becomes narrower, allowing the tunneling of electrons through the barrier [188, 189].

3.4 Conclusions

Using gas-source molecular-beam epitaxy (GSMBE) accompanied by structural studies like reflection high energy electron diffraction (RHEED) and x-ray measurements, pseudomorphically strained modulation-doped $Al_xGa_{1-x}As/In_yGa_{1-y}As/GaAs$ and doped-channel $Al_xGa_{1-x}As/GaAs/In_yGa_{1-y}As$ heterostructures were grown. Just the

$Al_xGa_{1-x}As/In_yGa_{1-y}As/GaAs$ modulation-doped system was used as the most appropriate reference structure for a projected growth optimization. The used optical (photoluminescence and Raman spectroscopy), transport and noise techniques are most informative and sensitive to the growth conditions just in this system. The results discussed in the following were applicable for an optimized growth of the doped-channel heterostructures, too.

Based on the found growth recipe, relatively thick and dislocation-free $In_yGa_{1-y}As$ layers of 280 Å, 144 Å and 30 Å could be grown successfully at an In content of 10 %, 20 % and 30 %, respectively.

Fitting simulated x-ray rocking curves in (004) symmetrical reflection to measured ones, the layer thicknesses, compositions and strain in the growth direction were estimated. These results were in good agreement with the data based on growth rate calibrations of the elemental sources in our GSMBE system.

Micro-Hall devices of different geometries (Hall and Greek cross) and square sizes (20 μm, 10 μm and 5 μm for the Greek cross geometry) were realized by standard optical photolithography with subsequent Au/Ge/Ni contact metallization [172] and thermal annealing. Investigating the effect of different annealing conditions, the specific contact resistivity of the metal-semiconductor barrier was optimized.

The measurements of specific contact resistivity ρ_c, contact resistance R_c, and sheet resistances of the semiconductor material below the contact R_s and between the contacts r_s were performed in the frame of the transmission-line model. For our heterosystem in contact to the metal, the specific contact resistivity exhibits a drastic dependence on the annealing temperature and the time at temperatures higher than 405^0C. Being similar to the U-shape specific contact resistivity dependence for Au/Ge/Ni metal films in contact to n-type GaAs, we conclude about the same diffusion mechanisms for our material system.

Chapter 4

Optical spectroscopy of 2D heterostructures

Optical methods like photoluminescence (PL) spectroscopy [190, 191, 192, 193, 194, 195, 196] and Raman scattering [146, 197, 198, 199] are mostly used as post-growth techniques for the characterization of thin epitaxial layer and heterointerface quality. Additionally to their high sensitivity and information content, they are non-destructive and usually require no additional sample preparation. Due to the interaction between solid state and photons, fundamental properties of both the phonon and the whole carrier subsystems can be studied.

Optical studies of strained AlGaAs/InGaAs/GaAs or AlGaAs/GaAs/InGaAs heterostructures have to be considered as a necessary prerequisite of the micro-Hall device fabrication, too.

Below its critical thickness, an InGaAs layer is purely pseudomorphically strained and free of misfit dislocations. Typically, the corresponding PL spectrum of an undoped QW is characterized by a strong narrow excitonic line, reflecting a high material and interface quality [200]. But within modulation-doped QWs, the PL spectrum is broadened due to the screening of the excitonic effect by the high-density electron gas and, especially, through disorder in the QW, resulting in a possible recombination of electrons with $k \neq 0$.

Here, both PL spectroscopy and Raman scattering are used as optical diagnostic tools characterizing the grown pseudomorphic modulation-doped AlGaAs/InGaAs/GaAs heterostructures. For layers being thinner than the critical thickness, the degree of disorder is shown to decrease with increasing InGaAs layer thickness. This disorder is ascribed to In content fluctuations and interface roughness.

Due to In content fluctuations, the potential for both valence and conduction bands will fluctuate, too. Consequently, conduction electrons scatter on these potential imperfections. This scattering process is more effective for a low sheet electron density within the conductive channel (electron subband only partially filled by carriers) and less effective in case of a completely filled band. Furthermore, it will cause local mobility fluctuations and an accordingly higher $1/f$ noise [24]. Altogether this will result in a poor noise performance of a micro-Hall sensor.

4.1 PL measurement technique

A schematic representation of the experimental setup for measurements of continuous wave (cw) photoluminescence is given in Fig. 4.1. It consists of three basic parts: (i) optical system (including laser source, monochromator and detector); (ii) signal-processing electrical circuitry; (iii) computer-assisted data acquisition and experiment control via standard GPIB (IEEE-488.2) interface.

A cw Ar^+ laser emitting at 514.5-nm was used as the excitation source. Excitation densities ranging from 50 mW/cm^2 to 20 W/cm^2 could be realized by

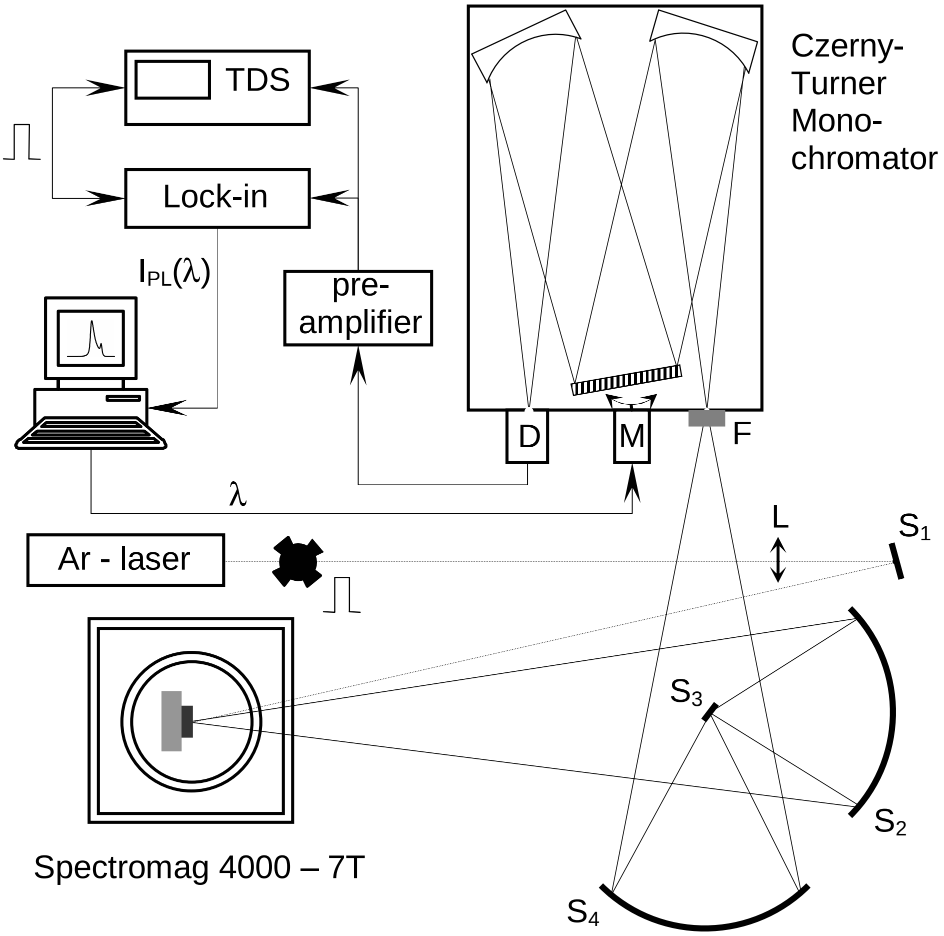

Figure 4.1: Photoluminescence measurement setup (adapted after [201]).

various neutral-density filters. The laser radiation was modulated by a mechanical chopper in the 40 Hz to 4 kHz frequency range, well focused by lens L and guided by the mirror S_1 onto the sample surface. The samples were mounted in an Oxford Instruments SPECTROMAG 4000 − 7T cryostat system, allowing optical measurements in stationary (or slowly varying) magnetic fields up to 7 T and in the 1.7 to 300 K temperature range. The measurements were performed within the standard reflection geometry. The luminescence radiation emitted from the sample was collected by a mirror set consisting of collimating and imaging parabolic mirrors (S_2, S_4) and a flat mirror S_3. Thus, the collected emission was imaged on the monochromator entrance slit. An optical high-pass filter F blocked the laser radiation there. The photoluminescence light was dispersed through a 3/4-m Czerny-Turner monochromator SPEX 1702 with a spectral resolution better than 0.1 meV in the 260 nm to 1550 nm range. Depending on the spectral range under investigation, a thermoelectrically cooled photomultiplier tube with a GaAs:Cs photocathode or a LN_2 cooled high-purity Ge detector was used.

The AC signal output from the detector was amplified by an ultra-low noise pre-amplifier type 5004 from EG&G and then fed into an EG&G PAR 5207 lock-in amplifier. For signal adjustment and monitoring purposes, a digital Tektronix TDS 520 oscilloscope was applied. The experiment control and data acquisition were realized by self-written software running on a standard PC.

4.2 PL studies of 2D heterostructures

PL spectra of modulation-doped $Al_xGa_{1-x}As/In_yGa_{1-y}As/GaAs$ heterostructures were measured at low temperature (T=6 K) under the same excitation density.

In the following two sample sets are considered: (i) with compositions of $y = 0.1$ and $x = 0.2$ for $In_yGa_{1-y}As$ and $Al_xGa_{1-x}As$ layers, respectively, and a varying QW width equal to 20 nm (MD1), 15 nm (MD2) and 10 nm (MD3); (ii) with compositions of $y = 0.15$ and $x = 0.15$ and QW widths equal to 20 nm (MD4), 13 nm (MD5) and 10 nm (MD6).

The Si-doping in the $Al_xGa_{1-x}As$ barrier layer provides a corresponding InGaAs QW conduction band filling with electrons. They are confined due to conduction band bending at the AlGaAs/InGaAs heterointerface and due to the width of the InGaAs QW itself. The effective bandgap of the InGaAs quantum well depends on the InGaAs layer thickness. Since the InGaAs is under compression strain, the first light hole subband is located about 60 meV below the first heavy hole subband. Using Hall measurements, the two-dimensional density of electrons in the conduction band was estimated for each sample.

Representative measured PL spectra of the first sample set are shown in Fig. 4.2. The narrow luminescence peak from sample MD1 results from the

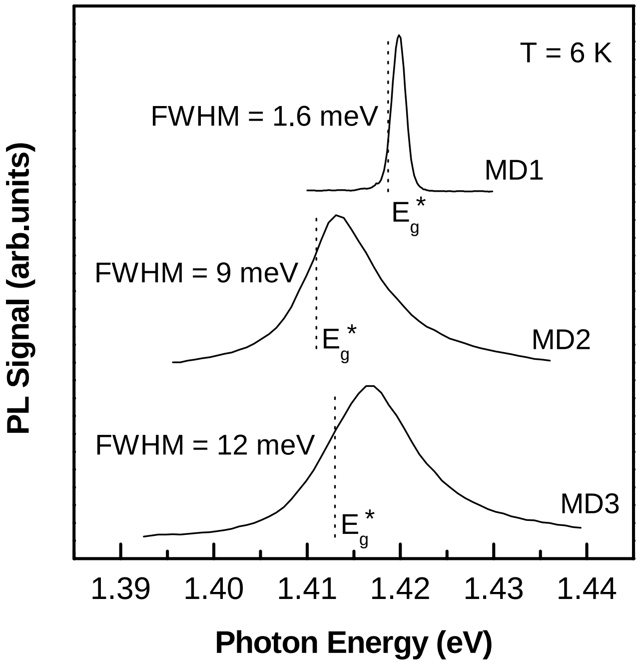

Figure 4.2: PL spectra for samples with $y \approx 0.10$. Sample MD1 with $D_w = 20$ nm exhibits a narrow spectrum, characteristic of luminescence restricted to Γ-point recombination. The samples MD2 ($D_w = 15$ nm) and MD3 ($D_w = 10$ nm) show a broader spectrum, characteristic of radiative recombination over a greater range of k near Γ. The spectral energetic position of sample MD1 is slightly shifted to higher energies due to an In composition of $y = 0.09$ in MD1, compared to 0.10 in samples MD2 and MD3.

recombination of photoexcited $n = 1$ heavy holes with $k \approx 0$ and $n = 1$ electrons from the Fermi sea also at $k \approx 0$. The PL peak of sample MD1 is slightly shifted to a higher energy, compared to the other two samples. This is due to an In mole fraction of 0.09, being smaller than the intended 0.10. The luminescence line shape analysis revealed a full width at the half of maximum (FWHM) of about 1.6 meV.

A broadening in the PL line shape is usually observed due to impurity-assisted processes or interface roughness [202]. The effect of impurity scattering is (i) to broaden the electron and hole levels, thereby causing an uncertainty for the energy conservation condition for direct processes and (ii) to introduce additional higher-order impurity assisted processes, i.e. electrons contributing to the radiant recombination with photon emission can be scattered into intermediate (virtual) states in the conduction band or valence band.

Figure 4.3 represents the three possible radiant electron-hole recombination processes: (i) direct recombination with momentum conservation; (ii) an electron is scattered into an intermediate virtual state by an impurity (solid circle) and then recombines with hole; (iii) an electron decays into an intermediate virtual

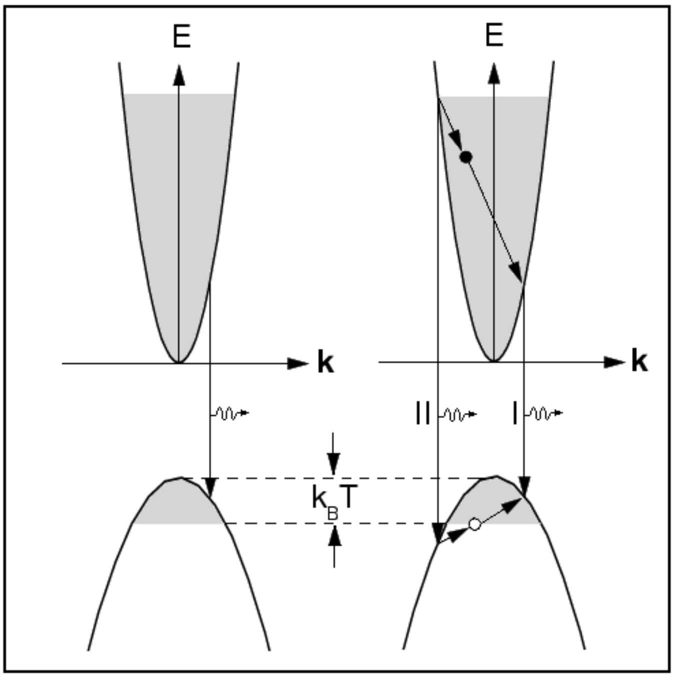

Figure 4.3: Three possible channels of the radiant electron-hole recombination through direct process and indirect processes: involving an electron-intermediate state (path I) or involving hole-intermediate state (path II).

hole via photon emission and is then scattered into a hole by an impurity (open circle). Therefore, the impurity-assisted processes result in a violation of the momentum conservation, causing a broadened spectral profile of the luminescence line. Furthermore, a significant blue shift of the PL line will be observed [202].

Since no broadening of the luminescence line was observed for sample MD1, we conclude about a negligible influence of impurity-assisted processes and high quality of the InGaAs layer and his interfaces.

Another possible reason of a PL line broadening can be the disorder within the InGaAs layer. This disorder due to In content fluctuations results in a spatial hole localization. The effect of the hole localization in the real space reflects the hole delocalization within the k-space allowing recombination over a range of k, i.e. the hole wavefunction has a sizable component for $k \neq 0$ and allows optical recombination with electrons from the Fermi sea over a range of k away from Γ. Thus, the spreading of the recombination energy will be observed as an energetic broadening of the PL line. The PL spectra measured for the samples MD2 and MD3 are a direct evidence of this broadening effect.

Using the theory developed by Lyo and Jones [202], the high-energy part of the PL spectrum can be accurately fitted. According to this theory, the theoretical

PL line shape is given by

$$S_{ij}(\varepsilon) \propto \int_0^{\varepsilon} f(\tau - \mu_{vj}) f(\varepsilon - \tau - \mu_{ci}) K(\varepsilon, \tau)\, dt, \tag{4.1}$$

where ε is the relative photon energy with respect to the effective band gap and f the Fermi distribution function. μ_{vj} and μ_{ci} are the chemical potentials in the jth valence and ith conduction bands, respectively. The term K is a Lorentzian accounting for the processes associated with direct transitions in k-space and indirect impurity-assisted processes. Following the procedure described within the Ref. [202], a fit can be done. To be more accurate, the Urbach tail at energies below the bandgap describing the low-energy side of luminescence line has to be included into the fitting procedure [203, 204]. Accordingly, we found FWHM values of 9 meV and 12 meV for the PL spectra of samples MD2 and MD3, respectively. A significant PL spectral broadening is revealed for both samples. We attribute it to the degree of disorder within the InGaAs layer. Furthermore, a decreasing InGaAs layer thickness causes an additional spectral broadening, i.e. thinner InGaAs layers are obviously of a higher degree of disorder than thicker ones.

Based on the optical detection of quantum oscillations (ODQO) via PL monitoring during a slow magnetic field ramp up to 7 T [203], a quantitative study of the hole localization was performed. Examining a sample structure being very similar to our MD2, two classes of hole localization were revealed: a shallow one, primarily resulting in hole scattering, and a deep localization resulting in a 10 meV shift of the quantum oscillations. The hole localization observed in these experiments serves as an evidence of the disorder due to In content fluctuations.

The PL spectra of the other sample set with $y = 0.15$ and $x = 0.15$ (samples MD4, MD5 and MD6) exhibit the same trend and behavior. The essential data of all six samples are summarized in Table 4.1.

	$MD1$	$MD2$	$MD3$	$MD4$	$MD5$	$MD6$
y in In$_y$Ga$_{1-y}$As	0.09	0.10	0.10	0.15	0.15	0.15
x in Al$_x$Ga$_{1-x}$As	0.20	0.20	0.20	0.15	0.15	0.15
D_W (nm)	20	15	10	20	13	10
Hall data (300 K)						
N_s (10^{12} cm^{-2})	0.99	1.03	1.28	0.93	0.93	0.89
μ_{Hall} (cm^2/Vs)	6900	6600	6100	5300	6900	6700
PL line width (meV)	1.6	9.1	12	4	9.3	14

Table 4.1: Structural, electronic and optical parameters of the two sample sets studied.

4.3 Raman spectroscopy of 2D heterostructures

The same sample sets were also investigated with the Raman scattering technique [205]. Figure 4.4 exhibits representative Raman spectra, measured at room temperature for the two samples MD3 and MD6 with the same quantum well width of 10 nm but different mole fractions for In and Al (see Table 4.1). Four optical phonon modes are clearly observed in the 250–310 cm^{-1} spectral range. The spectral feature near $\nu = 291\ \mathrm{cm}^{-1}$ is a superposition of the GaAs-like LO-phonons in GaAs and in InGaAs. The position of the GaAs-like LO-phonon in $\mathrm{Al}_x\mathrm{Ga}_{1-x}\mathrm{As}$ depends on the x value; in Fig. 4.4 it appears at $\nu = 285\ \mathrm{cm}^{-1}$ [206, 207]. The feature at $\nu = 268\ \mathrm{cm}^{-1}$ is due to the coupled LO-phonon-plasmon L^- mode in n-doped $\mathrm{Al}_x\mathrm{Ga}_{1-x}\mathrm{As}$ [206] and the same phonon mode in the InGaAs [208], and due to the nominally forbidden contribution of the GaAs-like TO-phonon [209]. A deconvolution of the three modes within the 280–300 cm^{-1} range is accomplished by a detailed line-shape analysis according to Mintairov and Temkin [210]. The spectral position of the $\mathrm{In}_y\mathrm{Ga}_{1-y}\mathrm{As}$ LO-phonon peak agrees very well with earlier data for pseudomorphically strained layers [211, 212, 213] being easily distinguished from relaxed layers. In addition to the intense PL being characteristic of dislocation-free InGaAs, this allows us to conclude that the structures are purely pseudomorphically strained.

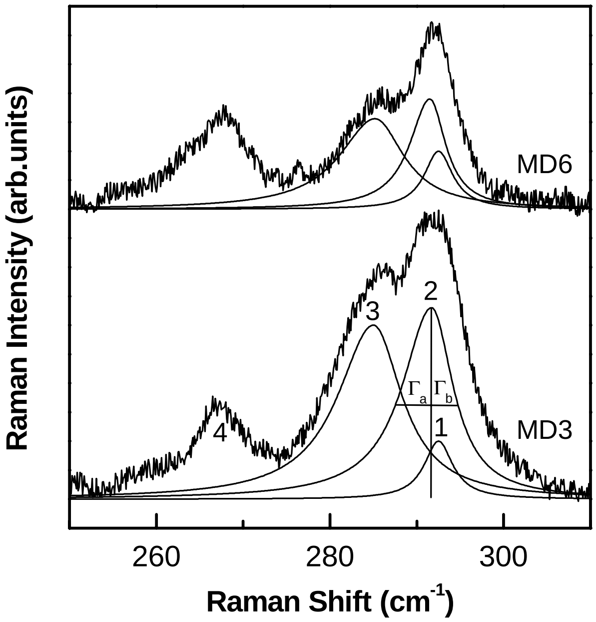

Figure 4.4: Unpolarized Raman spectra of two representative samples recorded at room temperature. The deconvolution of superimposed peaks is shown by thin solid lines: 1 - $\mathrm{LO}_{\mathrm{GaAs}}$ in GaAs bulk; 2 - $\mathrm{LO}_{\mathrm{GaAs}}$ in $\mathrm{In}_y\mathrm{Ga}_{1-y}\mathrm{As}$ layer; 3 - $\mathrm{LO}_{\mathrm{GaAs}}$ in $\mathrm{Al}_x\mathrm{Ga}_{1-x}\mathrm{As}$ layer; 4 - L^- - mode in $\mathrm{Al}_x\mathrm{Ga}_{1-x}\mathrm{As}$ layer.

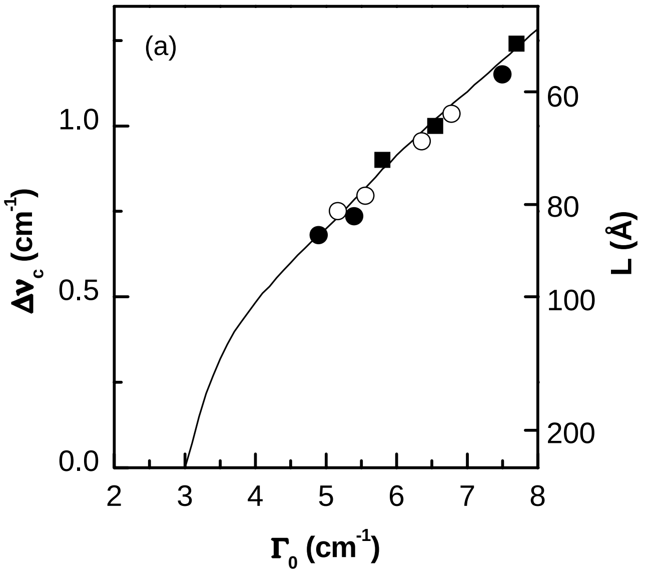

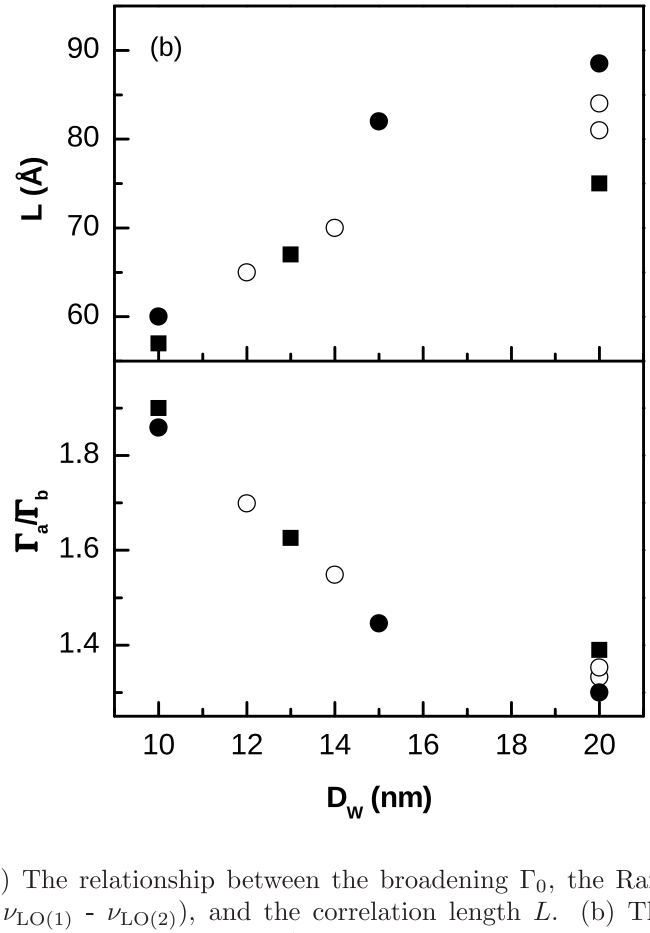

Figure 4.5: (a) The relationship between the broadening Γ_0, the Raman frequency shift ($\Delta\nu_c = \nu_{LO(1)}$ - $\nu_{LO(2)}$), and the correlation length L. (b) The relationship between correlation length L and InGaAs thickness D_w together with the relationship between LO-phonon asymmetry and D_w. Data points: • - first sample set (MD1, MD2, MD3), ■ - second sample set (MD4, MD5, MD6), ○ - other measured samples with $y \approx 0.10$.

In an "ideal" system with perfect translational symmetry, the spatial correlation L of the phonons is infinite in extent ($L \rightarrow \infty$) and the phonons can be described as plane waves. This leads to the conventional $\overrightarrow{q} = 0$ momentum selection rule in Raman scattering. When the L value becomes smaller due to disorder in the plane of the epitaxial layers, the mode correlation becomes of a finite value, and a relaxation of the $\overrightarrow{q} = 0$ law takes place. In the InGaAs system, the symmetry violation resulting in finite L values originates from alloy potential fluctuations and non-uniformities in the well thickness.

These results are also consistent with those derived from a "spatial correlation" model [214]. Using a Gaussian correlation function, this model quantitatively explains the broadening and asymmetry of the first-order LO Raman spectrum induced by alloy potential fluctuations. The Raman intensity is written as [214]

$$I(\omega) \propto \int_0^1 \exp(-q^2L^2/4)\left\{\left[\omega - \omega(q)\right]^2 + (\Gamma_0/2)^2\right\}^{-1} d^3q. \tag{4.2}$$

Here Γ_0 is the FWHM of the intrinsic Raman line shape of the end-point materials, and L is a correlation length. The dispersion $\omega\,(q)$ of the LO phonons is taken as for the one-dimensional linear-chain model. Applied to our Raman spectra, Fig. 4.5 depicts the relationship between the frequency of the GaAs-like LO phonon peak from the InGaAs and its width. These data are well described by Eq. 4.2 and allow the determination of the correlation length L for each sample. The resulting relationship between correlation length L and InGaAs thickness D_w is shown in Fig. 4.5, too. The general trend from these Raman data is the same as from the PL data: the disorder in the InGaAs becomes less for thicker layers.

In addition to the LO phonons measured in the 250–310 cm^{-1} frequency range, nominally forbidden acoustic phonons are observed for $\nu < 200$ cm^{-1}. In particular, as seen in Fig. 4.6, the structures with $D_w < 20$ nm show a Raman peak at $\nu = 160$ cm^{-1}. This peak has been studied by Kakimoto and Katoda in thick relaxed In$_y$Ga$_{1-y}$As as a function of y [208]. They identify it as the disorder-activated longitudinal acoustic (DALA) phonon mode of In$_y$Ga$_{1-y}$As. The frequency is independent of y and its intensity is a direct measure of the breaking of translational symmetry in the epitaxial layer plane resulting from disorder. From Fig. 4.6, we see that, consistent with the data from PL and the optical phonon Raman data, the DALA peaks occur only in the structures with thinner InGaAs.

4.4 Conclusions

Photoluminescence spectroscopy was applied successfully to examine the quality of pseudomorphically strained InGaAs layers and interfaces in

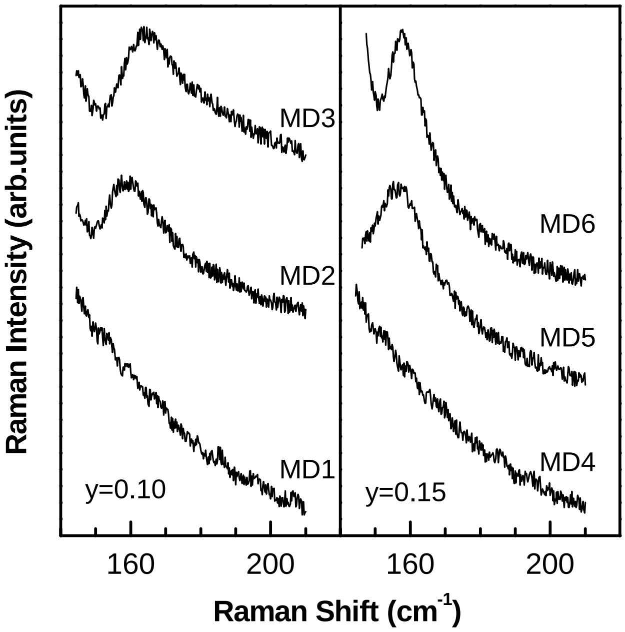

Figure 4.6: Raman spectra in the spectral region of disorder-activated LA (DALA) modes of InGaAs. The DALA signal is only present in the thinner InGaAs layers.

$Al_xGa_{1-x}As/In_yGa_{1-y}As/GaAs$ modulation-doped heterostructures grown by gas-source MBE. Analyzing the PL line width and its intensity, the strained layer epitaxy was optimized.

Even for optimized growth conditions, a disorder within the strained InGaAs layer due to In content fluctuation was revealed. Causing a hole delocalization in the k-space, the disorder was observed as an increasing PL line FWHM with decreased InGaAs layer thickness. From the results we conclude that the disorder degree is higher for thinner InGaAs quantum wells and significantly decreases with increased strained layer thickness.

Additionally applying the Raman scattering technique, the assumption of disorder due to In fluctuations within the strained InGaAs layer was confirmed. Relying on measurements of the correlation length and an examination of the LO phonon asymmetry as well as on the observation of the disorder-activated longitudinal acoustic (DALA) phonon mode at $\nu = 160$ cm^{-1}, the same disorder-thickness behavior was found.

Since disorder in strained InGaAs layers due to In content fluctuation results in fluctuations of the potential for both valence and conduction bands, carrier scattering on fluctuations of potential is more pronounced in thinner strained InGaAs layers, negatively affecting the noise and transport properties of the studied heterostructures. Demanding highest sensitivity and lowest noise, we conclude that thicker strained InGaAs layers are more suitable for low-noise micro-Hall devices of enhanced sensitivity.

Chapter 5

Low frequency noise spectroscopy of 2D systems

5.1 Low frequency noise measurement technique

Accurate low frequency noise measurements of semiconductor materials make some difficulties. First of all, the noise signal expected from the bulk semiconductor material is rather small, i.e. in the nV-range. Certainly, the measurement of such low signal levels requires some effort with respect to the experimental apparatus. In order to avoid interfering signals affecting the measurement results, the whole circuitry should be well shielded. A very low noise and wideband preamplifier is necessary for the required nV sensitivity, preferably with differential signal input for common mode rejection. Even the preamplifier appears as the most crucial part of the noise measuring setup.

Figure 5.1 presents the low frequency noise measurement setup applied for our noise studies of micro-Hall effect devices based on III-V semiconductor heterostructures at constant temperature. The circuitry includes the following main parts: (i) the device under test (four terminal micro-Hall device), (ii) a low noise preamplifier with differential input (Model 113 from Princeton Applied Research Corporation) and (iii) a digital oscilloscope (Lecroy 9400). A standard PC is used for data acquisition via GPIB interface and subsequent processing. The biasing is realized by a low noise battery pack and a set of series metal film resistors. For higher electric fields, a Keithley 236 source-measure unit serves as low noise voltage source.

Using this setup, noise spectra can be measured in the 300 mHz to 100 kHz frequency range at a fixed temperature (300 K and 77 K). The measurements at 77 K are easily realized with the micro-Hall device immersed in liquid nitrogen.

Using the digital oscilloscope, the noise signal is sampled at 2^{15} points within an according time window. This time domain signal is submitted to a computer-

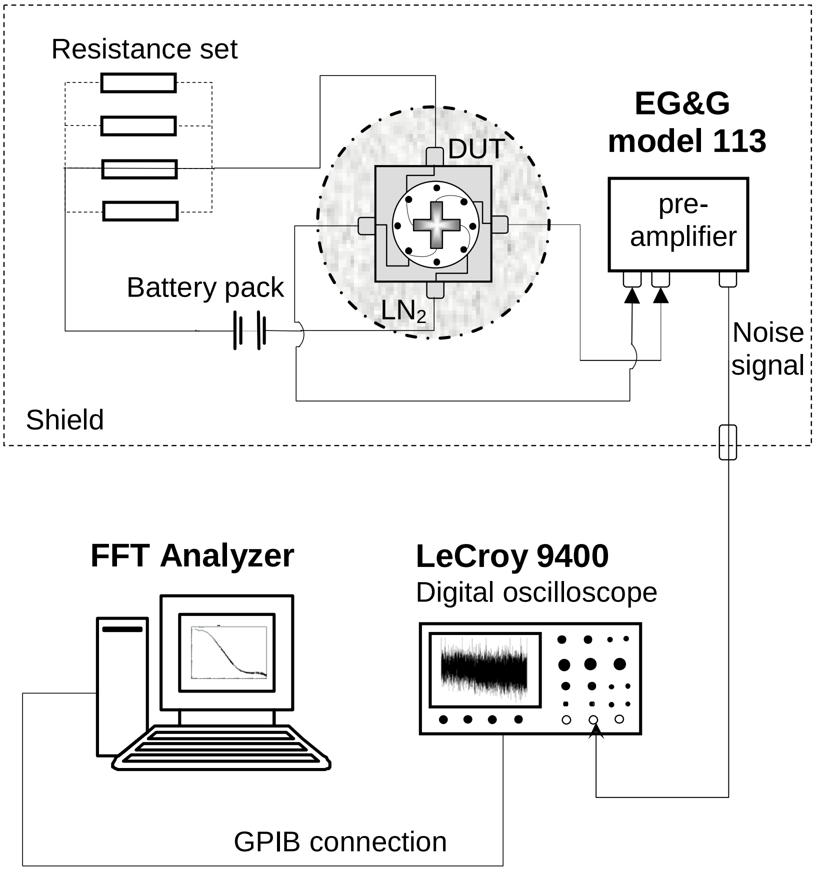

Figure 5.1: Noise measurement setup used for extraction of noise spectra at constant temperature.

aided FFT (Fast Fourier Transform). A number of individual frequency spectra is averaged in order to get the final noise spectrum.

Here, the attainable measurement accuracy depends on the total time window used for signal sampling. The relative error of measurement within the equivalent noise bandwidth Δf is given by

$$D = \frac{1}{\sqrt{\Delta f \cdot t}} \cdot 100\,\% \;, \tag{5.1}$$

where t is the time window width. Thus, this time has to be 100 times the according signal period (for the frequency under investigation) for an accuracy of 10 %. For a required accuracy being constant over the whole frequency range, the widest time windows are necessary for low frequencies, whereas smaller windows are required for higher frequencies.

In order to be accurate, here the measured noise power is summarized from three non-correlated noise sources: (i) the noise coming from the device under test, (ii) the inherent noise of the preamplifier and (iii) the internal noise of the measuring instrument (i.e. digital oscilloscope). Hence, both contributions of the preamplifier and the digital oscilloscope have to be estimated separately in order to extract the real device noise from the summary spectrum.

The voltage noise spectral density of the device is given by

$$S_{V,noise}(f) = \frac{\overline{\Delta V_{noise}^2}}{\Delta f} = \frac{P_1 - P_2}{K^2 \Delta f}, \tag{5.2}$$

where P_1 is the total measured noise power, P_2 the noise power of both the preamplifier with short-circuited inputs and the digital oscilloscope. K denotes the preamplifier gain.

To estimate the preamplifier gain K and equivalent noise bandwidth Δf, a calibration of the the noise measurement setup is necessary. Due to the resistance accuracy of the metal film resistors used as a noise generator, a calibration within about 10 % accuracy can be achieved. A more accurate calibration would be achievable with a commercial noise generator.

The voltage noise spectral density of the calibrating resistor R_{calibr} is given by

$$S_{V_R,noise}(f) = 4k_B T_{calibr} R_{calibr}. \tag{5.3}$$

The total measured noise power P_3 with the calibrating resistor loaded on the input of the preamplifier is given by

$$P_3 = P_2 + K^2 \Delta f 4k_B T_{calibr} R_{calibr}. \tag{5.4}$$

Extracting $K^2 \Delta f$ from Eq. (5.4) and using Eq. (5.2), the real noise from the device under test can be estimated as

$$S_{V,noise} = \frac{P_1 - P_2}{P_3 - P_2} 4k_B T_{calibr} R_{calibr}. \tag{5.5}$$

An estimation of the additional excess noise superimposed to thermal noise is also needed. This can be easily done, subtracting the thermal noise (Johnson noise) from the device noise $S_{V,noise}(f)$:

$$S_{V,\,excess} = S_{V,noise}(f) - 4k_B T_{sample} R_{sample}. \tag{5.6}$$

Some care is necessary with respect to the device noise signal: Depending on the device wiring within the whole circuit, one can measure either pure bulk noise or both bulk and contact noise.

For noise measurements, the two terminal technique can be applied. Accordingly, the device is driven through two biasing contacts and the noise voltage fluctuations are measured on the same contact pair. Then the total measured noise voltage spectral density is

$$S_{V,noise}(f) = S_{V,\,contacts}(f) + S_{V,\,bulk}, \tag{5.7}$$

where $S_{V,\,contacts}(f)$ and $S_{V,\,bulk}$ are the contact noise and bulk noise contributions, respectively. It is commonly accepted that the contact noise is much higher than the bulk noise. Therefore, measurements in the two terminal mode estimate the contact noise.

On the other hand, the four terminal technique allows one to estimate the clean bulk noise. Here, the device under test is biased through two opposite contacts (biasing contacts) and the noise signal is measured between the other contact pair. According to the device geometry on hand, either the longitudinal or the transversal noise can be measured. The first one requires the sense contacts located on the same strip side parallel to the current flow realized in Hall bar geometry. The latter implies a sense contact pair perpendicular to the current flow realized in both Hall bar and Greek cross geometries.

Applying the four point method, a low noise resistor R_{load} ($R_{load} \gg R_{sample}$) is connected in series with the device sample. Then the current flowing in the circuit is constant. Furthermore, the fluctuations of the contact resistance and within the area close to the contacts extend only to distances in the order of the diffusion length.

Noise measurements are applicable to studies of local semiconductor levels in form of deep level noise spectroscopy (DLNS). This technique offers some advantages over deep level transient spectroscopy (DLTS) being commonly regarded as the standard method for the characterization of the semiconductor local levels. At some not uncommon situations, the DLTS technique fails fundamentally: (i) levels with very small capture cross sections [84, 215], (ii) levels in semiinsulators [216] and (iii) resonant levels [67]. On the other hand, just noise spectroscopy does not disappoint in these cases. Furthermore, DLNS is a direct measurement method, i.e. it is applied to fully processed devices. This is of particular interest here. In contrast to DLTS studies, no further structure overgrowth or other additional test device preparation/structuring is necessary.

The DLNS method relies on the fact that each generation and recombination process within the semiconductor bulk is characterized by a specific time constant τ, related via $\tau = 1/2\pi f$ to the frequency. For a time constant depending exponentially on temperature, the local level parameters can be extracted [67, 68, 83, 90].

Of course, the above discussed experimental requirements for noise measurements are also valid for the DLNS. However, different from noise spectra measurements, the temperature dependencies of the noise signal within an equivalent bandwidth Δf have to be measured at fixed frequencies.

An adequate experimental realization of narrow-band measurements is based on a lock-in amplifier, here a commercial model SR510 from Stanford Research

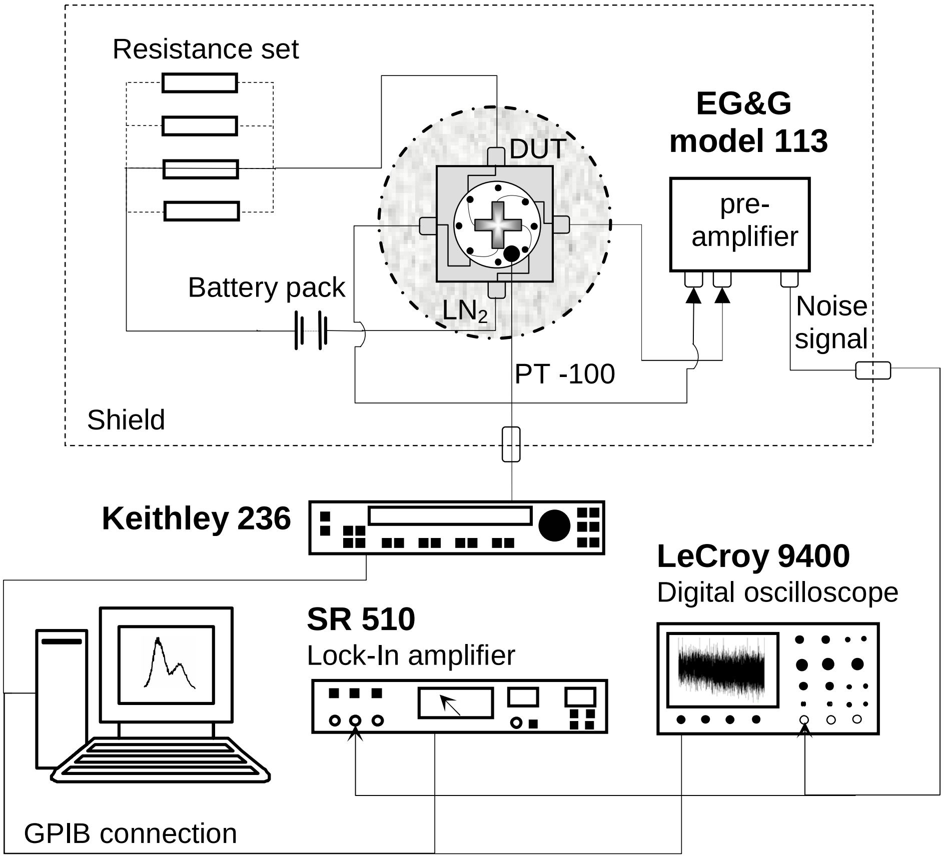

Figure 5.2: Noise measurement setup applied to record the noise signal as function of frequency and temperature.

[217]. The according measurement setup is shown in Fig. 5.2. A well calibrated commercial $\mathrm{PT}-100$ resistance sensor from Lake Shore Cryotronics was used for temperature measurements. The measurement data acquisition and processing was realized by a standard PC.

5.2 Noise spectroscopy of GaAs based micro-Hall devices

Due to its influence on the absolute detection limit, the low frequency (LF) noise level essentially contributes to the Hall device performance. A better physical understanding of the low frequency noise origins should contribute to further device improvements with respect to signal-to-noise sensitivity as well as lower detection limits. Additionally, new magnetic sensor applications can be developed. As an example, a pT-range resolution would be of high particular interest for biological studies [18, 19]. For measurements with high spatial resolution based on small active areas of micro-Hall devices, the LF noise level becomes crucial.

Scaling the device size down, the total number of electrons in the device as well as the absolute Hall sensitivity (scales linearly with the device width) are reduced. Therefore, smaller devices exhibit a significantly reduced SNS [91]. Additionally, the smaller sizes imply much higher electric fields in the device active area. Potentially, this causes additional generation-recombination (G-R) processes between trap levels and the conduction band (hot-electron trapping) due to electrical activation of electrons [218]. Obviously, this results in an increased noise density. Due to thermal activation of electrons, traps can act as temperature dependent sources of generation-recombination noise in the semiconductor device bulk. Comprising this consideration, deep levels contribute to both reduced signal-to-noise sensitivity and degraded thermal stability due to changes in conductivity. The noise spectroscopy of local levels can be successfully used as a powerful and direct method in optimization of any devices based on lateral transport, in particular for micro-Hall sensors.

5.2.1 LF noise studies of doped-channel devices

Low frequency noise spectra in the 0.3 Hz to 100 kHz frequency range were measured in micro-Hall devices based on different heterosystems: (i) a lattice matched system based on doped-channel $Al_{0.3}Ga_{0.7}As/GaAs$ heterostructure and (ii) a pseudomorphically strained system based on doped-channel $Al_{0.3}Ga_{0.7}As/GaAs/In_{0.3}Ga_{0.7}As$ heterostructure. For comparability, the noise measurements were performed for the same geometries and device sizes in both systems. Here we restrict our consideration to Greek cross geometry of 20 μm square size.

As an example, Fig. 5.3 depicts typical noise spectra for a micro-Hall device based on doped-channel $Al_{0.3}Ga_{0.7}As/GaAs$ heterostructure. The measurements were accomplished at room temperature and a bias current of 10 μA for two different device interconnections: two-probe and four-probe configurations, respectively. In accordance to our considerations above, the noise spectral density is much higher in two-probe than in four-probe configuration.

The observed difference is due to the influence of contact noise. For two-probe measurements, the noise spectral density is given by Eq. (5.7). Usually, the contact noise is much higher than the bulk semiconductor noise. Thus, we assume the result of the two-probe method is due to prevailing noise of our metal Au/Ge/Ni contacts.

Using the four-probe technique, noise spectra were measured for both possible contact alignments and in both current flow directions, thus excluding geometry effects. An excellent symmetry was demonstrated, i.e. the noise spectral density

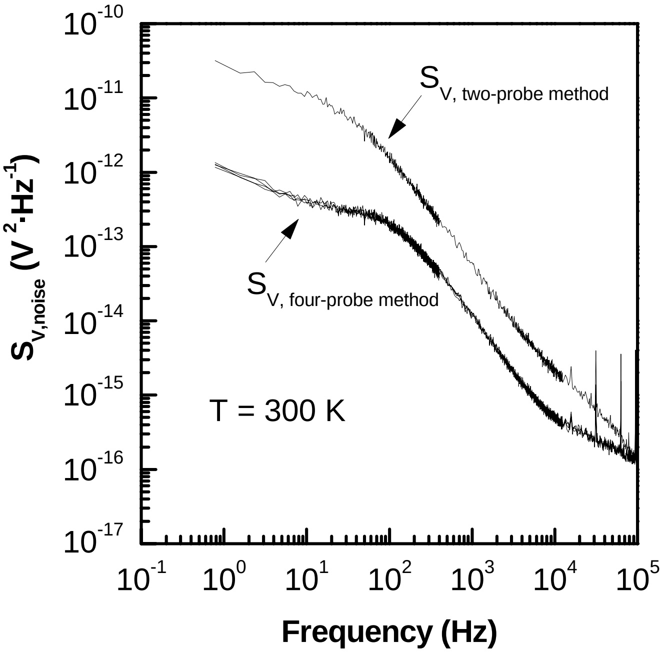

Figure 5.3: Typical noise spectra of micro-Hall device based on $Al_{0.3}Ga_{0.7}As$/GaAs heterostructure measured at 300 K for both possible contact alignments and current flow directions at a bias current of 10 μA.

is independent on biasing conditions.

The total measured noise spectral density is given by

$$S_{V,noise} = \frac{A}{f} + \frac{B}{1 + (2\pi f \tau)^2} + 4k_B T R, \tag{5.8}$$

where A and B are the amplitudes of flicker noise and generation-recombination noise, respectively. τ is the characteristic time constant for generation-recombination noise, k_B the Boltzmann constant, T the temperature and R the sample resistance.

At the lowest measured frequencies, all spectra exhibit a plateau. We attribute this to low-frequency noise due to generation and recombination processes between trap levels and the conduction band. This part of noise spectra is described by the second term in (5.8). The characteristic time constant τ can be estimated from the noise spectrum as $\tau = 1/2\pi f_0$, where f_0 is the frequency at which the spectral noise density is half the plateau value. An example characteristic time constant τ evaluation is shown in Fig. 5.7, obtaining $\tau = 1.2$ ms for sample DC8. Such big time constants are considered as typical for DX centers [219].

Between 1 Hz and about 10 kHz, the noise spectrum is dominated by the flicker noise with its characteristic $1/f$ behavior. Empirically, the actual form of the noise spectral density is $1/f^n$, with $n = 1.5$. The measured noise spectra can be fit as a sum of generation-recombination noise with its $1/f^2$ frequency dependence and flicker noise with a pure $1/f$ behavior.

At higher frequencies the $1/f$ noise is small. Then the noise spectrum is dominated by thermal noise being is frequency independent and described by the third term in (5.8). At a bias current of 10 μA, the thermal noise is not clearly resolved due to an increased sample resistance and the non-linearity of the drift velocity vs. field dependence [73].

For clarification of this behavior, the noise spectra of sample DC8 were measured at different bias currents. Figure 5.4 presents the according results. At a low bias current of 0.333 μA, the noise spectra exhibit Johnson noise. A further increase of bias current significantly boosts the noise spectral density in the mid-frequency range, concealing the thermal noise.

The voltage noise spectral density $S_{V,\alpha}$ for the mid-frequency noise $1/f$ component, measured across the Hall voltage contacts, is given by [24, 75]

$$\frac{S_{V,\alpha}}{V^2} = \frac{S_{V,\alpha}}{I^2} = \frac{\alpha}{fN}. \tag{5.9}$$

Here V is the applied voltage, I the bias current, f the frequency, α the Hooge parameter and N the number of carriers. The number of carriers N should

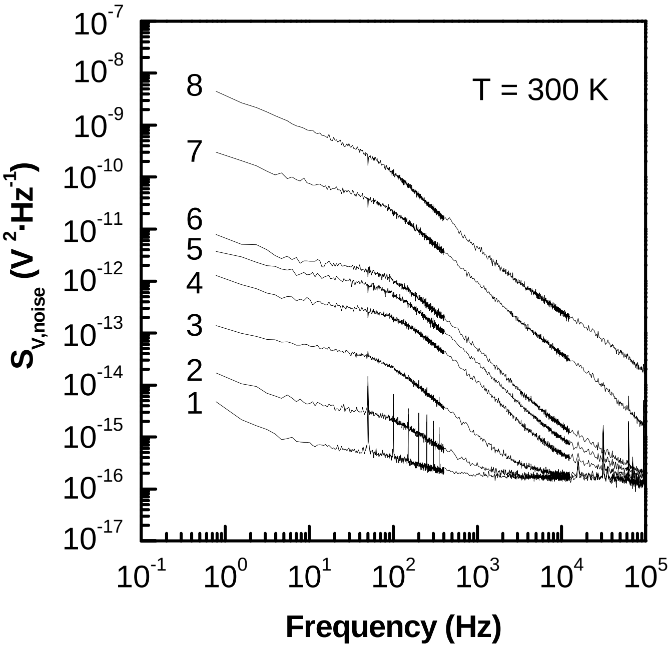

Figure 5.4: Noise voltage spectra measured at 300 K for different bias currents: 1 - 0.333 μA; 2 - 1 μA; 3 - 3.33 μA; 4 - 10 μA; 5 - 15.5 μA; 6 - 33.3 μA; 7 - 44.7 μA; 8 - 60 μA. The four-probe technique was used for the noise measurements.

not be confused with the free carrier concentration usually measured in a Hall experiment. The number of carriers scales with device active sizes like

$$N = n_{3D}QL = \frac{n_{2D}}{t}WtL = n_{2D}WL, \tag{5.10}$$

where n_{3D} is the three-dimensional electron concentration, n_{2D} the two-dimensional electron concentration, Q the cross section of device of width W and thickness t, and L is the device width.

Obviously, the mid-frequency noise spectral density increases quadratically with the bias current or applied voltage, assuming a constant Hooge parameter α. In order to prove this tendency, we consider a noise spectral density $S_{V,noise}$ versus bias current I plot (Fig. 5.5) in log-log scale at two fixed frequencies (1 Hz and 50 Hz). At currents lower than 30 μA, the voltage noise spectral density obeys Hooge's law (5.9).

Thus, we conclude that the increase of the total noise signal in the mid-frequency range with increasing electric field in the active device area occurs due to the increase of flicker noise.

The micro-Hall devices based on the pseudomorphically strained doped-channel $Al_{0.3}Ga_{0.7}As/GaAs/In_{0.3}Ga_{0.7}As$ heterostructures (sample DC13) show a similar tendency of the noise spectral density vs. frequency dependence. The noise spectra measured by the four-probe technique at different current flow directions and both possible contact alignments are presented on Fig. 5.6. For

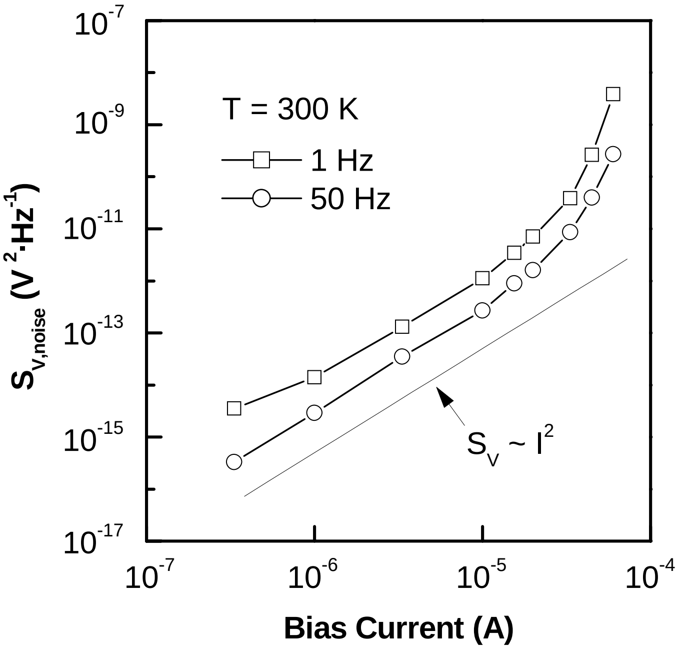

Figure 5.5: Dependency of voltage noise spectral density on bias current at frequencies of 1 Hz and 50 Hz, measured at 300 K in log-log scale.

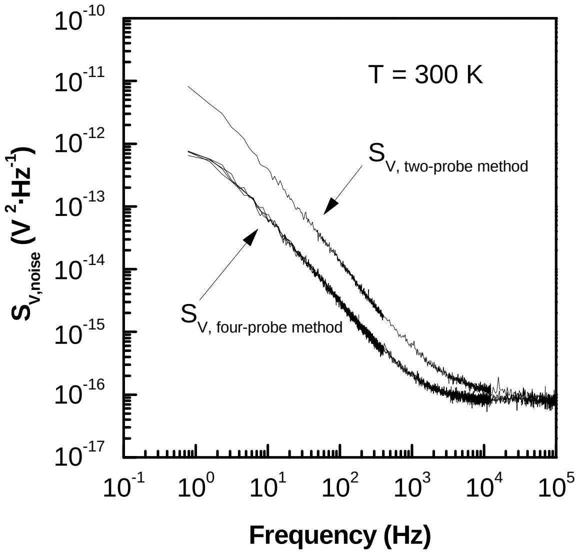

Figure 5.6: Noise spectra of micro-Hall device based on $Al_{0.3}Ga_{0.7}As/GaAs/In_{0.3}Ga_{0.7}As$ heterostructure measured at 300 K and a bias current of 10 μA for both current flow directions and contact alignments.

comparison, a noise spectrum measured in two-probe configuration is included. It is necessary to point out that the noise spectra measured by the four-probe technique are completely identical. This gives us evidence to assume the grown pseudomorphically strained heterostructures as completely isotropic.

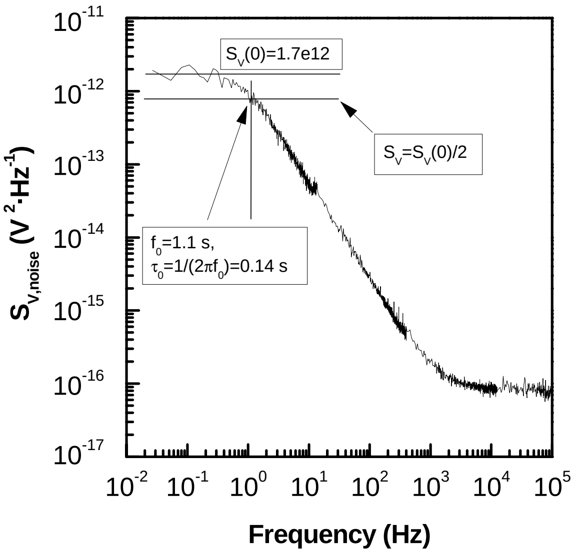

Figure 5.7: Noise voltage spectrum of sample DC13, measured across the Hall contacts by four-probe technique. The evaluation technique of the characteristic time constant τ is shown in the insert.

Obviously, the noise spectra exhibit a generation-recombination plateau at frequencies of about 1 Hz. To prove this tendency, the noise spectra of sample DC13 were measured in a wider frequency range down to 0.027 Hz. Figure 5.7 depicts the according results.

The characteristic time constant τ of generation-recombination noise is found to be about 140 ms, with the evaluation technique shown in the insert. The validity of the Hooge law was proved by measurements of noise spectra at different bias currents. We observed the same tendency as in sample DC8, i.e. the mid-frequency noise obeys Hooge law and occurs due to conductivity fluctuations.

5.2.2 Hooge parameter and crystal quality

As stated in earlier reports on $1/f$ noise, the Hooge parameter α is assumed as a constant of about 2×10^{-3} [75]. However, later investigations proved the Hooge parameter to depend on the crystal quality [59, 76, 220, 221, 222] and the scattering mechanisms determining the electron mobility μ [77, 78, 79, 80, 113], respectively. An additional study on the Hooge parameter vs. electric field dependency was done [223] in a quarter-micron GaAs Hall device. There the Hooge parameter was shown to be field-independent up to 5 kV/cm, but rising at higher field values.

Therefore, a comparison of both the Hooge parameter and the noise in the mid-frequency range for both lattice matched and pseudomorphically strained heterostructures should be quite informative.

The noise spectra of $Al_{0.3}Ga_{0.7}As/GaAs$ and $Al_{0.3}Ga_{0.7}As/GaAs/In_{0.3}Ga_{0.7}As$ heterostructures are shown in Fig. 5.8, measured at room temperature and a bias current of 10 μA. Both the geometry and device sizes were identical. Obviously, the noise voltage spectral density of the pseudomorphically strained $In_{0.3}Ga_{0.7}As$ doped-channel is much lower in the mid-frequency range than that of the lattice matched GaAs doped-channel. It is worth mentioning the measured two-dimensional electron concentrations of both materials being of the same order of magnitude at 300 K: For sample DC8 with $Al_{0.3}Ga_{0.7}As/GaAs$ heterostructure, a value of $n_{2D} = 1.3 \times 10^{12}$ cm^{-2} was estimated. Sample DC13 with $Al_{0.3}Ga_{0.7}As/GaAs/In_{0.3}Ga_{0.7}As$ heterostructure exhibited $n_{2D} = 1.5 \times 10^{12}$ cm^{-2}.

An analysis of the noise spectral density vs. bias current as a function of frequency, based on Eq. (5.9), was used for the Hooge parameter evaluation in both structures. At 300 K, we found a Hooge parameter of $\alpha = 1.5 \times 10^{-4}$ for the micro-Hall device based on $Al_{0.3}Ga_{0.7}As/GaAs$ heterostructure. For the micro-Hall device based on $Al_{0.3}Ga_{0.7}As/GaAs/In_{0.3}Ga_{0.7}As$ heterostructure, a value of $\alpha = 1.1 \times 10^{-4}$ was estimated. These values can be considered as typical results, according to [78, 224]. Like in [78] for n-type GaAs, the temperature dependence

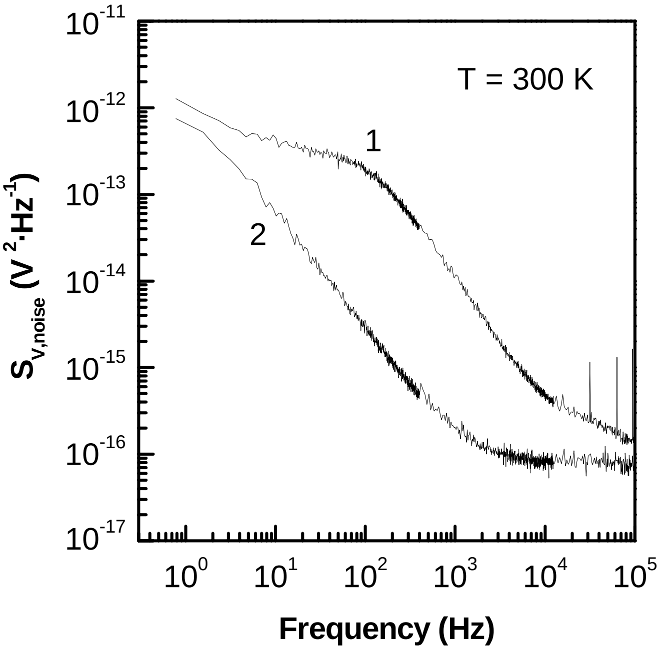

Figure 5.8: Comparison of noise voltage spectra measured across the Hall contacts for a lattice matched GaAs QW (spectrum 1) and a pseudomorphically strained $In_{0.3}Ga_{0.7}As$ QW (spectrum 2) as measured by the four-terminal technique. The measurements were carried out at a bias current of 10 μA on devices of the same size and geometry, respectively. The mid-frequency noise of the pseudomorphically strained $In_{0.3}Ga_{0.7}As$ doped QW is much lower than that of the lattice matched GaAs doped QW.

of the Hooge parameter is given by

$$\alpha_{GaAs} = 0.1 \exp\left[\frac{-0.13 \text{ eV}}{k_B T}\right] + 7 \times 10^{-5}. \tag{5.11}$$

The Hooge parameter temperature dependence for an intrinsic InGaAs layer embedded between AlGaAs barriers is given by [224]

$$\alpha_{InGaAs} = 3 \times 10^{-3} \exp\left(-\frac{T}{150}\right). \tag{5.12}$$

Thus, we conclude the insertion of a pseudomorphically strained InGaAs layer leading to lower the noise spectral density in mid-frequency range with dominating $1/f$ noise. This feature can be successfully used for the design of low noise micro-Hall devices grown on GaAs substrates.

5.2.3 G-R noise in doped-channel devices

For clarification of the low-frequency noise plateau origin, we analyzed the dependence of noise voltage on temperature and frequency. According measurements were performed at a low bias current of 11.25 μA in the 77 - 300 K temperature range. Figure 5.9 depicts the noise voltage as a function of temperature, measured at different frequencies. A pronounced and broad peak is clearly observed.

At a fixed frequency, a maximum in the noise voltage versus temperature relation $S_{V,\mathrm{noise}}(T)$ is expected in two distinct situations: (i) the capture cross section of electrons, σ_n, depends exponentially on activation energy E_1 and temperature according to

$$\sigma_n = \sigma_0 \exp\left(-\frac{E_1}{k_B T}\right) \ , \tag{5.13}$$

(ii) the capture cross section is temperature-independent or depends only slightly on it, but the Fermi level is located below the trap level E_0.

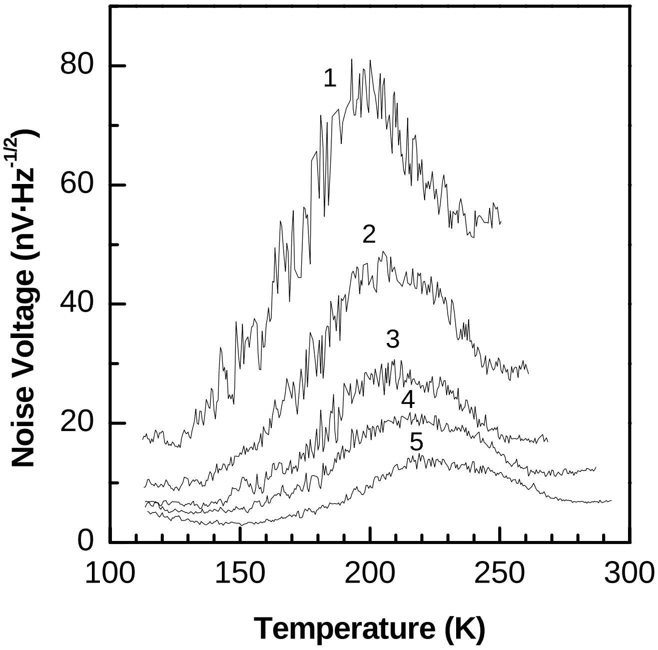

Figure 5.9: Temperature dependence of noise voltage at low bias current for different frequencies: (1) - 10 Hz, (2) - 30 Hz, (3) - 60 Hz, (4) - 120 Hz and (5) - 380 Hz.

In these devices, the Fermi level is located above the conduction band minimum. Accordingly, a degenerate electron gas is confined between the $Al_{0.3}Ga_{0.7}As$ barriers. For an Al composition of about 30%, the DX centers are energetically located below the Γ conduction band minimum [225]. Thus, one has to consider a situation with the Fermi level above the trap level, i.e. $E_F - E_0 >> k_B T$ (see Appendix A). Under this condition, the relative spectral noise density is given according to Ref. [68] by

$$S = \frac{S_{V,noise}}{V^2} = A\tau_{c0}\frac{N_c}{N_d}\frac{\exp\left[(E_1 - E_0)/k_B T\right]}{1 + \omega^2 \tau_{c0}^2 \exp(2E_1/k_B T)}. \tag{5.14}$$

Here V is the voltage applied to the device, N_c the effective density of states for electrons, N_d the shallow donor concentration (shallow donors assumed as fully ionized), ω the angular frequency, E_1 the activation energy and E_0 the ionization energy of the deep level. The constant A is defined by

$$A = 4N_t/V_0N_d^2 \tag{5.15}$$

and the capture time constant τ_{c0} by

$$\tau_{c0} = 1/(\sigma_0 v_T n_0), \tag{5.16}$$

where v_T is the thermal velocity, n_0 is the (three-dimensional) measured electron concentration, V_0 the sample volume, and N_t the deep level concentration.

As described in Ref. [68] for an E_F located above the trap level, the noise voltage versus temperature relation will have a maximum only when the electron capture cross section depends exponentially on temperature and $E_1 > E_0$. As revealed by Fig. 5.9, these conditions are satisfied in our structures. The corresponding maximum in the noise voltage spectral density $S_{V,\max}$ depends on frequency in following manner: The slope in the $\ln(S_{V,\max})$ versus $\ln(\omega)$ dependence can take values between 0 (for $E_1 = E_0$) and 1 (for $E_1 >> E_0$) [68].

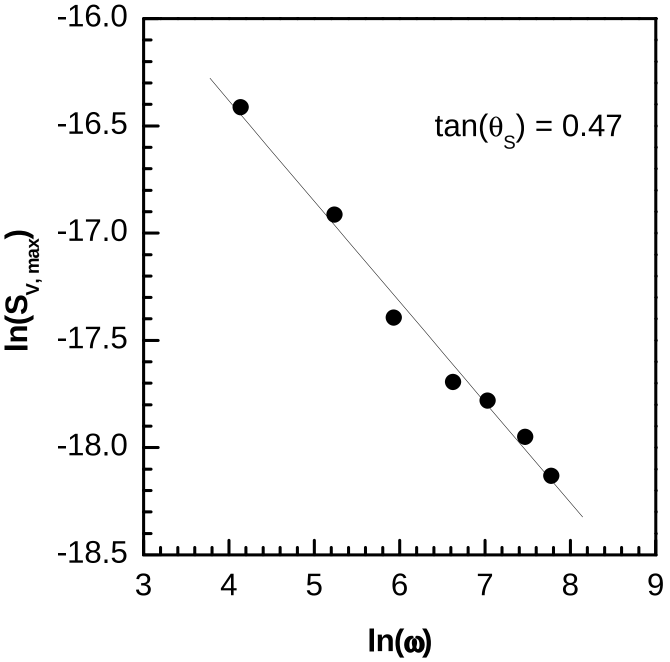

Figure 5.10: Frequency dependence of the detected noise maximum $S_{V,\max}$ in the temperature range of 77-300 K.

Figure 5.10 depicts the $\ln(S_{V,\max})$ versus $\ln(\omega)$ relation as extracted from our experimental data, indicating a slope of about 0.47. This value lies within the expected range and is consistent with $E_1 > E_0$, but not with $E_1 >> E_0$.

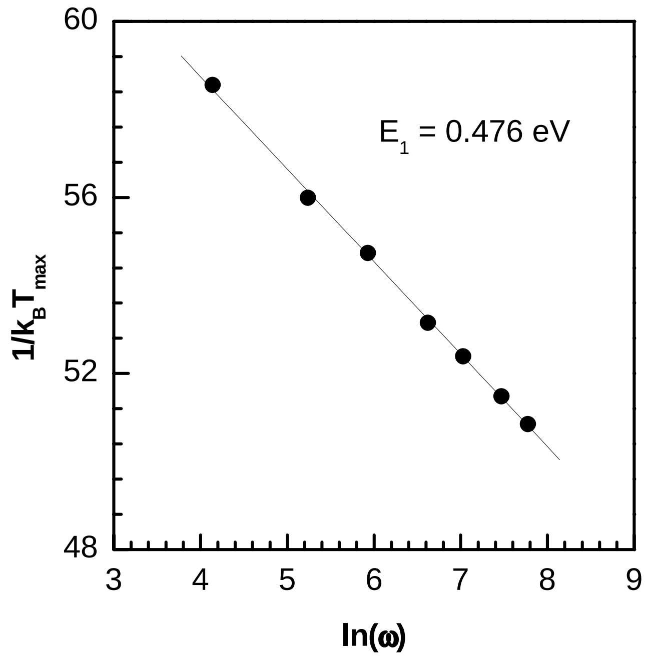

Figure 5.11: The Arrhenius plot for the determination of an activation energy in the approximation $E_F - E_0 >> k_BT$ and $E_1 > E_0$. The slope of the plot determines the activation energy as $\tan(\theta_T) = 1/E_1$.

The according temperature for maximum noise $S_{V,noise} = S_{V,\max}$ is given as $T_{\max}(\omega)$. This allows an estimate of both the activation and trap ionization energies. To be more specifically, the $1/(k_BT_{\max})$ versus $\ln(\omega)$ Arrhenius plot like in Fig. 5.11, together with the data of Fig. 5.10, can be used for an estimate of the activation (E_1) and ionization (E_0) energies via

$$E_1 = \frac{1}{\tan(\theta_T)} \quad \text{and} \quad E_0 = \frac{1 - \tan(\theta_S)}{\tan(\theta_T)}. \tag{5.17}$$

Here $\tan(\theta_T)$ and $\tan(\theta_S)$ are the slopes of $1/(k_BT_{max})$ versus $\ln(\omega)$ and of $\ln(S_{max})$ versus $\ln(\omega)$, respectively .

The analysis of our data indicates an activation energy of 476 meV ± 30 meV. Earlier studies of DX centers in bulk AlGaAs (using DLTS) and in AlGaAs/GaAs heterostructures (using DLNS) [67, 112] reported an DX center activation energy of 430±30 meV, being in very good agreement with our present results. Therefore, it is justified to regard the DX center as the primary source of G-R noise in the structures under investigation.

According to Lang's explanation of the DX center [226] and the configuration diagram presented in Fig. 5.12 (after Mooney [112]), the caption and emission kinetics can be explained. The parabolas on the left side represent the total energy in case of ionized DX center and electrons located in the conduction band.

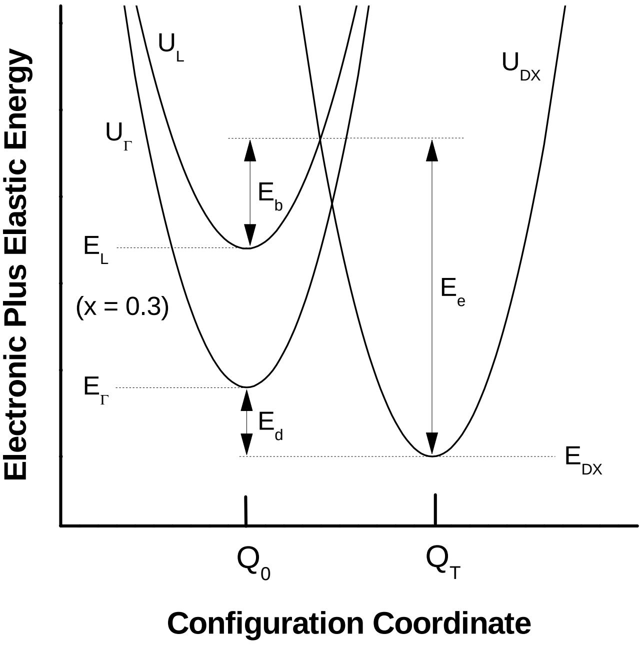

Figure 5.12: Configuration coordinate diagram illustrating the capture and emission kinetics of the DX center in the large lattice relaxation model after Mooney [112].

An occupied DX center is described by the parabola on the right side. The shift along the x axis represents a change in the atomic configuration around the donor atom when the charge state of the DX level is changed. E_d is the donor binding energy usually determined from the temperature dependence of the free carrier concentration in Hall experiments.

Electronic transitions between conduction band and trap occur at vibronic levels near the top of the classical potential barriers E_b and E_e. Thus, the energy E_b is the capture activation energy depending on the composition of the AlGaAs layer [112, 227]. E_e is the emission activation energy. Experimental data obtained by the DLTS technique revealed the emission activation energy being independent on the Al composition and amounting about 430 meV ± 30 meV [219, 228].

Using Eq. (5.17), an analysis of the noise data provides an ionization energy of about 0.252 eV. The electron capture cross section of the level is given by

$$\sigma_0 = \frac{1}{\tau_{c0} v_T n_0}, \tag{5.18}$$

where the time constant τ_{c0} can be expressed via

$$\tau_{c0} = \frac{1}{\omega} \left(\frac{E_1 - E_0}{E_1 + E_0} \right)^{1/2} \exp \left(-\frac{E_1}{k_B T} \right) \; . \tag{5.19}$$

Assuming the transitions to and from the trap occuring via L band states, both electron capture cross section and trap concentration can be estimated.

Based on a thermal electron velocity of $v_T = 1.5 \times 10^7$ cm/s for electrons in the L valleys and using Eqs. (5.18) and (5.19), an electron capture cross section of about $\sigma_0 \simeq 1 \times 10^{-11}$ cm^2 is estimated.

Using Eq. (5.15), the integral deep level concentration can be calculated. As a precondition, the constant A was determined by solving the extreme value problem for Eq. (5.14). Then, using the expression

$$N_{ts} = \frac{1}{4} ALWn_s^2 \tag{5.20}$$

with the length L and the width W of the device, a trap concentration of about $N_t \simeq 1.4 \times 10^{10}$ cm^{-2} is calculated.

5.2.4 G-R noise in pseudomorphic modulation-doped devices

Temperature-dependent noise measurements were used to investigate the deep centers causing G-R processes in pseudomorphic modulation-doped $Al_{0.2}Ga_{0.8}As/In_{0.1}Ga_{0.9}As/GaAs$ devices. The appropriate technique to estimate both emission activation energy and capture activation energy was introduced by Kirtley et al. [67]. Carey et al. [90] used it for studies of deep traps in GaAs/AlGaAs heterostructures. The noise power spectrum $S(f_p)$ for a two level system can be written according to Ref. [229]

$$f_p \cdot S(f_p) = \frac{1}{4\pi^2} \cdot \frac{\tau_e \tau_c}{(\tau_e + \tau_c)^2}. \tag{5.21}$$

Here τ_e and τ_c are the emission and capture times, respectively. The measurement frequency is $f_p = 1/(2\pi\tau)$ with the time constant τ written as

$$\frac{1}{\tau} = \frac{1}{\tau_e} + \frac{1}{\tau_c}. \tag{5.22}$$

The capture and emission times are assumed to be exponentially dependent on temperature [90] as

$$\tau_c = \frac{\tau_{c0}}{\sqrt{T}} \cdot \exp\left(-\frac{E_c}{kT}\right), \tag{5.23}$$

$$\tau_e = \frac{\tau_{e0}}{\sqrt{T}} \cdot \exp\left(-\frac{E_e}{kT}\right). \tag{5.24}$$

Here E_c and E_e are the capture and emission energies, respectively.

Figure 5.13 shows the temperature dependence of the noise voltage fluctuations for different frequencies. Two separate noise peaks (marked as A and B) are clearly resolved, changing their position and amplitude with varying frequency. According to Carey et al. [90], this behavior is assigned to deep traps

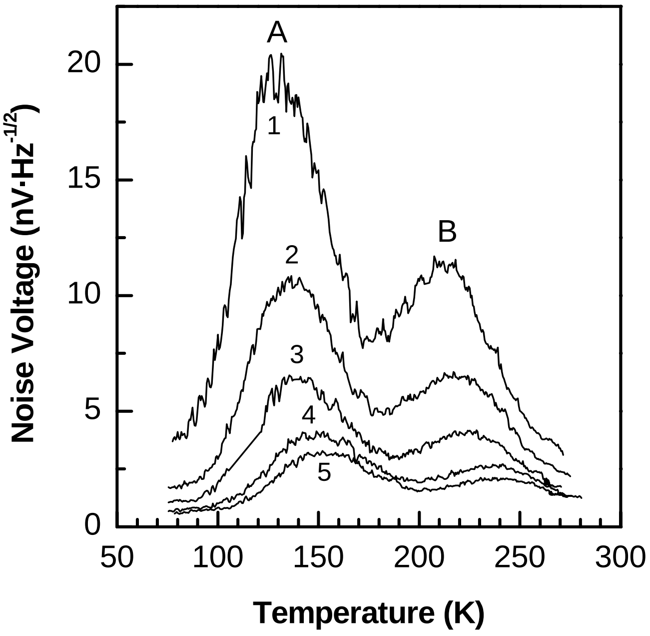

Figure 5.13: Temperature dependence of noise voltage fluctuations, measured at different frequencies of (1) 10 Hz, (2) 30 Hz, (3) 60 Hz, (4) 180 Hz and (5) 280 Hz.

in the semiconductor material. Measuring the peak position shift with increasing frequency, both capture and emission activation energies can be determined. Assuming $\tau_c \gg \tau_e$, these energies can be directly obtained from the slope of the graphs $\ln(\sqrt{T_p}/2\pi f_p)$ and $\ln\left[\sqrt{T_p}/8\pi^3 f_p^2 \left(\langle\Delta V^2\rangle / V^2 \Delta f\right)\right]$ vs. $1/T_p$, where T_p is the according peak temperature.

Figure 5.14 contains the Arrhenius plots for both noise peaks. The emission energies E_e are determined as 242 meV and 474 meV for peaks A and B, respectively. The corresponding capture energies E_c are 207 meV and 487 meV. The estimated experimental uncertainty for these values is $\triangle E = \pm$ 30 meV. Using Ref. [68] (see Appendix A), the density of the 474-meV center was estimated of about 1×10^{10}cm^{-2}.

From earlier DLTS studies [112], an emission energy of 430 ± 30 meV is characteristic for the DX center in AlGaAs, independent of alloy composition. This value is consistent with the emission energy measured for peak B in our devices, suggesting the DX center being a main source of G-R processes in our micro-Hall devices. With the presence of a relatively thick and heavily-doped $Al_{0.2}Ga_{0.8}As$ barrier in the structure, this result is not surprising.

As earlier reported by Mosser et al. [230], the barrier thickness has to be optimized. Thereby, any parasitic parallel conduction in the barrier region and undesirable effects on thermal stability of micro-Hall devices can be avoided. Thermal trapping effects on DX centers degrade the thermal stability of the micro-Hall

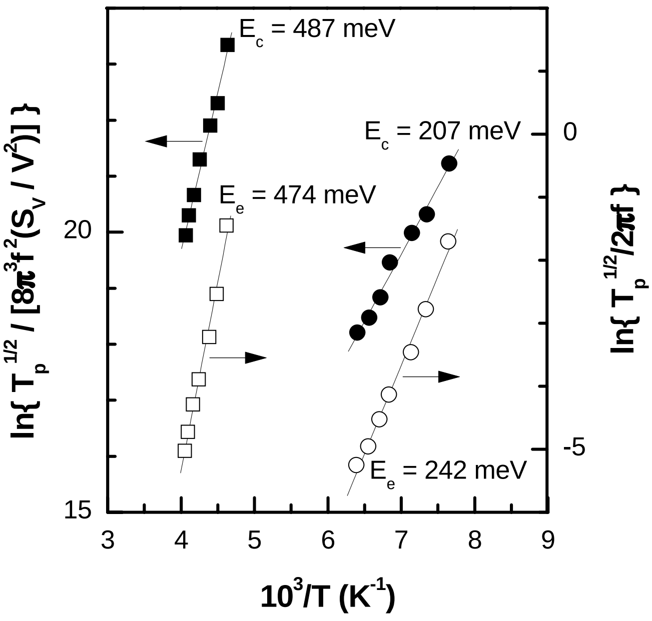

Figure 5.14: The Arrhenius plot used for the estimation of capture and emission activation energies.

device due to electron concentration changes. Furthermore, electron trapping on DX centers within the barrier region is often a main source of generation-recombination noise and results in poor noise performance, even at lower Al composition as in our case. Accordingly, both the SNS and magnetic field detection limit would suffer from an increased noise density. Hall experiments [225] verified the DX level E_{DX} for Al compositions $x \leq 0.22$ being energetically localized above the band edge E_Γ. Therefore a metastable level is constituted, with the capability to localize electrons [67]. With $x \simeq 0.2$ here, our experimental results indicate approximately the same value for both emission and activation energies within the measurement uncertainty. These data are in good agreement with DLTS [112] and DLNS [67] results obtained in MODFET structures ($x \leq 0.22$). According to [67], the situation of $\tau_e \approx \tau_c$ causes a maximized noise signal. Thus, even a metastable DX center as found in our structures can highly degrade both the SNS and the minimal detectable magnetic field.

The absolute Hall sensitivity S_A is proportional to both electron drift velocity v and device width W according to

$$S_A \equiv \frac{dV_H}{dB} \approx G{\cdot}v{\cdot}W, \tag{5.25}$$

where G is the geometric correction factor. Obviously, maximum values of the absolute sensitivity will occur for peak drift velocity saturation in micro-Hall devices. Within modulation-doped structures, the velocity begins to saturate for electric fields of about 2 kV·cm^{-1}. At these fields, hot-electron trapping by DX centers can dominate [218], resulting in additional G-R processes. Hence, mainly hot-electron trapping effects will degrade small-size device characteristics. Additionally, two further effects have to be accounted for: The $1/f$ noise depends quadratically on the electric field. The thermal noise is increased due to both increased resistance and increased electron temperature. Therefore, higher electric fields are expected to cause an increased noise within the entire frequency spectrum.

A larger peak A is detected in addition to peak B (see Fig. 5.13). The level resulting in peak A exhibits capture and emission energies of 207 and 242 meV, respectively. Earlier investigations by DLTS [231, 232] of deep traps in InGaAs layers also determined activation energies comparable to our results. Using the DLNS technique, G-R noise was investigated in a structure similar to ours, i.e. in pseudomorphic field-effect transistors (pHEMTs) [233]. In addition to the DX center, another level with unspecified activation energy was found in this study and associated with the InGaAs channel. However, a conclusive interpretation of these data has not been given until now. The density of this center was also estimated to be about $0.5 \times 10^{9}\text{cm}^{-2}$, using Ref. [68] and based on the identification of this level as associated with the Γ valley of InGaAs. While the trap density is much smaller than that of the DX center, the noise level is comparable. This is probably due to the Fermi level position, being close to resonance with this trap.

Photoluminescence (PL) spectroscopy and cathodoluminescence (CL) scanning electron microscope imaging at 77 K were used as accompanying characterization techniques for our studies. Although the PL spectra are quite intense, CL imaging reveals regions of low intensity. These dark contrasts due to enhanced non-radiative recombination could indicate the presence of point defect regions.

5.3 Conclusions

Probing the epitaxial layer and contact quality as well as examining deep levels in the active device region by the low frequency noise technique, both doped-channel AlGaAs/GaAs, AlGaAs/GaAs/InGaAs and modulation-doped AlGaAs/InGaAs/GaAs heterostructures were studied. The noise spectra at constant temperatures for different contact alignments and current flows exhibit the same noise voltage densities, being an evidence of (i) isotropic material properties for both lattice matched GaAs and pseudomorphically strained InGaAs layers; and (ii) high quality device processing including mesa structuring and contact performance.

Hooge parameters of $\alpha = 1.5 \times 10^{-4}$ and $\alpha = 1.1 \times 10^{-4}$ were found for GaAs lattice matched and InGaAs pseudomorphically strained layers, respectively. These data indicate a high quality epitaxial growth. Being of the same sizes and geometries and possessing the same electron density within the conductive channel, the devices with an inserted pseudomorphically strained InGaAs layer exhibit a significantly lower $1/f$ noise.

Analyzing the noise spectra at different electric fields applied to the device, the noise spectral density in the mid-frequency range was found to follow the Hooge's law (5.9) at moderate electric fields, but deviating from it at high fields.

Noise spectra of doped-channel heterostructures revealed a pronounced plateau at frequencies lower than 10 Hz due to generation-recombination noise. Related time constants of $\tau = 1.2$ ms for AlGaAs/GaAs and $\tau = 140$ ms for AlGaAs/GaAs/InGaAs doped-channel heterostructures were estimated. Using deep level noise spectroscopy, a deep center with an emission activation energy of 476 meV was detected. Based on these results, DX centers located on both AlGaAs/GaAs heterointerfaces are assigned as the primary source of generation-recombination noise within the investigated structures.

Modulation-doped AlGaAs/InGaAs/GaAs heterostructures were also studied with the DLNS technique. The results indicate two levels contributing to the noise spectral density with an emission and activation energies of 474 meV and 242 meV, respectively. The first one is a metastable level capable to localize electrons and attributed to DX centers located in the AlGaAs Si-doped barrier. The second center with the smaller activation energy is believed as related to defects in the InGaAs layer, being probably point-like defects. Based on the theory proposed in [68], capture cross sections and defect concentrations of the levels were estimated.

Chapter 6

Micro-Hall devices as magnetic sensors

6.1 Signal linearity

Signal linearity of the Hall voltage as the useful signal is a key device characteristic. The Hall voltage V_H is given by Eq. (2.69) (see Chapter 2). Using (2.69) and (2.43), it can be expressed as

$$V_H = G\mu EWB = GvWB, \tag{6.1}$$

where G is the geometrical correction factor and v the electron drift velocity. W is the width of the device and B the magnetic field.

Within magnetic sensor applications of a Hall effect device, the proportionality $V_H \sim IB$ or $V_H \sim \ VB$ (depending on the device biasing conditions) should be met to a high degree of accuracy.

In order to analyze the linearity of the studied micro-Hall devices, measurements of the Hall voltage vs. magnetic field and bias current were performed. Figure 6.1 depicts according results for sample DC8 and sample DC9 at T=300 K. Obviously, the micro-Hall devices exhibit a high signal linearity at low and high bias currents and, therefore, at various electric fields in the active device region.

Using Eq. (2.79) (see Chapter 2), a quantitative analysis of the Hall voltage non-linearity can be done. Figure 6.2 represents the results for sample DC8 at two bias currents: $I = 50$ μA and $I = 400$ μA. The estimated non-linearity does not exceed 4 % and is mainly due to measurement errors at very low magnetic fields.

Studies of the Hall voltage non-linearity in these micro-Hall devices were performed in the 77 - 300 K temperature range, too. A detailed analysis revealed the non-linearity of the studied micro-Hall devices being not temperature-dependent and not exceeding 4 % at low and high electric fields.

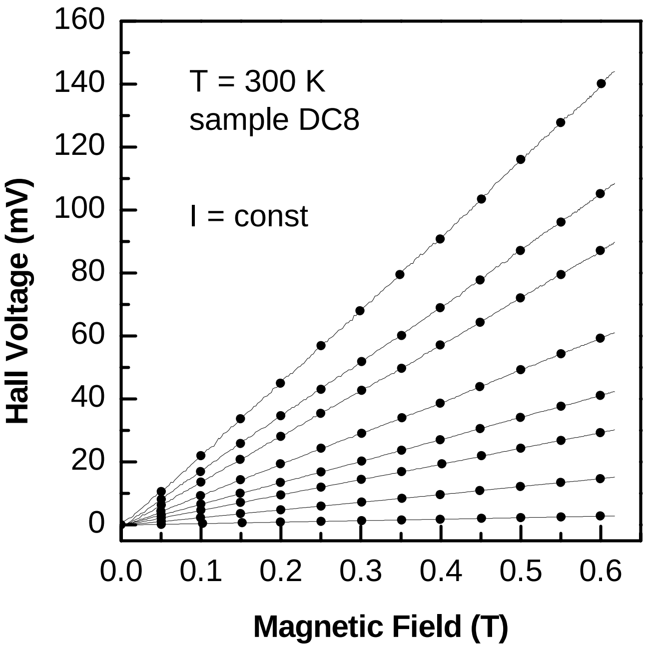

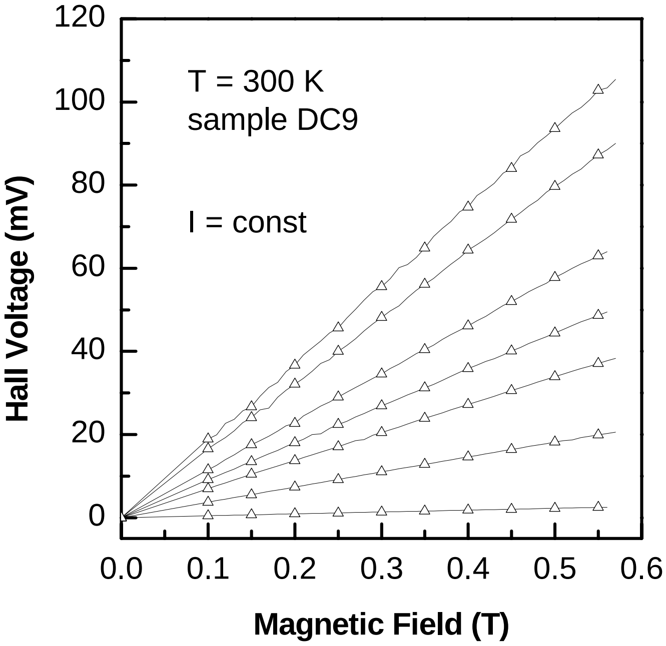

Figure 6.1: Dependence of the Hall voltage on magnetic field at various bias currents. The measurements were done at 300 K for samples DC8 (at bias currents: 10, 50, 90, 120, 170, 250, 300, and 400 μA) as well as for sample DC9 (at bias currents: 10, 70, 110, 130, 150, 190, 220 μA). The relation $V_H \sim IB$ holds true to a high degree of accuracy.

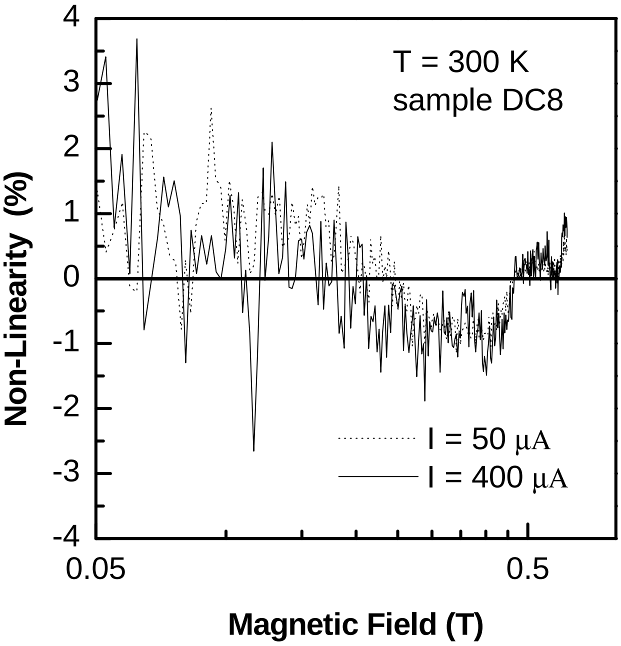

Figure 6.2: Non-linearity of the Hall voltage $[(V_H(I,B)-V_{H,fit})/V_{H,fit}]$ vs. magnetic field at T = 300 K for sample DC8: dotted line, $I = 50\mu$A; full line, $I = 400\mu$A.

6.2 Hall sensitivity

Signal-to-noise sensitivity and detection limit of micro-Hall devices are determined by the absolute sensitivity. In Section 2.3.4 the absolute sensitivity value was shown to be proportional to both electron drift velocity v and device size W. Thus, high electron drift velocity materials are desirable for an absolute sensitivity enhancement. Previous studies of the velocity-field characteristics revealed the peak electron drift velocity depending on the scattering mechanisms acting in the device bulk. In this section, we study micro-Hall devices based on both doped-channel and modulation-doped heterostructures with fundamentally different carrier scattering. We show the sensor's performance determined more by electron drift velocity than by low-field mobility.

In addition to absolute sensitivity, we consider the supply-voltage-related sensitivity (SVRS) S_V and supply-current-related sensitivity (SCRS) S_I. The first can be successfully used for studies of different carrier scattering mechanisms determining the basic device characteristics. On the other hand, the SCRS gives insight in the carrier dynamics at low and high electric fields. Furthermore, both quantities are used for comparison of our devices with micro-Hall sensor characteristics previously published.

6.2.1 Absolute sensitivity

The absolute sensitivities of 10 μm square size micro-Hall devices based on doped-channel $Al_{0.3}Ga_{0.7}As/GaAs$ (sample DC8) and $Al_{0.3}Ga_{0.7}As/GaAs/In_{0.2}Ga_{0.8}As$ (sample DC9) heterostructures were measured at 300 K and 77 K. Figure 6.3 shows the absolute sensitivity vs. electric field dependencies for both structures at 300 K. The absolute sensitivity was determined from the slope in the Hall voltage V_H vs. magnetic field B dependence, expressed via

$$S_A \equiv \frac{dV_H}{dB} = G\mu EW = GvW. \tag{6.2}$$

Here μ is the electron mobility and E the electric field.

The absolute sensitivity follows the velocity-field characteristics, i.e. it increases with rising electric field in the device active region, saturating at some electric field. The measured absolute sensitivities indicate the micro-Hall devices being not in peak drift velocity saturation. For sample DC8, the largest measured value is $S_A = 176$ mV/T for an electric field of about 1.35 kV/cm. For sample DC9, a value of $S_A = 182$ mV/T was measured at an electric field of about 1.1 kV/cm.

Obviously, the micro-Hall device absolute sensitivity for the pseudomorphically strained $In_{0.2}Ga_{0.8}As$ doped-channel is higher compared to the lattice-matched doped GaAs channel. This result is not surprising and can be explained

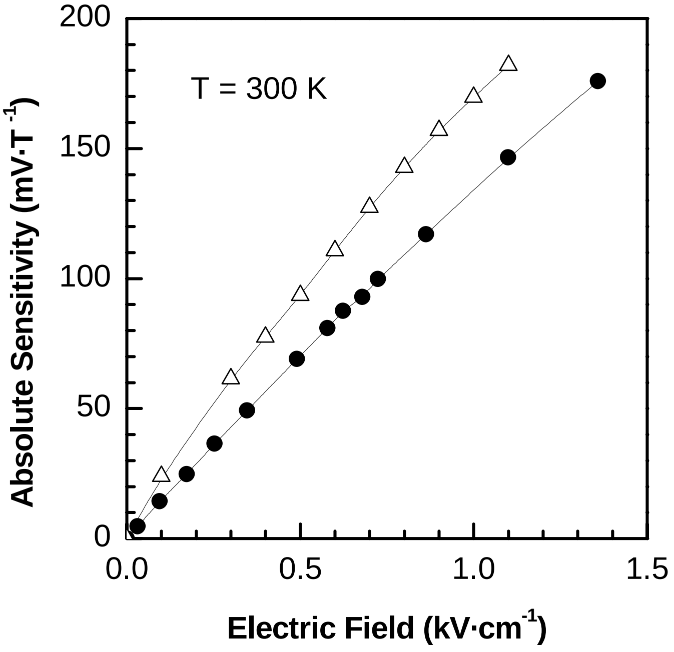

Figure 6.3: Absolute sensitivity vs. applied electric field for sample DC8 and sample DC9 at $T = 300$ K - (●) : sample DC8, (△) : sample DC9.

as a result of (i) the strained InGaAs layer inserted into the doped GaAs channel and (ii) the doping profile.

The low-field mobility of electrons is given by Eq. (2.23) (see Chapter 2):

$$\mu = \frac{e\tau}{m^*}, \tag{6.3}$$

where e is the electron charge, τ the relaxation time and m^* the electron effective mass. Due to the lower effective mass in InGaAs, the electron low-field mobility in InGaAs is higher than in equivalently-doped GaAs material [36, 52]. Since the electron drift velocity at low and moderate electric fields is given by

$$v(E) = \mu(E)E, \tag{6.4}$$

the electron drift velocity in InGaAs is higher compared to GaAs. At high electric fields, InGaAs has an additional advantage over GaAs and other semiconductors due to the higher peak electron drift velocity: The energy difference between the lowest Γ valley and the higher L and X valleys in InGaAs is much greater than in most other semiconductors. Thus, electrons in InGaAs tend to remain in the Γ valley at larger electric fields, resulting in a higher peak drift velocity. Since the absolute sensitivity is proportional to the electron drift velocity, higher sensitivities are expexted for micro-Hall devices based on heterostructures with a pseudomorphically strained InGaAs channel embedded into a GaAs layer.

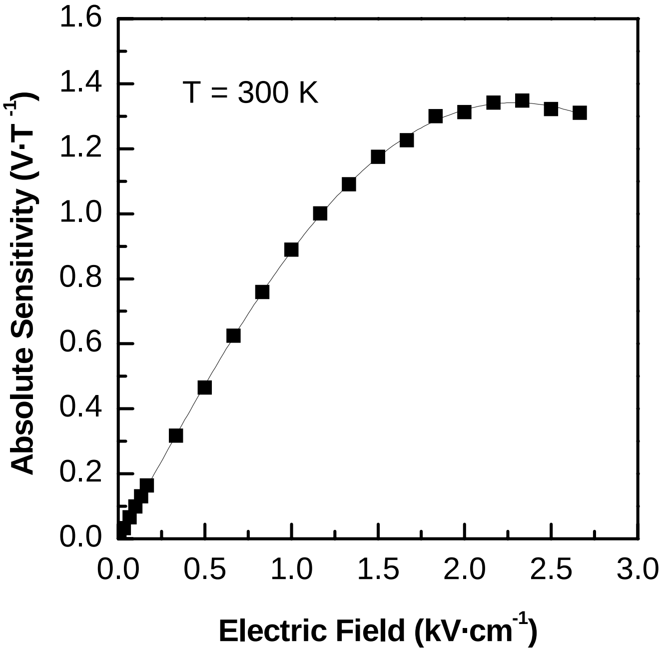

Figure 6.4: Absolute sensitivity as a function of applied electric field for 20 μm square size micro-Hall device based on modulation-doped $Al_{0.2}Ga_{0.8}As/In_{0.1}Ga_{0.9}As/GaAs$ heterostructure. The measurements were performed at 300 K.

The growth of InGaAs on GaAs with a thickness well below the critical one is accompanied by additional strain due to different lattice constants. This causes an additional enhancement of both low-field mobility and peak velocity saturation due to the further increase of the intervalley separation between Γ and L valleys.

The micro-Hall device sample DC9 is δ-doped with the spike centered within the InGaAs quantum well. Sample DC8 has a uniformly doped GaAs channel. Heterostructures with centered δ-doping in the quantum well were shown to exhibit a higher electron drift velocity than heterostructures with uniformly doped quantum well [23].

The absolute sensitivity as a function of electric field for a 20 μm square size micro-Hall device based on modulation-doped $Al_{0.2}Ga_{0.8}As/In_{0.1}Ga_{0.9}As/GaAs$ heterostructure (sample MD28) is shown in Fig. 6.4. The observed behavior complies to the velocity-field dependence. During the measurements, electric fields up to electron drift velocity saturation were applied. The saturation was observed for an electric field of about 2.3 kV/cm, causing a plateau in the sensitivity-field dependence at a maximum absolute sensitivity value of 1.34 V/T. The electric field strength is typical for the heterostructure type studied here [234].

6.2.2 Supply-voltage-related sensitivity

Driving the micro-Hall device by a constant voltage, the supply-voltage-related sensitivity (SVRS) S_V can be estimated by Eq. (2.64) (see Chapter 2). For our micro-Hall devices with Greek cross geometry (with the same length L and width W of the device), the SVRS given by Eq. (2.64) can be rewritten as

$$S_V = \frac{1}{V}\frac{dV_H}{dB} \approx G\mu. \tag{6.5}$$

Thus, the measurement of supply-voltage-related sensitivity vs. electric field dependencies can serve as a direct method for mobility-field characteristics studies. Both mobility-field and velocity-field dependence investigations are essential keys to a clarification of the signal-to-noise sensitivity degradation, being a subject of the present work.

Now we consider micro-Hall devices based on doped-channel heterostructures. Measurement results for the supply-voltage-related sensitivity (SVRS) as a function of the electric field are shown in Fig. 6.5 for 300 K (a) and 77 K (c). The sample DC9 is a micro-Hall device based on a doped-channel $Al_{0.3}Ga_{0.7}As/GaAs/In_{0.2}Ga_{0.8}As$ heterostructure. Obviously, the SVRS behavior is completely different for high and low temperatures.

At high temperatures, the SVRS decreases with increasing electric field. The straightforward explanation is as follows: At room temperature, the transport properties of the two-dimensional electron gas are determined by scattering on polar optical phonons and on ionized impurities. An increasing electric field causes heating of the electron gas. The excess energy of the electron gas is

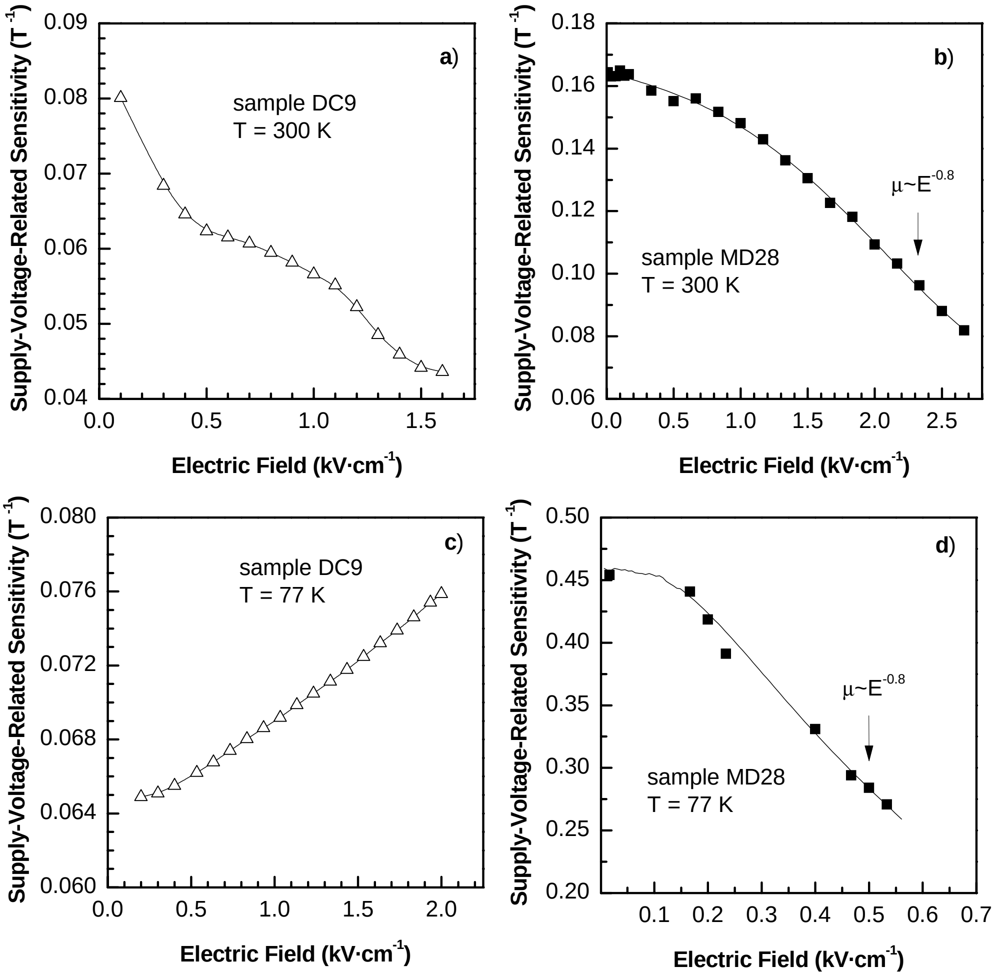

Figure 6.5: Supply-voltage-related sensitivity as a function of the electric field at different temperatures: (a) - for micro-Hall device based on the doped-channel $Al_{0.3}Ga_{0.7}As/GaAs/In_{0.2}Ga_{0.8}As$ heterostructure at 300 K; (b) - for micro-Hall device based on the modulation doped $Al_{0.2}Ga_{0.8}As/In_{0.1}Ga_{0.9}As/GaAs$ heterostructure at 300 K; (c) - for micro-Hall device based on the doped-channel $Al_{0.3}Ga_{0.7}As/GaAs/In_{0.2}Ga_{0.8}As$ heterostructure at 77 K; (d) - for micro-Hall device based on the modulation doped $Al_{0.2}Ga_{0.8}As/In_{0.1}Ga_{0.9}As/GaAs$ heterostructure at 77 K.

transferred to the phonon subsystem, i.e. to the lattice. This effect is usually observed as lattice heating. Finally, it results in decreasing electron mobility and decreasing SVRS, consequently.

At low temperatures, the electric field affects the electron subsystem in the same manner. However, scattering on ionized impurities dominates at low temperature and low field due to intentional doping of the quantum well. The heating of the electron gas leads to a decreased scattering on ionized impurities and increased electron mobility, respectively. The mobility increase usually follows a

$\mu \propto T_e^n$ law, where T_e^n is the electron temperature and n is a positive exponent with $0 < n < 1.5$ [235]. If the temperature of the two-dimensional electron gas is high enough, scattering through phonon emission becomes more significant and eventually dominates. Thus, the mobility decreases with rising temperature. While we observe only a monotonous increase in the SVRS, electron gas temperatures with significant scattering on optical phonons are not achieved. For example, for doped bulk GaAs ($n_{3D} = 1 \times 10^{18}$) the according decrease in mobility was observed at an electric field of about 3 kV/cm [58]. For an AlGaAs/GaAs heterostructure, the mobility decrease was measured at electric fields higher than 4 kV/cm.

Proving the mobility-field dependence and accordingly SVRS-field characteristics, additional measurements of geometrical magnetoresistance were performed at 6 K. The results are shown in Fig. 6.6. At such low temperature, the influence of scattering on the polar optical phonons is negligible and ionized impurity scattering dominates. Obviously, the mobility of the two-dimensional electron gas increases with rising electric field. These results support our conclusion with respect to mobility-field behavior. At 77 K, the mobility is supposed to exhibit the same tendency, except for the threshold field for decreasing mobility due to higher lattice temperature.

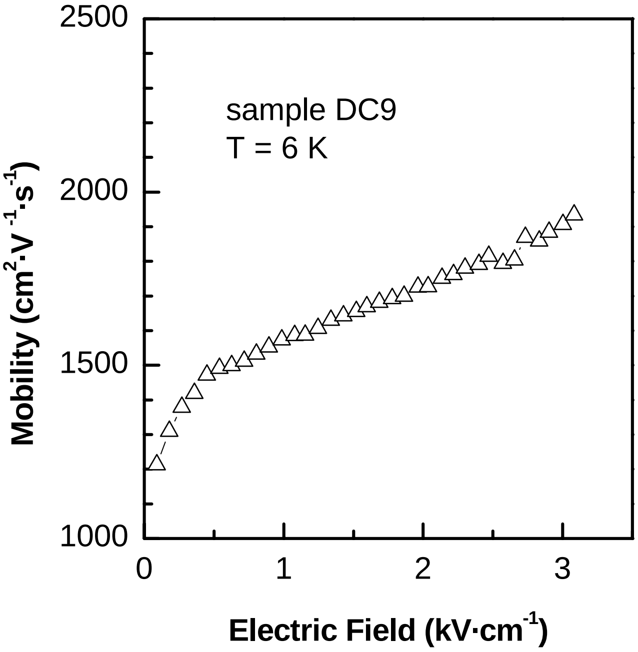

Figure 6.6: Mobility-field dependence of a doped-channel $Al_{0.3}Ga_{0.7}As/GaAs/In_{0.2}Ga_{0.8}As$ heterostructure measured at 6 K. The measurements were performed in rectangular geometry with ohmic contacts along two opposite edges of width $W = 100$ μm separated by a channel of length $L = 10$ μm.

The SVRS measurement results of micro-Hall devices based on modulation-doped $Al_{0.2}Ga_{0.8}As/In_{0.1}Ga_{0.9}As/GaAs$ heterostructures are shown in Fig. 6.5 for temperatures of 300 K (b) and 77 K (d). The mobility-field dependence is approximately the same for both temperatures, differing only in the SVRS values.

Modulation-doped heterostructures are well known for increasing mobility with decreasing temperature. This is caused by a decrease in the scattering rate on polar optical phonons and a negligible influence of ionized-impurity scattering due to the spatial separation of two-dimensional electron gas and ionized donors [236, 237]. Thus, the SVRS should be higher at low temperature than at 300 K. Consistently, a SVRS of $0.165\ T^{-1}$ at 300 K and $0.455\ T^{-1}$ at 77 K were measured.

Initially, the SVRS is relatively high but decreases rapidly as the electric field is increased. This result resembles the previously reported mobility-field behavior for the modulation-doped system [48]. At low fields, the mobility is constant. An increasing electric field causes decreasing mobility. For mid-range electric fields, the mobility follows the electric field as $\mu \sim E^{-0.8}$. At higher fields, the mobility must ultimately go as $\mu \sim E^{-1}$ [49]. The analysis of our experimental data reveals the following: In the range of electric fields of 1.8 - 2.7 kV/cm at 300 K and 200 - 500 V/cm at 77 K, the SVRS (accordingly the mobility) follows the electric field as $E^{-0.8\pm0.1}$, being in good agreement with earlier reported data.

6.2.3 Supply-current-related sensitivity

As pointed out above, studies of the supply-current-related sensitivity (SCRS) give additional insight into the carrier dynamics at low and high electric fields. Since the SCRS is inversely proportional to the two-dimensional electron concentration n_{2D}

$$S_I = \frac{1}{I}\frac{dV_H}{dB} = \frac{G}{en_{2D}}, \tag{6.6}$$

the SCRS - field dependence serves as an indicator of electron concentration behavior at low and high electric fields. With respect to the application of micro-Hall sensors, ideally the SCRS should be field-independent. SCRS studies can probe the carrier dynamics in the active device region. For example, an increasing SCRS indicates a decreasing electron concentration in the studied structures. That might be due to trapping effects on deep levels in the heterostructure. Therefore, beside SCRS measurements just noise measurements can be useful for an intended structure optimization. On the other hand, a decreasing SCRS at high electric fields indicates an increasing electron concentration. This is usually due to parallel conduction in the barrier region [238] or carrier injection from the contacts [239, 240].

The SCRS measurement results are shown in Fig. 6.7 for a 20 μm square size doped-channel micro-Hall device based on an $Al_{0.3}Ga_{0.7}As/GaAs/In_{0.2}Ga_{0.8}As$ heterostructure (sample DC9). The SCRS versus bias current at 300 K (figure a) dependence exhibits a quite complicated behavior. At low currents (and,

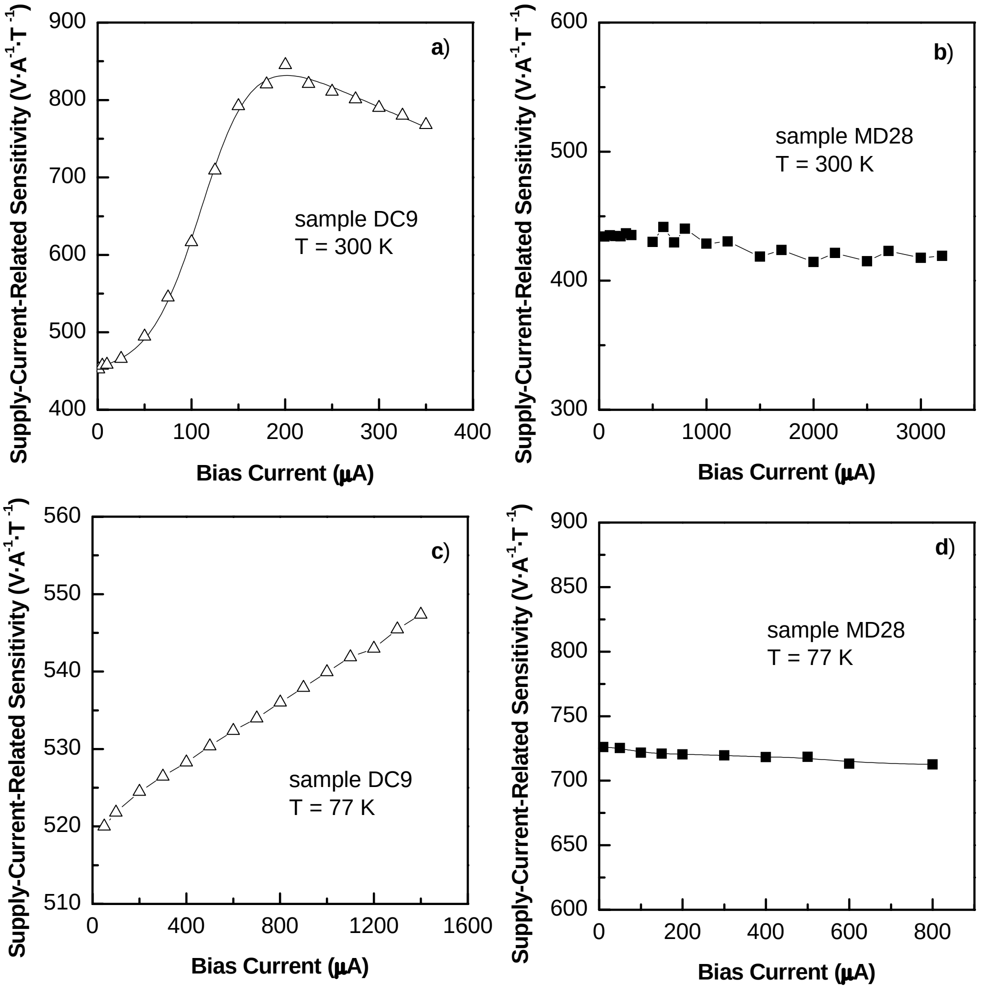

Figure 6.7: Measurements of supply-current-related sensitivity (SCRS) as a function of bias current for doped-channel (sample DC9) (figures *a* and *c*) and modulation-doped (sample MD28) (figures *b* and *d*) micro-Hall devices. The measurements were performed at 300 K and 77 K.

therefore, low electric fields), the SCRS is constant at about 450 V/A/T. A further bias current increase in the range of 50-150 μA leads to a significant SCRS rise. Starting with $I = 150$ μA, the SCRS saturates at a magnetic sensitivity of 830 V/A/T. For further bias current increase, the SCRS slightly decreases. Results of measurements at 77 K are shown in figure (c). The supply-current magnetic sensitivity increases monotonous with rising bias current. It amounts 520 V/A/T at low bias currents ($I = 50$ μA) and reaches 548 V/A/T at $I = 1400$ μA. A similar tendency in SCRS behavior was observed for sample DC8 and sample DC13. This significant SCRS increase is caused by the reduced two-dimensional electron concentration. This mechanism of free electron depletion within the quantum well is assumed to be due to a thermal or field induced trapping of carriers on DX centers. Indeed, using the DLNS technique, deep traps with an activation energy of $E_a = 476$ meV were detected (see Section 5.2.3) and identified as DX centers. Just DX centers created at both interfaces during epitaxial growth can cause generation and recombination processes in the studied micro-Hall device types.

The SCRS measurement results for 20 μm modulation-doped $Al_{0.2}Ga_{0.8}As/In_{0.1}Ga_{0.9}As/GaAs$ quantum well micro-Hall devices are shown in Fig. 6.7, too. Obviously, here the supply-current magnetic sensitivity is nearly independent on the bias condition (and, therefore, electric field). We found values of $S_I = 430$ V/A/T and $S_I = 725$ V/A/T at 300 K and 77 K, respectively. For a classification of our results, they should be compared with SCRS values reported in the literature for the best micro-Hall sensors based on heterostructures. For Hall devices based on modulation-doped AlGaAs/InGaAs/GaAs heterostructures, values ranging from 400 V/A/T up to 1200 V/A/T were reported [230]. A value of $S_I = 320$ V/A/T was measured for a Hall sensor based on strained modulation-doped $In_{0.52}Al_{0.48}As/In_{0.8}Ga_{0.2}As$ heterostructure grown on an InP substrate [241]. Highly sensitive $In_{0.52}Al_{0.48}As/In_{0.75}Ga_{0.25}As$ micro-Hall sensors grown on semi-insulating InP substrates were reported with a magnetic sensitivity of 580 V/A/T [242]. Using a 2DEG channel $InP/In_{0.53}Ga_{0.47}As$ double heterostructure, magnetic sensors with a SCRS of 1350 V/A/T were realized [243, 244].

Based on doped-channel and modulation-doped heterostructures, our micro-Hall devices exhibit competitive SCRS values. A summary of selected results for devices studied in this work is given in Table 6.1.

Sample	DC8	DC9	DC13	MD28
μ_H at 300 K ($cm^2 \cdot V^{-1} \cdot s^{-1}$)	1651	2193	2046	6750
n_{2D} at 300 K (cm^{-2})	1.3×10^{12}	1.3×10^{12}	1.5×10^{12}	9.7×10^{11}
S_A at 300 K (77 K) ($V \cdot T^{-1}$)	0.24 (0.23)	0.21 (0.21)	0.19 (0.18)	0.18 (0.29)
at I_{bias}, μA	400	400	400	400
$S_{I,max}$ at 300 K (77 K) ($V \cdot A^{-1} \cdot T^{-1}$)	590 (565)	531 (596)	520 (454)	430 (726)

Table 6.1: Presented data were measured for micro-Hall devices of 10 μm square size, except for sample MD28 with 20 μm square size.

6.3 Signal-to-noise sensitivity

The signal-to-noise sensitivity proves to be another important parameter of micro-Hall device, determining its application. In fact, the SNS defines the magnetic field detection limit. Advanced micro-Hall devices based on III-V materials are able to detect magnetic fields down to the nT-range [241, 242, 245, 246]. However, some applications demand an even lower detection limit. For example, some in-situ biological applications require sensitivities on a pT-scale. Micro-Hall devices could replace SQUID devices (scanning superconducting quantum interference susceptometers) where they are not suitable in magnetic probes.

Recently, micro-Hall devices approaching the pT-range were successfully fabricated on InGaAs/InP [247] and AlGaAs/InGaAs/GaAs [248] heterostructures. Some device-related problems are subject to further in-depth studies: SNS-field dependence, geometry and size influence on SNS, etc.

The SNS was defined in Section 2.3.4 as

$$SNS \equiv \frac{S_A}{\overline{V}_{noise}}, \tag{6.7}$$

where S_A is the absolute sensitivity and $\overline{V}_{noise} = \sqrt{S_{V,noise}(f)\Delta f}$ the noise voltage measured within the band width Δf.

In the following, we restrict our consideration to two doped-channel micro-Hall devices based on $Al_{0.3}Ga_{0.7}As/GaAs$ (sample DC8) and $Al_{0.3}Ga_{0.7}As/GaAs/In_{0.3}Ga_{0.7}As$ (sample DC13) heterostructures.

Measurement results of the noise voltage vs. frequency are shown in Fig. 6.8 for both devices. As a matter of fact, an increasing bias current and consequently rising electric field causes a higher noise voltage and noise voltage spectral density. Within the mid-frequency range with dominating $1/f$ noise, the noise spectral density is given by

$$S_{V,\alpha} = \alpha E^2 \left(n_{2D} f\right)^{-1}, \tag{6.8}$$

where α is the Hooge parameter, f the frequency and E the electric field.

As long as the noise is dominated by flicker noise, the noise voltage scales approximately linearly with the electric field. Indeed, the noise voltage measured at 1 kHz in sample DC8 is proportional to E. For sample DC13 we find at small fields a superlinear behavior, but a sub-linear one at large fields. The thermal noise is expected to rise only slightly due to increasing resistance.

Figure 6.9 presents the SNS dependence on electric field measured at several frequencies within a bandwidth of $\Delta f = 1$ Hz. Within the electric field range under investigation, the noise is still dominated by $1/f$ noise. Therefore the SNS is roughly constant, since both S_A and $\bar{V}_{1/f}$ rise approximately linearly with the applied electric field. Additionally, one concludes from Fig. 6.9 that the SNS does not degrade even at higher electric fields ($E > 1.5$ kV·cm^{-1}). Maximum SNS values of 80 dB/T at 10 Hz and 98 dB/T at 1 kHz are achieved for the

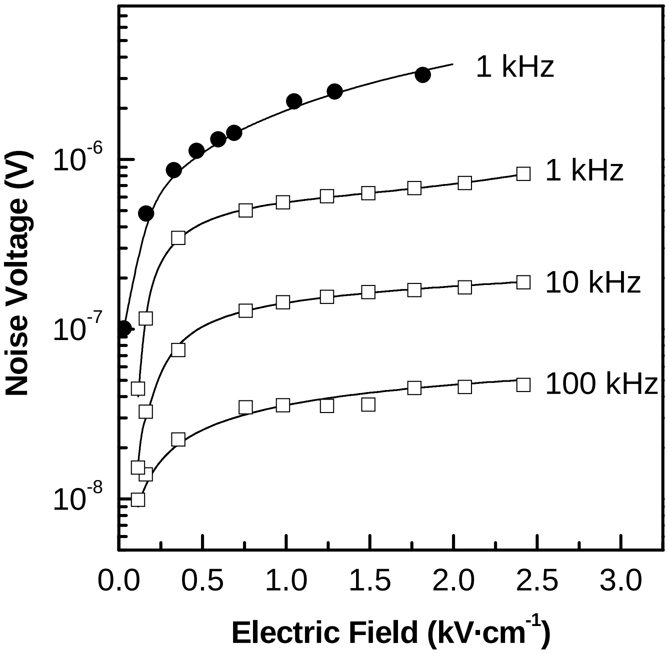

Figure 6.8: Noise voltage vs. applied electric field for micro-Hall devices DC8 (●) and DC13 (□), $\Delta f = 1$ Hz, $T = 300$ K.

micro-Hall device on sample DC8. For the micro-Hall device DC13, maximum SNS magnitudes of 88 dB/T at 10 Hz, 114 dB/T at 1 kHz and 138 dB/T at 100 kHz are measured.

In the following, we estimate the expected values of the SNS for a cross-shaped Hall device with width W measured in the frequency band width Δf. For the $1/f$ (flicker noise) one has

$$\mathrm{SNS} \approx \mu W \sqrt{\frac{f\, n_s}{\alpha}} \sqrt{\frac{1}{\Delta f}} \tag{6.9}$$

and

$$\mathrm{SNS} \approx v\, W \sqrt{\frac{e n_s \mu}{4 k_B T}} \sqrt{\frac{1}{\Delta f}} \tag{6.10}$$

for thermal noise, respectively.

At medium frequencies with dominating $1/f$ noise, the SNS can be approximately constant in electric field, as long as the electron mobility does not change significantly. At the highest frequencies with dominating thermal noise, the SNS can continue to increase until velocity saturation is reached. In the case of our doped structures, the electron mobility is dominated at low temperatures by ionized impurity scattering and at room temperature by both ionized impurity scattering and phonon scattering. At low temperature, in contrast to high-mobility

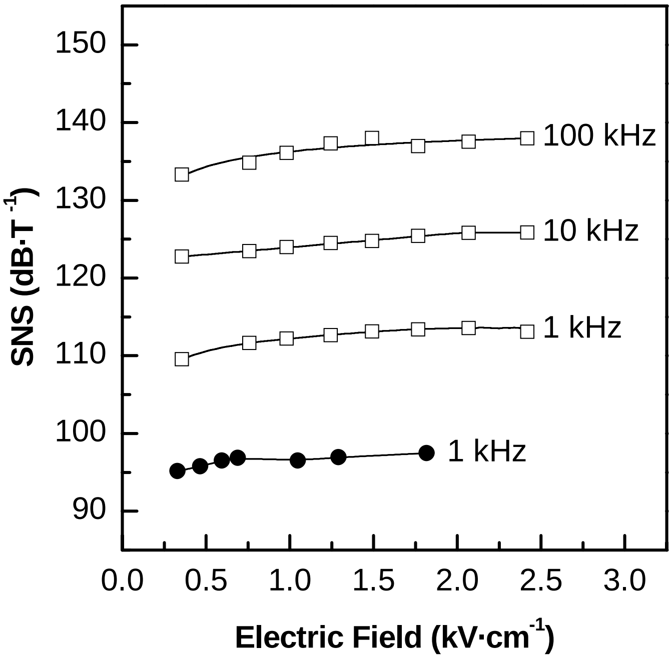

Figure 6.9: Signal to noise sensitivity as a function of the applied electric field at room temperature for micro-Hall devices DC8 (●) and DC13 (□).

structures, the mobility is relatively constant, increasing somewhat with increasing electron temperature [21, 51].

Our results in Fig. 6.9 do not give any evidence for a SNS degradation for electric fields up to 2.5 kV·cm^{-1}. As noticed above, the structures investigated here can exhibit a decreasing electron concentration at rising electric field due to trapping on DX centers. Accordingly, these changes of the electron concentration could decrease the SNS (see Eqs. (6.9) and (6.10)). To avoid this, we propose to use δ-doped $In_{0.3}Ga_{0.7}As$ QW separated from the $Al_{0.3}Ga_{0.7}As$ barrier by undoped GaAs.

The estimations of the detection limit at different frequencies were performed as

$$B_{DL} = [S_{v,noise}(f)\Delta f/S_A^2]^{1/2} = 1/SNS. \qquad (6.11)$$

The micro-Hall devices based on $Al_{0.3}Ga_{0.7}As$/GaAs heterostructures exhibit lowest detection limits of 103 μT at 10 Hz and 14 μT at 1 kHz, within a bandwidth of 1 Hz. Compared to it, lowest detection limits of of 41 μT and 2 μT at 10 Hz and 1 kHz were revealed for the devices with the InGaAs active channel.

Figure 6.10 presents the results of a detailed analysis of the detection limit vs. applied electric field dependence at various frequencies for micro-Hall device DC13. Obviously, the lowest detection limit can be achieved at higher electric fields and higher frequencies, here amounting 127 nT at 2.4 kV·cm^{-1} and 100 kHz for a bandwidth of 1 Hz. Since the absolute sensitivity is proportional

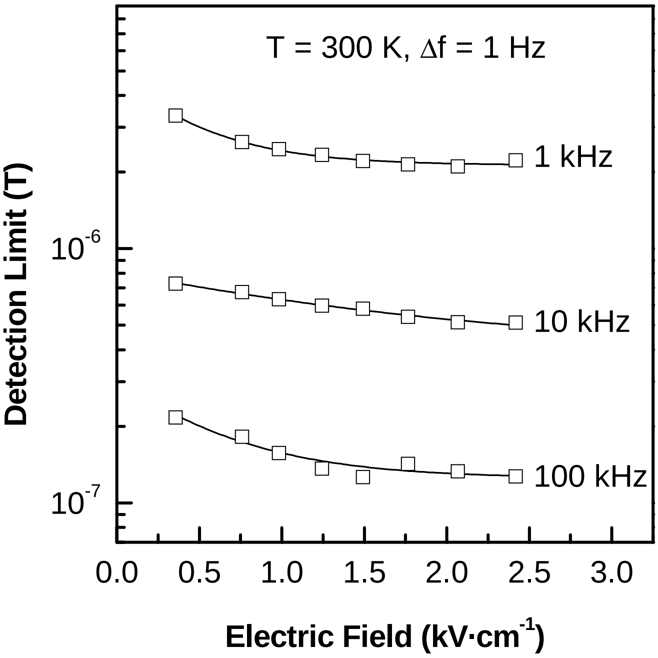

Figure 6.10: Detection limit for sample DC13 as a function of the applied electric field, measured at several frequencies.

to the electron drift velocity, the highest value will be achieved within velocity saturation at high electric fields. For doped pseudomorphic InGaAs with the drift velocity approaching 2×10^7 cm/s, an absolute sensitivity of $S_A = 2$ V·T^{-1} can be attained. On the other hand, the $1/f$ noise increases at high electric fields. Therefore, the signal-to-noise sensitivity in Fig. 6.9 does not improve much with increasing electric field. However, the data imply that the $1/f$ noise falls off at sufficiently high frequencies and only the thermal noise remains at a value not higher than 2×10^{-8} V for a 1 Hz measurement bandwidth. Thus, for high frequencies, we anticipate a signal-to-noise sensitivity of 160 dB $\cdot$ T^{-1} (or expressed with arbitrary bandwidth, 160 dB $\cdot$ T^{-1} $\cdot$ Hz$^{1/2}$) at 300 K for 10×10 μm^2 Hall devices.

Identical studies were performed on micro-Hall devices based on a modulation-doped $\mathrm{Al_{0.2}Ga_{0.8}As/In_{0.1}Ga_{0.9}As/GaAs}$ heterostructure (sample MD28). Figure 6.11 represents the results of these studies for 300 K and 77 K for the low-field range ($E < 200$ V/cm). The analysis of both SNS and detection limit B_{DL} was performed at 70 kHz with thermal noise dominating for a 1 Hz frequency bandwidth. At 300 K and a bias current $I = 325\mu$A, the SNS arrives at a maximum value of about 141 dB/T, corresponding to a detection limit of about 80 nT. The current of 325 μA corresponds to an electric field in the active device region of about 166 V/cm. At higher electric fields, degradations of both SNS and detection limit were observed.

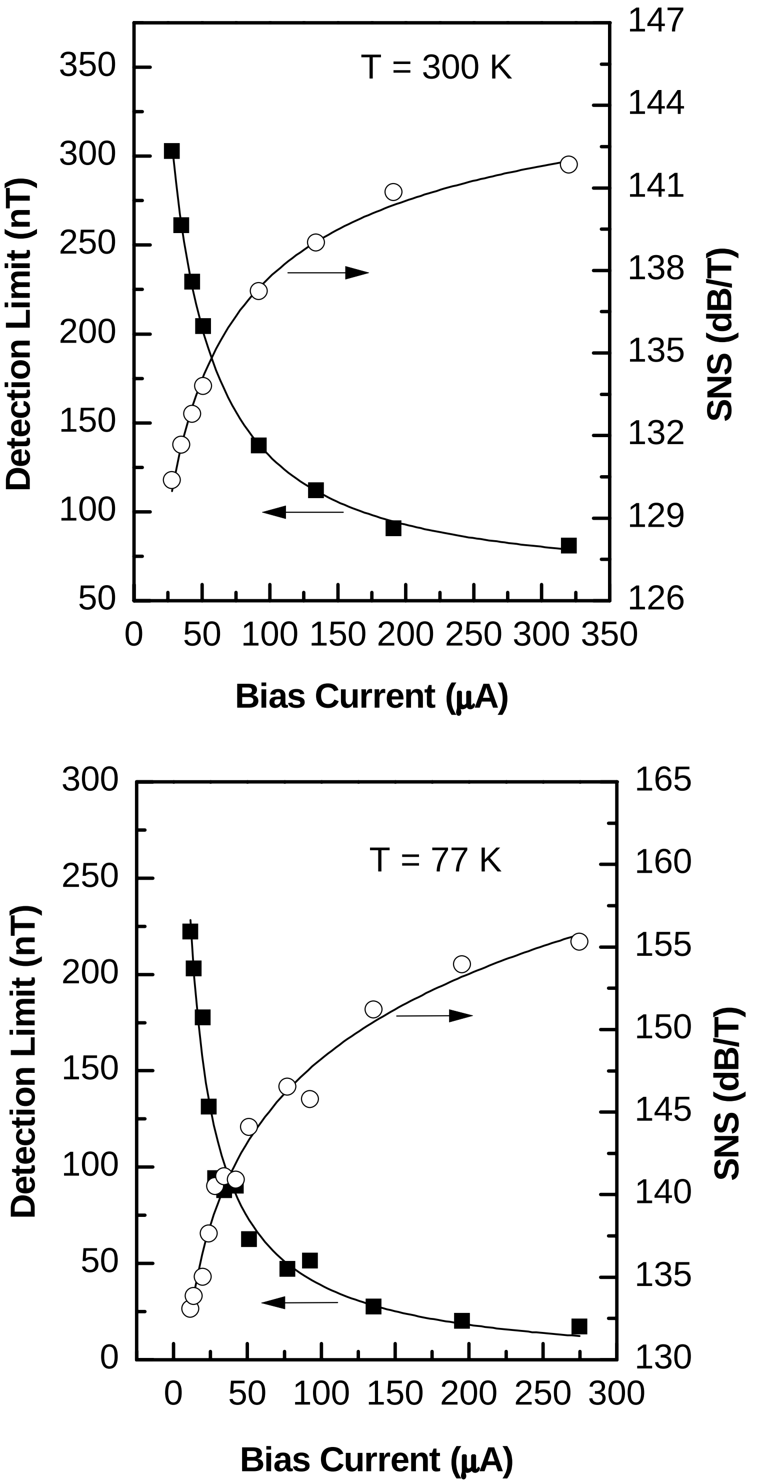

Figure 6.11: SNS and detection limit at 300 K and 77 K for a micro-Hall device based on a modulation-doped $Al_{0.2}Ga_{0.8}As/In_{0.1}Ga_{0.9}As/GaAs$ heterostructure (sample MD28) as a function of bias current.

At 77 K, a similar behavior was observed. A maximum SNS of about 155 dB/T and a detection limit of about 17 nT were revealed at a bias current of $I = 275\ \mu$A corresponding to an electric field of 45 V/cm. Obviously, the detection limit and SNS at low temperature are improved compared to ones at higher temperatures. However, the value of the critical electric field (i.e. the field with beginning degradation of both characteristics) at low temperature is three times lower than at 300 K. This effect can be easily explained in terms of mobility and electron concentration versus electric field behavior. Since the electron concentration in the studied range of electric fields is constant but the mobility decreases significantly with rising field, a decreasing SNS at higher fields is inevitable. Furthermore, the mobility decreases more distinctly at low temperatures compared to higher temperatures, see Fig. 6.5). Consequently, the results for micro-Hall devices based on the modulation-doped system are in good agreement with theoretical predictions (see Eq. 6.10).

6.4 Thermal drift effects

Any magnetic sensor application of micro-Hall devices to measurements with temperature variation demands a high temperature stability. Mostly, micro-Hall sensors were fabricated on modulation-doped heterostructures AlGaAs/GaAs [249], AlGaAs/GaAs/InGaAs [230, 246], InP/InGaAs [243, 244], InAlAs/InGaAs [242]. Compared to Hall sensors based on bulk materials, the key transport characteristics were improved essentially. A significantly higher 2DEG mobility can be realized by barrier doping distant from the interface. Thus, the 2D electron concentration is increased - but without rising the ionized impurity concentration at the interface itself. These devices exhibit both high absolute sensitivity and low noise. However, further attempts to higher thermal stability meet some critical difficulties.

Biasing the Hall device by a constant current (current drive mode), the thermal stability is determined by the electron concentration temperature dependence (see Eq. (2.76), Section 2.3.5). A high doping level within the AlGaAs or InAlAs barrier regions can cause additional electron concentration fluctuations due to electrical and/or thermal activation from DX centers [250]. Moreover, a heavily doped potential barrier can act as an undesirable conductive channel. In order to suppress the parallel barrier conductivity, an optimization of the barrier thickness and δ-doping instead of uniform doping were proposed by several groups [230, 246]. In voltage drive mode, i.e. Hall device biasing by constant voltage, the temperature drift is ruled by temperature dependent mobility (see Eq. (2.77), Section 2.3.5). The unavoidable strong temperature dependence of the mobility in modulation-doped heterostructures is usually due to decreased scattering on phonons and (less significant) on ionized impurities at lower temperatures.

Until now, only minor endeavors [223, 245, 251, 252] were dedicated to studies on micro-Hall devices based on doped-channel heterostructures. But using high electron drift velocity materials, these heterostructures are very promising due to very low noise, high sensitivity and excellent thermal stability.

In the following we will focus on the thermal stability optimization of doped-channel micro-Hall devices based on AlGaAs/GaAs/InGaAs heterostructures.

6.4.1 Prerequisites to thermal drift reduction

Targeting on micro-Hall devices with lowest thermal drift, one has to consider the following four key aspects: (i) an almost temperature independent position of the Fermi level with respect to the bottom of the conduction band; (ii) minimized temperature dependence of the Hall scattering factor; (iii) suppression of any undesirable parallel conductivity in the barriers by appropriate measures in structure design; and (iv) minimized trapping effects.

Designing a Hall device of high thermal stability, the uniformly doped-channel $Al_{0.3}Ga_{0.7}As$/GaAs heterojunction can serve as a reference structure. Due to detailed studies in the past, its transport properties are well known, in particular the scattering on ionized impurities [21]. Furthermore, this system is suitable for high-performance Hall devices due to the high mobility in GaAs without impurities and the almost perfect interface between GaAs and $Al_xGa_{1-x}As$ [236]. Using a doped-channel quantum well, the Hall scattering factor $r_H = 1$ is temperature independent over a wide range. A doped GaAs layer serves as the conductive channel within the device. A parallel conductivity within the undoped AlGaAs barrier is excluded, as well as any carrier generation or trapping on DX centers. However, DX centers can be created near the AlGaAs/GaAs interface in this system [245, 253]. Fortunately, they can be suppressed by a doping profile comprising 84 % of the well width [21]. The mobilities in doped quantum channels are expected to be significantly lower than in doped bulk materials (at the same doping level) or in modulation-doped heterostructures. According to [21], the quasi-two-dimensional confinement results in increased ionized-impurity scattering and therefore in decreased mobility over a wide temperature range. Furthermore, the results in [21] give a clear evidence for progressively wider GaAs wells leading to progressively higher mobilities, apparently asymptotically approaching the bulk GaAs value.

Considering the ionized-impurity scattering as the predominant mechanism at low temperatures and including degenerate statistics, the mobility vs. temperature dependence can be described by

$$\mu_{ion}(T) = e \left\langle \tau_{ion} \right\rangle / m^*, \tag{6.12}$$

where $\langle \tau_{ion} \rangle$ is the average relaxation time (see Ref. [21]), e the electron charge and m^* the electron effective mass. Accordingly, the temperature dependence of the relaxation time governs that of the mobility. Experimentally, the mobility vs.

temperature dependence is almost independent of temperature in the $100-300$ K range for n-type heavily doped semiconductors. Using this feature, one can design micro-Hall devices with minimized thermal drift under constant voltage biasing.

Certainly, any fabrication of Hall sensors with low thermal drift and high signal-to-noise sensitivity (SNS) should rely on highest possible absolute sensitivity S_A. Concluding from the relation between absolute sensitivity and electron drift velocity, materials with very high electron drift velocity are most suitable. In the preceding considerations, an InGaAs layer was already proposed as an appropriate solution. The motivation is based on high peak drift velocity for n-type InGaAs compared to n-type GaAs [52], strain enhanced low-field mobility and peak electron drift velocity and the application of a Si-δ-doping leading to higher peak velocity [23].

Without appropriate countermeasures in device design, the insertion of a pseudomorphically strained InGaAs layer could result in an enhanced thermal instability. This is due to the higher band gap GaAs material, possibly providing an undesirable conductive channel with strongly temperature dependent parasitic parallel conductivity. This problem can be prevented by a proper heterostructure device design. Therefore, preliminary calculations - based on the self-consistent solution of the Schrödinger-Poisson equations and the Fermi-Dirac statistics in

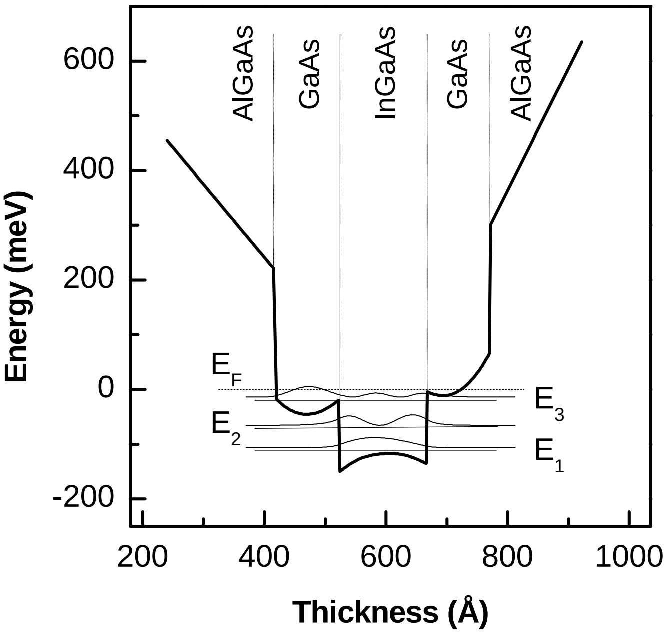

Figure 6.12: Calculated conduction band profile for a $Al_{0.3}Ga_{0.7}As/GaAs/In_{0.2}Ga_{0.8}As$ micro-Hall device at 77 K. The squared envelope functions for electrons are also shown. Distance is measured from device top surface.

the Hartree approximation - were necessary.

Correlating to an experimentally investigated structure, a representative example of calculation results is shown. Figure 6.12 presents the results at a temperature of 77 K for a 144 Å $In_{0.2}Ga_{0.8}As$ quantum well embedded into a uniformly doped GaAs channel.

Obviously, three electronic states are located below the Fermi level. At low bias currents, i.e. under low-injection condition, electrons will be distributed among these states. As indicated by the squared envelope function for the third level, an electron conductive channel is formed not only within the inserted InGaAs but also in both adjacent GaAs layers, causing the above discussed parasitic parallel conductivity. Apparently, this effect can be reduced by downsizing the GaAs layer thicknesses. Additionally, the electronic states will descend energetically with increased InGaAs thickness. Therefore, much less electrons can be redistributed to levels within the adjacent GaAs layers even at increased temperatures.

Inevitably, the Fermi level raises with increasing temperature. Then Fermi-level pinning on the states at raising temperature causes an additional thermal drift due to electron redistribution between upper and lower states. Additionally, the population of the states in GaAs increases due to redistribution from states in InGaAs. Again, parasitic conductive channels would arise from increased tem-

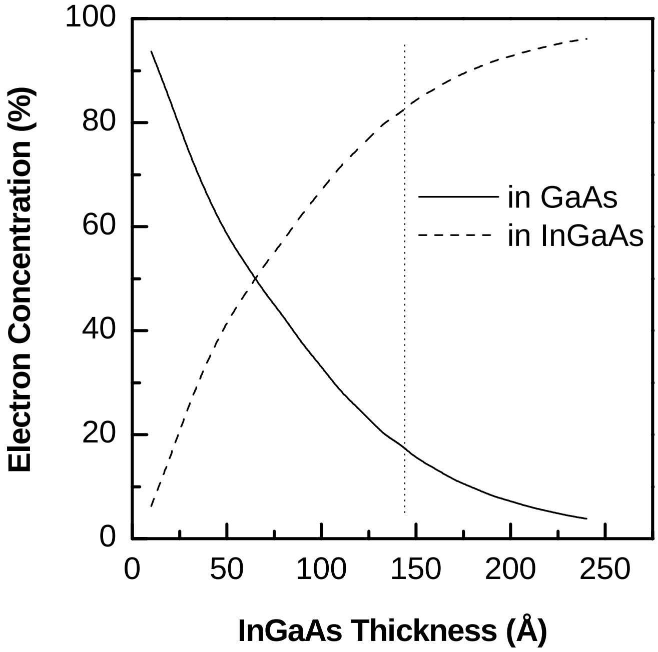

Figure 6.13: Electron population of states in GaAs and InGaAs QWs in percent of total sheet carrier density vs. InGaAs layer thickness. Thickness of InGaAs QW used in experimental studies is marked additionally by a dotted line.

peratures, too.

Finally, this interplay between the undesirable parallel conductivity in both GaAs layers and the InGaAs channel conductivity contributes significantly to thermal device instability.

For comparison purposes, we will hold a constant total quantum well thickness in the following. Accordingly, some compromise will be necessary between the InGaAs and GaAs layer thicknesses.

Figure 6.13 depicts the calculated 2D electron concentrations of GaAs and InGaAs layers normalized to the total carrier density as a function of InGaAs thickness. As expected, an increasing InGaAs layer thickness results in increasing electron concentration within the InGaAs channel itself. On the other hand, the InGaAs layer thickness will be always limited to the critical one for a given composition. For $In_{0.2}Ga_{0.8}As$, a value of about 144 Å is well below the critical thickness for our growth conditions.

6.4.2 Experimental results for doped-channel devices

Evaluating the thermal drift, both the low-field mobility and the electron concentration were measured for different samples at temperatures ranging from 77 K up to 300 K. Figure 6.14 exhibits the results for doped GaAs QW and doped

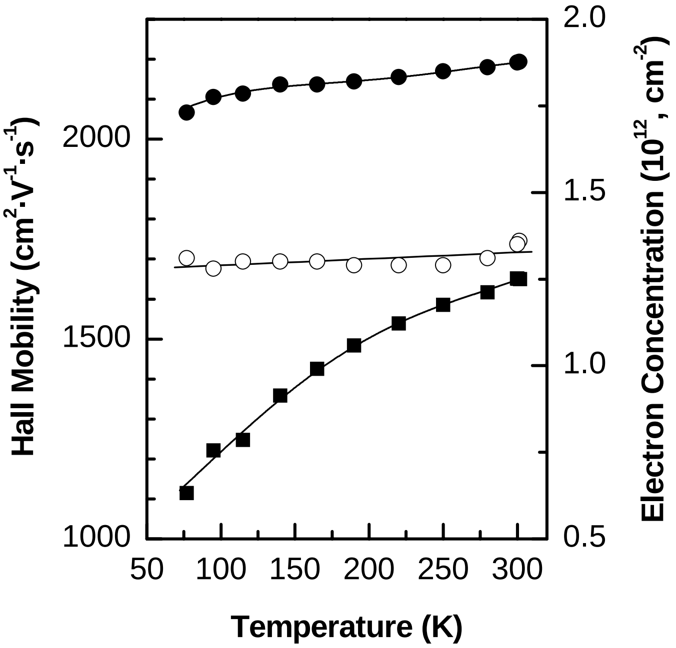

Figure 6.14: Temperature dependence of the Hall mobility [■ - GaAs QW (sample DC8); • - InGaAs/GaAs QW (sample DC9)] and sheet electron concentration [○ - InGaAs/GaAs QW (sample DC9)].

InGaAs/GaAs channel devices, respectively.

As predicted, the insertion of the strained Si-δ-doped InGaAs layer into the uniformly doped GaAs quantum well causes a significant mobility increase. At room temperature, a 25 % improvement from 1650 cm^2·V^{-1}·s^{-1} for the uniformly doped GaAs quantum well to 2193 cm^2·V^{-1}·s^{-1} for doped channel with inserted strained InGaAs layer is revealed at the same value of sheet electron concentration.

Furthermore, the mobility of the reference GaAs doped QW exhibits a perceptible mobility fall with decreasing temperature. This is an inherent feature of a heavily doped channel due to prevailing scattering on ionized impurities. As desired, the mobility of the strained structure is almost temperature independent. Due to the continuing theoretical and experimental investigations of this structure type, a really satisfying explanation can not be given at present.

Using the mobility data, the thermal drift in voltage drive mode can be estimated as

$$K_{cs,\,V} = \frac{1}{\mu_H}\frac{\partial \mu_H}{\partial T}, \tag{6.13}$$

where μ_H is the Hall mobility.

Figure 6.14 also depicts the electron concentration temperature dependence for the strained structure being rather weak. This measurement result permits

	*Sample DC*8 (reference)	*Sample DC*9 (optimized)	*Sample DC*13 (non-optimized)
Device			
channel material	GaAs	$In_{0.2}Ga_{0.8}As$	$In_{0.3}Ga_{0.7}As$
thickness d (Å)	350	144	30
square size (μm)	10 × 10	10 × 10	10 × 10
Hall measurements			
at $T = 300\ K$			
μ_e (cm^2·V^{-1}·s^{-1})	1651	2193	2046
n_e (10^{12} cm^{-2})	1.28	1.3	1.5
Thermal stability			
for $T < 300\ K$			
(in current drive mode)			
$K_{cs,I}$ (ppm·K^{-1})	358	90	654
(in voltage drive mode)			
$K_{cs,V}$ (ppm·K^{-1})	996	192	305

Table 6.2: Device characteristics for studied samples.

one to estimate the thermal drift value in current drive mode according to

$$K_{cs,\,I} = \frac{1}{n_{2D}} \frac{\partial n_{2D}}{\partial T}, \tag{6.14}$$

where n_{2D} is the equilibrium channel electron density and T the absolute temperature.

The thermal drift estimated in the 77 − 300 K temperature range differs significantly for various structures. Representative results are listed in Table 6.2.

By far the best value is found for the 144 Å InGaAs/GaAs quantum well device biased in current drive mode, being about 90 ppm$\cdot$K^{-1}. For this particular structure, we suppose a slight Fermi level shift (with respect to the bottom of conduction band) changing the electron concentration being responsible for the weak temperature drift. This valuable result supports our above considerations with respect to device optimization.

6.5 Size and geometry effects affecting the sensor parameters

The application of micro-Hall devices to measurements with high spacial resolution demands devices of miniaturized area. However, decreasing active device areas cause in part different undesirable effects: non-linearity, decreasing absolute sensitivity, increased noise level, SNS and detection limit degradation, etc. These effects are due to the extremely high electric field non-uniformly distributed in the small active device area, being partially simply unavoidable. Nevertheless, the basic micro-Hall sensor characteristics can be improved by a proper choice of the device geometry.

In the following, we consider here as a model case the micro-Hall devices based on a doped-channel $Al_{0.3}Ga_{0.7}As/GaAs/In_{0.2}Ga_{0.8}As$ heterostructure (sample DC9). The investigated devices are of the same geometry, but with different sizes of active area being 20, 10 and 5 μm square size.

Results of absolute sensitivity measurements for three different device sizes are shown in Fig. 6.15(a). The highest absolute sensitivity was measured in the device with the largest area, i.e. for 20 μm square size. The lowest value was obtained for 5 μm square size. This result is not surprising because the absolute sensitivity is proportional to device size (see Eq. 2.70). Normalizing the absolute sensitivity to the device size for the same device geometry, one would expect for all devices the same value $S_A/W \sim v$, with the electron drift velocity v. However, Fig. 6.15(b) reflects results contradicting to this assumption. Obviously, an increased device size results in lower normalized absolute sensitivity.

A similar effect was observed during I-V measurements in two-dimensional AlGaN/GaN-based conducting channels [254]. The according current-voltage

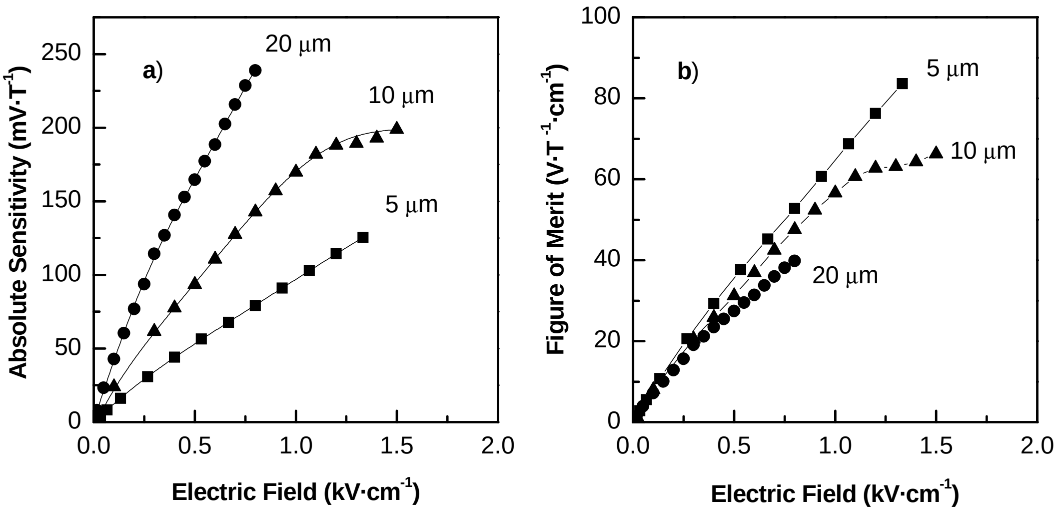

Figure 6.15: (a) Absolute sensitivities measured at room temperature for doped-channel Greek cross micro-Hall devices of different square sizes: 20, 10 and 5 μm. The geometries were the same for all three samples. (b) Size normalized absolute sensitivity vs. electric field in the active device region.

characteristics were shown to depend strongly on the channel length. At the same value of the electric field, the measured current in a conductive channel of 1 μm length was significantly higher than in a 25 μm channel. Additionally, a current saturation (or negative differential resistance) region was revealed for larger channels. These results were explained by a simple theoretical model: The Joule self-heating effect can lead to current saturation or a negative differential resistance regime. Based on this, a current reduction due to (i) hot-electron effects and (ii) channel temperature rise caused by the self-heating were distinguished. The I-V characteristics track the velocity-field characteristics. Therefore, we can conclude that the influence of channel length on the $v(E)$ characteristics will be exactly the same. The measured velocity-field characteristics will asymptotically approach the real $v(E)$ for sub-micron channels. However, thicker channels will exhibit a reduced peak velocity saturation due to self-heating effects [255]. Based on this consideration, we assume the observed difference in absolute sensitivity measurements to be not only due to size effects but also due to both self-heating and hot-electrons effects. Indeed, within the low-field region for all three devices, no difference is seen in the normalized sensitivity-field characteristics. The deviations appear at moderate electric fields, where a channel temperature increase can be supposed.

Measured noise spectra for devices of two different sizes are shown in Fig. 6.16. The measurements were done at room temperature and a bias current of 28 μA. Since the resistances of both devices are equal (the resistance depends only on the channel depth for a laterally square-sized device), the measured thermal noise

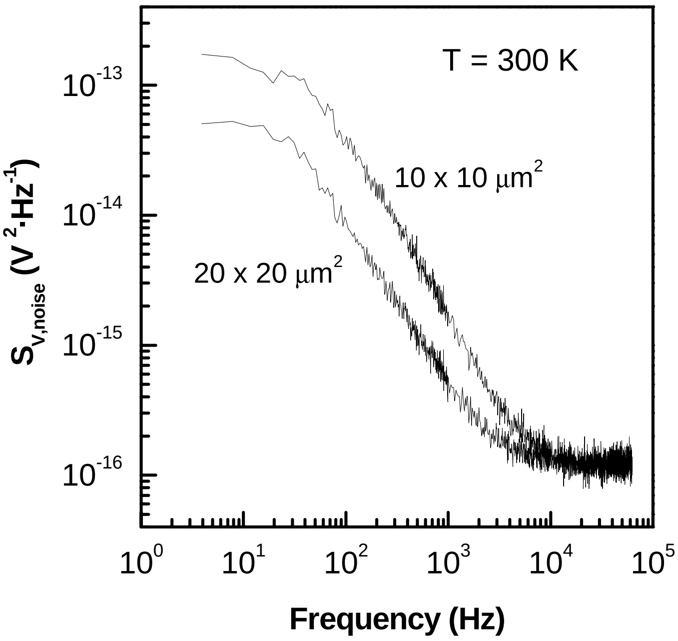

Figure 6.16: Noise spectra measured at room temperature for two devices of different sizes: 10×10 μm^2 and 20×20 μm^2.

level is the same for both sizes. However, within the low- and mid-frequency ranges, the noise spectral density differs significantly due to different electric fields in both devices. Obviously, both the generation-recombination and the flicker or $1/f$ noise are observed here.

Presuming a symmetrical Greek cross geometry, the $1/f$ noise is given by

$$S_{V,1/f} = \frac{\alpha V^2}{fN} \approx 1.2\frac{\alpha E^2}{f n_{2D}}. \tag{6.15}$$

The factor of 1.2 follows from the calculation of the number of carriers N for our Greek cross geometries. Evidently, the voltage noise spectral density for the $1/f$ noise exhibits a quadratic dependence on the applied electric field, but is independent on the lateral size. Comparing the electric field values at given bias current, the observed difference in noise spectral density was proved to follow exactly to the above Eq. (6.15). Thus, the devices being of different size exhibit the same values of the $1/f$ noise at the same low electric fields.

On the other hand, both devices deviate significantly from the Hooge law given by (6.15) at higher electric fields. Exemplary, Fig. 6.17 illustrates this for the 10 μm square size device. The measurements were done at room temperature and a frequency of 10 Hz. Conforming with Eq. (6.15), the measured increase in the noise level can result from the field induced electron concentration decrease within the quantum well due to carrier trapping on DX centers. The

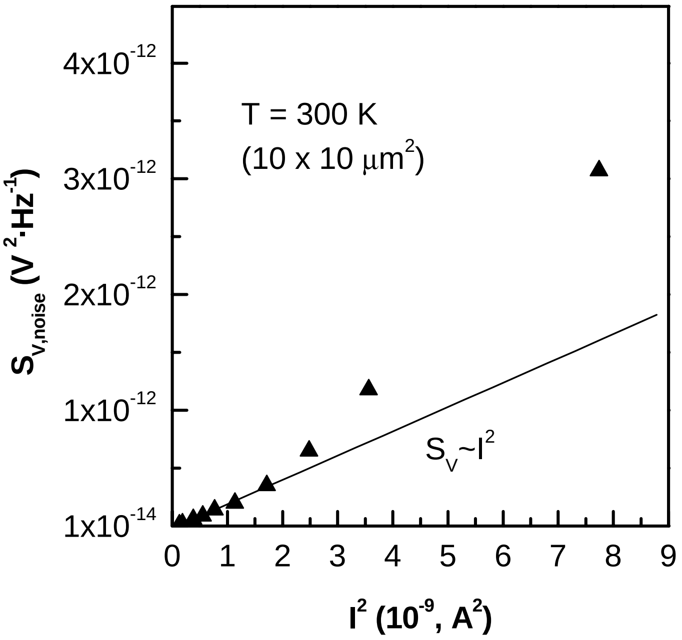

Figure 6.17: The noise spectral density as a function of the squared current, measured at 10 Hz for a 10 μm square size device. Higher fields in the active device area cause a significant deviation from the Hooge law (6.15).

carrier concentration fluctuations in the conductive channel would also cause an increased generation-recombination noise and increased differential resistance of the sample. These findings coincide well with the results of our previous DLNS (see Section 5.2.3) and SCRS (see Section 6.2.3) studies.

Measuring the noise voltage at a frequency of 65 kHz within $\Delta f = 1$ Hz bandwidth, the signal-to-noise sensitivity (SNS) can be estimated for dominating thermal noise. According to Eq. (2.73), the larger area devices exhibit a higher SNS compared to the smaller ones. Figure 6.18 represents the SNS as a function of the applied electric field and the device active area. These experimental results are in a good agreement with the preceding theoretical predictions: The SNS rises with increasing electric field, saturating at some higher electric fields.

Since the SNS scales with device geometrical sizes, it is reasonable to normalize the SNS to the device size. Therewith, we are able to compare our results with other data published in the last decade. Table 6.3 presents this overview of data.

Summarizing the above experimental results, the following conclusions can be drawn: The geometrical size of the device has a crucial influence on the device performance due to the increasing electric field within smaller active device area. This results in both hot-electron and self-heating effects being responsible for decreasing absolute sensitivity. Furthermore, the high fields are accompanied by additional generation and recombination processes within the device bulk causing

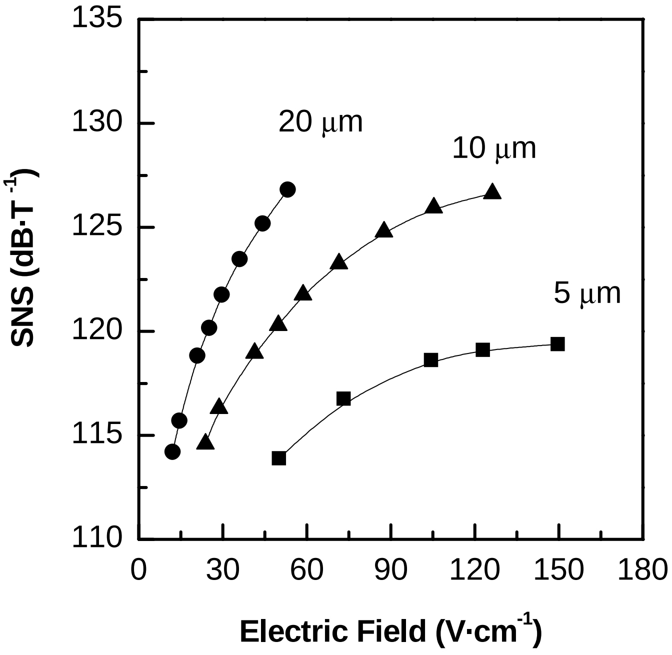

Figure 6.18: The SNS as a function of the applied electric field and device size. The measurements were performed at room temperature.

Material system	W (μm)	$SNS \cdot W^{-1}$ (dB/mm/T)	$B_{DL} \cdot W$ ($nT \cdot mm$)	Reference
modulation-doped:				
InAlAs/InGAs	200	185	12	[241]
InAlAs/InGaAs	200	152	24	[242]
AlAs/GaAs	200	204	0.2	[250]
AlGaAs/InGaAs/GaAs	100	164	6	[246]
AlGaAs/InGaAs/GaAs (sample MD28)	20	175	1.8	this work
doped-channel:				
AlGaAs/GaAs/InGaAs (sample DC13)	10	178	1.27	this work
AlGaAs/GaAs/InGaAs (sample DC9)	5	173	2.19	this work

Table 6.3: Normalized sensitivities and detection limits for studied micro-Hall devices, compared to earlier published data.

degraded stability and poor noise performance.

Until now, a uniform and homogeneous distribution of the electric field in the device bulk was assumed for the analysis. In reality, the electric field distribution in the active device region will strongly depend on the device geometry. Any field distribution inhomogeneity like field spikes will cause an additional device instability. Therefore, the device geometry has to be revised. Numerical methods are appropriate for the field distribution calculations and the required geometry optimization.

Here we applied the finite element method (FEM) in order to calculate the real distribution of the electric field within the device [256]. The distribution of the local electrostatic potential $\varphi(x, y)$ was computed in the 2D plane of a Hall element with Greek cross geometry. The elliptic partial differential equation

$$\mathrm{div}\sigma\,\mathrm{grad}\varphi = 0, \tag{6.16}$$

with the conductivity tensor σ had to be solved as a boundary value problem. Here, the Neumann-type boundary conditions were used: No current flow occurs normal to the all boundaries of the structure, except for the bias contacts. Thus, for the bias contacts we used Dirichle-type boundary conditions. Using the resulting potential $\varphi(x, y)$, the electric field distribution in the 2D plane of the Hall sensor was calculated as

$$E\,(x, y) = -\mathrm{grad}\varphi\,(x, y)\,. \tag{6.17}$$

Figures 6.19 and 6.20 illustrate the computational results for two different device geometries.

The Greek cross Hall plate with rectangular corners as shown in Fig. 6.19 is the real geometry used in our studies. The computational results indicate a very high electric field inhomogeneity at all four corners of the structure. These electric field spikes could cause carrier trapping on deep levels within the bulk device, resulting in conductivity fluctuations and accordingly higher noise level and device instability. Obviously, this result is due to the sharp rectangular corners.

Alternatively, a Greek cross geometry with rounded corners would be more suitable with respect to a desired field homogeneity. Figure 6.20 represents the according numerical results. Even though the electric field distribution also spikes at the corners, this inhomogeneity is much smaller.

Furthermore, a dependence of the peak electric field E_p on the radius r of the rounded corners has to be expected. Fig. 6.21 depicts the results of according numerical calculations. Using these computational results and denoting the contact width as w, the peak electric field at an applied voltage V can be analytically expressed as

$$\frac{E_p}{E_d} = \left[\frac{r}{w}\right]^{-0.267}. \tag{6.18}$$

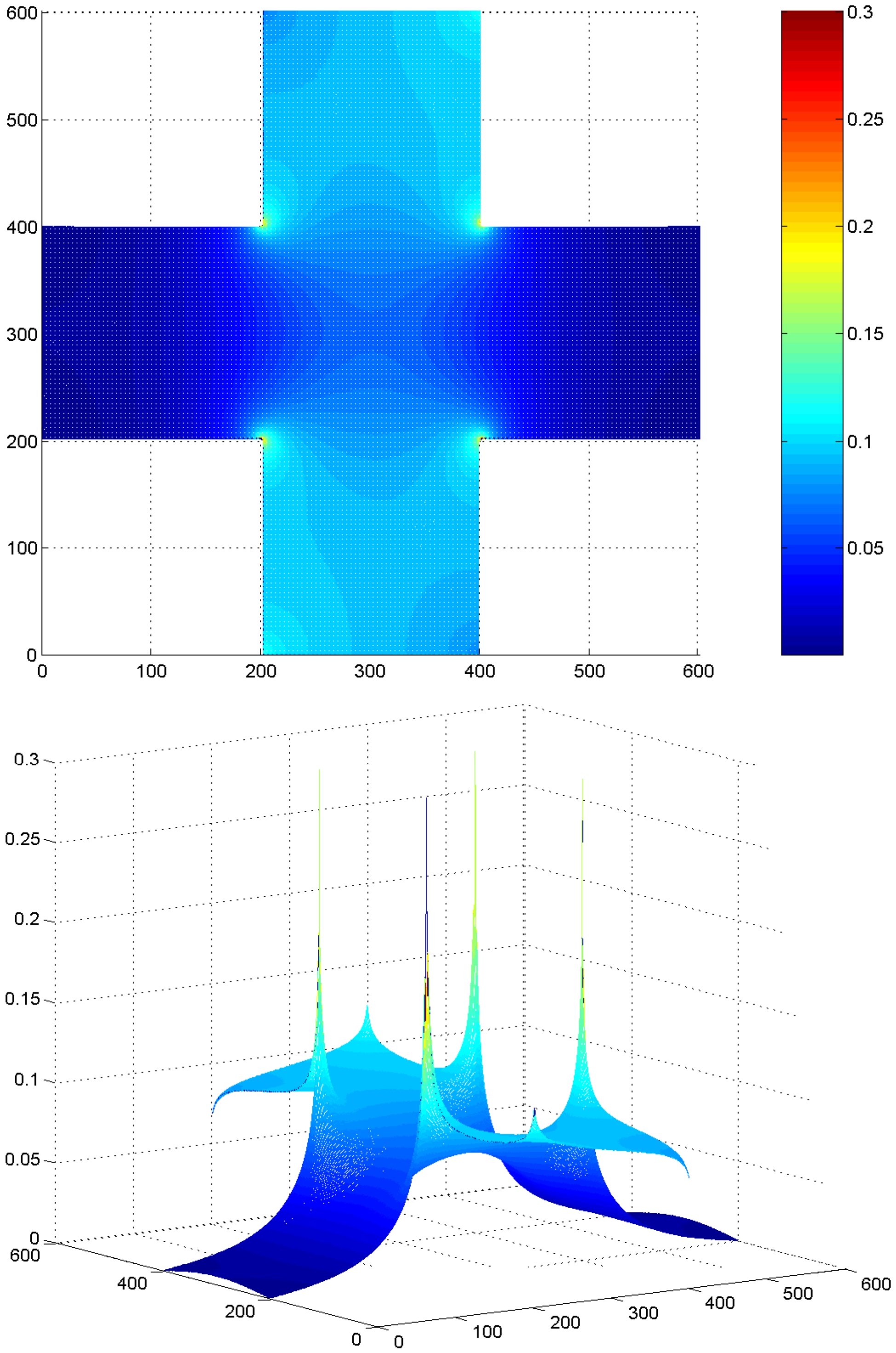

Figure 6.19: The distribution of the electric field in the active area of Greek cross micro-Hall device with rectangular corners. The 2D and 3D maps are presented. The device lateral sizes and electric field within device are expressed in arbitrary units.

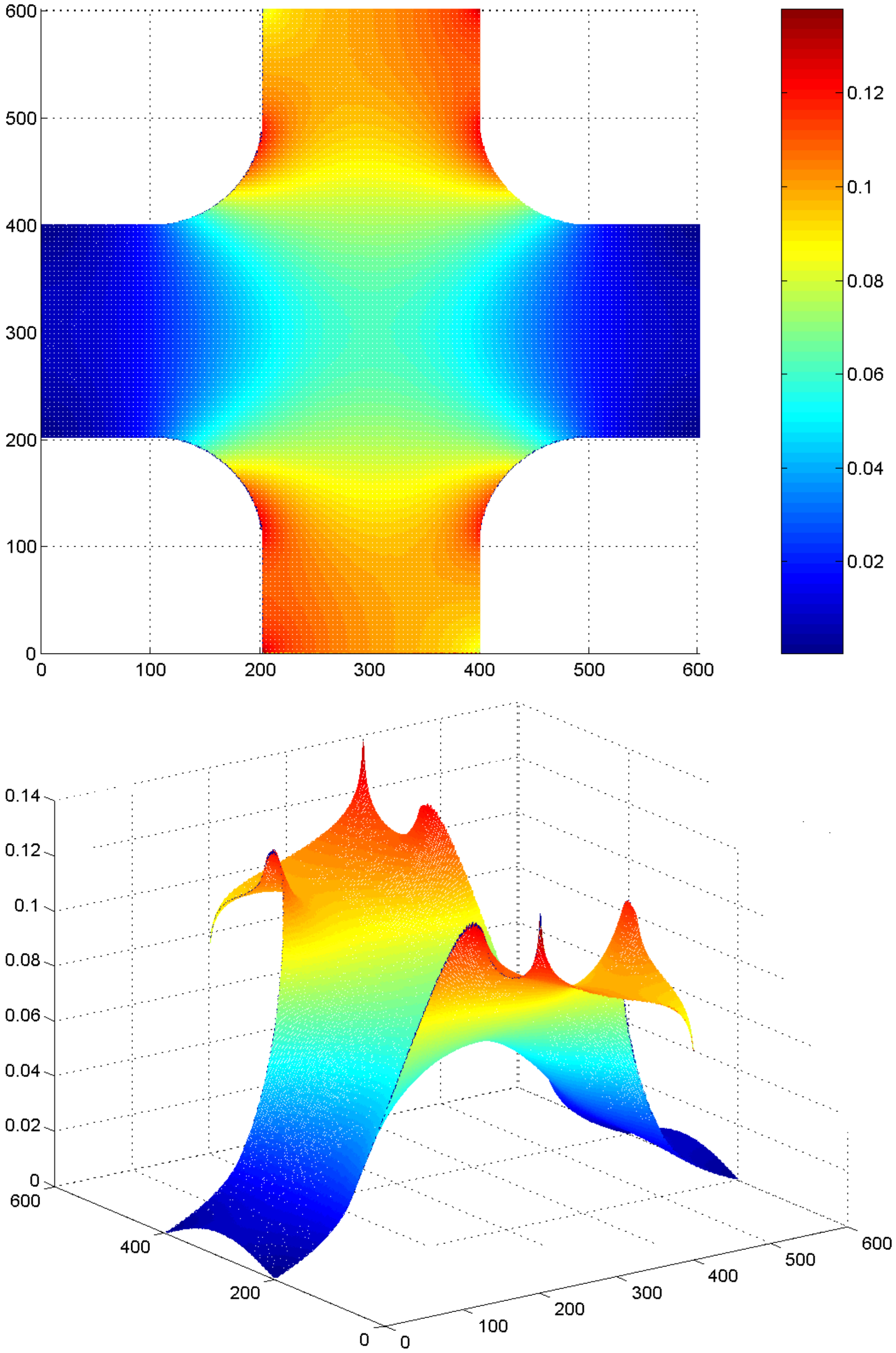

Figure 6.20: The distribution of the electric field in the active area of Greek cross micro-Hall device with rounded corners. The 2D and 3D maps are presented. The device lateral sizes and electric field within device are expressed in arbitrary units.

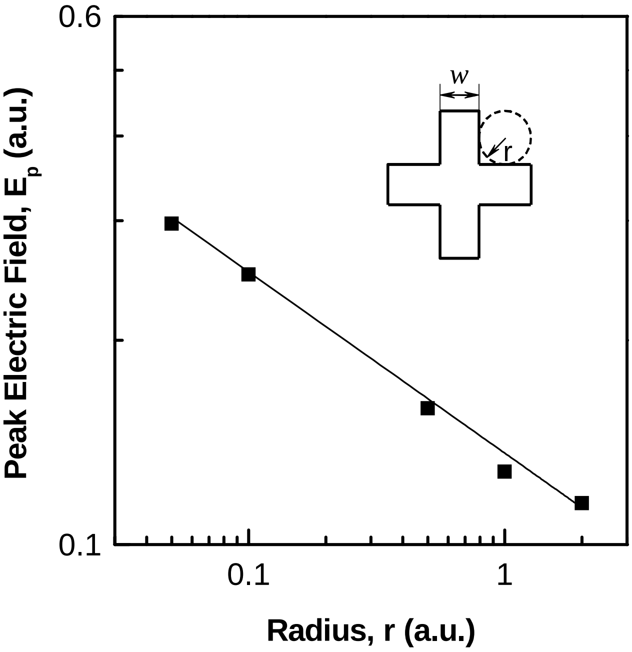

Figure 6.21: Peak electric field dependence on rounded corner radius. The solid line is a fit according to Eq. (6.18).

E_d is the electric field, for our geometry given by $E_d = V/W$ with $W = 3w$. The appropriate fit by Eq. 6.18 is shown in Fig. 6.21, too.

6.6 Conclusions

The micro-Hall devices based on doped-channel AlGaAs/GaAs, AlGaAs/GaAs/InGaAs as well as modulation-doped AlGaAs/InGaAs/GaAs heterostructures were characterized in terms of signal linearity, device sensitivity and thermal stability.

The studied micro-Hall devices exhibit a high signal linearity, being independent on temperature in the range of 77 – 300 K. The non-linearity of the doped-channel micro-Hall devices does not exceed 4 % even at electric fields higher than 1.8 kV/cm.

The study of the absolute sensitivity for doped-channel devices indicates that devices with a strained InGaAs layer exhibit a higher absolute sensitivity, compared to ones based on the lattice matched AlGaAs/GaAs system. This result coincides well with the theoretical statements in Section 3.1.1. An in-depth analysis of the supply-current-related sensitivity vs. electric field dependence greatly expands the noise studies, being helpful for a better understanding and interpretation of carrier dynamics at high electric fields. Acting as a probe of the mobility-field dependence, the supply-voltage-related sensitivity in conjunction with supply-current-related sensitivity and noise studies contributes to an understanding of the signal-to-noise sensitivity behavior at higher fields.

The device sensitivity analysis together with noise studies permits one to estimate both the signal-to-noise sensitivity and the detection limit. Signal-to-noise sensitivities were estimated at low and high frequencies. At high frequencies where thermal noise dominates and T = 300 K, the pseudomorphically strained $Al_{0.3}Ga_{0.7}As/GaAs/In_yGa_{1-y}As$ doped-channel devices exhibit signal-to-noise sensitivities of 127 dB/T and 138 dB/T for InGaAs layers with $y = 0.2$ and $y = 0.3$, respectively. The micro-Hall sensors based on modulation-doped $Al_{0.2}Ga_{0.8}As/In_{0.1}Ga_{0.9}As/GaAs$ heterostructures exhibit a better low-field signal-to-noise sensitivity of about 141 dB/T measured at room temperatures for 20 μm square size devices. However, the signal-to-noise sensitivity vs. electric field behavior is completely different for doped-channel and modulation-doped devices. Doped-channel heterostructures show no degradation of the SNS up to high electric fields. The maximum of the SNS and the lowest detection limit were reached at electric fields of about 2.4 kV/cm. On the other hand, the micro-Hall devices based on the modulation-doped system exhibit the highest SNS and the lowest detection limit at low electric fields, but degrading with increasing electric field.

Applying sensitivity and noise measurements to micro-Hall devices of different sizes, the influence of the lateral device dimensions on noise and sensitivity was analyzed. Based on numerical calculations, the electric field distribution inside the device active area was estimated. Within the studied Greek cross micro-Hall sensors, extremely high electric fields appear in the rectangular corners of the lateral structure. They can impair the noise performance of micro-Hall sensors, degrading their signal-to-noise sensitivity and detection limit, respectively. In order to refuse this problem, rounded corners were proposed for the Greek cross geometry.

Finally, thermal drift effects were studied in detail. Based on the experimental data, the parallel conductivity in the doped GaAs channel was revealed as substantially degrading the thermal stability performance. From a device modelling based on a self-consistent solution of Schrödinger-Poisson equations, we conclude that a trade-off decision between InGaAs and GaAs layer thicknesses is necessary. Considering this, for a Si-δ-doped 144 Å $In_{0.2}Ga_{0.8}As$ quantum well embedded into a uniformly doped GaAs channel, thermal drifts of 90 ppm/K in current drive mode and 192 ppm/K in voltage drive mode were achieved.

Chapter 7

Summary and outlook

Considering the electron drift velocity as the key parameter defining the most essential micro-Hall device characteristics, the III-V high electron drift velocity materials GaAs and InGaAs appear as appropriate candidates for micro-Hall device fabrication. This work was on target for micro-Hall devices of high sensitivity, low noise and reduced thermal drift for operation at high electric fields. The studies were restricted to two different heterosystems: AlGaAs/GaAs and AlGaAs/GaAs/InGaAs with doped-channel as well as modulation-doped AlGaAs/InGaAs/GaAs.

All investigated heterostructures were grown by gas-source molecular-beam epitaxy in a ISA-RIBER 32-P facility. To optimize the strained layer epitaxy, reflection high energy electron diffraction and x-ray measurements as well as optical and transport techniques were applied.

Using standard optical photolithography, Greek cross micro-Hall devices of 20, 10 and 5 μm square sizes were fabricated on both doped-channel and modulation-doped heterostructures with further Au/Ge/Ni metallization [172]. The contact specific resistivity as related to the quality of the metal-semiconductor interface was optimized by an in-depth investigation of the thermal annealing conditions and characterized in the frame of the transmission line model. The performed studies agree well with earlier results reported on n-type GaAs in contact with Au/Ge/Ni metal films.

The processed micro-Hall devices were investigated within a wide range of electric fields and compared in terms of signal linearity, sensitivity and noise. The results reveal the doped-channel quantum well devices at high electric fields to be superior to the high mobility structures. They exhibit an excellent signal linearity even at electric fields higher than 1.8 kV/cm. Furthermore, the use of a pseudomorphically strained InGaAs layer results in better sensor performance than does GaAs. The strained Si-δ-doped quantum well AlGaAs/GaAs/InGaAs micro-Hall devices exhibit much higher sensitivities compared to uniformly doped-channel AlGaAs/GaAs devices at the same electron concentration within the channel. This results from the following premises: (1) usage of InGaAs material with higher electron drift velocity; (2) induced strain due to lattice misfit; and (3) properly designed doping profile. Furthermore, the strained doped-channel quantum well devices exhibit a significantly lower $1/f$ noise compared to the lattice-matched structures. A lowest detection limit of 127 nT at a frequency of 100 kHz was determined with no degradation up to 2.4 kV/cm; this value represents the best reported at such high electric fields up to now. This observed advantage was ascribed to the high-field behavior of both mobility and electron concentration in structures with dominant scattering on ionized impurities.

Regardless of significantly improved Hall absolute sensitivity and better noise performance of doped-channel quantum well devices with pseudomorphic InGaAs, the thermal drift can be intolerably high due to parallel conductivity within the doped GaAs channel. In-depth studies based on numerical calculations of self-consistent solutions of the coupled Schrödinger-Poisson equations show that a trade-off decision is necessary between InGaAs and GaAs layer thicknesses. At a fixed total thickness of the GaAs/InGaAs channel, the pseudomorphic InGaAs layer has to be thick as possible. An optimized structure regrowth allowed to obtain very low thermal drifts of 90 ppm/K in current-drive mode and 192 ppm/K in voltage drive mode, respectively. These values belong to the best currently reported data on micro-Hall devices based on the AlGaAs/GaAs/InGaAs heterosystem.

Besides, the optical techniques like photoluminescence spectroscopy and Raman scattering revealed the disorder in the strained InGaAs layers due to In content fluctuations resulting in fluctuations of the valence and conduction band potentials, respectively. This can degrade the $1/f$ noise performance of micro-Hall devices due to an additional electron scattering on potential imperfections causing local mobility fluctuations.

Four different and distinct optical measurements reveal the disorder degree to decrease significantly for thick pseudomorphic InGaAs layers and to increase for thinner strained layers:

(1) The PL line width and shape probe the spread of the hole wave function in k-space and therefore its localization in real space resulting from the disorder potential fluctuations.

(2) The correlation length derived from the frequency and width of the GaAs-like LO phonon mode originating from the InGaAs indicates in-plane disorder.

(3) The degree of asymmetry of the LO phonon also shows disorder as a function of the InGaAs well width.

(4) The disorder activated longitudinal acoustic phonon mode observed as a peak at $\nu = 160$ cm^{-1} in Raman spectra occurs only in thinner InGaAs layers.

Thus, the insertion of a thick pseudomorphic InGaAs layer results in improved micro-Hall sensor characteristics like sensitivity, noise and thermal stability.

Admittedly, the epitaxial growth of strained layers near the critical layer thickness can be accompanied by defect nucleations. To examine the layer quality, the deep level noise spectroscopy was applied for probing deep levels in semiconductor heterostructures as a very sensitive and direct method requiring no structure overgrowth or other additional device preparation.

Two different deep centers were detected, degrading not only the noise performance but also the thermal stability of the micro-Hall elements.

One of these levels was observed in both doped-channel and modulation-doped heterostructures. Within both systems, the same emission activation energy of about 470 meV was found. This level was ascribed to DX centers acting as an additional source of generation-recombination noise. Within doped-channel heterostructures, these defects are located at the AlGaAs/GaAs heterointerface. They can be avoided by δ-doping in the middle of the quantum well, on its side enhancing the device sensitivity due to higher peak electron drift velocity. Additionally, the lowest noise is found with this doping profile [113]. However, within modulation-doped heterostructures with the doping usually realized in the high band gap material, the creation of DX centers is almost unavoidable during the AlGaAs layer epitaxy with Si dopant. Even for an Al composition of 20 %, the DX center acts as a metastable level degrading the device performance. The other center with an emission activation energy of 242 meV was observed only in the modulation-doped heterostructures. The nature and origin of this level is not clearly evidenced yet. However, I tend to the assumption that it is probably related to point-like defects within the InGaAs layer. An acceptance of this suspicion needs further investigation and clarification efforts, of course.

Additionally, the low frequency noise technique accompanied by optical and transport studies can successfully probe the crystal quality of MBE grown structures of any dimensionality. Therefore, low frequency noise studies will be also applicable to 1D heterostructures, probing not only the system anisotropy but also its quality by an evaluation of the defects in the [110] and $[\bar{1}10]$ crystallographic directions independently.

The effect of the device scaling on its sensitivity and noise properties was studied. These studies indicate both the signal-to-noise sensitivity and the detection limit as size-dependent. Out of it, a comparison of the achieved device characteristics to the results available in the literature has to be done with respect to device sizes. A detection limit of $1.3\ \mathrm{nT} \cdot \mathrm{mm} \cdot \mathrm{Hz}^{-1/2}$ is found for the doped-channel devices based on the $\mathrm{Al}_{0.3}\mathrm{Ga}_{0.7}\mathrm{As/GaAs/In}_{0.3}\mathrm{Ga}_{0.7}\mathrm{As}$ heterostructure at an applied electric field of 2.4 kV/cm and room temperature. Comparatively, the modulation-doped devices exhibit a detection limit of $340\ \mathrm{pT} \cdot \mathrm{mm} \cdot \mathrm{Hz}^{-1/2}$ at low fields and $\mathrm{T} = 77$ K, substantially degrading with increasing electric field. These device characteristics are competitive to the best reported results on micro-Hall sensors.

Applying numerical simulations, the geometry effects for Greek cross shaped micro-Hall devices were studied. The data indicate the currently used Greek cross shape with rectangular corners as not optimal due extremely high electric field spikes in all four corners. Projecting the geometry with rounded corners, these undesirable field spikes can be clearly eliminated. Such geometries should be a subject of future studies and can be easily realized by advanced electron beam lithography.

Although this work was restricted to AlGaAs/GaAs and AlGaAs/GaAs/InGaAs doped-channel as well as AlGaAs/InGaAs/GaAs modulation-doped heterostructures, the conclusions outlined here should be applicable to other systems like InAlAs/InGaAs and InAlAs/InGaAs/InAs grown on InP. They are also valid for the promising antimonide based structures like AlGaSb/InAs with extremely high mobilities measured at room temperature for Si-δ-doping centered in the InAs quantum well [251]. Thus, the absolute magnetic sensitivities can be significantly improved, resulting in excellent detectivity even very low magnetic fields.

Appendix A

Levinshtein-Rumyantsev noise theory

Levinshtein and Rumyantsev [68] proposed a method for the local level parameter extraction from noise spectroscopic data. In case of electron capture cross sections σ_n depending exponentially on temperature like $\sigma_n = \sigma_0 \exp\left(-E_1/k_B T\right)$, the activation energy E_1, the ionization energy E_0, the trap density N_t and the electron capture cross section σ_n itself can be estimated. In the following, a brief overview of this noise theory - being applicable to noise studies of micro-Hall devices - is given.

We consider a n-type crystal containing a shallow donor level of a concentration N_d exceeding the concentration of all other levels. Furthermore, the shallow donors are supposed to be fully ionized ($n_0 \simeq N_d$ and E_F is below E_d). The position of the Fermi level is determined by

$$E_F = k_B T \ln\left(\frac{N_c}{N_d}\right). \tag{A.1}$$

Here k_B is the Boltzmann constant, T the absolute temperature and N_c the effective density of states for electrons. According to [174], the density of states for a bulk material can be written as

$$N_c \equiv 2\left(\frac{2\pi m_{de} k_B T}{h^2}\right)^{3/2} M_c. \tag{A.2}$$

m_{de} is the density-of-state effective mass, h the Planck constant and M_c the number of equivalent minima in the conduction band. The existence of a deep level with a concentration N_t and an ionization energy E_0 is assumed.

The relative spectral noise density S is given by [84, 257]

$$S = \frac{S_{V,noise}}{V^2} = \frac{S_{I,noise}}{I^2} = A\frac{\tau F(1-F)}{1+(\omega\tau)^2}. \tag{A.3}$$

Here R is the sample resistance, I the current and V the voltage, $S_{V,noise}$ the noise voltage spectral density and $S_{I,noise}$ the noise current spectral density. The factor $A = 4N_t/V_0N_d^2$ depends on the sample volume V_0. The time constant τ is expressed as a combination of emission and capture time constants via

$$\frac{1}{\tau} = \frac{1}{\tau_e} + \frac{1}{\tau_c} = \frac{1}{\tau_c F}. \tag{A.4}$$

Here τ_e is the emission time and τ_c the capture time constant given by $\tau_c = 1/\sigma v_T n_0$. The level occupancy F is given by

$$F = \frac{1}{1 + \exp\left[(E_F - E_0)/k_BT\right]}. \tag{A.5}$$

The energy is measured down from the conduction band bottom. For a capture cross section depending exponentially on the temperature, the capture time constant can be expressed via

$$\tau_c = \tau_{c0} \exp\left(\frac{E_1}{k_BT}\right), \tag{A.6}$$

where $\tau_{c0} = 1/\sigma_0 v_T n_0$.

Thus, Eq. (A.3) can be rewritten as

$$S = A\frac{\tau_{c0}\exp\left(E_1/k_BT\right)F^2\left(1-F\right)}{1+\omega^2\tau_{c0}^2\exp\left(2E_1/k_BT\right)F^2}. \tag{A.7}$$

Here, two marginal cases can be considered: 1) the Fermi level is located below the trap level, i.e. $(E_F - E_0) \gg k_BT$; or 2) the Fermi level lies above the trap level over the whole temperature range $(E_0 - E_F) \gg k_BT$. We annotate here that in our studies we measure the energy in opposite direction: for the first case we consider $(E_0 - E_F) \gg k_BT$ and $(E_F - E_0) \gg k_BT$ for the second.

1) *The Fermi level is below the trap level over the whole temperature range of measurements:*$E_F - E_0 \gg k_BT$.

Assuming $E_F - E_0$ being not less than several k_BT even at the lowest temperature, the level occupancy F is approximately

$$F \simeq \frac{N_d}{N_c}\exp\left(\frac{E_0}{k_BT}\right) \ll 1. \tag{A.8}$$

Using the new variable $\tau_1 = \tau_{c0}N_d/N_c$, the relative noise spectral density S (see Eq. A.7) can be modified as

$$S = \frac{A}{\tau_{c0}}\frac{\tau_1^2\exp\left[(2E_0+E_1)/k_BT\right]}{1+\omega^2\tau_1^2\exp\left[(2E_0+2E_1)/k_BT\right]}. \tag{A.9}$$

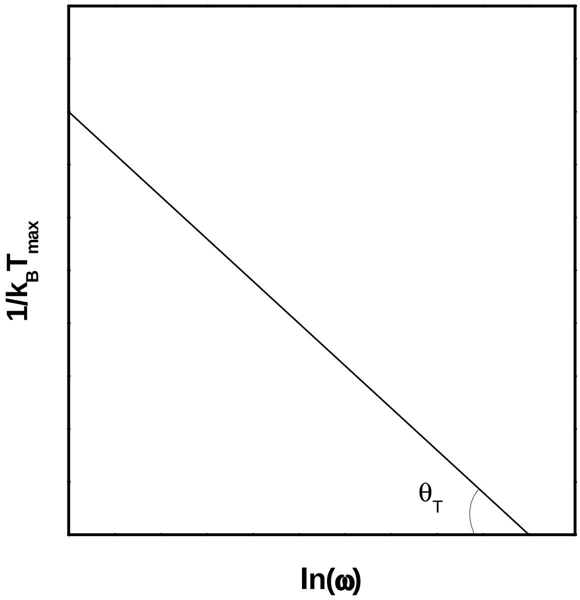

Figure A.1: Schematic Arrhenius plot representation: The value $1/k_BT$ as a function of $\ln(\omega)$ used for the determination of the activation energy E_1. For the Fermi level below the trap level one has $1/\tan(\theta_T) = E_0 + E_1$, and $1/\tan(\theta_T) = E_1$ for the Fermi level located above the trap level E_0 over the whole temperature range.

The temperature dependencies of the time constants τ_1 and τ_{c0} as well as of the thermal velocity v_T and the effective density of states N_c are neglected here.

In order to determine the temperature T_{max} corresponding to the maximum $S(T)$ at a fixed frequency ω, the extremal value problem resulting from Eq. (A.9) - with respect to T - has to be solved. The according solution can be written as

$$\frac{1}{k_B T_{\max}} = \frac{1}{2\,(E_0 + E_1)} \ln \frac{2E_0 + E_1}{E_1 \tau_1^2} - \frac{1}{E_0 + E_1} \ln \omega. \tag{A.10}$$

From (A.10) one concludes that the slope of $1/k_BT$ versus $\ln\omega$ depends on the sum $E_0 + E_1$ (Fig. A.1).

Using Eqs. (A.10) and (A.9), the maximum value of relative noise spectral density S_{max} is found as

$$S_{\max} = \frac{A}{\tau_{c0}} \frac{\tau_1^2 \left[(2E_0 + E_1)/\omega^2 \tau_1^2 E_1\right]^{(2E_0+E_1)/(2E_0+2E_1)}}{1 + (2E_0 + E_1)/E_1}. \tag{A.11}$$

The expression in (A.11) can be rewritten in the form

$$\ln S_{\max} = \text{const} - \frac{2E_0 + E_1}{E_0 + E_1} \ln \omega \tag{A.12}$$

with the activation energy E_1 and the ionization energy E_0.

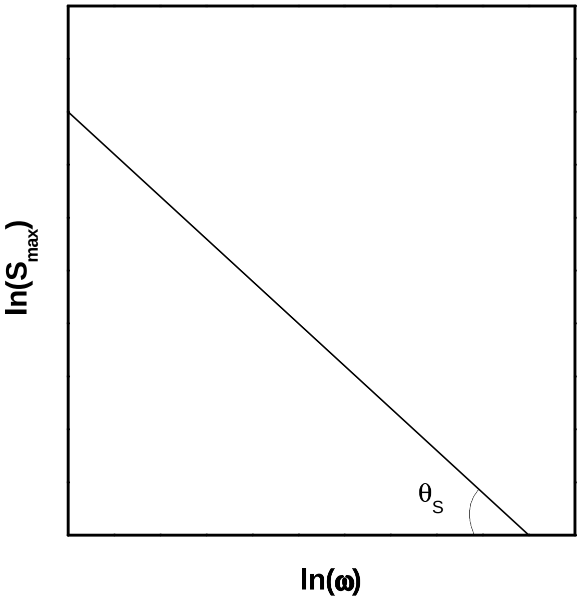

Figure A.2: Plot of $\ln S_{max}$ versus $\ln\omega$ used for determination an ionization energy E_0 and position of the Fermi level.

A corresponding plot of the $\ln(S_{max})$ versus $\ln(\omega)$ dependence (see Fig. A.2) estimates the Fermi level position with respect to the trap level. Under distinct conditions, it allows to establish the relation between E_1 and E_0:

(i) For $E_1 \ll E_0$, the $\ln S_{max}$ versus $\ln\omega$ plot is a straight line with a slope of about 2 (i.e. $\ln S_{max} \sim 1/(\ln\omega)^2$). Neglecting the temperature dependence of σ, the ionization energy E_0 can be calculated from the slope of $1/k_B T_{max}$ versus $\ln\omega$.

(ii) For $E_1 \simeq E_0$, both the activation energy E_1 and the ionization energy E_0 can be easily estimated from the slopes $\tan(\theta_T) = 1/(E_0 + E_1)$ and $\tan(\theta_S) = (2E_0 + E_1)/(E_0 + E_1)$ via the expressions

$$E_1 = \frac{2 - \tan(\theta_S)}{\tan(\theta_T)} \quad \text{and} \quad E_0 = \frac{\tan(\theta_S) - 1}{\tan(\theta_T)} \tag{A.13}$$

(iii) For $E_1 \gg E_0$, the slope of $\ln S_{max}$ versus $\ln\omega$ plot is close to one. This is the most unfavorable situation for an E_0 estimate.

One meets a very valuable situation when the $S(T)$ dependencies cannot be plotted over a suitable frequency range. Then the half width δ of the maximum $S(1/T)$ dependency provides additional information about the local trap parameters (see Fig. A.3). Differentiating (A.9) twice with respect to $(1/T)$, one

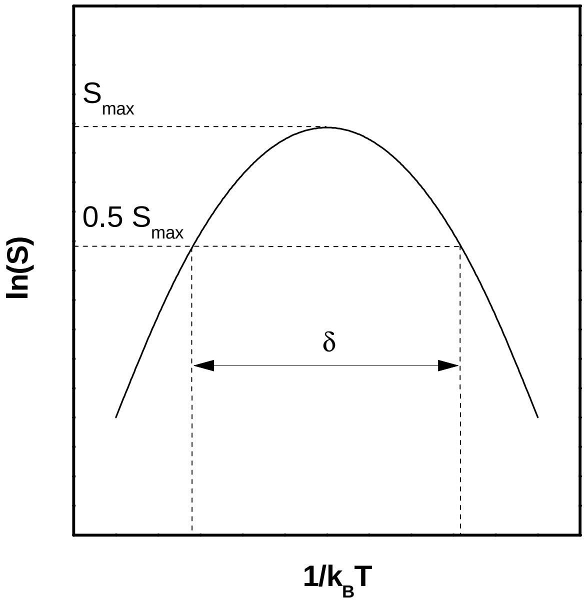

Figure A.3: The Arrhenius plot of the noise spectral density lnS_{max} versus $1/k_BT$ at fixed measurement frequency f. δ represents the full width at half maximum value.

gets

$$\left.\frac{\mathrm{d}^2 S}{\mathrm{d}\left(1/k_B T\right)^2}\right|_{\max} = -E_1\left(2E_0 + E_1\right) S_{\max}. \tag{A.14}$$

Within the $1/k_BT$ coordinates, δ is expressed as

$$\delta = \frac{2}{\sqrt{E_1\left(2E_0 + E_1\right)}}. \tag{A.15}$$

Obviously, δ does not depend on the frequency f at all. According to (A.14), the activation energy E_1 can be calculated at a given E_0 from the $S(T)$ dependence measured at a single frequency f. If the energies E_0 and E_1 are known, the time constants τ_1 and τ_{c0} at any frequency f can be calculated from Eq. (A.10) with

$$\tau_1 = \left(\frac{2E_0 + E_1}{E_1\omega^2}\right)^{1/2} \exp\left(-\frac{E_0 + E_1}{k_B T_{\max}}\right) \tag{A.16}$$

and the electron capture cross section σ_0 can be estimated via

$$\sigma_0 = \frac{1}{\tau_{c0} v_T n_0}. \tag{A.17}$$

Using Eq. (A.9) for the calculation of the constant A at a given electron concentration N_d and sample volume V_0, the trap concentration in the bulk of the semiconductor is provided by the expression

$$N_t = \frac{1}{4} A V_0 N_d^2. \tag{A.18}$$

2) *The Fermi level is located above the trap level within the whole measurement temperature range*: $E_0 - E_F \gg k_B T$.

Then the approximations

$$\begin{gathered} F^2 \simeq 1 \\ 1 - F \simeq \exp\left(\tfrac{E_F - E_0}{k_B T}\right) \simeq \tfrac{N_c}{N_d} \exp\left(-\tfrac{E_0}{k_B T}\right) \end{gathered} \tag{A.19}$$

hold true. Accordingly, the relative noise spectral density is given by

$$S = A\tau_{c0} \frac{N_c}{N_d} \frac{\exp\left[(E_1 - E_0)/k_B T\right]}{1 + \omega^2 \tau_{c0}^2 \exp\left(2E_1/k_B T\right)}. \tag{A.20}$$

For $E_1 < E_0$, the relative noise spectral density S increases monotonously with the temperature at any f. Hence, if the cross section does not depend exponentially on temperature ($E_1 = 0$) and E_F is above E_0, the dependence $S(T)$ has no maxima at all.

For $E_1 > E_0$, the dependence $S(T)$ has a maximum. The activation energy E_1 can be directly estimated from the $1/k_B T_{max}$ versus lnω Arrhenius plot as

$$\tan(\theta_T) = \frac{1}{E_1}. \tag{A.21}$$

Following a procedure similar to the above described, the maximum noise density at $T = T_{max}$ can be estimated via

$$S_{\max} = A\tau_{c0} \frac{N_c}{N_d} \frac{\left(a/\omega^2 \tau_{c0}^2\right)^{(E_1 - E_0)/2E_1}}{1 + a}, \tag{A.22}$$

where $a = (E_1 - E_0)/(E_1 + E_0)$.

The slope of lnS_{max} as a function of lnω is defined by $\tan(\theta_S) = (E_1 - E_0)/E_1$. The $\tan(\theta_S)$ values can range from zero ($E_1 = E_0$) to unity ($E_1 \gg E_0$).

Thus, the activation E_1 and ionization E_0 energies can be written as

$$E_1 = \frac{1}{\tan(\theta_T)} \quad \text{and} \quad E_0 = \frac{1 - \tan(\theta_S)}{\tan(\theta_T)}. \tag{A.23}$$

The half width of the maximum value - expressed in $1/k_B T$ coordinates - is

$$\delta = \frac{2}{\sqrt{E_1^2 - E_0^2}}. \tag{A.24}$$

For given E_1 and E_0 values, the time constant τ_{c0} can be calculated at any frequency f:

$$\tau_{c0} = \frac{1}{\omega}\left(\frac{E_1 - E_0}{E_1 + E_0}\right)^{1/2} \exp\left(-\frac{E_1}{k_B T_{\max}}\right). \tag{A.25}$$

The electron capture cross section σ_0 and trap concentration can be calculated at a given A. The amplitude A can be obtained from Eq. (A.22).

Bibliography

[1] E.H. Hall, *On a new action of the magnet on electric current*, Am. J. Math. **2**, 287–292 (1879).

[2] H.L. Störmer, A.C. Gossard, W. Wiegmann, K. Baldwin, *Dependence of electron mobility in modulation-doped GaAs-(AlGa)As heterojunction interfaces on electron density and Al concentration*, Appl. Phys. Lett. **39** (11), 912–914 (1981).

[3] J.C.M. Hwang, A. Kastalsky, H.L. Störmer, V.G. Keramidas, *Transport properties of selectively doped GaAs-(AlGa)As heterostructures grown by molecular beam epitaxy*, Appl. Phys. Lett. **44** (8), 802–804 (1984).

[4] G. Weimann, W. Schlapp, *Molecular beam epitaxial growth and transport properties of modulation-doped AlGaAs-GaAs heterostructures*, Appl. Phys. Lett. **46** (4), 411–413 (1985).

[5] H. Morkoç, P.M. Solomon, *The HEMT: A superfast transistor*, IEEE Spectrum **21** (2), 28–35 (1984).

[6] V. Mosser, S. Aboulhouda, J. Denis, S. Contreras, Ph. Lorenzini, F. Kobbi, J.L. Robert, *High-performance Hall sensors based on III-V heterostructures*, Sens. Actuators A **42** (1-3), 450–454 (1994).

[7] Y. Sugiyama, *Recent progress on magnetic sensors with nanostructures and applications*, J. Vac. Sci. Technol. B **13** (3), 1075–1083 (1995).

[8] A. Oral, S.J. Bending, M. Henini, *Scanning Hall probe microscopy of superconductors and magnetic materials*, J. Vac. Sci. Technol. B **14** (2), 1202–1205 (1996).

[9] A.M. Chang, H.D. Hallen, L. Harriot, H.F. Hess, H.L. Kao, J. Kwo, R.E. Miller, R. Wolfe, J. van der Ziel, T.Y. Chang, *Scanning Hall probe microscopy*, Appl. Phys. Lett. **61** (16), 1974–1976 (1992).

[10] A. Mosser, H.J. Hug, I. Parashikov, B. Stiefel, O. Fritz, H. Thomas, A. Varatoff, H.-J. Güntherodt, P. Chaudhari, *Observation of single vortices condensed into a vortex-glass phase by magnetic force microscopy*, Phys. Rev. Lett. **74** (10), 1847–1850 (1995).

[11] L.T. Kuhl, A.K. Geim, J.G.S. Lok, P. Hedegard, K. Ylänen, J.B. Jensen, E. Johnson, P.E. Lindelof, *Magnetization of isolated single crystalline Fe-nanoparticles by a ballistic Hall micro-magnetometer*, Eur. Phys. J. D **10** (2), 259–263 (2000).

[12] Y. Li, P. Xiong, S. von Molnár, S. Wirth, Y. Ohno, H. Ohno, *Hall magnetometry on a single iron nanoparticles*, Appl. Phys. Lett. **80** (24), 4644–4646 (2002).

[13] S. Wirth, S. von Molnar, *Hall cross scaling and its application to measurements on nanometer-size iron particle arrays*, Appl. Phys. Lett. **76** (22), 3283–3285 (2000).

[14] M. Charalambous, R.H. Koch, W.T. Masselink, T. Doany, C. Feild, F. Holtzberg, *Subpicovolt resolution measurements of the current-voltage characteristics of twinned crystalline $YBa_2Cu_3O_{7-x}$: new evidence for vortex-glass phase*, Phys. Rev. Lett. **75** (13), 2578–2581 (1995).

[15] E. Zeldov, D. Majer, M. Konczykowski, V.B. Geshkenbein, V.M. Vinokur, H. Shtrikman, *Thermodynamic observation of first-order vortex-lattice melting transition in $Bi_2Sr_2CaCu_2O_8$*, Nature **375**, 373–376 (1995).

[16] A.K. Geim, S.V. Dubonos, I.V. Grigorieva, K.S. Novoselov, V.A. Peeters, V.A. Schweigert, *Non-quantized penetration of magnetic field in the vortex state of superconductors*, Nature **407**, 55–57 (2000).

[17] G. Boero, P.A. Besse, R. Popovic, *Hall detection of magnetic resonance*, Appl. Phys. Lett. **79** (10), 1498–1500 (2001).

[18] R.E. Dunin-Borkowski, M.R. McCartney, R.B. Frankel, D.A. Bazylinski, M. Posfai, P.R. Buseck, *Magnetic microstructure of magnetotactic bacteria by electron holography*, Science **282** (5395), 1868–1870 (1998).

[19] J.L. Kirschvink, *Homing in on vertebrates*, Nature **390**, 339–340 (1997).

[20] R.B. Proksch, T.E. Schäffer, B.M. Moskowitz, E.D. Dahlberg, D.A. Bazylinski, R.B. Frankel, *Magnetic force microscopy of the submicron magnetic assembly in a magnetotactic bacterium*, Appl. Phys. Lett. **66** (19), 2582–2584 (1995).

[21] W.T. Masselink, *Ionized-impurity sacttering of quasi-two-dimensional quantum-confined carriers*, Phys. Rev. Lett. **66** (11), 1513–1516 (1991).

[22] M.B. Das, W. Kopp, H. Morkoç, *Determination of carrier saturation velocity in short-gate-length modulation-doped FET's*, IEEE Electron Device Lett. **EDL-5**, 446–449 (1984).

[23] W.T. Masselink, *High-differential mobility of hot electrons in delta-doped quantum wells*, Appl. Phys. Lett. **59** (6), 694–696 (1991).

[24] F.N. Hooge, *1/f noise sources*, IEEE Trans. Electron Devices **41** (11), 1926–1935 (1994).

[25] K. Ploog, in: *Crystals: Growth, Properties and Applications,* H.C. Freyhardt, editor, volume 3, Springer-Verlag, Berlin (1980).

[26] L.L. Chang, in: *Handbook of Semiconductors,* T.S. Moss, editor, volume 3, North-Holland Publ., Amsterdam (1980).

[27] P.D. Dapkus, *Metalorganic chemical vapor deposition*, Annu. Rev. Mater. Sci. **12**, 243–269 (1982).

[28] S.D. Hersee, J.P. Duchemin, *Low-Pressure chemical vapor deposition*, Annu. Rev. Mater. Sci. **12**, 65–80 (1982).

[29] H. Kinoshita, H. Fujiyasu, *$PbTe$-$Pb_{1-x}Sn_xTe$ superlattices prepared by a hot wall technique*, J. Appl. Phys. **51** (11), 5845–5846 (1981).

[30] D.C. Tsui, R.A. Logan, *Observation of two-dimensional electrons in LPE-grown $GaAs$-$Al_xGa_{1-x}As$ heterojunctions*, Appl. Phys. Lett. **35** (2), 99–101 (1979).

[31] G. Bastard, J. A. Brum, R. Ferreira, *Electronic states in semiconductor heterostructures*, in: Solid State Physics, volume 44, Academic press (1991).

[32] G. Bastard, *Superlattice band structure in the envelope function approximation*, Phys. Rev. B **24** (10), 5693–5697 (1981).

[33] A. Fasolino, M. Altareli, in: Solid-State Science, volume 59, Springer Series (1984).

[34] J.M. Luttinger, *Quantum theory of cyclotron resonance in semiconductors: General theory*, Phys. Rev. **102** (4), 1030–1041 (1956).

[35] D.K. Ferry, S.M. Goodnick, *Transport in nanostructures*, Cambridge University Press (1997).

[36] B.R. Nag, *Electron transport in compound semiconductors*, Springer-Verlag, Berlin (1980).

[37] G.E. Stillman, C.M. Wolfe, *Electrical characterization of epitaxial layers*, Thin Solid Films **31** (1-2), 69–88 (1976).

[38] T. Ando, *Self-consistent results for a $GaAs/Al_xGa_{1-x}As$ heterojunction. II. Low temperature mobility*, J. Phys. Soc. Jpn. **51** (12), 3900–3907 (1982).

[39] T. Ando, *Self-consistent results for a $GaAs/Al_xGa_{1-x}As$ heterojunction. I. Subband structure and light-scattering spectra*, J. Phys. Soc. Jpn. **51** (12), 3893–3899 (1982).

[40] F.F. Fang, W.E. Howard, *Negative field-effect mobility on (100) Si surface*, Phys. Rev. Lett. **16** (18), 797–799 (1966).

[41] T. Ando, A.B. Fowler, F. Stern, *Electronic properties of two-dimensional systems*, Rev. Mod. Phys. **54** (2), 437–672 (1982).

[42] D.K. Ferry, *Scattering by polar-optical phonons in quasi-two-dimensional semiconductor*, Surf. Sci. **75** (1), 86–91 (1978).

[43] K. Hess, *Impurity and phonon scattering in layered structures*, Appl. Phys. Lett. **35** (7), 484–486 (1979).

[44] P.K. Basu, B.R. Nag, *Lattice scattering mobilty of two-dimensional electron gas in GaAs*, Phys. Rev. B **22** (10), 4849–4852 (1980).

[45] P.J. Price, *Two-dimensional electron transport in semiconductor layers II: Screening*, J. Vac. Sci. Technol. **19** (3), 599–603 (1981).

[46] V.V. Mitin, V.A. Kochelap, M.A. Stroscio, *Quantum heterostructures*, Cambridge University Press, New York (1999).

[47] S.M. Goodnick, P. Lugli, *Effect of electron-electron scattering on nonequilibrium transport in quantum-well systems*, Phys. Rev. B **37** (5), 2578–2588 (1988).

[48] K. Inoue, H. Sakaki, J. Yoshino, *Field-dependent transport of electrons in selectively doped AlGaAs-GaAs/AlGaAs double-heterojunction systems*, Appl. Phys. Lett. **47** (6), 614–616 (1985).

[49] W.T. Masselink, T.S. Henderson, J. Klem, W.F. Kopp, H. Morcoç, *The dependence of* 77 *K electron vlocity-field characteristics on low-field mobility in AlGaAs-GaAs modulation-doped structures*, IEEE Trans. Electron Devices **ED-33** (5), 639–645 (1986).

[50] W.T. Masselink, N. Braslau, W.I. Wang, S.L. Wright, *Electron velocity and negative differential mobility in AlGaAs/GaAs modulation-doped heterostructures*, Appl. Phys. Lett. **51** (19), 1533–1535 (1987).

[51] W.T. Masselink, *Electron velocity in GaAs: bulk and selectively-doped heterostructures*, Semicond. Sci. Technol. **4** (7), 503–512 (1989).

[52] W.T. Masselink, *Real-space-transfer of electrons in AlGaAs/InAlAs heterostructures*, Appl. Phys. Lett. **67** (6), 801–803 (1995).

[53] J.H. English, A.C. Gossard, H.L. Störmer, K.W. Baldwin, *GaAs structures with electron mobility of* 5×10^6 cm^2/Vs, Appl. Phys. Lett. **50** (25), 1826–1828 (1987).

[54] J.G. Stern, S. Das Sarma, *Electron energy levels in* $GaAs\text{-}Ga_{1-x}Al_xAs$ *heterojunctions*, Phys. Rev. B **30** (2), 840–848 (1984).

[55] J.G. Ruch, G.S. Kino, *Transport properties of GaAs*, Phys. Rev. **174** (3), 921–932 (1968).

[56] K. Ashida, M. Inoue, J. Shirafuji, Y. Inuishi, *Microwave frequency dependence of velocity-field characteristics in n-GaAs*, Technol. Rep. Osaka Univ. (Japan) **23** (1121–1154), 475–484 (1974).

[57] N. Braslau, P.S. Hauge, *Microwave measurement of the velocity-field characteristic of GaAs*, IEEE Trans. Electron Devices **ED-17** (8), 616–622 (1970).

[58] W.T Masselink, T.F. Kuech, *Velocity-field characteristics of electrons in doped GaAs*, J. Electron. Mater. **18** (5), 579–584 (1989).

[59] L.K.J. Vandamme, *Noise as a diagnostic tool for quality and reliability of electronic devices*, IEEE Trans. Electron Devices **41** (11), 2176–2187 (1994).

[60] B.K. Jones, *Electrical noise as a measure of quality and reliability in electronic devices*, Advances in Electronics and Electron Phys. **87**, 201–257 (1993).

[61] L.K.J Vandamme, R. Alabedra, M. Zommiti, *1/f noise as a reliability estimation for solar cells*, Solid-State Electron. **26** (7), 671–674 (1983).

[62] T.G.M. Kleinpenning, F. Schurink, J.H.C. van der Veer, *1/f noise as a sensitive parameter in the life prediction testing of photovoltaic modules*, Solar Cells **12**, 363–370 (1984).

[63] M. Fukuda, T. Hirono, T. Kurusaki, F. Kano, *Correlation between 1/f noise and semiconductor laser degradation*, Europe Symp. on Reliability of Electron Devices, Failure Physics and Analysis (ESREF 93), Bordeaux , 335–339 (1993).

[64] B. Grzybowski, A. Konczakowska, L. Spiraloki, *1/f noise as the indicator of manufacturing process quality of bipolar transistors*, 9th Int. Conf. on Noise in Physical Systems, Montreal , 485–488 (1987).

[65] X. Li, L.K.J. Vandamme, *1/f noise in MOSFET as a diagnostic tool*, Solid-State Electron. **35** (10), 1477–1481 (1992).

[66] L. Loreck, H. Dambkes, K. Heime, K. Ploog, G. Weinmann, *Deep-level analysis in (AlGa)As-GaAs 2-D electron gas devices by means of low frequency noise measurements*, IEEE Electron Device Lett. **EDL-5** (1), 9–11 (1984).

[67] J.R. Kirtley, T.N. Theis, P.M. Mooney, S.L. Wright, *Noise spectroscopy of deep level (DX) centers in GaAs-*$Al_xGa_{1-x}As$ *heterostructures*, J. Appl. Phys. **63** (5), 5141–1548 (1988).

[68] M.E. Levinshtein, S.L. Rumyantsev, *Noise spectroscopy of local levels in semiconductors*, Semicond. Sci. Technol. **9** (6), 1183–1189 (1994).

[69] S. Kugler, *Evaluation of the trap concentration in highly doped semiconductors from low-frequency noise spectra*, J. Appl. Phys. **66** (1), 219–222 (1989).

[70] Y. Chen, C.M. Van Vliet, G.L. Larkis, H. Morcoç, *Generation-recombination noise in nongated and gated* $Al_xGa_{1-x}As/GaAs$ *TEGFETs in the range* 1 *Hz to* 1 *MHz*, IEEE Trans. Electron Devices **47** (11), 2045–2053 (2000).

[71] Y. Chen, C.M. Van Vliet, P.M. Koenraad, G.L Larkis, *Lorentzian noise in the two-dimensional electron gas of* $Al_xGa_{1-x}As/GaAs$ *quantum wells*, J. Appl. Phys. **86** (11), 6206–6212 (1999).

[72] A.J. Kil, R.J.J. Zijlstra, M.F.H. Schuurmans, J.P. Andre, *Noise spectroscopy as a tool to investigate the temperature dependence of localization in a quantum Hall system*, Phys. Rev. B **41** (8), 5169–5173 (1990).

[73] A. Matulionis, V. Aninkevićuis, J. Liberis, I. Matulioniené, J. Berntgen, K. Heime, H.L. Hartnagel, *Hot-electron energy relaxation, noise, and lattice strain in InGaAs quantum well channels*, Appl. Phys. Lett. **74** (13), 1895–1897 (1999).

[74] L.K.J. Vandamme, X. Li, D. Rigaud, *1/f noise in MOS devices, mobility or number fluctuations?*, IEEE Trans. Electron Devices **41** (11), 1936–1945 (1994).

[75] F.N. Hooge, $1/f$ *noise is no surface effect*, Phys. Lett. **29A** (3), 139–140 (1969).

[76] F.N. Hooge, L.K.J. Vandamme, *Lattice scattering causes* $1/f$ *noise*, Phys. Lett. **66A** (4), 315–316 (1978).

[77] T.G.M. Kleinpenning, *Scattering mechanisms and* $1/f$ *noise in semiconductors*, Physica B **103** (2-3), 345–347 (1981).

[78] L. Ren, F.N. Hooge, *Temperature dependence of* $1/f$ *noise in epitaxial n-type GaAs*, Physica B **176** (3), 209–212 (1992).

[79] X.Y. Chen, M.R. Leys, *Study of* $1/f$ *noise in InP grown by CBE*, Solid-State Electronics **39** (8), 1149–1153 (1996).

[80] L. Ren, M.R. Leys, *1/f noise in an* $Al_xGa_{1-x}As/GaAs$ *heterostructure between* 77 *and* 300 *K*, Physica B **192** (4), 303–310 (1993).

[81] L. Ren, M.R. Leys, $1/f$ *noise at room temperature in n-type GaAs grown by molecular beam epitaxy*, Physica B **172** (3), 319–323 (1991).

[82] V.N. Abakumov, V.I. Perel, I.N. Yassievich, *Nonradiative recombination in semiconductors*, in: Modern problems in condensed matter science, volume 33, Amsterdam (1991).

[83] A.J. Madenach, J. Werner, *Deep-level-noise spectroscopy of ion-implanted polysilicon thin films*, Phys. Rev. B **38** (3), 1958–1962 (1988).

[84] J.A. Copeland, *Semiconductor impurity analysis from low-frequency noise spectra*, IEEE Trans. Electron Devices **18**, 50–53 (1971).

[85] L.D. Yau, C.T. Sah, *Theory and experiments of low-frequency generation-recombination noise in MOS transistors*, IEEE Trans. Electron Devices **16** (2), 170–177 (1969).

[86] F. Hoffman, R.J.J. Zijlstra, C.M. Henning, *Current noise in N-type* $Al_xGa_{1-x}As$, Phys. Lett. **31** (2), 279–282 (1988).

[87] M. Tacano, T. Kanayama, Y. Sugiyama, *1/f noise in quarter-micron filaments of GaAs and InP made by focused ion-beam implantation*, Solid-State Electron. **34** (2), 193–196 (1991).

[88] M. Tacano, Y. Sugiyama, *Comparison of 1/f noise of AlGaAs/GaAs HEMTs and GaAs MESFETs*, Solid-State Electron. **34** (10), 1049–1053 (1991).

[89] S.L. Rumyantsev, N. Pala, M.S. Shur, E. Borovitskaya, A.P. Dmitriev, M.E. Levinshtein, R. Gaska, M.A. Khan, J. Yang, X. Hu, G. Simin, *Generation-recombination noise in GaN/AlGaN heterostructure field effect transistors*, IEEE Trans. Electron Devices **48** (3), 530–534 (2001).

[90] D.D. Carey, S.T. Stoddart, S.J. Bending, J.J. Harris, C.T. Foxon, *Investigation of deep metastable traps in Si δ-doped* $GaAs/Al_{0.33}Ga_{0.67}As$ *quantum-well samples using noise spectroscopy*, Phys. Rev. B **54** (4), 2813–2821 (1996).

[91] R.S. Popović, *Hall Effect Devices*, Adam Hilger Publishing, Bristol (1991).

[92] A.S. Grove, *Physics and technology of semiconductor devices*, New York: Wiley (1967).

[93] R. Muller, T. Kamins, *Device electronics for integrated circuits*, New York, Wiley (1977).

[94] A.D. Kent, S. von Molnar, S. Gider, D.D. Awschalom, *Properties and measurements of scanning tunneling microscope fabricated particle arrays*, J. Appl. Phys. **76** (10), 6656–6660 (1994).

[95] A. Oral, S.J. Bending, M. Henini, *Real-time scanning Hall probe microscopy*, Appl. Phys. Lett. **69** (9), 1324–1326 (1996).

[96] T. Tamegai, L. Krusin-Elbaum, P. Santhanam, M.J. Brady, W.T. Masselink, C. Feild, F. Holtzberg, *Spatially resolved magnetic hysteresis in* $YBa_2Cu_3O_{7-y}$ *crystal measured by a Hall-probe array*, Phys. Rev. B **45** (5), 2589–2592 (1992).

[97] M. Charalambous, R. Koch, A.D. Kent, W.T. Masselink, *Hall magnetometry measurements of bulk single crystalline rings of* $YBa_2Cu_3O_7$, Phys. Rev. B **58** (14), 9510–9523 (1998).

[98] H.J. Lippmann, F. Kuhrt, *Der Geometrieeinfluss auf den Hall-Effect bei rechteckigen Halbleiterplatten*, Z. Naturforsch. **13a**, 474–483 (1958).

[99] W. Versnel, *The geometrical correction factor for a rectangular Hall plate*, J. Appl. Phys. **53** (7), 4980–4986 (1982).

[100] J. Haeusler, *Die Geometriefuktion vierelektrodiger Hallgeneratoren*, Arch. Elecktrotech. **52**, 11–19 (1968).

[101] W. Versnel, *Analysis of symmetrical Hall plates with finite contacts*, J. Appl. Phys. **52** (7), 4659–4666 (1981).

[102] R.S. Popovic, B. Hälg, *Nonlinearity in Hall devices and its compensation*, Solid State Electon. **31** (12), 1681–1688 (1988).

[103] T.G.M. Kleinpenning, L.K. Vandamme, *Comment on 'Transverse* $1/f$ *noise in InSb thin films and the SNR of related Hall elements'*, J. Appl. Phys. **50** (8), 5547 (1979).

[104] M.V. Fischetti, *Monte Carlo simulation of transport in technologically significant semiconductors of the diamond and zinc-blende structures - Part I: Homogeneous transport*, IEEE Trans. Electron Dev. **38** (3), 634–649 (1991).

[105] G.A. Acket, *Hall mobility of hot electrons in GaAs*, Phys. Lett. **24 A**, 500 (1967).

[106] N. Braslau, *Velocity-field characteristics of GaAs from measurement of the conductivity in a microwave field*, Phys. Lett. **24 A** (10), 531–533 (1967).

[107] C. Hamaguchi, T. Kono, Y. Inuishi, *Microwave measurements of differential negative conductivity due to intervalley transfer of hot electrons in n-type GaAs*, Phys. Lett. **24 A** (10), 500–501 (1967).

[108] G.E. Stillman, C.M. Wolfe, J.O. Dimmock, *Hall coefficient factor for polar mode scattering in n-type GaAs*, J. Phys. Chem. Solids **31** (6), 1199–1204 (1970).

[109] A. Okamoto, I. Shibasaki, *Transport properties of Sn-doped InSb thin films and applications to Hall element*, J. Cryst. Growth **251** (1-4), 560–564 (2003).

[110] M. Oszwaldowski, *Hall sensors based on heavily doped n-InSb thin films*, Sens. Actuators A **68** (1-3), 234–237 (1998).

[111] E.D. Marshall, M. Murakami, *Ohmic contacts to GaAs and other III-V compounds: correlation of microstructure with electrical properties*, in: *Contacts to semiconductors: fundamentals and technology,* L.J. Brillson, editor, 1–66, Noyes Publications (1993).

[112] P.M. Mooney, *Deep donor levels (DX centers) in III-V semiconductors*, J. Appl. Phys. **67** (3), R1–R26 (1990).

[113] J. Berntgen, A. Behres, J. Kluth, K. Heime, W. Daumann, U. Auer, F.J. Tegude, *Hooge parameter of InGaAs bulk material and InGaAs 2DEG quantum well structures based on InP substrates*, Microelectronic Reliability **40** (11), 1911–1914 (2000).

[114] M.A. Herman, H. Sitter, *Molecular beam epitaxy*, in: *Springer series in materials science,* M.B. Panish, editor, volume 7, Springer-Verlag (1996).

[115] J. Jeans, *Introduction to the kinetic theory of gases*, Cambridge University Press, London (1940).

[116] R.A. Kubiak, S.M. Newstead, P. Sullivan, *The technology and design of molecular beam epitaxy systems*, in: Molecular beam epitaxy: application to key materials, 1–275, Noyes Publications, New Jersey (1995).

[117] G.J. Davies, D. Williams, *III-V MBE growth systems*, in: *The technology and physics of molecular beam epitaxy,* E.H.C. Parker, editor, p. 15, Plenum, New York (1985).

[118] F. Hatami, *Indium Phosphide Quantum Dots in GaP and in $In_{0.48}Ga_{0.52}P$: Growth and Properties*, PhD Thesis (2002).

[119] W. Braun, *Applied RHEED*, Springer-Verlag, Berlin (1999).

[120] O. Bierwagen, *Wachstum und transportuntersuchungen von selbstorganisierten quantendräten im InAs/InP materialsystem*, Diploma Thesis (2001).

[121] A. Madhukar, *Far from equilibrium vapour phase growth of lattice matched III-V compound semiconductor interfaces: Some basic concepts and Monte-Carlo computer simulations*, Surf. Sci. **132** (1-3), 344–374 (1983).

[122] L.D. Schmidt, *Condensation kinetics and mechanisms*, in: *The physical basis for hetergeneous catalysis,* E. Drauglis, editor, Plenum, New York (1975).

[123] M.A. Herman, *Semiconductor superlattices*, Akademie-Verlag, Berlin (1996).

[124] P. N. Fawcett, J. H. Neave, J. Zhang, B.A. Joyce, *Study of the epitaxial growth of GaAs(110) films by molecular beam epitaxy*, J. Vac. Sci. Tech. A **12** (4), 1201–1203 (1994).

[125] T. Fujii, M. Ekawa, *Origin of compositional modulation of InGaAs in selective area metalorganic vapor phase epitaxy*, J. Appl. Phys. **78** (9), 5373–5386 (1995).

[126] Ch. Heyn, M. Harsdorff, *Simulation of GaAs growth and surface recovery with respect to gallium and arsenic surface kinetics*, Phys. Rev. B **55** (11), 7034–7038 (1996).

[127] M. Asai, F. Sato, H. Imamoto, K. Imanaka, M. Shimura, *Low-temperature (350° C) growth of AlGaAs/GaAs laser diode by migration enhanced epitaxy*, J. Appl. Phys. **64** (1), 432–434 (1988).

[128] Y.C. Chen, P.K. Bhattacharya, J. Singh, *Comparison of growth front profile of strained layers grown by migration-enhanced epitaxy and molecular-beam epitaxy using reflection high-energy electron diffraction*, J. Vac. Sci. Tech. B **10** (2), 766–768 (1992).

[129] Y. Horikoshi, M. Kawashima, H. Yamaguchi, *Low-temperature growth of GaAs and AlAs-GaAs quantum-well lasers by modified molecular beam epitaxy*, Jpn. J. Appl. Phys. **25** (10), L868–L870 (1986).

[130] S.C. Jain, M. Willander, H. Maes, *Stress and strains in epilayers, stripes and quantum structures of III-V compound semiconductors*, Semicond. Sci. Technol. **11** (5), 641–671 (1996).

[131] M. Volmer, A. Weber, Z. Phys. Chem. **119**, 277 (1926).

[132] J.N. Stranski, L. Krastanov, In Sitzungsberichte d. Akad. d. Wissenschaften in Wien, Abt. IIb **146**, 797 (1937).

[133] F.C. Frank, J.H. van der Merwe, *One dimensional dislocations*, Proc. R. Soc. London, Ser. A **198**, 205–225 (1949).

[134] K.-N. Tu, J.W. Mayer, L.C. Feldman, *Electronic thin films science for electrical engineers and materials scientists*, Macmillan, New York (1992).

[135] J.W. Matthews, A.E. Blakeslee, *Defects in epitaxial multilayers: I. Misfit dislocation*, J. Cryst. Growth. **27**, 118–125 (1974).

[136] K. Nii, R. Kuriyama, T. Hiraoka, T. Kitada, S. Shimomura, S. Hiyamizu, *Larger critical thickness determined by photoluminescence measurements in pseudomorphic* $In_{0.25}Ga_{0.75}As/Al_{0.32}Ga_{0.68}As$ *quantum well grown on (411) GaAs substrates by molecular beam epitaxy*, J. Vac. Sci. Technol. B **17** (3), 1167–1170 (1999).

[137] B. Elman, E.S. Koteles, P. Melman, K. Ostreicher, C. Sung, *Low substrate temperature molecular beam epitaxial growth and the critical layer thickness of InGaAs grown on GaAs*, J. Appl. Phys. **70** (5), 2634–2640 (1991).

[138] W.-C. Hsu, S.-Z. Chang, W. Lin, *A study of layer thickness and interface qualities of strained* $In_xGa_{1-x}As/GaAs$ *layers*, Jpn. J. Appl. Phys. **31** (1), 26–29 (1992).

[139] T. Saeki, T. Motakawa, T. Kitada, S. Shimomura, A. Adachi, Y. Okamoto, N. Sano, S. Hiyamizu, *Extremely flat interfaces in* $In_xGa_{1-x}As/Al_{0.3}Ga_{0.7}As$ *quantum wells grown on (411)A GaAs substrates by molecular beam epitaxy*, Jpn. J. Appl. Phys. **36** (3B), 1786–1788 (1997).

[140] M.J. Ekenstedt, S.M. Wang, T.G. Andersson, *Temperature-dependent critical layer thickness for* $In_{0.36}Ga_{0.64}As/GaAs$ *single quantum wells*, Appl. Phys. Lett. **58** (8), 854–855 (1991).

[141] N. Hiroshi, Y. Takafumi, *Surface lattice strain relaxation at the initial stage of heteroepitaxial growth of* $In_xGa_{1-x}As$ *on GaAs by molecular beam epitaxy*, Jpn. J. Appl. Phys. **29** (3), L352–L355 (1989).

[142] T. Taguchi, Y. Takeuchi, K. Matugatani, Y. Ueno, T. Hattori, Y. Sugiyama, M. Tacano, *Critical layer thickness of* $In_{0.80}Ga_{0.20}As/In_{0.52}Al_{0.48}As$ *heterostructures*, J. Cryst. Growth **134** (1-2), 147–150 (1993).

[143] S.F. Yoon, H.M. Li, K. Radhakrishnan, Z.Y. Han, *Optical characterization of strained* $In_xGa_{1-x}As$*-*$Al_{0.28}Ga_{0.72}As$ *heterostructures grown by molecular beam epitaxy*, J. Cryst. Growth **134** (3-4), 240–246 (1993).

[144] O. Brafman, D. Fekete, R. Sarfaty, *On the evolution of GaInAs/GaAs strained epitaxial layers*, J. Appl. Phys. **71** (4), 1744–1747 (1992).

[145] Z.C. Feng, A.A. Allerman, P.A. Barnes, *Raman scattering of InGaAs/InP grown by uniform radial flow epitaxy*, Appl. Phys. Lett. **60** (15), 1848–1850 (1992).

[146] A. Sacedón, F. Calle, A.L. Alvarez, E. Calleja, E. Muñoz, R. Beanland, P. Goodhew, *Relaxation of InGaAs layers grown on (111)B GaAs*, Appl. Phys. Lett. **65** (25), 3212–3214 (1994).

[147] C.A. Wang, S.H. Groves, J.H. Reinold, D.R. Calawa, *Critical layer thickness of strained-layer InGaAs/GaAs multiple quantum wells determined by double-crystal x-ray diffraction*, J. Electron. Mater. **22** (11), 1365–1368 (1993).

[148] J.Y. Yao, T.G. Andersson, G.L. Dunlop, *Microstructures and critical thicknesses of* $In_xGa_{1-x}As/GaAs$ *strained-layer structures*, Semicond. Sci. Technol. **9** (5), 1086–1095 (1994).

[149] P.M. Maree, J.C. Barbour, J.F. van der Veen, K.L. Kavanagh, C.W.T. Bulle-Lieuwma, M.P.A. Viegers, *Generation of misfit dislocation in semiconductors*, J. Appl. Phys. **62** (11), 4413–4420 (1987).

[150] S.C. Jain, *Germanium-silicon strained layers and heterostructures*, Academic Press, Boston (1994).

[151] S.C. Jain, T.J. Gosling, J.R. Willis, D.H. Totterdell, R. Bullough, *A new study of critical layer thickness, stability and strain relaxation in pseudomorphic* Ge_xSi_{1-x} *strained epilayers*, Phil. Mag. A **65** (5), 1151–1167 (1992).

[152] A.Y. Cho, *Growth of III-V semiconductors by molecular beam epitaxy and their properties*, Thin Solid Films **100** (4), 291–317 (1983).

[153] T. Mizutani, *Correct substrate temperature monitoring with infrared optical pyrometer for molecular-beam epitaxy of III-V semiconductors*, J. Vac. Sci. Technol. B **6** (6), 1671–1677 (1988).

[154] L. Däweritz, K. Ploog, *Contribution of reflection high-energy electron diffraction to nanometre tailoring of surfaces and interfaces by molecular beam epitaxy*, Semicond. Sci. Technol. **9** (2), 123–136 (1994).

[155] L. Däweritz, R. Hey, *Reconstruction and defect structure of vicinal GaAs (001) and* $Al_xGa_{1-x}As$ *(001) surfaces during MBE growth*, Surf. Sci. **236** (1-2), 15–22 (1990).

[156] S.M. Newstead, R.A.A. Kubiak, E.H.C Parker, *On the practical applications of MBE surface phase diagrams*, J. Crys. Growth **81** (1-4), 49–54 (1987).

[157] H.H. Farrell, C.J. Palmstrom, *Reflection high energy electron diffraction characteristic absences in GaAs (100)* (2×4)*-As: A tool for determining the surface stoichiometry*, J. Vac. Sci. Techol. B **8** (4), 903–907 (1990).

[158] D.K. Bowen, B.K. Tanner, *High resolution x-ray diffractometry and topography*, Taylor & Francis (1998).

[159] L. Tapfer, K. Ploog, *X-ray interference in ultrathin epitaxial layers: A versatile method for the structural analysis of single quantum wells and heterointerfaces*, Phys. Rev. B **40** (14-15), 9802–9810 (1989).

[160] D. Taupin, *Dynamic theory of x-ray diffraction in crystals*, C. R. Acad. Sci. (France) **87** (4), 469–511 (1964).

[161] S. Takagi, *Dynamical theory of diffraction for a distorted crystal* **26** (5), 1239–1253 (1969).

[162] B.C. Larson, J.F. Barhorst, *X-ray study of lattice strain in boron implanted laser annealed silicon*, J. Appl. Phys. **51** (6), 3181–3185 (1980).

[163] Yu.N. Belyaev, A.V. Kolpakov, *On the theory of X-ray diffraction in a perfect crystal with distorted surface layer*, Phys. Stat. Solidi A **76** (2), 641–646 (1983).

[164] Secondary electron images (SEI) by Dr. U. Müller at Humboldt University, Berlin .

[165] E.H. Rhoderick, R.H. Williams, *Metal-semiconductor contacts*, University Press, Oxford (1988).

[166] J.-L. Lee, Y.-T. Kim, H.M. Yoo, J.Y. Lee, *Au/Ge-based ohmic contact to an AlGaAs/InGaAs pseudomorphic high electron mobility transistor with an undoped cap layer*, J. Vac. Sci. Technol. B **17** (3), 1034–1039 (1999).

[167] J.-L. Lee, Y.-T. Kim, J.Y. Lee, *Microstructural evidence on direct contact of Au/Ge/Ni/Au ohmic metals to InGaAs channel in pseudomorphic high electron mobility transistor with undoped cap layer*, Appl. Phys. Lett. **73** (12), 1670–1672 (1998).

[168] Y.-T. Kim, J.-L. Lee, B.-T. Lee, *Microstructural and electrical investigation of Pd/Ge/Ti/Au ohmic contact to pseudomorphic high electron mobility transistor with undoped cap layer*, J. Appl. Phys. **84** (2), 911–917 (1998).

[169] P.H. Hao, L.C. Wang, F. Deng, S.S. Lau, J.Y. Cheng, *On the low resistance Au/Ge/Pd ohmic contact to n-GaAs*, J. Appl. Phys. **79** (8), 4211–4215 (1996).

[170] R.A. McTaggart, K.Y. Hur, P.J. Lemonias, W.E. Hoke, L.M. Aucoin, *Thermally stable AuGe-Au ohmic contacts for single doped InP high electron mobility transistor structures*, J. Vac. Sci. Technol. B **13** (1), 163–165 (1995).

[171] J.R. Waldrop, R.W. Grant, *Correlation of interface composition and barrier height for model AuGeNi contacts to GaAs*, Appl. Phys. Lett. **50** (5), 250–252 (1987).

[172] Device processing including the standard optical photolitography with further Au/Ge/Ni metallization by Dr. H. Kostial and E. Wiebicke at Paul-Drude Institute für Festkörperelektronik, Berlin .

[173] E.D. Marshall, M. Murakami, *Ohmic contacts to GaAs and other III-V compounds: correction of microstructure with electrical properties*, in: *Contacts to semiconductros: fundamentals and technology,* L.J. Brillson, editor, 1–66, Noyes Publications, New Jersey (1993).

[174] S.M. Sze, *Physics of semiconductor devices*, Wiley, New York (1981).

[175] F.A. Padovani, *Semiconductors and semimetals*, volume 7, chapter 2, 75–146, Academic Press, New York (1971).

[176] D.C. Look, *Electrical characterization of GaAs materials and devices*, John Wiley & Sons, New York (1989).

[177] G.K. Reeves, H.B. Harrison, *Obtaining the specific contact resistance from transmission-line model measurements*, IEEE Electron. Dev. Lett. **EDL-3** (5), 111–113 (1982).

[178] S.J. Proctor L.W. Linholm, *A direct measurement of interfacial contact resistance*, IEEE Electron. Dev. Lett. **EDL-3** (10), 294–296 (1982).

[179] K. Lee, M.S. Shur, K.W. Lee, T. Vu, P. Roberts, M. Helix, *A new interpretation of end resistance measurements*, IEEE Electron. Dev. Lett. **EDL-5**, 5–7 (1984).

[180] J.G.J. Chern, W.G. Oldham, *Determining specific contact resistivity from contact end resistance measurement*, IEEE Electron Device Lett. **EDL-5** (5), 178–180 (1984).

[181] S. Chaudhuri, M.B. Das, *An investigation of the MESFET 'end' resistance using a distributed diode/resistance model*, IEEE Trans. Electron Dev. **ED-32**, 2262–2268 (1985).

[182] A. Callegari, E.T.-S. Pan, M. Murakami, *Uniform and thermally stable AuGeNi ohmic contacts to GaAs*, Appl. Phys. Lett. **46** (12), 1141–1143 (1985).

[183] M. Murakami, K.D. Childs, J.M. Baker, A. Callegari, *Microstructure studies of AuGeNi ohmic contacts to n-type GaAs*, J. Vac. Sci. Technol. B **4** (4), 903–911 (1986).

[184] M. Ogawa, *Alloying behavior of Ni/Au-Ge films on GaAs*, J. Appl. Phys. **51** (1), 406–412 (1980).

[185] Y.C. Shin, M. Murakami, E.L. Wilkie, A. Callegari, *Effects of interfacial microstructure on uniformity and thermal stability of AuNiGe ohmic contact to n-type GaAs*, J. Appl. Phys. **62** (2), 582–590 (1987).

[186] T.S. Kuan, P.E. Batson, T.N. Jackson, H. Rupprecht, E.L. Wilkie, *Electron microscope studies of an alloyed Au/Ni/Au-Ge ohmic contact to GaAs*, J. Appl. Phys. **54** (12), 6952–6957 (1983).

[187] W.O. Barnard, J.B. Malherbe, B.M. Lacquet, *Formation of ohmic contacts to n-GaAs by ion beam mixing and annealing*, Appl. Surf. Sci. **31** (4), 437–444 (1988).

[188] M. Heiblum, M.I. Nathan, C.A. Chang, *Characteristics of AuGeNi ohmic contacts to GaAs*, Solid State Electron. **25** (3), 185–195 (1982).

[189] R.P. Gupta, W.S. Khokle, *Gallium-vacancy-dependent diffusion model of ohmic contacts to GaAs*, Solid State Electron. **28** (8), 823–830 (1985).

[190] M. Quillec, L. Goldstein, G. Le Roux, J. Burgeat, J. Primot, *Growth conditions and characterization of InGaAs/GaAs strained layers superlattices*, J. Appl. Phys. **55** (8), 2904–2909 (1984).

[191] F-Y. Juang, P.K. Bhattacharya, J. Singh, *Determination of the microscopic quality of InGaAs-InAlAs interfaces by photoluminescence: Role of interrupted molecular beam epitaxial growth*, Appl. Phys. Lett. **48** (4), 290–292 (1986).

[192] R.L.S. Devine, W.T. Moore, *Effect of interface structure on photoluminescence of InGaAs/GaAs pseudomorphic single quantum wells*, J. Appl. Phys. **62** (9), 3999–4001 (1987).

[193] M.A. Herman, D. Bimberg, J. Christen, *Heterointerfaces in quantum wells and epitaxial growth processes: Evaluation by luminescence techniques*, J. Appl. Phys. **70** (2), R1–R52 (1991).

[194] Y.-H. Zhang, D.-S. Jiang, R. Cingolani, K. Ploog, *Fermi edge singularity in the luminescence of modulation-doped* $Ga_{0.47}In_{0.53}As/Al_{0.48}In_{0.52}As$ *single heterojunctions*, Appl. Phys. Lett. **56** (22), 2195–2197 (1990).

[195] Y.-H. Zhang, N.N. Ledentsov, K. Ploog, *Effect of hole-localization mechanisms on photoluminescence spectra of two-dimensional-electron-gas systems*, Phys. Rev. B **44** (4), 1399–1402 (1991).

[196] O. Brandt, L. Tapfer, R. Cingolani, K. Ploog, M. Hohenstein, F. Phillipp, *Structural and optical properties of (100) InAs single-monolayer quantum wells in bulklike GaAs grown by molecular-beam epitaxy*, Phys. Rev. B **41** (18), 12599–12606 (1990).

[197] S.F. Yoon, *Surface morphology and quality of strained InGaAs grown by molecular-beam epitaxy on GaAs*, J. Vac. Sci. Technol. B **11** (3), 562–566 (1993).

[198] F. Peiro, A. Cornet, J.A. Morante, M. Beck, M.A. Py, *Surface roughness in InGaAs channels of high electron mobility transistors depending on the growth temperature: Strain induced or due to alloy decomposition*, J. Appl. Phys. **83** (12), 7537–7541 (1998).

[199] K. Radhakrishnan, T.H.K. Patrick, H.Q. Zheng, P.H. Zhang, S.F. Yoon, *Study of doping concentration variation in InGaAs/InP high electron mobility transistor layer structures by Raman scattering*, J. Vac. Sci. Technol. A **18** (2), 713–716 (2000).

[200] S.M. Wang, T.G. Andersson, V.D. Kulakovskii, J.Y. Yao, *Critical layer thickness in* $In_xGa_{1-x}As/GaAs$ *quantum wells studied by photoluminescence and transmission electron microcopy*, Superlattices and Microstructures **9** (1), 123–126 (1991).

[201] H. Kissel, *Photolumineszez- und magnetooptische Untersuchungen von Vielteilcheneffekten in AlGaAs/InGaAs/GaAs-Heterostructuren*, PhD Thesis (2002).

[202] S.K. Lyo, E.D. Jones, *Photoluminescence line shape in degenerate semiconductor quantum wells*, Phys. Rev. B **38** (6), 4113–4119 (1988).

[203] G.G. Tarasov, U. Müller, Yu.I. Mazur, H. Kissel, Z.Ya. Zhuchenko, C. Walther, W.T. Masselink, *Direct investigations of localized hole states in pseudomorphic modulation-doped* $Al_xGa_{1-x}As/In_yGa_{1-y}As/GaAs$ *heterostructures by optical detection of quantum oscillations*, Phys. Rev. B **58** (8), 4733–4739 (1998).

[204] K.H. Herrmann, M. Happ, H. Kissel, K.P. Möllmann, J.W. Tomm, C.R. Becker, M.M. Kraus, S. Yuan, G. Landwehr, *A new model for the absorption coefficient of narrow-gap (Hg,Cd)Te that simultaneously considers band tails and band filling*, J. Appl. Phys. **73** (7), 3486–3492 (1993).

[205] The measurements of Raman spectra by Dr. V. Yukhimchuk at Institute of Semiconductor Physics, Ukrainian National Academy of Science, Kiev (see Ref. [201]) .

[206] T. Yuasa, S. Naritsuka, M. Mannoh, K. Shinozaki, K. Yamanaka, Y. Nomura, M. Mihara, M. Ishii, *Raman scattering from coupled plasmon-LO-phonon modes in n-type* $Al_xGa_{1-x}As$, Phys. Rev. B **33** (2), 1222–1232 (1986).

[207] T. Yuasa, M. Ishii, *Raman scattering study of coupled hole-plasmon-LO-phonon modes in p-type GaAs and p-type* $Al_xGa_{1-x}As$, Phys. Rev. B **35** (8), 3962–3970 (1987).

[208] K. Kakimoto, T. Katoda, *Raman spectra from* $Ga_{1-x}In_xAs$ *epitaxial layers grown on GaAs and InP substrates*, Appl. Phys. Lett. **40** (9), 826–828 (1982).

[209] K.P. Jain, R.K. Soni, S.C. Abbi, M. Balkanski, *Resonant Raman scattering at the saddle-point singularity in* $In_xGa_{1-x}As$, Phys. Rev. B **32** (2), 1005–1008 (1985).

[210] A.M. Mintairov, H. Temkin, *Lattice vibrations and phonon-plasmon coupling in Raman spectra of p-type* $In_{0.53}Ga_{0.47}As$, Phys. Rev. B **55** (8), 5117–5123 (1997).

[211] G. Burns, C.R. Wie, F.H. Dacol, G.D. Pettit, J.M. Woodall, *Phonon shifts and strains in strain-layered* $(Ga_{1-x}In_x)As$, Appl. Phys. Lett. **51** (23), 1919–1921 (1987).

[212] M.J.L.S. Haines, B.C. Cavenet, S.T. Davey, *Optical phonon energies in pseudomorphic alloy strained layers*, Appl. Phys. Lett. **55** (9), 849–851 (1989).

[213] J.M. Gilperez, F. Gonzalez-Sanz, E. Calleja, E. Munoz, J.M. Calleja, N. Mestres, J. Castagne, E. Barbier, *Photoluminescence and Raman analysis of strain and composition in InGaAs/AlGaAs pseudomorphic heterostructures*, Semicond. Sci. Technol. **7** (4), 562–566 (1992).

[214] P. Parayanthal, F.H. Pollak, *Raman scattering in alloy semiconductors: "Spatial correlation" model*, Phys. Rev. Lett. **52** (20), 1822–1825 (1984).

[215] N.V. Dyakonova, M.E. Levinshtein, S.L. Rumyantsev, *Temperature dependence of the low-frequency noise in structurally perfect GaAs and after destructive compression*, Sov. Phys. Semiconductors **25** (2), 217–218 (1991).

[216] D.V. Lukyanchikova, *Noise research in semiconductor physics*, Gordon and Breach science publishers (1997).

[217] *Model SR510 lock-in amplifier (manual)*, Stanford Research Systems, Inc. (1987).

[218] T.N. Theis, B.D. Parker, P.M. Solomon, S.L. Wright, *Hot-electron capture to DX centers in* $Al_xGa_{1-x}As$ *at low Al mole fractions* ($x < 0.2$), Appl. Phys. Lett. **49** (22), 1542–1544 (1986).

[219] P.M. Mooney, N.S. Caswell, S.L. Wright, *The capture barrier of the DX center in Si-doped* $Al_xGa_{1-x}As$, J. Appl. Phys. **62** (12), 4786–4797 (1987).

[220] L.K.J Vandamme, *Annealing of implants reduces lattice defects and 1/f noise*, Solid State Phenomena **1-2**, 153–158 (1988).

[221] L.K.J Vandamme, S. Oosterhoff, *Annealing of ion-implanted resistors reduces the 1/ f noise*, J. Appl. Phys. **59** (9), 3169–3174 (1986).

[222] L. Ren, *Intrinsic and extrinsic 1/f noise source in proton-irradiated n-GaAs*, J. Appl. Phys. **74** (7), 4534–4539 (1993).

[223] M. Tacano, T. Kanayama, H. Hiroshima, M. Komura, Y. Sugiyama, *1/f noise in a quarter-micron GaAs Hall device made by focused ion-beam implantation*, J. Appl. Phys. **62** (10), 4301–4303 (1987).

[224] S. Hashiguchi, H. Horiuchi, M. Ohki, M. Yajima, M. Tacano, *Temperature dependence of 1/f noise in AlGaAs/InGaAs HEMT*, AIP Conf. Proc. **285**, 228–231 (1993).

[225] N. Chand, T. Henderson, J. Klem, W.T. Masselink, R. Fisher, Y.C. Chang, H. Morkoç, *Comprehensive analysis of Si-doped* $Al_xGa_{1-x}As$ *(x=0 to 1): theory and experiments*, Phys. Rev. B **30** (8), 4481–4492 (1984).

[226] D.V. Lang, in: Deep centers in semiconductors, edited by S.T. Pantelides, 489–539, Gordon and Breach, New York (1986).

[227] P.M. Mooney, S.L. Calleja, S.L. Wright, M. Heiblum, in: *Defects in semiconductors, Materials Science Forum 10-12,* H.J. von Bardeleben, editor, Trans. Tech., Switzerland (1986).

[228] O. Kumagi, H. Kawai, Y. Mori, K. Kaneko, *Chemical trends in the activation energies of DX centers*, Appl. Phys. Lett. **45** (12), 1322–1323 (1984).

[229] S. Machlup, *Noise in semiconductors: Spectrum of a two-parameter random signal*, J. Appl. Phys. **25** (3), 341–345 (1954).

[230] V. Mosser, S. Contreras, S. Aboulhouda, Ph. Lorenzini, F. Kobbi, J.L. Robert, K. Zekentes, *High sensitivity Hall sensors with low thermal drift using AlGaAs/InGaAs/GaAs heterostructures*, Sens. Actuators A **43** (1-3), 135–140 (1994).

[231] S. Dhar, U. Das, P.K. Bhattacharya, *Deep levels in as-grown and Si-implanted* $In_{0.2}Ga_{0.8}As$*-GaAs strained-layer superlattice optical guiding structures*, J. Appl. Phys. **60** (2), 639–642 (1986).

[232] D. Pal, E. Gombia, R. Mosca, A. Bosacchi, S. Franchi, *Deep levels in virtually unstrained InGaAs layers deposited on GaAs*, J. Appl. Phys. **84** (5), 2965–2967 (1998).

[233] T. Mizutani, M. Yamamoto, S. Kishimoto, K. Maezawa, *Low-frequency noise characteristics of AlGaAs/InGaAs pseudomorphic HEMTs*, IEICE Trans. Electron. **E84-C** (10), 1318–1322 (2001).

[234] T. Henderson, W.T. Masselink, W. Kopp, H. Morkoç, *Determination of carrier saturation velocity in high performance* $In_{0.15}Ga_{0.85}As/Al_{0.15}Ga_{0.85}As$ *modulation doped field-effect transistor (*$0 < y < 0.2$*)*, IEEE Electron Dev. Lett. **EDL-7**, 288–290 (1986).

[235] E.M. Conwell, *High field transport in semiconductors*, Academic Press, New York (1967).

[236] L. Pfeiffer, K.W. West, H.L. Störmer, K.W. Baldwin, *Electron mobilities exceeding* 10^7 cm^2/Vs *in modulation-doped GaAs*, Appl. Phys. Lett. **55** (18), 1888–1890 (1989).

[237] B.J.F. Lin, D.C. Tsui, *Experimental and theoretical studies of the 2DEG mobility in modulation-doped* $GaAs/Al_{1-x}Ga_xAs$ *heterostructures*, Surf. Sci. **174** (3), 397–398 (1986).

[238] M. Inoue, M. Inayama, S. Hiyamizu, Y. Inuishi, *Parallel electron transport and field effects of electron distributions in selectively-doped GaAs/n-AlGaAs*, Jpn. J. Appl. Phys. **22** (4), L213–L215 (1983).

[239] W.T. Masselink, W. Kopp, T. Henderson, H. Morcoç, *Velocity-field characteristics of AlGaAs-GaAs modulation-doped structures*, in: Proc. 1985 IEEE Cornell Conf. (Ithaca, NY), July , 29–31 (1986).

[240] W.T. Masselink, W. Kopp, T. Henderson, H. Morcoç, *Measurements of the electron velocity-field characteristic in modulation-doped structures using the geometrical magnetoresistance method*, IEEE Electron Device Lett. **EDL-6**, 539–541 (1985).

[241] Y. Sugiyama, Y. Takeuchi, M. Tacano, *Highly-sensitive InGaAs-2DEG Hall device made of pseudomorphic* $In_{0.52}Al_{0.48}As/In_{0.8}Ga_{0.2}As$ *heterostructure*, Sens. Actuators A **34** (2), 131–136 (1992).

[242] S. Del Medico, T. Benyattou, G. Guillot, M. Gendry, M. Oustric, T. Venet, J. Tardy, G. Hollinger, A. Chovet, N. Mathieu, *Highly sensitive* $In_{0.75}Ga_{0.25}As$*/AlInAs Hall sensors*, Semicond. Sci. Technol. **11** (4), 576–581 (1996).

[243] R. Kyburz, J. Schmid, R.S. Popovic, H. Melchior, *High Performance* $In_{0.53}Ga_{0.47}As/InP$ *Hall sensors with doped and 2DEG channels and screening front and back gate layers*, Sensor and Materials **6**, 273–291 (1994).

[244] R. Kyburz, J. Schmid, R.S. Popovic, H. Melchior, *Highly sensitive* $In_{0.53}Ga_{0.47}As/InP$ *Hall sensor grown by MOVPE*, IEEE Trans. Electron. Devices **ED-41**, 315–320 (1994).

[245] Vas.P. Kunets, W. Hoerstel, H. Kostial, H. Kissel, U. Müller, G.G. Tarasov, Yu.I. Mazur, Z.Ya. Zhuchenko, W.T. Masselink, *High electric field performance of* $Al_{0.3}Ga_{0.7}As/GaAs$ *and* $Al_{0.3}Ga_{0.7}As/GaAs/In_{0.3}Ga_{0.7}As$ *quantum well micro-Hall devices*, Sens. Actuators A **101** (1-2), 62–68 (2002).

[246] J.S. Lee, Y.H. Ahn, K.H. Jeong, D.M. Kim, *Highly sensitive* $Al_{0.25}Ga_{0.75}As/In_{0.25}Ga_{0.75}As/GaAs$ *quantum-well Hall devices with Si-delta-doped GaAs layer grown by LP-MOCVD*, Sens. Actuators A **57** (3), 183–185 (1996).

[247] V. Cambel, G. Karapetov, P. Eliás, S. Hasenörl, W.-K. Kwok, J. Krause, J. Maňka, *Approaching the pT range with a 2DEG InGaAs/InP Hall sensor at* 77 *K*, Microelectron. Enginneering **51-52**, 333–342 (2000).

[248] Vas.P. Kunets, R. Pomraenke, J. Dobbert, H. Kissel, U. Müller, H. Kostial, E. Wiebicke, G.G. Tarasov, Yu.I. Mazur, W.T. Masselink, *Generation-recombination noise in pseudomorphic modulation-doped* $Al_{0.2}Ga_{0.8}As/In_{0.1}Ga_{0.9}As/GaAs$ *micro-Hall devices*, accepted to IEEE Sensors Journal , 1–10 (2003).

[249] Y. Sugiyama, T. Taguchi, M. Tacano, *Highly sensitive magnetic sensor made of AlGaAs/GaAs heterojunction semiconductors*, in: Proceedings of the 6th Sensor Symposium (Japan), 55–60 (1986).

[250] Y. Sugiyama, H. Soga, M. Tacano, *Highly-sensitive Hall element with quantum-well superlattice structures*, J. Cryst. Growth **95** (1-4), 394–397 (1989).

[251] M. Behet, J. Bekaert, J. De Boeck, G. Borghs, $InAs/Al_{0.2}Ga_{0.8}Sb$ *quantum well Hall effect sensors*, Sens. Actuators A **81** (1-3), 13–17 (2000).

[252] Vas.P. Kunets, J. Dobbert, W. Hoerstel, U. Müller, G.G. Tarasov, W.T. Masselink, H. Kostial, E. Wiebicke, H. Kissel, Yu.I. Mazur, *Low thermal drift in highly sensitive doped channel* $Al_{0.3}Ga_{0.7}As/GaAs/In_{0.2}Ga_{0.8}As$ *micro-Hall element*, to be published , 1–7.

[253] Vas.P. Kunets, U. Müller, J. Dobbert, R. Pomraenke, H. Kostial, H. Kissel, Yu. I. Mazur, G.G. Tarasov, W.T. Masselink, *Generation-recombination noise in doped-channel* $Al_{0.3}Ga_{0.7}As/GaAs/In_{0.2}Ga_{0.8}As$ *quantum well micro-Hall devices*, J. Appl. Phys. **94** (12), 7590–7593 (2003).

[254] S.A. Vitusevich, S.V. Danylyuk, N. Klein, M.V. Petrychuk, A.Yu. Avksentyev, V.N. Sokolov, V.A. Kochelap, A.E. Belyaev, V. Tilak, J. Smart, A. Vertiatchikh, L.F. Eastman, *Separation of hot-electron and self-heating effects in two-dimensional AlGaN/GaN-based conducting channels*, Appl. Phys. Lett. **82** (5), 748–750 (2003).

[255] V.A. Kochelap, V.N. Sokolov, N.A. Zakhleniuk, *Limitation and suppression of hot-electron fluctuations in submicrometer semiconductor structures*, Phys. Rev. B **48** (4), 2304–2311 (1993).

[256] Numerical calculation of electric field distribution within Greek cross micro-Hall devices by O. Bierwagen at Humboldt University, Berlin .

[257] A. Van der Ziel, *Noise: sources, characterization, measurement*, Englewood Cliffs, NJ:Prentice Hall (1973).

Curriculum vitae

Name: Vasyl Kunets
Date of birth: February 20, 1975
Place of birth: Brovary, Ukraine
Nationality: Ukrainian
Marital status: married, one daughter (born in April 2003)

Education

1982–1992	Secondary school, Brovary
1992–1997	Study of physics and mathematics at the Shevchenko University, Kiev
1996–1997	Diploma thesis: *Investigation of absorption spectra of* CdS_xSe_{1-x} *nanocrystals synthesized in borosilicate matrix* (Advisor: Dr. sc. N.R. Kulish)
1997	M.S. in Physics at the Shevchenko University, Kiev Specialization: Solid-State Physics

Scientific Career

1997–1999	Junior research assistant at the Institute of Semiconductor Physics, Ukrainian Academy of Sciences, Kiev • Optical spectroscopy of II-VI semiconductor structures
1999-present	Ph.D. student at Humboldt University Berlin, Department of Physics (Advisor: Prof. Dr. W. T. Masselink) • Development of micro-Hall sensor technology based on III-V semiconductor heterostructures • MBE growth of III-V semiconductor structures and accompanying characterization by electrical and optical measurements • Development and implementation of noise spectroscopy for Hall sensor characterization • Teaching activities like assistance in basic physics laboratory course

Acknowledgements

First of all, I want to express my gratitude to Prof. Dr. W.T. Masselink as my scientific advisor. He offered the unique chance to work in his research team for some years. Relying on his excellent experience and attitude towards modern electron device physics, I had the great opportunity to study and review modern semiconductor physics and technology. In particular, I have to thank for frequent and fruitful scientific discussions as well as for his continuous guidance and support. This applies not only to this thesis but also to my participation in the project No. MA 1749/4-1(2) granted by the Deutsche Forschungsgemeinschaft.

I am indebted to Prof. Dr. G.G. Tarasov and Dr. Yu. Mazur commending me to Prof. Dr. W.T. Masselink. In particular, I want to express my gratitude to Prof. G.G. Tarasov for countless scientific discussions offering new prospects to me.

Many thanks to Dr. W. Hoerstel for his valuable introduction and supervision in transport measurements. Especially, I am indebted for his kindly and qualified support in writing a new proposal for the micro-Hall sensor project being successfully approved. This gave me the real chance to finish this thesis. Many thanks to B. Herrmann for the practical assistance in Hall measurements.

Furthermore, I have to express my gratitude to Dr. Kostial for his permanent support in device processing, numerous advices and scientific discussions leading to many new ideas realized in my work. Additionally, I thank E. Wiebicke and A. Riedel for the technical help in device processing.

It is difficult to put into words my gratitude to my colleagues Dr. H. Kissel and Dr. U. Müller. Due to their permanent assistance and care about me as well as my family, I could feel myself in Berlin as at home. Many thanks for the numerous optical measurements, discussions and assistance in many computer problems. Due to their careful and critical reading of this thesis, I could somewhat improve my imperfect writing style, therefore helping the reader to understand the subject of the thesis better.

Dr. Däweritz and Dr. Hey gave me their kind permission to work in their MBE laboratory and gain experience in MBE growth.

R. Reichmann deserves my great gratitude for solving many organizational and management problems.

Many thanks to my mates Dr. C. Walter, Dr. F. Hatami, O. Bierwagen,

J. Dobbert, R. Pomraenke, S. Dressler for the collaboration and kindly support.

Last but not least, many thanks to my whole family. First of all to my parents. My brother Vladimir supported me morally and as an experienced physicist at the beginning of my scientific career when I met the most difficulties. Thanks to my patient wife Liliya for her endurance and my daughter Angelika.

Erklärung

Hiermit erkläre ich, die vorliegende Arbeit selbständig und nur unter Verwendung der angegebenen Literatur und Hilfsmittel angefertigt zu haben.
Ich habe mich anderwärts nicht um einen Doktorgrad beworben und besitze einen entsprechenden Doktorgrad nicht.
Ich erkläre die Kenntnisnahme der dem Verfahren zugrunde liegenden Promotionsordnung der Mathematisch-Naturwissenschaftlichen Fakultät I der Humboldt-Universitat zu Berlin.

Berlin, den 30.01.2004

Vasyl Kunets